Étude de photocatalyseurs en couches minces de TiO2 pour la production d'H2 : compréhension des mécanismes qui régissent la décomposition de molécules d'eau et rôle de nanoparticules plasmoniques

Maria-Isabel Mendoza-Diaz

Université Fédérale
Toulouse Midi-Pyrénées

THÈSE

En vue de l'obtention du
DOCTORAT DE L'UNIVERSITÉ DE TOULOUSE

Délivré par l'Université Toulouse 3 - Paul Sabatier

Présentée et soutenue par

Maria Isabel MENDOZA DIAZ

Le 24 novembre 2022

Étude de photocatalyseurs en couches minces de TiO_2 pour la production d'H_2 : compréhension des mécanismes qui régissent la décomposition de molécules d'eau et rôle de nanoparticules plasmoniques

---

Ecole doctorale : **GEETS - Génie Electrique Electronique,Télécommunications et Santé : du système au nanosystème**

Spécialité : **MicroNano Systèmes**

Unité de recherche :
LAAS - Laboratoire d'Analyse et d'Architecture des Systèmes

Thèse dirigée par
Carole ROSSI et Alain ESTEVE

Jury

M. Lionel SANTINACCI, Rapporteur
M. Pascal LENORMAND, Examinateur
Mme Carole ROSSI, Directrice de thèse
M. Mikhael BECHELANY, Président

Acknowledgements

Undertaking this PhD would not have been possible without the scientific and human support that I received from many people. I want to thank all of them for how much they have done for me.

First, I would like to express my deepest gratitude to my advisors Dr. Carole Rossi and Dr. Alain Estève. Thank you for your patience and for believing in my abilities since I contacted you when I was in Mexico in the fall of 2017. For motivating me, for giving me all the tools to achieve my goals and for your great support since the moment I arrived to LAAS. I'm boundlessly thankful for your help and guidance throughout all my PhD. For your wise directions that helped me finalize the dissertation. I will always be grateful and in debt to you.

I would also like to extend my gratitude from the funding received by the Mexican National Council for Science and Technology (CONACyT), I am honored for receiving this scholarship that allowed me to pursue my PhD. I am also grateful to the French National Centre for Scientific Research and the Occitan Region, which funding allowed to undertake the investigation projects.

I also wish to thank the reporters and members of the jury, Dr. Mikhael Bechelany and Dr. Lionel Santinacci, thank you for taking the time to read my manuscript and your feedback on my research. To Dr. Christophe Turpin and Dr. Pascal Lenormand, to all thank for your wise and thoughtful comments. I gratefully acknowledge the assistance too of Dr. Andrea Balocchi from LPCNO, your collaboration was key to one big part of my program, thank you tests, the discussions and meetings. To Dr. Mehdi Djahfari thank you for your invaluable insight and helpful contribution. To Dr. Kui Tan and Dr. Kolade from UTD, thank you for the measurements and responsive feedback, your work has

complemented greatly the studies. To the members of the clean room and LAAS, Ludovic, Aurèlie, Laurent Bouscayrol, Guillaume, Laurent, Adrien, Séverine, Benjamin, Jean Baptiste, Sandrine, Xavier, who listened to our problems and always found solutions.

I could not have finished this dissertation without the emotional support from my family. A mi mamá Maria Ema, gracias por tu inmenso e incondicional apoyo. Me has enseñado a superarme y luchar. Siempre serás mi mejor modelo a seguir. A mi abuela Victoria, por su amor y cariño. A mis familia y amigos en México Beatriz, Miguel M., Margarita, Carlos, Luz, Rosario, Petra, Alfonso, Miguel, Jesús Arturo, Luis, Rosita, Christian A., Christian, Marianela, Margarita, Victoria, Carolina, Fili, Alfonso, Hortensia, Arturo Mascareño, gracias su motivación y ánimos, y sobre todo por su inestimable apoyo hacia nosotras.

To Florent, thank you brighten my days and offering me your hand. To Cathy and Jean-Marie, thank you for opening your home to me, for your kind words and invaluable attentions.

This could not be a proper acknowledgement if I did not recognize all the group members and friends that have helped to achieve this. To Jeremy who introduce me to this great project, and taught me a lot. To Tao, thank you for your friendship, for teaching me and being there for me. To Baptiste, thank you for your support, for showing me the ways in the clean room and in LAAS. To Vidushi, thank you for being kind and fun and training me. To Sylvain, thank you all for sharing your wisdom and for your patience. Also, to my friends Raul, Vitek, Kamil, Felipe, Kostis and Corbi. You're all The Guy! You have enriched this journey in so many ways. Thank you for the discussions, jokes, games, advices, suggestions, all the memories I will cherish forever.

Abstract

An attractive approach for the energy industry's transition to sustainable and clean energy is the use of solar radiation to produce H_2. Among the different artificial photocatalytic processes, H_2 production through water splitting is probably the most intensely studied as the molecular gas exhibits a high volumetric energy density, no carbon footprint and can be either directly burned or used in fuel cells to produce electricity. In this process, light irradiation drives the redox reactions, as the photon excitation causes electronic transitions, that generate electron–hole pairs. Holes decompose water into protons (H^+), while the electrons reduce the absorbed H^+ to H_2.

Among various transition metal oxides, TiO_2 is widely used as a photocatalyst due to its low cost, high chemical stability, good optical activity and non-toxic nature. Although great strides have been made over the last decades on the development of TiO_2 based nanomaterials, identifying the factors that govern the kinetics of photocatalytic processes and understand their role is currently a subject of fundamental research.

In this context, this dissertation explores technological solutions, and discusses the principal mechanisms that yield the H_2 production under UV and visible light irradiation on TiO_2-based thin film photocatalysts, which were fabricated at the clean room facility of LAAS-CNRS.

The manuscript is composed of four chapters where three specific studies are addressed. The first study presents the fabrication of hybrid TiO_2/Au nanoparticle structures. Multiple characterization evidenced improvement on the charge carrier transport thanks to the synergistic mechanisms involving the Schottky barrier formation and plasmonic effects. In the second study, a technological approach is developed for the fabrication of 3D photocatalysts based on a silicon micromachining process, where

TiO_2/Au and Pd nanoparticles are further integrated. The influence of the enlarged surface on the morphology, quality, and catalytic performance is thoroughly investigated and correlated to the H_2 production. In the third study, the type and nature of defects, being oxygen vacancies and Ti interstitials are induced through thermal annealing on TiO_2 thin films, which are analyzed from the viewpoint of the electronic structure. The formation of intrinsic intermediate states in the band gap was correlated to the presence of these defects, which play a decisive role in the charge carrier kinetics. Discussion about promising results and challenges are also covered. Hence, these results give new directions for the fabrication of robust and light-driven photocatalysts for a broad range of applications from photocatalysis, electronics, sensing elements, to 3D metamaterials.

Résume

Une approche importante pour assurer une transition industrielle s'appuyant sur une énergie durable et propre est l'utilisation du rayonnement solaire pour la production d'H_2. Parmi les différents processus photocatalytiques artificiels, la production de H_2 par craquage de molécules d'eau est probablement la plus étudiée car le gaz moléculaire présente une densité d'énergie volumétrique élevée, une empreinte zéro carbone, et peut être directement brûlé ou utilisé dans des piles à combustible pour produire de l'électricité.

Dans ce processus, l'irradiation lumineuse entraîne des réactions redox, car l'excitation photonique provoque des transitions électroniques qui génèrent des paires électron-trou. Les trous permettent de décomposer l'eau pour générer des protons (H^+), tandis que les électrons réduisent les protons adsorbés en H_2. Parmi divers oxydes s métaux de transition, le TiO_2 est largement utilisé comme photocatalyseur en raison de son faible coût, de sa stabilité chimique élevée, de sa bonne activité optique et de sa nature non toxique. Bien que de grands progrès aient été réalisés au cours des dernières décennies pour le développement de nanomatériaux à base de TiO_2, les facteurs qui régissent la cinétique des processus photocatalytiques demeurent encore aujourd'hui mal compris et caractérisés. Ils font ainsi actuellement l'objet de recherches fondamentales.

Cette thèse explore des solutions technologiques et discute des principaux mécanismes qui conduisent à la production d'H_2 sous irradiation UV via l'utilisation de photocatalyseurs à base de TiO_2 déposé en couches minces dans la salle blanche du LAAS-CNRS.

Le manuscrit est composé de cinq chapitres incluant trois études distinctes. La première étude présente la fabrication de structures hybrides films minces TiO_2/nanoparticule d'Au. Nous démontrons l'amélioration du transport des porteurs de charge grâce aux mécanismes synergiques impliquant la formation de barrières Schottky et des effets plasmoniques. Dans la deuxième étude, une approche technologique est développée pour la fabrication de photocatalyseurs 3D basée sur un procédé de micro-usinage silicium, où le photocatalyseur hybride TiO_2/Au et TiO_2/Pd sont davantage intégrées. L'influence de l'augmentation de surface sur la morphologie, la qualité et les performances catalytiques du photocatalyseur est détaillé et corrélé à la production d'H_2. Dans la troisième étude, le type et la nature des défauts, à savoir des lacunes d'oxygène et des interstitiels de Ti, sont induits par recuits thermiques et caractérisés du point de vue de la structure électronique des surfaces photocatalytiques. La formation d'états intermédiaires intrinsèques dans la bande interdite est bien corrélée à la présence de défauts qui jouent un rôle déterminant dans la cinétique des porteurs de charge. Nous discutons l'ensemble de ces résultats et les défis qu'ils soulèvent. De nouvelles orientations pour la fabrication de photocatalyseurs robustese pour un large éventail d'applications allant de la photocatalyse, de l'électronique, des éléments de détection, aux métamatériaux 3D.

Table of contents

List of figures

List of tables

Abbreviations

a.u.	Arbitrary units
AEF	Area enlargement factor
AEF_{EAS}	Experimental area enlargement factor
AFM	Atomic force microscopy
AGS	Average grain size
ALD	Atomic layer deposition
APS	Average pore size
AR	Aspect ratio
c.p.s	Counts per second
CB	Conduction band
CBE	Conduction band edge
DC	Direct current
DFT	Density functional theory
DOS	Density of states
DRIE	Deep reactive ion etching
e^-	Electron
EASA	Electrochemical active surface area
EDS	Energy dispersive X-ray spectroscopy
EELS	Electron Energy Loss Spectroscopy
E_F	Fermi level
E_g	Band gap
EMP	Electron Probe Microscopy
E_{op}	Optical band gap
E_u	Ubarch energy
FFT	Fast Fourier transform
g	Dimensionless geometric factor

GHG	Greenhouse gas
h^+	Hole
H^+	Hydrogen protons
H_2	Hydrogen
HE	High energy component
HER	Hydrogen evolution reaction
hv	Energy of a photon (Planck's constant and frequency of light)
LE	Low energy component
LSPR	Localized surface plasmon resonance
LSV	Linear swept voltammetry
NPs	Nanoparticles
OER	Oxygen evolution reaction
OH^-	Hydroxyl species
PL	Photoluminescence
PVD	Physical vapor deposition
QE	Quantum efficiency
SAED	selected area electron diffraction
SEM	Scanning electron microscopy
SPR	Surface plasmonic resonance
TEM	Transmission electron microscopy
Ti(i)	Titanium interstitials
Ti^{3+}	Titanium (III) ions
TiO_2	Titanium dioxide
VB	Valence band
VBE	Valence band edge
Vis	Visible
Vo	Oxygen vacancies
XPS	X-ray photoelectron spectroscopy
XRD	X-ray diffraction
α	Absorption coefficient
Φ	Work function

General Introduction

The supply of secure, clean and sustainable energy is arguably the most important scientific and technical challenge facing humanity in the 21st century.[1,2] As the global population is expected to increase to 9.8 billion by 2050, is necessary to create new solutions to cover the energy global demand.[3,4]

At present, oil is still the largest primary fuel with a share of more than one third of the global primary energy mix and more than 95% of transport energy demand. The World Energy Assessment Report estimates that the future energetical demand can be covered by the total global fossil reserves (oil and gas).[4] However, the oil cost and its demand have risen substantially in the past few years. Therefore, a mounting anxiety about the economic and geopolitical implications of possible shortages in the supply of oil are expected in the future.

Moreover, considering the forecasted consumption of fossil sources, a significant problem in terms of climate change is expected. Proof of this is the production of energy through burning of fossil fuels, which constitutes around three-quarters of global greenhouse gas (GHG) emissions.[5] Among these gases, CO_2 is the single most important climate-relevant GHG in Earth's atmosphere, followed by ozone, N_2O, CH_4, and chlorofluorocarbons. Climate models have established the correlation between the Earth's temperature and GHG emissions. Considering the scenario predicted with an increase of 67.5% of carbon emission rate by 2050, major concerns rise about geophysical and biophysical impacts; and, effects on human health and wellbeing.[6]

Among the technological solutions: carbon sequestration, nuclear energy systems, and renewable energy resources, the later remains the best option to produce carbon-

neutral power. Furthermore, solar energy is one of the most attractive routes, as more energy from sunlight strikes the earth in 1 h (4.3×10^{20} J) than all of the energy currently consumed on the planet in 1 year (4.1×10^{20} J).[1] Solar conversion systems fall into three categories according to their primary energy product: (1) solar thermal systems, (2) solar electricity (photovoltaic technology), and (3) solar fuels.[7] Compared to photovoltaic devices and thermal technologies, solar fuels allow the production of a gas by means of photocatalysis that can be readily stored. This overcomes the drawbacks of intermittent solar radiation (inherent day-night and sunny-cloudy cycles), by storing the produced gas during day hours and allowing its posterior dispatchment and distribution.[8]

Molecular hydrogen (H_2) is a fuel that does not produce carbon dioxide and it exhibits the highest specific enthalpy of combustion of any chemical fuel. The utilization of H_2 is highly essential as a reactant in industrial chemical processes, *i.e.*, oil refining, ammonia and methanol production; and also for power generation of electric vehicles through fuel cells, which is one of the most attractive commercial uses nowadays.[9] Hence, the production of H_2 through low-cost environmentally clean processes appears to be a promising pathway enabling longer-term storage of renewable power and decarbonizing industry and transportation.[10]

The concept of H_2 production via water splitting was first reported in 1972 by Fujishima and Honda using a TiO_2 photo-electrochemical cell.[11] Furthermore, photocatalysis uses light to directly decompose water into H_2 and O_2 by using a semiconductor at ambient temperatures.[12] This represents an effective method for converting sunlight into clean and renewable H_2.

Water dissociation or water splitting by photocatalysis consists in a reaction related to the evolution of the stoichiometric amount of H_2 and O_2 driven by the consumption of photons by a photocatalytic material.[13] The redox reactions start with light irradiation with energy greater or equal to the band gap (E_g) of the photocatalyst (*i.e.*, $h\nu > E_g$). The photon excitation causes electronic transitions, called charge separation: electrons are excited from the valence band (VB) to conduction band (CB), leaving holes in the VB, generating thus e^-–h^+ pairs. Holes trigger the oxygen evolution reaction (OER) reaction to decompose water into hydrogen protons (H^+), while the electrons participate in hydrogen evolution reaction (HER) reaction to reduce the adsorbed of H^+ and produce H_2.[14,15]

Thus, the overall H_2 production efficiency of any photocatalytic system is governed by several factors, the surface area, as it delimits the concentration of chemically active reaction sites, and, the electronic structure, since the band gap determines the utmost light harvesting capability. Moreover, during the charge transport process where the photogenerated e^-–h^+ pairs separate and migrate to the semiconductor/solution interface, the charge carriers can suffer from serious

recombination. Hence a suitable morphology and stability of the photocatalyst would allow their efficient transport to the surface.[16]

TiO_2 is a widely used photocatalyst, which breakthrough dates back to the 1960s, due to its unique characteristics of low cost (less expensive than other catalysts such as ZnO, CdS or ZnS), good optical activity, high chemical stability, long durability, and non-toxic nature.[17] However, the photocatalytic efficiency is limited by its large bandgap (~3.2 eV), meaning that its activation requires an irradiation source with wavelengths lower than 388 nm, which is in the near-UV region.[18]

Till date, numerous studies explored nanostructured TiO_2 materials as potential photocatalysts, as they allow to increase the surface area-to-volume ratio, thus, increasing the number of catalytic active sites on their surface compared to bulk TiO_2.[19] Also, fabrication of TiO_2 based heterostructures with different dimensional materials (nanoparticles, nanorods, nanofilms, etc.) has been reported to be effective for photocatalysis, as the tuning of each component and its morphology is adjusted to create multifunctional architectures.[18] This includes the addition of noble metals, such as Pt, Au, Pd, Rh, Ni, Cu and Ag, enabling quantum confinement effects, such as localized surface plasmonic resonance (LSPR), which enhances the charge separation and allows the generation of hot electrons; and, is also well known to extend the absorption spectra to the visible.[20–22] Moreover, the enhancement of the photocatalytic activity has also been ascribed to the fermi level alignment, by the Schottky barrier formation. Thus, photo-excited electrons can be transferred from the CB to metal particles deposited on the surface of TiO_2, while photo-generated VB holes remain in the semiconductor.[23,24]

Although great strides have been made on the TiO_2 based heterostructure nanoengineering, the fundamental kinetics of photocatalytic processes and their potential charge transport synergies are still lacking. Which are mandatory to achieve the desired goal of developing more efficient catalytic systems.

At the Laboratory for Analysis and Architecture of Systems (LAAS), preliminary work was conducted by Jeremy Cure[25–27]. The development of TiO_2 films produced by DC sputtering in the clean room facility, showed promising results for the further development of large-surface and heterogenous TiO_2-based photocatalysts.

The program of work of this thesis was built in continuation with Cure's contribution with two main goals:

(1) the study of the principal structural factors and mechanisms that lead the water splitting reactions in TiO_2 thin films; and,

(2) the exploration of technological solutions to increase the H_2 production yield under UV and Visible (Vis) light irradiation while using bare TiO_2 thin films and TiO_2 thin films decorated with noble metal nanoparticles. Deposition of TiO_2 thin films was

carried by magnetron sputtering, as is a robust, cost-effective technique, which allows the fabrication of compact and resistant thin films with great adhesion on a large variety of substrates.

Results are detailed in the manuscript, organized into four chapters as follows:

Chapter 1 presents the motivations and problematics. The global energetic demand and climate model projections are introduced, followed by solar energy conversion systems with an emphasis in solar fuel technologies as potential solutions. Next, an overview of the H_2 present demand, renewable production technologies and the economy implications are given. A brief state of the art section is provided as well, starting with the water splitting photocatalysis mechanism and recent works on nanostructured photocatalysts. The chapter ends with a summary of fabrication techniques for TiO_2 and parameters that influence its photocatalytic activity: crystal structural properties, electronic band structure, charge carrier transport and local defects; overall constituting the basis of the photocatalysts that are developed in this work.

Chapter 2 presents the plasmonic and non-plasmonic contributions that drive the water splitting reactions in TiO_2 films decorated with Au nanoparticles (NPs), by evaluating the respective photocatalytic response under UV and Vis light. The chapter details the integration of particles at different depths into TiO_2 films in order to elucidate the specific contributions of the components on the electronic and chemical processes by selective light irradiation. As the Au NPs are deeply buried in the TiO_2 film, an increase in H_2 production by a factor of 52 compared to the bare TiO_2 is obtained. This is attributed mainly to the surface plasmon resonance effect that allows the energy transfer to the charge carriers at the particle/semiconductor interface and the generation of hot electrons under UV+Vis light.

Chapter 3 presents a technological study exploring silicon deep reactive etching to fabricate robust and repeatable TiO_2 3D photocatalysts with enlarged surface (surface area increased by 9.6 times compared to flat TiO_2). A first section discusses five pattern designs considering the technological constraints imposed by the use of magnetron sputtering technique to deposit the TiO_2 thin film. The influence of the area enlargement factor on the morphology, quality, and H_2 production under UV+Vis irradiation of the 3D photocatalyst is then presented. A 3D photocatalyst exhibits an enhancement of H_2 production by a factor of 13 when the specific surface is 3 times that of the planar TiO_2. An additional enhancement factor of 48 and 213 are obtained when Au and Pd NPs, respectively, are deposited onto the 3D photocatalysts.

Chapter 4 presents an in-depth study of the local defects present in TiO_2: oxygen vacancies (Vo) and Ti interstitials (Ti(i)), focused on their influence on the semiconductor band structure, as gap states acting as trap charges that boost the charge separation. Structural and morphological studies, chemical and optical-electronic spectroscopy

techniques supported by photoluminescence measurements and DFT calculations, were carried for plain TiO_2 films annealed at different temperatures from 200 to 700 °C in inert atmosphere. The electronic structure and photocatalytic activity, determined the correlation between surface defects and intrinsic intermediate gap states, which play a decisive role in the charge carrier kinetics. The presence of Ti^{3+} species on the surface was attributed to Ti(i) that generate shallow and deep electron traps, whereas OH^- adsorbates create deep hole traps, hence extending selectively the lifetime of the photogenerated charges.

A general conclusion is presented summarizing the major findings, as well as an outlook and perspectives for the future research. The reader will also find an Annex section at the end of each chapter with complementary information of characterization results and methods.

Chapter 1

State of the Art, problematics and objectives

1.1 Introduction

1.1.1 The energetic demand and climate change

Energy crises in the latter part of the 20th century, as well as the current increase in the cost of oil, emphasize the need for alternative sources of energy. The supply of secure, clean, sustainable energy is arguably the most important scientific and technical challenge facing humanity in the 21st century.[1,2] In 2001, worldwide primary energy consumption was 425×10^{18} J, which is equivalent to a rate of 13.5 TW. Yet, the global demand for energy is expected to continue to escalate in the coming decades. The Intergovernmental Panel on Climate Change, an organization established by the World Meteorological Organization and the United Nations Environment Program outlines an energetic global scenario depicted in Table 1.1. As predicted, the global population is expected to increase to 9.8 billion by 2050. With no changes in the average energy intensity, the world energy consumption rate would grow as well by 50% in 2050 to 27.6 TW.[4] However, the global average energy intensity has declined over the past 100 years, due to improvements in technology throughout the energy production, distribution, and end-use chain.[28] This

scenario raises a question about the economy security and the availability of energy sources on the planet.

Table 1.1 World energy statistics and projections.

Definition	Units	2001 [1]	2050 [2]	2100 [2]
Population	Billion persons	6.145	9.8	10.4
Energy consumption rate	TW	13.50	27.6	43.0
Carbon emission rate	GtC $year^{-1}$	6.57	11.0	13.3
Equivalent CO_2 emission rate	$GtCO_2$ $year^{-1}$	24.07	40.3	48.8

[1] Adapted from Ref. [29]

[2] Scenario B2 adapted from Ref. [3]

The global energy mix demand, defined by the primary energy consumption, has evolved over the last few centuries. After the industrial revolution, the rise of coal increased, followed by oil and gas, and by the turn of the 20th century, hydropower. Figure 1.1 shows the global energy consumption by source after 1965, note that the use of fossil fuels, which are the sum of coal, oil and gas, dominate the energetic consumption. In 2019, 84.3% of the global demand, was coming from fossil fuels, whereas the 15.7% left came from low-carbon sources, *i.e.,* nuclear and renewable energies: hydropower, wind, solar, bioenergy, geothermal and wave and tidal.[5]

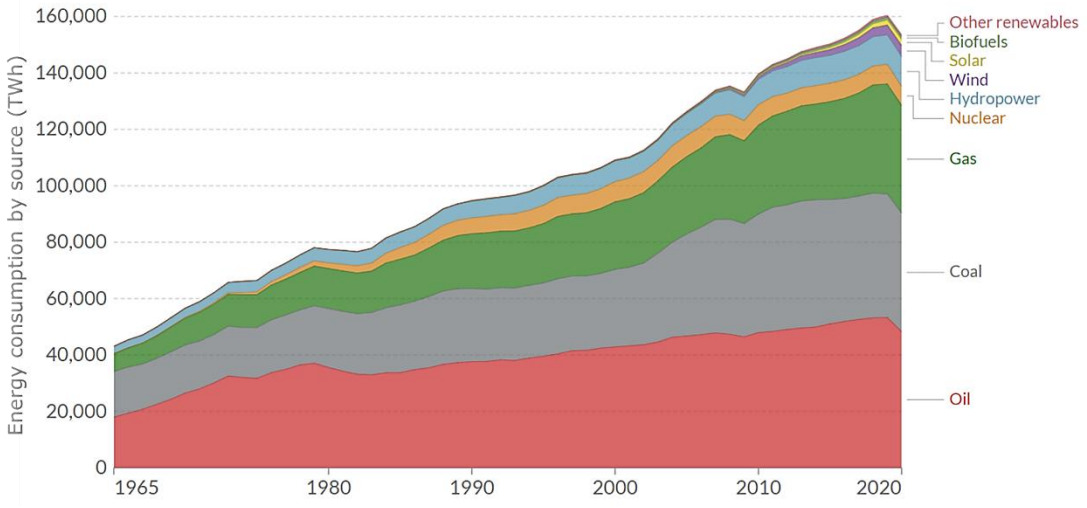

Figure 1.1 Global primary energy consumption by source. Note: 'Other renewable resources' include geothermal, biomass and waste energy.[5,30]

At present, oil is still the largest primary fuel with a share of more than one third in the global primary energy mix and more than 95% of transport energy demand.[31] The World Energy Assessment Report estimates that the future energetical demand can be covered by the total global fossil reserves (*i.e.* 90% confidence) including oil and gas

reserves (*i.e.* natural gas and methane clathrates); coal, shales and tar sands. Hence, the current sources could support the energy consumption rate globally for at least several centuries.[4]

However, due to the increased demand from developing countries the oil cost has increased substantially in the past few years, the amount of imported petroleum is likely to rise to 60% by 2025 in US.[32] On the other hand, there is a high geographical concentration of oil with a growing dependency on a few countries, often politically unstable. Therefore, a mounting anxiety about the economic and geopolitical implications of possible shortages in the supply of oil are expected in the future. Moreover, considering that the current sources would provide an economically viable panorama, the consumption of fossil energy at that rate, will produce a potentially significant global issue in terms of energy supply and climate change.

Climate change establishes the correlation between the Earth's temperature and greenhouse gas (GHG) emissions. The average annual temperature of the Earth has increased since 1800, and the present temperature of Earth is higher than any in thousands of years.[33] Most scientists agree that global warming is attributable to human activities that may have overtaken natural variations as the principal factor influencing the temperature. Proof of this is the production of energy through burning of fossil fuels which constitutes around three-quarters of global greenhouse gas (GHG) emissions.[5] Among these gases, CO_2 is the single most important climate-relevant GHG in Earth's atmosphere, followed by ozone, N_2O, CH_4, and chlorofluorocarbons.

Over a timescale of 10 to 30 years, emitted CO_2 accumulates in the atmosphere (~50%) and the near-surface layer of the oceans.[34] This is because CO_2 does not condensate and precipitate from the atmosphere by any natural mechanism, unlike water vapor.[35] It has been reported that CO_2 will persist globally for the next 500 to 2000 years or more.[36] During the past 650,000 years the atmospheric CO_2 concentration has been highly correlated, but is not necessarily the cause, to temperature swings that have caused ice ages on the planet. Over this period, the CO_2 concentration has variated between 210 and 300 ppm.[37] In 2010, the CO_2 concentration was 390 ppm, which is far in excess of the 280 ppm that is more typical for the interglacial maximum.[36] Climate models predict a variety of different global responses in terms of serious sea level rises and changes in the hydrological cycle for CO_2 levels of 550 ppm.[38] Currently, local air pollution from road transport is becoming an alarming issue for urban air quality.[39] Considering the scenario predicted in Table 1.1 with an increase of 67.5% of carbon emission rate for 2050 (~650 ppm of CO_2 concentration), a major concern rises about environmental effects.

With regard to the impacts of climatic change, there will be an increasing number of negative impacts as greater climatic change occurs. These modifications will depend on concurrent changes in the amount, timing, and nature of seasonal precipitation; and

also on the extent to which previous human disturbances increase the vulnerability of natural ecosystems to climatic change, to mention a few factors.[6] Despite these uncertainties, given current knowledge, geophysical impacts, biophysical impacts, and impacts on human health and wellbeing, are predicted. Furthermore, it has been stated that at a change in the global mean temperature between 1 and 2 K can lead to trespass the threshold for significant rise of the sea level, and harms in the socio-economic and food-producing systems, and terrestrial ecosystems and forests.[40]

Hence, security of supply and climate change represent two major concerns about the future of the energy sector. Urging the need for technology development towards a carbon-neutral power and the intervention of mitigation policies.[41] Regarding technological development, three prominent options for sustainable production of carbon-free energy actively discussed in the literature are:

- carbon sequestration,
- nuclear energy systems, and
- renewable energy resources

The challenge for carbon sequestration is finding secure storage for the 25 billion metric tons of CO_2 produced annually on Earth. This yearly global emission would occupy a huge volume of 12,500 km^3. Additionally, beyond finding storage volume, carbon sequestration also must prevent leakage. A 1% leak rate would nullify the sequestration effort in a century. Nuclear power, even though has been a key source of low-carbon energy for many countries across the world, relies on finite resources, for instance the terrestrial uranium resource base would be exhausted in 10 years.[42] Moreover, nuclear waste end products constitute an irreversible cycle.[43] On the other side, renewable resources (*i.e.*, wind, hydropower, solar, wind, geothermal, biomass and tidal energy) remain the best option to produce carbon-neutral power. In 2019, around 11% of global primary energy came from renewable technologies, where hydropower represented 60.25% of the energy generated.[30] However, within the various renewable technologies, solar energy is by far the most available resource. More energy from sunlight strikes the earth in 1 h (4.3×10^{20} J) than all of the energy currently consumed on the planet in 1 year (4.1×10^{20} J in 2001).[1] In the next section the advantages and limitations of solar energy will be exposed briefly, important aspects correlating light intermittency to the different types of solar technologies will be discussed in terms of the technology principle and feasibility.

1.1.2 Solar energy

The sun is a major source of inexhaustible free energy for the planet Earth. The solar energy concept consists in the harvesting and utilization of light and/or heat energy generated by the Sun and technologies involved in achieving such goals. 7.6 PW in solar power is incident on the desert regions around the world, and if only tap 10% of it at an energy conversion efficiency of 10%, it would be possible to generate five times the

current world's energy requirement.[43] Figure 1.2 depicts the annual average intensity of solar radiation over the surface of the earth. Research has shown that "black dot" areas could provide more than the entire world's total primary energy demand, assuming a conversion efficiency of 8%.[44] Despite this huge potential and increase in awareness, the contribution of solar energy to the global energy supply is still negligible, in 2019 only 1.04% of the global primary energy consumption was solar.[30] Indicating that the solar technologies are not yet mature enough to meet the energy demand.

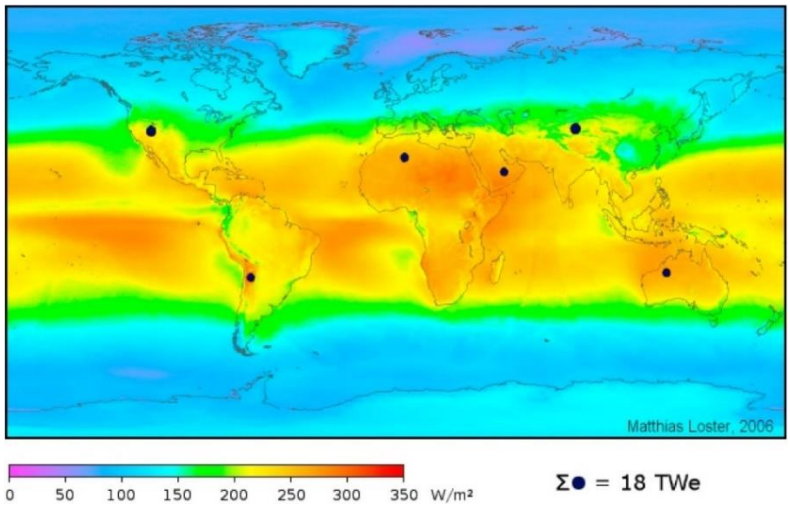

Figure 1.2 Annual average solar irradiance distribution over the surface of the Earth. Retrieved from [44].

Solar energy conversion systems fall into three categories according to their primary energy product: (1) solar thermal systems, (2) solar electricity (photovoltaic technology), and (3) solar fuels. Solar thermal energy systems absorb solar irradiation by a solar collector as heat which is then transferred to a working fluid. The heat carried by the working fluid can be used to either provide domestic hot water/heating, which can further be stored.[7] Thermal energy can also be used for electricity generation by the transmission of energy from the working fluid to a generator. Nevertheless, this technology requires a complex design with big areas and the use of materials economically competitive.[45]

Photovoltaic technology is based on the principle of solar-to-electric power conversion. In recent years, photovoltaic technology involving the use of semiconductors has become a highly attractive option to address the energy demand. The intense research efforts of scientists regarding solar options have helped to yield an improved efficiency of photovoltaic technology. A triple-junction GaInP/(Al)GaAs/Si device overlying III–V cell combination reported a combined efficiency of 34.5%; and in the case of hybrid perovskite cells, an efficiency increase of ca. 25.5% was reported in 2020 [46,47]. The

technology is also available on the market, yet, the systems involved the use traditional crystalline silicon or gallium arsenide, commercial thin-film cells (CdTe, amorphous silicon, $CuInSe_2$). Constant progress is done to use thin-film technologies composed of perovskites, organic materials and quantum dots [48].

One of the drawbacks of thermal and electrical solar systems is that the generated energy cannot be directly used as fuel. This factor is also important considering the intermittency of sunlight and its intensity fluctuations. Solar irradiation depends on geographical position, day, time, and season;[49] meaning that once the fuel is produced is necessary to facilitate its distribution and storage. Thermal devices only allow to store heat, which cannot be transformed easily to electricity. Compared to photovoltaic devices and thermal technologies, solar fuels allow the production of a gas that can be readily stored. This overcomes the drawbacks of intermittent solar radiation (inherent day-night and sunny-cloudy cycles), by storing the produced gas during day hours and allowing its posterior dispatchment and distribution. In this way, solar fuels are capable of replacing electricity, by supplying the energy for transport, space conditioning, fabrication processes, cooking, lighting, and communication.[8]

Solar fuels technologies involve the production of a gas by means of photocatalysis, and these can be further boosted by means of photoelectrocatalysis. A number of potentially important reactions can be driven by solar light to produce fuels. The two most common photocatalytic reactions are CO_2 reduction, to produce fuels such as CO, formate, methane and methanol, ethanol and ethane; and water splitting, to produce H_2.[50,51] Figure 1.3 depicts these and other common reactions of solar fuels. These reactions involve multiple electron and proton transfer steps, and they can require electrocatalysts for efficient energy conversion, this is the case for CO_2 reduction. Some inroads to CO_2 reduction have been made on photo- and electro- catalytic fronts, but generally the precise path to CO_2 reduction requires high temperatures ranging from 300 to 400 °C and hence, additional CO_2 is generated for producing the energy required to reach such temperatures.[42,52] In addition, the voltage supply for CO_2 formation is very negative in water and in most common solvents; consequently, it is necessary a high overpotential for the reaction to occur.[53]

On the other hand, hydrogen can be readily produced from water and its reduction can take place at ambient temperatures. Powerful developments have been reported in the last years on artificial nanoscale assemblies of new organic and inorganic materials and morphologies. New methods of nanoscale fabrication, characterization, and simulation create new opportunities for understanding and manipulating the molecular and electronic pathways of solar energy conversion. However, while these laboratory successes demonstrate the appealing promise of direct solar fuel production, there is an enormous gap between the present state of the art and a deployable technology. In the next section

a summary about Hydrogen energy is provided, a brief discussion on the hydrogen economy is depicted as well as the means to produce it.

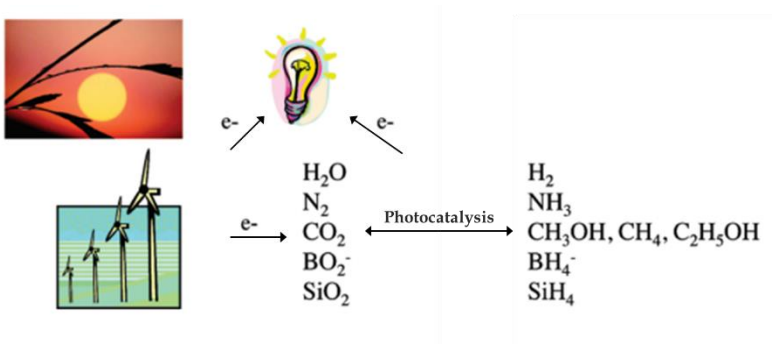

Figure 1.3 Scheme of fuels produced by solar energy [50].

1.1.3 Hydrogen

Nowadays, hydrogen is primarily used in the chemical industry, but its carbon-free characteristics represent a highly attractive solution. Molecular hydrogen is a fuel that does not produce carbon dioxide, it exhibits the highest specific enthalpy of combustion of any chemical fuel,[12] and it can be obtained from renewable sources such as water as will be explained later. From the market perspective, hydrogen is both an energy carrier and a chemical product involved in a range of industrial processes. Overall, hydrogen can be produced from any energy source, whether fossil, nuclear, or renewable. In this respect, the production of hydrogen through low-cost environmentally clean processes by means of renewable energy sources,[54] appears to be a promising pathway to enabling longer-term storage of renewable power and decarbonizing industry and transportation.[10] In this section, the present applications of hydrogen will be described, as well as a brief overview of the production technologies and an introduction into the so-called hydrogen economy.

1.1.3.1 Hydrogen uses and present demand

The utilization of hydrogen is highly essential as a reactant in industry chemical processes, and in a small scale as a chemical energy. In 2020 hydrogen demand was ~90 Mt (million metric tons), with more than 70 Mt used as pure hydrogen and less than 20 Mt mixed with carbon-containing gases in methanol production and steel manufacturing. Almost all this demand was for its use in oil refining, followed by ammonia and methanol production.[9] Table 1.2 summarizes the main applications of hydrogen by industry sector.

Oil refining is the largest consumer of hydrogen today (close to 40 Mt in 2020), hydrogen is used as a reactant in process such as hydrocraking, where it reacts with a hydrocarbon in the presence of a catalyst, for petroleum production. And for ammonia, it is used to hydrogenate sulfur and nitrogen compounds in hydro-processing of ammonia. In the metallurgical and nuclear industry, hydrogen is used to scavenge the oxygen level

in boiling water reactors. Another use of hydrogen as direct energy is applied by the NASA as propellant fuel in a mixture of H_2 and O_2.[55]

One of the most attractive commercial uses of hydrogen, is for power generation through fuel cells, which commenced in the early 1990s. A fuel cell engine is an electrochemical cell that splits the cation and the anion in the reactant produce direct current (DC) power to run electric vehicles. Since its powered with hydrogen, the product of the chemical reaction is water.[56] Thanks to this a wide variety of fuel cell vehicles (FCVs) are now commercialized (see Table 1.2).[57,58]

Table 1.2 Uses of hydrogen in different industries.

Industry	Uses
Oil	▪ Removal of sulfur and other impurities ▪ Hydrocracking of large hydrocarbons to fuel distillates (*i.e.*, petroleum, methanol, refined fuels)
Chemical	▪ Reactant for production of fertilizers through hydro-processing (*i.e.*, ammonia)
Food	▪ Conversion of sugars to polyols ▪ Conversion of edible oils to fast ▪ Conversion of tallow and grease to animal feed ▪ Hydrogenation of unsaturated fatty acids
Plastics	▪ Synthesize of nylons, polyurethanes, polyesters, polyolefin ▪ Cracking used plastics to produce lighter molecules that can be recycle
Metals	▪ O_2 scavenger ▪ Reductive atmosphere for production of iron, magnesium, molybdenum, and etc. ▪ Welding torches ▪ Heat treatment to improve ductility and machining quality, to relieve stress, to harden, to increase the tensile strength, changing magnetic or electrical characteristics
Electronics	▪ 'Epitaxial' growth of polysilicon ▪ Manufacture of vacuum tubes ▪ Heat bonding material ▪ Semiconductor manufacturing
Glass	▪ High temperature cutting torches ▪ Glass polishing ▪ Heat treatment of optical fibers ▪ Reductive atmosphere for float-glass process
Electric power	▪ Coolant for large generators of motors ▪ Nuclear fuel processing ▪ Fuel cells for transportation (*i.e.*, power cars, buses, forklift trucks, submarines and ships)
Fuel	▪ Automotive (in internal combustion engine)

- Aerospace as rocket propellant

1.1.3.2 Production of hydrogen: available technologies

The technologies related to hydrogen production are not only based on renewable resources but on fossils as well. Around 95% of the current hydrogen production is done through processes using fossil fuels, with the remainder produced predominantly via electrolysis. Meanwhile, hydrogen produced from renewable sources, *i.e.,* green hydrogen, makes up less than 0.1% of the world's annual hydrogen supply, according to the Green Hydrogen Coalition, a California-based nonprofit advocacy group.[59] Table 1.3 shows the different technologies specifying the feed source a brief review of them is described here. Both technologies will be briefly explained next.

Fuel technologies that involve hydrocarbons are called reforming technologies, these are steam and autothermal reforming and partial oxidation. Reforming consists in an endothermic reaction of a hydrocarbon material such as gasoline, ammonia, or methanol heated by an external source in order to oxidize the fuel and produce the hydrogen stream. However, these processes produce large amounts of CO and CO_2, requiring secondary water gas-shift reactors with temperatures ranging 200 to 350°C.[60] The technology dates back to 1924; and nowadays is an important building block in the bulk chemicals industry for the synthesis of ammonia, methanol, synthetic natural gas (SNG) and hydrogen for refinery operations and fuel cells.[61] Among these technologies, steam reforming of methane is the most common hydrogen production method in commercial use today.[32]

Other similar fuel reforming technologies which are not based on hydrocarbons, are plasma reforming, similar to conventional reforming, but the reaction is initiated with electricity or heat. Technologies still under development, are aqueous phase, which can use fuels that cannot be vaporized such as glucose, works a low temperature and suppress CO;[62] and ammonia reforming, which allows to work with the inexpensive fuel at low pressures.[32]

Table 1.3 Summary of hydrogen production technologies.[32]

Technology	Feed stock	Efficiency	Maturity
Steam reforming	Hydrocarbons	70-85%	Commercial
Partial oxidation	Hydrocarbons	60-75%	Commercial
Autothermal reforming	Hydrocarbons	60-75%	Near term
Ammonia reforming	Ammonia	NA	Near term
Biomass gasification	Biomass	35-50%	Commercial
Photocatalysis	Sunlight + water	0.5%	Long term
Dark fermentation	Biomass	50-80%	Long term
Photo fermentation	Biomass + sunlight	0.1%	Long term
Alkaline electrolyser	Water + electricity	50-60%	Commercial

Solid oxide electrolysis cells	Water + electricity + heat	40-60%	Med. Term
Photoelectrochemical water splitting	Water + sunlight	12.4%	Long term

Renewable-based technologies, which were briefly discussed in the previous section, are divided into two approaches 1) biomass-based and 2) hydrogen from water. These are explained as follows:

1. *Biomass-based approaches.* Biomass is available from a wide range of sources such as animal wastes, municipal solid wastes, crop residues, short rotation woody crops, agricultural wastes, sawdust, aquatic plants, short rotation herbaceous species (*i.e.*, switch grass), waste paper, corn, and many more. For hydrogen generation, the current biomass technologies include gasification, pyrolysis, conversion to liquid fuels by supercritical extraction, liquefaction, hydrolysis, etc. followed in some cases by reformation, and biological hydrogen production.[32] Research in bio-hydrogen has substantially increased over the last years since it allows the modification of microorganisms to improve their photocatalysis using solar energy. As denoted in Table 1.3, most of these technologies are still under development. One of the major challenges to this technology is the slow hydrogen production rate. According to Levi,[63] a bioreactor ranging from 1 to 1700 m^3 would be required to provide residential power with a 5 kW proton exchange membrane (PEM) fuel cell.

2. *Hydrogen from water*. Also called water splitting, it can be divided into three categories: electrolysis, thermolysis, and photocatalysis.
   - *Electrolysis.* An electrical current pass through two electrodes to break water into hydrogen and oxygen using a microporous separation or a membrane.[64] Commercial low temperature electrolyzers have system efficiencies of 56 – 73% (70.1 – 53.4 kWh kg^{-1} H_2 at 1 atm and 25 °C). Yet, electrolyzers are not capable of producing high purity hydrogen, and due to the electricity intake, it results in higher emissions compared to natural gas reforming.[65]

   - *Thermolysis.* Heat alone is used to decompose water to hydrogen and oxygen. Research in this area stopped after the mid-1980s. Since the water decomposes at 2500 °C, chemical reagents have been proposed (such as corrosive materials) to lower the temperatures, but this typically requires high pressures. Hence, it is still not competitive compare to other hydrogen generation technologies.[66,67]

   - *Photocatalysis.* The concept of hydrogen production via water splitting was first reported in 1972 by Fujishima and Honda using TiO_2 a photo-electrochemical cell.[11] The use of sunlight to directly decompose water into hydrogen and oxygen

by using semiconductor makes it an effective method for converting solar energy or sunlight into renewable energy source, as hydrogen provides nearly zero global warming and air pollutants.[68,69] This technology is divided in (1) photochemical-cell reactions and (2) photo-electrochemical-cell reactions, where the latter requires external voltage. The mechanisms that drive these two processes will be detailed in the next section. The advantages of the technology are that it operates the oxidative and reductive reactions simultaneously reactions; thus, representing a comparatively low cost.[70] Requirements for photocatalytic materials include stability and durability in aqueous solutions. Furthermore, structural and electronic properties of semiconductor photocatalysts basically determine the process of photocatalytic H_2 production.[16]

1.1.3.3 Hydrogen economy

In order to ensure a sustainable and cost-efficient energy system, hydrogen economy is presumed to be one of the solutions to these challenges due to its carbon-free characteristics. In the 1970s, the term 'hydrogen economy' was defined as a "substantial fraction of energy is delivered by hydrogen made from sources of energy that have no net emissions of greenhouse gases".[58]

Presently, there are three major technological barriers to be resolved for a transition from a carbon-based to a hydrogen-based economy:

- cost of efficient and sustainable hydrogen production,
- storage and distribution,
- final use

Other important aspects also play an important role on the pathway to stablish hydrogen as a strong economical actor, such as the rate of advances of various technologies that use hydrogen and for the implementation of restrictions and polices on greenhouse gases.[39] This subsection discusses briefly the current status with regard to each functional area.

As mentioned in the previous section the most mature technology to produce hydrogen is from fossil fuels by steam reforming: 50% from natural gas, 30% from oil, and about 20% from coal. Electrolysis of water represents 4% of world production. Despite the fact that the cost of hydrogen from hydrocarbon resources is still too expensive compared to gasoline;[58] it is the most mature technology and least expensive method of hydrogen production.[58] In this regard, the safe carbon capture, utilization and storage (CCUS) of CO_2 may pose serious problems, not because of inadequate technology, but with respect to logistics, infrastructure, costs, safety, and energy consumption.

However, strong efforts are being implemented in refineries to capture CO_2 from the gasification units and changing the technology to electrolytic H_2.[9] As well as the development of strategies to decarbonize the industry. According to the type of CO_2 capture strategies and type of energy driver for the process, hydrogen is classified in gray, brown, blue and green. Figure 1.4 depicts each process:

- *Gray.* Produced from natural gas through steam methane reforming (SMR) where CO_2 emissions are not mitigated.
- *Brown.* Produced from coal through biomass gasification, CO_2 emissions are not mitigated.
- *Blue.* Produced from natural gas through steam methane reforming (SMR), the carbon generated is captured and stored underground through industrial carbon capture and storage (CSS).
- *Green.* Produced by using clean energy from surplus renewable energy sources, such as solar or wind power, to conduct the water splitting via electrolysis. Also referred to as "clean hydrogen".

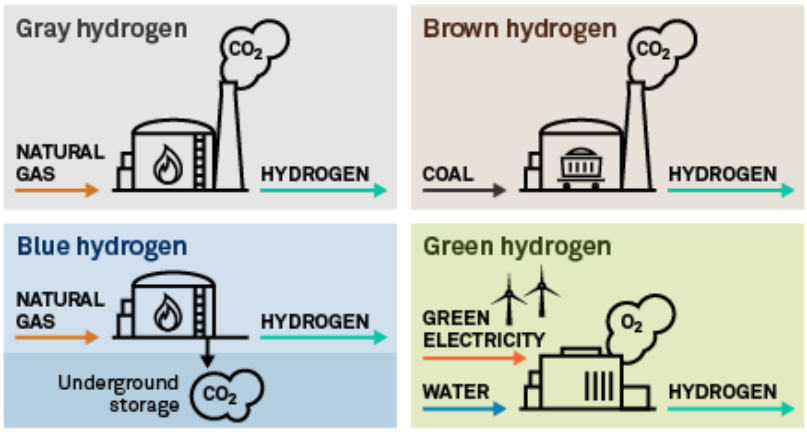

Figure 1.4 Color classification of hydrogen by environmental impact. [59]

Yet, at present the production of renewable-based technologies, incurs in high conversion losses, and –in the case of gaseous fuels– new distribution and infrastructure are required (*i.e.*, fuel cells to convert the gas to electricity).[31] Depending on regional gas prices, the levelized cost of hydrogen production from natural gas ranges 0.5 to 1.7 USD kg^{-1}. Using CCUS technologies to reduce the CO_2 emissions increases the to 1 to 2 USD kg^{-1}. Using renewable electricity to produce hydrogen costs 3 to 8 USD kg^{-1}.

Storage of hydrogen material is crucial for mobile and stationary applications. One of the main drawbacks of hydrogen is associated with its huge on-board storage tank because of extremely low density of hydrogen,[39] since at standard temperature and pressure (STP), the storage volume of hydrogen gas is 3000 times larger than an equivalent amount of gasoline. The main storage methods include:

– high-pressure gas cylinders (up to 800 bar),
– liquid hydrogen in cryogenic tanks (at 21 K),
– adsorbed hydrogen on materials with a large specific surface area (at T < 100 K),
– absorbed in a host metal (at ambient pressure and temperature), etc.

Cryogenic systems would allow to store hydrogen with a big density, however these systems have high energy loses. The immediate challenge is to find a storage material that satisfies three competing requirements including (i) high hydrogen density, (ii) reversibility of the release/charge cycle to be compatible with the present fuel cells technology; and, (iii) fast release/charge kinetics with minimum energy barriers to hydrogen release and charge.[39]

The third state strategical challenge of the hydrogen economy is the use of hydrogen. The future demand is expected to grow, in 2020 the global hydrogen demand was 88.48 Mt, and it is forecasted to be 210 Mt in 2030. Furthermore, according to the normative Net Zero Emissions by 2050 Scenario (NZE) by the IEA, hydrogen energy will cover 10% of the total global energy demand in 2050. Within the future, hydrogen applications are expected to grow in the following sectors [71]:

– Oil refining powered by hydrogen, in order to meet the standards.
– Hydrogen mobility (through synthetic fuels, biofuels, full-hydrogen cars or range extenders) will develop.
– Interconnection between energy carriers (through power-to-gas).

The implementation of demand-pull measures into hydrogen business opportunities (combined with accurate technology-push measures) has been notorious in the last years. In 2021, 17 governments released hydrogen strategies, more than 20 governments have publicly announced they are working to develop strategies. Sixteen projects for producing hydrogen from fossil fuels with carbon capture are operational today, producing 0.7 Mt of hydrogen annually. Another 50 projects are under development and, which promise an annual production of 9 Mt by 2030.[72]

Overall, green hydrogen appears to be a promising pathway to enable long-term storage of renewable power and decarbonizing industry and transportation. Among the technologies, photocatalysis, in which the inexhaustibly abundant, clean, and safe energy of the sun can be harnessed for sustainable, nonhazardous, and economically viable technologies, is a major advance in this direction. In the subsequent subsection the fundamentals of photocatalysis water-splitting is presented, followed by an overview of materials used as photocatalyst for the production of hydrogen.

1.2 Fundamentals of water splitting photocatalysis

Water dissociation or water splitting by photocatalysis consists in a reaction related to the evolution of the stoichiometric amount of H_2 and O_2 driven by the consumption of

photons by a photocatalytic material.[13] Furthermore, water splitting is a thermodynamically uphill reaction; under standard conditions the Gibbs free energy for the conversion of one mole of water to one mole of hydrogen and half mole of oxygen is +237.2 kJ mol^{-1} analogous to $\Delta E° = 1.23$ eV, hence the photocatalyst must possess a minimal band gap value of 1.23 eV for the efficient photocatalyzed hydrogen evolution [19,73]. Semiconductor's band structure is composed of a valence band (VB) and conduction band (CB), which are separated from one another by the band gap (Eg). This makes semiconductors the first choice for this application, furthermore its electronic structure and intrinsic nature allows the improvement of the charge separation,[21] this mechanism will be detailed next.

The water splitting processes can be classified into two mechanisms: (1) photocatalysis (PC) and (2) photoelectrochemical (PEC) water splitting. Both processes involve the water splitting reaction redox reaction. Equation 1.1 and 1.2 show the oxygen evolution reaction (OER) and hydrogen evolution reaction (HER), respectively.[14] The redox reactions start with light irradiation with energy greater or equal to the band gap of the photocatalyst *i.e., hv* > Eg, where Eg is the band gap energy. The photon excitation causes electronic transitions, called charge separation: electrons are excited from the VB to CB, leaving holes in the VB, generating thus e^-–h^+ pairs. Holes trigger the OER reaction to decompose water into hydrogen protons (H^+) (Eq. 1). While the electrons participate in HER reaction to reduce the adsorbed H^+ and produce H_2 (Eq. 2).[16,19]

Oxygen evolution reaction (OER):

$$2H_2O + 4h^+ \rightarrow O_2 + 4H^+ \qquad \text{Equation 1.1}$$

Hydrogen evolution reaction (HER):

$$4H^+ + 4e^- \rightarrow 2H_2 \qquad \text{Equation 1.2}$$

Next, the two types of photocatalytic water splitting mechanisms will be detailed.

1.2.1 Photocatalytic water splitting

In PC water splitting, light energy is directly used to carry out the catalytic reactions.[49] Thus, the band gap determines the utmost light harvesting capability for solar water splitting. The photogenerated e^-–h^+ pairs are required to separate and migrate to the semiconductor/solution interface. Figure 1.5 depicts the OER and HER reactions already mentioned. During the oxidation reaction, the water decomposes into oxygen and protons (H^+). Next, the electrons reduce the absorbed of H^+ to produce H_2.

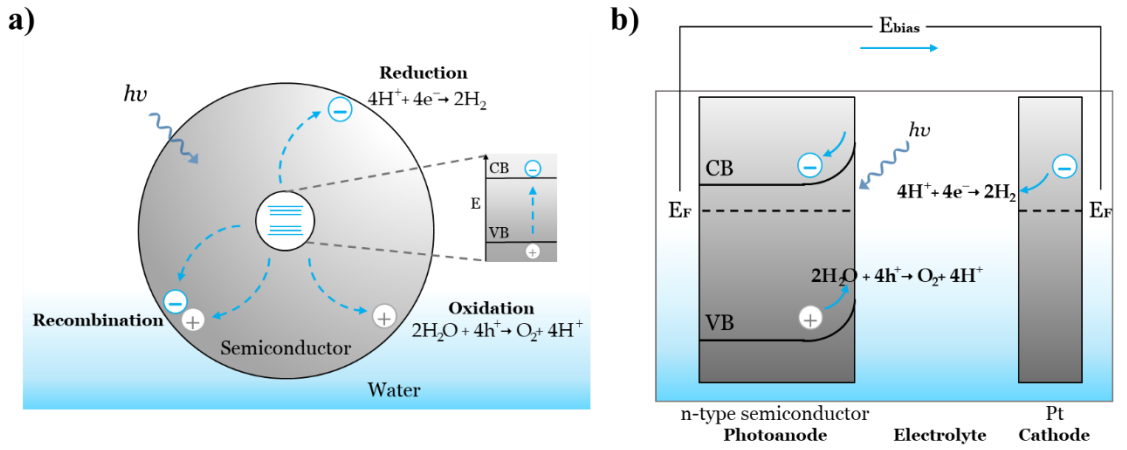

Figure 1.5 Schematic representation of energetics of different water splitting processes under illumination: (a) photocatalytic (PC) and (b) photoelectrochemical (PEC). E_{bias} is the voltage applied.

During the charge separation process, the charge carriers normally suffer from serious recombination, hence, suppressing the recombination of charges is a priority in achieving an efficient solar conversion process. For the survived photogenerated electrons that reach the chemically active surface sites, reactions will take place. With appropriate selection of cocatalysts, the surface reaction can be further accelerated, leading to improved solar conversion efficiency.[15]

1.2.2 Photoelectrochemical water splitting

PEC water splitting principle is similar to that of PC, except that additionally to light absorption, PEC process requires an external bias applied on the photocatalytic materials immersed in an electrolyte.[74] Here, the overall reaction takes place at two different electrodes, which can be both semiconductors (photoelectrode) or a semiconductor and a metal. Figure 1.5b depicts the dual PEC system electrode with an n-type semiconductor as photocatalyst. The photocatalyst is deposited on a conductive substrate to form the photoanode or photoelectrode. The assignation as anode or cathode of the photoactive material depends on the upward or downward band bending at the semiconductor–electrolyte interface, which is dictated by the semiconductor band structure.[19]

The absorption of photons takes place at the photoanode thus resulting into the creation of e^-–h^+ pairs upon irradiation. Since the Fermi level of the semiconductor is close to the CB, the redox potential of the electrolyte lies lower.[15] Therefore, in order to maintain the thermodynamic equilibrium, the upward band bending on the photoanode drives the photogenerated h^+ toward the photoelectrode–electrolyte interface, where O_2 is produced from H_2O molecules. The excess charge carrier (e^- in this case) generated also at the photoanode are transported to the counter electrode using the external circuit, thus H_2 evolution takes place at the cathode.[19,69,74]

Hence, the photocatalyst electrodes are capable of capturing the light, which provides energy for the reactions and the additional voltage required to carry out the reaction is provided by an externally applied bias. This externally applied bias overcomes the slow kinetics and provides sufficient voltage for the PEC cell to drive the reaction at a desired rate/current density.[74] Specifically, the degree of band bending is also adjusted by the applied bias.[15] A good combination of the two photoelectrodes with proper band alignment to allow efficient charge separation and transport is the key to realize good PEC water splitting performance.[15]

PEC water splitting efficiency depends strongly on the morphology and structural properties of the photoelectrode. Yet, other factors inherent to the setup are also an important fact in efficient water splitting mechanism. One of the drawbacks is the high temperatures at which experiments are conducted.[75] Mendes *et al*. studied the effect of temperature variations of a PEC system using Si-doped hematite. The results showed a photocurrent density increase with temperature; however, the optimal operation temperature of the PEC cell was 45 °C.[76,77] Additionally, the pH of the electrolyte solution affects greatly the equilibrium of water splitting reaction, because it determines the net total charge adsorbed at the surface. And, it affects also the stability of the photoelectrode. Even under corrosive conditions the photo-corrosion of the electrode should be reduced.[74]

Thus, the overall hydrogen production efficiency by any photocatalytic system is governed by several factors including amount of light harvested by a photocatalyst, the extent of charge separation and transportation as well as surface adsorption capacity of a material. These constraints place severe restrictions on the choice of suitable materials for photocatalytic water splitting. Essentially, these compounds are required to harvest solar radiation efficiently, to exhibit long-term stability, and to support rapid charge migration and surface reactions.[14] In order to deal with these factors numerous developments have been done in nanomaterials to tackle the limitations inherent of bulk materials.

The smaller dimensions can offer more favorable mass, heat, and charge transfer, as well as accommodate dimensional changes associated with some chemical reactions and phase transitions. For example, large specific surface area offers more sites for surface chemistry interactions and possibly charge separation. In the next section an overview of advances on nanostructures for energy to hydrogen conversion is presented.

1.3 Nanomaterials as photocatalysts for water splitting

Energy conversion and storage involve physical interaction and/or chemical reaction at the surface or interface, so the specific surface area, surface energy, and surface chemistry play a very important role. Considerable efforts have been devoted to the design of photocatalytic systems exhibiting a high conversion efficiency of light into chemical

energy such as the decomposition of H_2O into H_2 and O_2. In recent reports, much emphasis has been paid towards the development of photoactive nanomaterials.[19]

Till date, interesting studies have been reported for nanostructured photocatalysts semiconductor-based. The key advantage of using nanostructured materials is that they offer extensive surface area-to-volume ratio. Thus, enabling a larger number of catalytic active sites on their surface comparative to bulk material, hence affording high rate of redox reactions.[19] Based upon their dimensionality, nanostructured materials are classified as zero-dimension (0D), one-dimension (1D), two-dimension (2D). The 0D nanomaterials include nanoparticles & quantum dots; 1D nanomaterials are nanotubes, nanowires, nanorods & nanofibers; and 2D nanomaterials comprises nanosheets and nanoplates.

Nanomaterials also exhibit improved physical properties (melting point and hardness) and tunable electronic properties due to quantum confinement effects provoked when the particle size is smaller than the atom's Bohr radius.[21] Examples of quantum confinement effects are the increase of band gap thereby enhancing the charge separation and enabling the absorption of visible light for wide band gap semiconductors. The former represents a high area of opportunity as TiO_2 only accounts for the UV range which represents ~4.6% of the total irradiated solar energy (Figure 1.6).

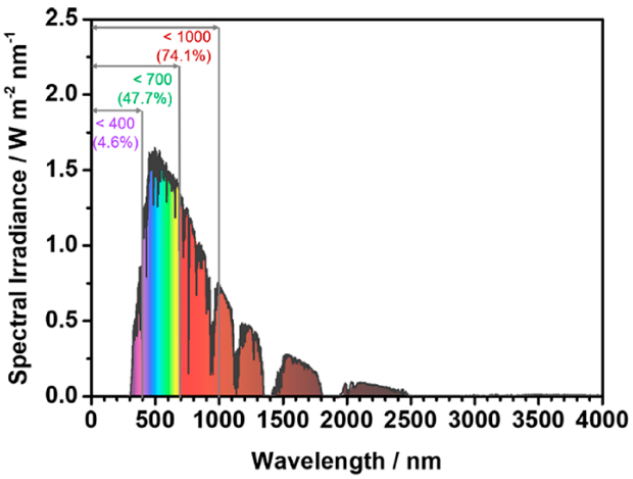

Figure 1.6 Air Mass coefficient (AM) 1.5G solar spectrum based on the ASTM G173-03 reference spectrum [14].

Different modification techniques of semiconductors can be conducted to enhance H_2 production, the most common involve[18]:

- *Noble metal loading.* Noble metals, including Pt, Au, Pd, Rh, Ni, Cu and Ag, have been reported to be very effective for enhancement of TiO_2 photocatalysis. As the Fermi levels of these noble metals are lower than that of TiO_2, photo-excited

electrons can be transferred from CB to metal particles deposited on the surface of TiO_2, while photo-generated VB holes remain on the semiconductor. These activities greatly reduce the possibility of electron-hole recombination, resulting in efficient separation and stronger photocatalytic reactions.

- *Ion doping.* Transitional metal ion doping and rare earth metal ion doping has been reported to expand the photo-response into visible spectrum. As metal ions are incorporated into the lattice and impurity energy levels in the band gap are formed. Among the metal ions studied, Fe, Mo, Ru, Os, Re, V, and Rh ions can increase photocatalytic activity, while dopants Co and Al ions cause detrimental effects.
- *Dye sensitization* is widely used to utilize visible light for energy conversion, the excitation of the dye provokes the injection of electrons into the semiconductor. Yet, the major disadvantage is the use of the liquid electrolyte, which has temperature stability problems. At low temperatures the electrolyte can freeze, halting power production and potentially leading to physical damage.
- *Heterostructures* can be composed of the previous mentioned 0D, 1D and 2D nanomaterials where the tuning of each component and its morphology can be assembled to create multifunctional architectures. For example, the induction of new charge transfer mechanisms, for example Park *et al.*[78] fabricated Au nanoparticles draped ZnO-TiO_2 core-shell nanowires (ZTA), and demonstrated that the multi-interface between the NPs and the nanowires ensued the generation, separation and transportation of plasmon induced hot electrons from Au nanoparticles. Other materials have also called the attention, such as the g-C_3N_4 due to its low band gap energy. However, it has been depicted that the g-C_3N4 photocatalyst is usually characterized by a small active surface area and thus provided a low efficiency.

In order to maximize the absorption of sun light, heterostructures with large surface area can also be fabricated describing diverse shapes and geometries.[79] Cho *et al.*[80] fabricated TiO_2 nanorods with an average diameter of 65 nm and length of 2.0 μm; next in a subsequent growth step TiO_2 short needle-shaped branches were grown, which represented a 4-fold increase in surface area. Due to the small diameters, the charge separation at the semiconductor/electrolyte interface was improved reaching a photon-to-current conversion efficiency of 67% (at 380 nm with an applied bias of 0.6 V vs. RHE), whereas the conversion efficiency just nanorods was 42%. Numerous heterostructures have been built demonstrating achievable laboratory-scale conversion efficiencies. These device efficiencies are calculated as solar-to-hydrogen (STH) efficiency, which is defined as the amount of chemical energy produced in the form of the hydrogen divided by the solar energy input, with no externally applied bias. Table 1.4 shows a comparative of reported hydrogen efficiencies, note that the experimental conditions differ, and factors such as the light source and the liquid reactant are specified.

Table 1.4 Literature data on photocatalyst for light-driven photocatalytic water splitting.

Photocatalyst	Surface loading	Reactant	H_2 evolution rate	Light source	Ref.
TiO_2 NPs	-	water	75 μmol h^{-1}	400-W Hg lamp	[81]
TiO_2 NPs	Au	methanol, water	1600 μmol h^{-1} g^{-1}	450-W Hg lamp λ > 300 nm	[82]
TiO_2 NPs	Ag QDs	ethylene glycol, water	8419 μmol h^{-1} g^{-1}	Natural Sun light	[83]
TiO_2 NRs	Au	ethanol, water	31800 μmol h^{-1} g^{-1}	100-W lamp λ = 365 nm	[84]
TiO_2 NPs	Pt	ethanol, water	41000 μmol h^{-1} g^{-1}	200-W UV lamp λ = 300 nm	[85]
TiO_2 NPs	Rh	EDTA*, water	4680 μmol h^{-1} g^{-1}	300-W Xe lamp	[86]
TiO_2 NRs	Rh	methanol, water	7850 μmol h^{-1} g^{-1}	300-W Xe lamp	[87]
Fe_2O_3-TiO_2	Pt	ethanol, water	8275 μmol h^{-1} g^{-1}	W-bulb	[88]
Ta_2O_5	NiO_x	water	3360 μmol h^{-1}	450-W Hg lamp	[89]
Ga_2O_3:Zn	Ni	water	2403 μmol h^{-1}	450-W Hg lamp	[90]
$SrTiO_3$:Li	$Rh_{0.3}Cr_{1.7}O_3$	water	1650 μmol h^{-1}	450-W Hg lamp	[91]
$SrTiO_3$:Mg	$Rh_{0.3}Cr_{1.7}O_3$	water	1500 μmol h^{-1}	750-W Hg lamp	[91]
$La_2Ti_2O_7$:Ba	NiO_x	water	2010 μmol h^{-1}	450-W Hg lamp	[92]
$NaTaO_3$:Sm	NiO	water	5300 μmol h^{-1}	400-W Hg lamp	[93]
$NaTaO_3$:Sr	NiO	water	13600 μmol h^{-1}	400-W Hg lamp	[94]

* Ethylenediaminetetraacetic acid.
Nanoparticles (NPs).
Nanorods (NRs).

1.4 TiO_2 based photocatalysts

TiO_2 is widely used as a photocatalyst due to its unique characteristics of low cost (less expensive than other catalysts such as ZnO, CdS or ZnS), good optical activity, high chemical stability (in acidic and basic medium), long durability, insoluble, and non-toxic nature. Furthermore, TiO_2 has a very good biocompatibility that allows its use for medical applications. Works have reported its use to reinforced materials or as coatings on bare titanium implants to compensate titanium implants deficiencies —like poor surface interaction with surrounding tissues—. Other uses include self-cleaning and antibacterial coatings. Furthermore, by combining high functional surface and photocatalytic activity, a TiO_2 nanostructure can be loaded by diversified drugs *i.e.*, osteoporosis drugs,

anticancer and antibiotics; and, be used as local drug delivery systems.[49] Investigation of their detailed reaction mechanism has led to the development of TiO_2 based photocatalysts with promising applications in various fields including environmental remediation and solar energy. Yet, as it was briefly discussed before, the use of TiO_2 in the production of solar fuels such as hydrogen has been widely studied.

The breakthrough of TiO_2 as photocatalyst dates back to the 1960s, when many research groups studied the photoinduced phenomena proceeding on semiconducting solids such as TiO_2 and ZnO under UV light irradiation. In 1964, S. Kato and F. Masuo[17] studied the surface properties of TiO_2 in correlation with the molecules absorbed or desorbed using UV, they reported the oxidation reaction of tetralin in the liquid phase of TiO_2 as photocatalyst. Later in 1972, pioneering work by Honda and Fujishima[11] demonstrated the water splitting into H_2 and O_2 by photosensitization with UV light of a titania (TiO_2) photoanode connected to a platinum cathode in an electrochemical cell. They proved that under UV light irradiation, the electrolysis of H_2O proceeded at a much lower bias voltage as compared to normal electrolysis. In 1977, G. N. Schrauzer and T. D. Guth[95] reported the photocatalytic decomposition of H_2O on powdered TiO_2 photocatalysts loaded with Pt or Rh particles. This led to the development of the charge mechanisms where the electrons from TiO_2 move to the Pt metal site where they induce reduction reactions, while photogenerated holes remain in the TiO_2 to conduct oxidation reactions. Thus establishing, the charge separation of electrons and holes as the most important process in photocatalysis employing semiconducting materials.

However, the photocatalytic efficiency of pure TiO_2 is limited due to its large band gap (~3.2 eV), corresponding to a wavelength of 388 nm, meaning that its activation needs an irradiation source with wavelength lower than 388 nm, which is in the near-UV region. Figure 1.6 shows the electromagnetic spectrum of the sun, where UV light only accounts for about 4.6% of the solar radiation energy while the visible light contributes about 50%, hence the inability to utilize visible light limits the efficiency of solar photocatalytic hydrogen production.[18]

Another important aspect for the redox water splitting reaction, as detailed in the photocatalysis subsection is the efficient charge separation of the photogenerated e^-–h^+ pairs. Nevertheless, TiO_2 has a high rate of recombination, CB electrons can recombine with VB holes very quickly and release energy in the form of unproductive heat or photons.[96]

In order to resolve overcome these limitations, continuous efforts have been made to promote the photocatalytic activity and enhance the visible light response. Numerous heterostructures TiO_2-based with carbonate salts, noble metal loading, metal ion doping, anion doping, dye sensitization, composite semiconductors, metal ion-implantation, among others, have exhibited remarkable results. However, the in-depth study of the material itself is important to tune the crystalline structure and the electronic properties

that impact directly the charge transport; properties, such as the presence of intermediate states within the band gap, and the surface chemistry can play an important role. Moreover, TiO_2 properties have proven to be strongly correlated to the fabrication techniques and even more to the structure morphology as discussed in the following subsections.

1.4.1 Crystal structure and properties

TiO_2 minerals are found in three different crystallographic structures; rutile, anatase, and brookite. These polymorphs exhibit different properties and consequently different photocatalytic performances. Another five phases of TiO_2 have been reported, such as TiO_2 II or srilankite, cubic fluorite-type polymorph and pyrite-type polymorph; though not very stable these are of minor significance for research. While rutile is the thermodynamically most stable phase, both anatase and brookite are metastable. Anatase transforms irreversibly to rutile at elevated temperatures, this transformation does not have a unique temperature.[97] Brookite has an orthorhombic crystal structure and transforms into rutile at quite low temperatures, yet it is difficult to synthesize and so poor experimental data is available.[98,99]

Both rutile and anatase TiO_2 exhibit tetrahedral geometry with unit cells consisting of 6 and 12 atoms of Ti and O respectively, while brookite has an orthorhombic geometry. Rutile and anatase structures are highly symmetrical where each Ti atom is surrounded by six O atoms forming a TiO_6. Figure 1.7 depicts the ball-and-stick models of the three polymorphs. The structures of rutile, anatase and brookite can be discussed in terms of TiO_2^{6-} octahedrals. The three crystal structures differ by the distortion of each octahedral and by the assembly patterns of the octahedral chains. In anatase, TiO_6 octahedra are sharing four adjacent edges, resulting in zigzagging chains running along the *a* and *b* lattice vectors. In rutile, octahedra share corners in the (001) plane, with their long axial axis alternating by 90°. The structure can therefore be defined as linear chains of edge-sharing octahedra where the chains themselves are connected by the octahedra corners. Table 1.5 reports the crystallographic parameters for both anatase and rutile structures. And in brookite, both vertices and edges are connected.[100,101] Next, a description of the most common surface geometries for anatase and rutile is given.

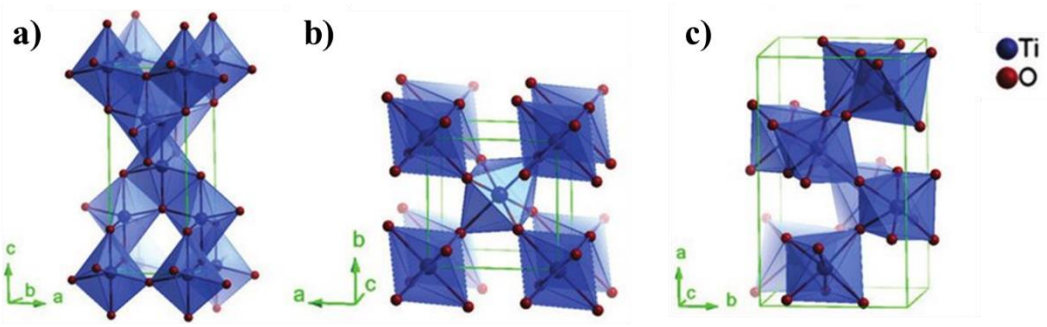

Figure 1.7 TiO_2 crystalline structures (a) anatase, (b) rutile, and (c) brokite. Retrieved from [102].

Table 1.5 Properties of anatase and rutile. Retrieved from [97].

Property	Anatase	Rutile
Crystal structure	Tetragonal	Tetragonal
Atoms per unit cell (Z)	4	2
Lattice parameters (nm)	a = 0.3785	a = 0.4594
	c = 0.9514	c = 0.29589
Calculated indirect Eg (eV)	3.23 – 3.59	3.02 – 3.24
Calculated experimental Eg (eV)	~ 3.2	~ 3.0
Density (kg m^3)	3830	4240

The anatase A-TiO_2(101) surface is commonly found in photosensitizing materials; generally, TiO_2 nanoparticles exhibit an entirely anatase form. In addition, the (100) surface is known for enhancing catalytic activity. The anatase (101) surface with a sawtooth like structure exposes two-folded oxygen atoms (O_1) bonded to five-folded titanium atoms (Ti_2) in the second layer. These cations are bonded to three-folded oxygens (O_3) in the [010] direction where channels are formed. Six atoms belong to the unit cell with the following sequence of planes: O–Ti–O–O–Ti–O.[101] For rutile, the R-TiO_2(110) surface has the lowest surface energy and is the most intensely studied because of the rich sights obtained in structural aspects of this surface. It exposes two kinds of titanium and oxygen atoms. Along the [110] direction, rows of six-fold-coordinated Ti atoms (as in the bulk) alternate with five-fold-coordinated Ti atoms with one 'dangling bond' perpendicular to the sur-atoms (as in the bulk) alternate with five-fold-coordinated Ti atoms with one 'dangling bond' perpendicular to the surface. Two kinds of oxygen atoms are present. Oxygen atoms within the main surface plane are three-fold-coordinated as in the bulk. The so-called bridging oxygen atoms are two-fold- coordinated.[99] Its unit cell is composed of six atoms with the following sequence of planes: O–Ti_2O_2–O. Other common surfaces for anatase and rutile are (100) and (100), (001), respectively.

Furthermore, as mentioned before, annealing makes it possible to transform the crystal structure from anatase to rutile, yet the stability during the thermal anneal process

should be explained on the basis of a molecular picture, where the nucleation and growth of the different polymorphs are determined by many complicated factors including the rate of heating, surface development, presence of dopants, grain size, etc.[103]

1.4.2 Band structure and charge carrier generation

To clarify the underlying electronic properties of TiO_2, the electronic band structure constitution has been determined for the three structural geometries. Experimental results by electrochemical impedance analysis (EIA) and X-ray photoelectron spectroscopy (XPS);[104] and theorical calculations by Density Functional Theory (DFT) have reported the Density of States (DOS) of anatase, rutile and brookite. Presently many theoretical reported values of most of the investigations are performed via DFT because DFT approaches provide a simple framework to quantum many body problems and is contributing significantly in designing new materials as well as tuning and investigating different properties of the materials.[105] Despite the limitations of DFT, exchange correlational (XC) functional parameters as well as specific electrical and optical properties of the materials allow to obtain reasonable band-structures approximations.

A semiconductor material can have two types of band structures, direct or indirect. The minimal-energy state in the conduction band and the maximal-energy state in the VB are characterized by a certain crystal momentum (k-vector) in the Brillouin zone. If the crystal momentum of electrons and holes is the same in both the conduction band and the VB; the semiconductor possess a direct band gap, here an electron can directly emit a photon upon recombination. Figure 1.8 demonstrates the recombination process by which an electron is reinjected into the VB. If the k-vectors are different, the material has an "indirect gap", the dissimilarity in k-vectors alludes to ‘misaligned’ bands which indicates the phonon assistance is required for an excited electron to move to into the CB to conserve the momentum.[106] Analogously this influences the charge carrier dynamics of the photogenerated charges as will explained next.

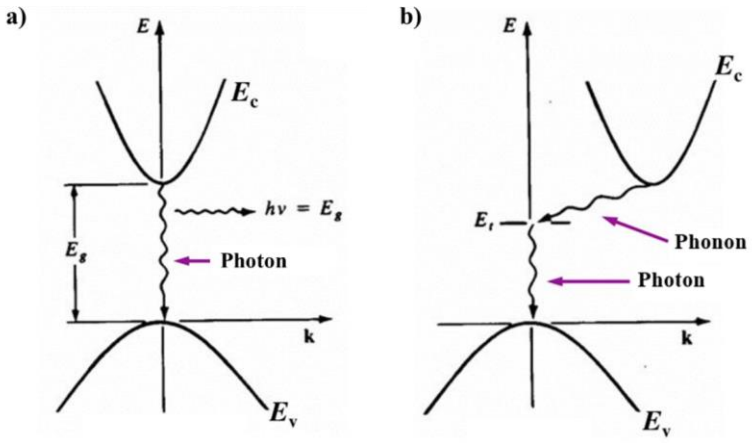

Figure 1.8 Energy vs crystal momentum of a photon emission process in (a) the direct and (b) the indirect band gap semiconductors.

The constitution of DOS in anatase, rutile and brookite are similar. The VB of stoichiometric bulk TiO_2 consists primarily of O 2p π-bonding states and a few Ti 3d states, indicating strong p-d hybridizations between O 2p and Ti 3d states. Furthermore, the hybridizations broaden the valence bands and promote the transfer of photogenerated holes. The conduction band is mainly composed by Ti 3d σ-bonding states, mixed with a few O 2p and Ti 3p states, here strong hybridization also appears between Ti 3d and O 2p states.[107,108]

DFT calculations utilizing a FP-LAW method report an indirect (N–Γ) band gap for anatase, with values ranging from 1.94 to 2.14 eV. Whereas, the band gap of rutile and brookite is direct (Γ–Γ) with values ranging from 1.86 to 1.94 eV.[98,105,109] Figure 1.9 shows the energy band structures, the Fermi level (shown by a dashed line) is set as zero. Thus, in anatase, the recombination of photoexcited electron and hole is assisted by phonon. The characteristic direct band gap of rutile and the theorized longer exciton lifetime of indirect band gaps explains the better photocatalytic performance of anatase, which results in an increase of the photogenerated electron–hole lifetime relative to that of rutile or brookite. It should be noted that these values are much smaller than the experimental values (3.2 for anatase, 3.0 for rutile and 3.3 eV for brookite, respectively). This is owing to the well-known shortcoming of the GGA function in DFT calculations.

Detailed studies at low temperatures showed that the optical response for rutile is characterized by a direct forbidden transition at 3.06 eV (1.6 K); however, the band gap near the edge is dominated by indirect transitions. In the case of anatase there is a consensus that the absorption edge is around 3.2 eV, associated with indirect transitions. Brookite is the least studied titania phase and experimental band gap energies ranging from 3.1 to 3.4 eV have been reported.[110]

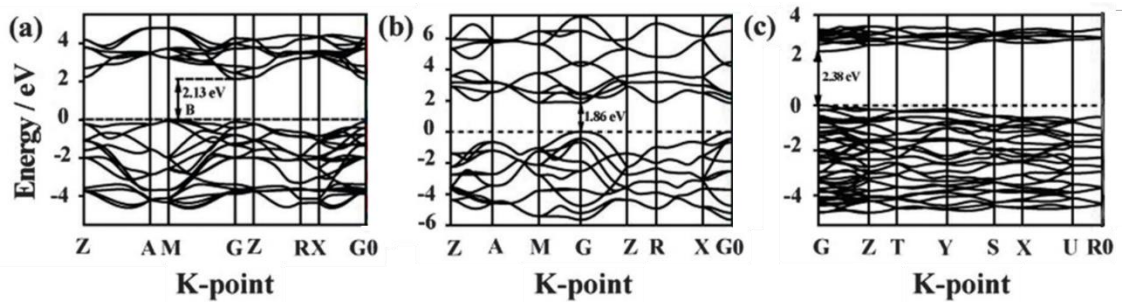

Figure 1.9 The band structure for (a) anatase, (b) rutile and (c) brookite TiO_2. Retrieved from [107].

TiO_2 materials possess a unique or a dominant structural phase, depending on the preparation method. Generally, hetero-structures constructed by rutile and anatase show higher photocatalytic activity than their pristine ones. For which the reason is that the photogenerated electrons and holes are separated spatially. However, the transfer directions of the charge carriers remain under debated, different mechanisms have been proposed about the band gap alignment between anatase and rutile.[104] Overall, the experimental results point out the presence of a depletion layer between both crystalline structures that subsequently, drift the electrons and holes to the two opposite sides of the hetero-junction, respectively. Hence, electrons and holes gain long lifetimes, allowing them to reach the catalyst's surfaces and to drive the redox reactions.

Moreover, in practical cases the CB states and the VB states, are not the key factors determining the charge carrier kinetics of TiO_2 materials, especially in nano-TiO_2 materials. In fact, charge carrier kinetics associated to defects in the band structure, and the presence of point defects and intermediate states play an important role in improving photocatalytic activity. These defects are discussed in the next subsection.

1.4.3 Defects in the electronic structure

The photocatalytic activity of TiO_2 is also dependent on the nature and density of defect sites. Intrinsic defects are important chemical entities that can introduce gap states in the band gap. The intrinsic defects of oxides, including vacancies and interstitial species, are formed during processing. Oxygen vacancies (Vo) and Titanium interstitials (Ti(i)) are two main kinds of point defects in TiO_2 lattice.[10]

The presence of these defects is associated to intrinsic intermediate gap states in the band gap. On an ideal band gap (with no intermediate states), upon excitation the charge carriers exist in a delocalized form when they reside at the CB and VB states for gap-state free TiO_2 materials. However, on the presence of intermediate states, they tend to be trapped there. These traps are universally found to exist in TiO_2 nanomaterials due to the presence of either intrinsic defects or extrinsic impurities.[111]

The effects of gap states on charge carrier kinetics depend on their chemical resources (entities), charge localization, energy distributions, densities of states (DOS), and spatial distributions.[10] Guo *et al.*[112] reported that the dominant defects in TiO_2 surface are Vo and in the bulk are Ti^{3+} interstitials, and these affect the adsorption states and reactions of adsorbates. Nevertheless, the consensus of an understanding of the formation of energy gaps and its correlation to the nature of electronic and optical properties is still lacking.

1.4.4 Synthesis and deposition techniques

In current studies, many kinds of TiO_2 nanomaterials have been prepared by means of microfabrication techniques, band structure engineering, defect structure modulation, and surface decoration, so as to promote photocatalytic performances.[111] TiO_2 can be prepared

in the form of powder, crystals, or thin films. Both powders and films can be built up from crystallites ranging from a few nanometers to several micrometers. The two fundamentally approaches for nanomaterials fabrication are usually used. While the so-called top-down approach starts with the bulk material and employs various techniques such as mechanical milling, laser ablation, sputtering, etc., to finally obtain the desired particle sizes; the bottom-up approach uses chemical synthesis methods starting from appropriate molecular precursors.

Next, an overview of the most used techniques for TiO_2 materials is given. The methods are mostly divided into two categories based on the type of precursors, and the equipment required. At the end a small comparison of the techniques is also given in terms of the nanomaterial morphological and structural properties.

Solution routes. Liquid-phase processing is one of the most convenient and utilized methods of synthesis. This method has the advantage of control over the stoichiometry, producing homogeneous materials, allowing formation of complex shapes, and preparation of composite materials. However, there are several disadvantages: expensive precursors, long processing times, and the presence of carbon as an impurity. The most commonly used solution methods are:

- *Precipitation(co-)methods.* These involve precipitation of hydroxides by the addition of a basic solution (NaOH, NH_4OH, urea) to a raw material followed by calcination to crystallize the oxide. $TiCl_3$ and $TiCl_4$ compounds are also widely used. The control of the particle size and size distribution is rather low, as fast precipitation often causes formation of larger particles instead of nanoparticles.
- *Sol–gel methods.* Used for the synthesis of thin films, powders, membranes and large mesoporous structures. This method involves the formation of a sol, gel or precipitation by hydrolysis and condensation (with polymer formation) of titanium alkoxides. In order to enhance the control over the evolution of the microstructure, different approaches can be used, such as complexation with coordination agents (*i.e.*, carboxylates). These reactions are followed by a thermal treatment (450–600 °C) to remove the organic part and to crystallize. Cleaning of particles can be done by centrifugation. Common precursors are $Ti(O–E)_4$, $Ti(i–OP)_4$, and $Ti(O–nBu)_4$.
- *Solvothermal methods*. Employ chemical reactions in aqueous (hydrothermal method) or organic media (solvothermal method) such as methanol, butanol, etc. Reaction takes place under self-produced pressures and at temperatures under 250 °C. It is useful to control grain size, particle morphology, crystalline phase, and surface chemistry. Yet, generally, post-thermal treatment is required to crystallize. Common precursors are $TiSO_4$, $H_2Ti_4O_9{\cdot}0.25\ H_2O$, and $TiCl_4$.
- Other methods include microemulsion, combustion synthesis, and electrochemical deposition.

Gas phase methods. For thin films, most synthesis routes are performed by these methods, via chemical or physical procedures. These allow depositing thin layers from a few microns thick down to individual atomic layers. To be able to deposit such thin layers with well-defined characteristics, the atoms and molecules that form a layer are usually collected from the gas phase at very low pressure (vacuum) so that the concentrations can be closely controlled, as can the rate at which layers build up. In addition to the coating materials and the used method, there are many parameters that can potentially affect the final characteristics of the coating, such as the substrate temperature, the energy of the impinging particles or the chemical bonds present on the surface of the substrate. The main gas phase techniques are:

- *Chemical vapor deposition (CVD).* Useful to coat large surface areas in a short span of time. Compounds, ranging from metals to composite oxides, are formed from a chemical reaction or decomposition of a precursor in the gas phase. Atomic layer deposition (ALD) is a type of CVD, the process consists of cycling sequences of surface self-saturating reactions and purging steps. It allows the deposition of ultra-thin layers, with a conformational thickness of < 2 nm for TiO_2.[113]
- *Physical vapor deposition (PVD).* Films are formed from the gas phase, but here without a chemical transition from precursor to product. The material is evaporated from a crucible and deposited onto a substrate, this leads to shadow effects, which are not present in CVD. Evaporation takes place under reduced pressure to minimize collisions of gas molecules and prevent pollution of the deposited films. A variant of this method is electron beam (E-beam) evaporation, where a focused beam of electrons heats the selected material.
- *Spray pyrolysis deposition (SPD).* An aerosol (mist of small droplets) is formed at ambient pressure from a precursor solution instead of a vapor as in CVD. The aerosol is directly focused onto a heated substrate. In fact, aerosol-based methods are hybrid because such techniques start from precursors in solutions, which can be further processed in a number of different ways. The advantages are simplicity, low cost, reproducibility, and the possibility of depositing large areas in a short time; however, uniformity is in most cases a problem.
- *Sputtering.* Uses direct current to produce a plasma under argon and oxygen. Accelerated Ar ions hit an electrode made of TiO_2 or Ti that evaporates to be later deposited on a substrate. Fast deposition rates and crystalline films are obtained.
- *Other methods:* molecular beam epitaxy (MBE) uses a (pulsed) laser to ablate parts of a TiO_2 ceramic target; ion implantation is based on the transformation of precursor plasma to TiO_2, which only becomes crystalline after an annealing step.

Concerning gas phase methods, the conformality and thickness vs. rate deposition are key parameters where the main differences can be observed. Whereas ALD allows 100% conformal films for 15:1 aspect ratio structures, the thickness achieved is not

greater than a few hundreds of nanometers (100 nm maximum for ALD), moreover the deposition rate is very low (< 0.2 nm cycle^{-1}). On the other hand, CVD and PVD can achieve thickness of 3 and 10 μm, respectively, at a deposition rate of 10 to 1000 nm cycle^{-1}. Although, the 0 to 100% and 15% conformal films are deposited (for PVD and ALD, respectively) only if a < 4:1 aspect ratio is maintained. Although these methods have the merit to control the film growth and the feasibility to obtain pure materials, they are energy intensive, require expensive equipment and precursors, and work at high temperatures and pressures.

In comparison, solution methods are cheaper, but the control over the synthetized materials is very low. Moreover, post-processing steps are generally essential for nanoparticles, *i.e.*, deagglomeration step, removal of organic agents and filtration [100]. Figure 1.10 depicts SEM images of TiO_2 obtained by two different solution and gas phase routes. Note the difference in the morphology and notably the grain size for the CVD and sputtering techniques. In some cases, the grains exhibit faceted surfaces which indicates the crystallinity of the structure. This feature is greatly affected by the processing parameters, Table 1.6 shows a summary of the phases obtained for different methods. For solution routes is common to obtain an amorphous phase, which can be further crystallized by calcination; as mentioned, before anatase and rutile are obtained through phase transition.

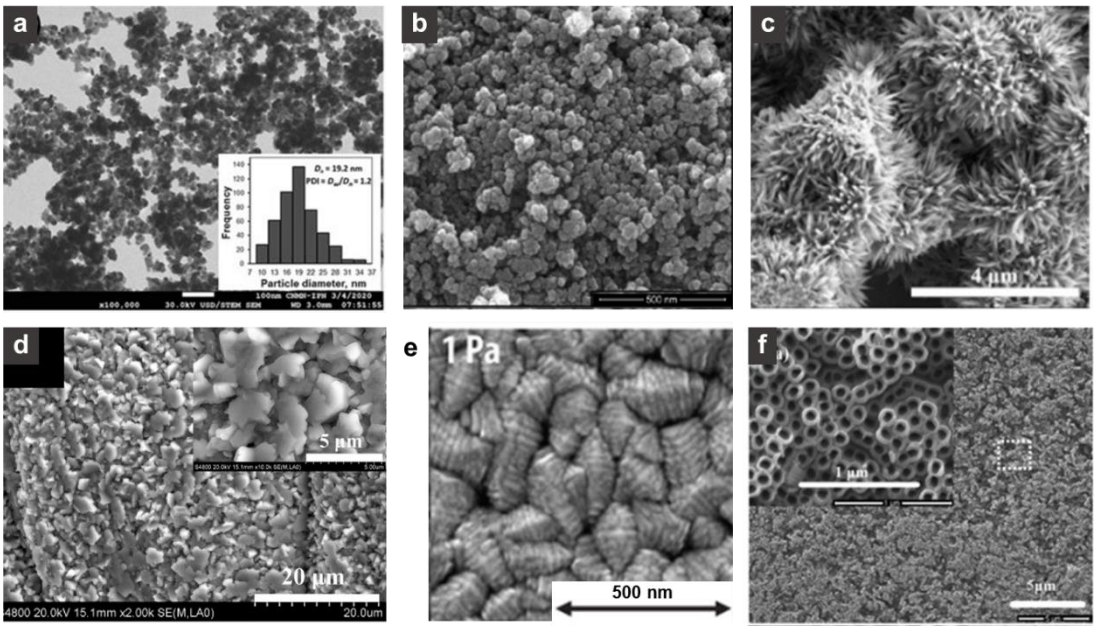

Figure 1.10 SEM images of TiO_2 nanostructures fabricated through (a) precipitation,[114] (b) sol-gel hydrolysis,[115] (c) solvothermal synthesis,[116] (d) CVD,[117] (e) sputtering [118] and (f) electrolytic anodization.[119]

Table 1.6 TiO_2 crystalline phases obtained for different deposition routes.

Synthesis method	Mechanism	Phases formed			
		A+R	A	R	Amp.
Room temperature hydrolysis of $TiCl_4$	Precipitation from room temperature solutions of $TiCl_4$				✓
Room temperature sol–gel synthesis	Hydrolysis of $TiCl_4$ or an organo-metallic compound				✓
Flame pyrolysis of $TiCl_4$	Combustion of $TiCl_4$ with oxygen; used in industrial processes	✓		✓	
Solvothermal/hydro-thermal	Precipitation of TiO_2 from aqueous or organic solution at elevated temperatures	✓	✓	✓	
Chemical vapor deposition	Spraying of Ti-bearing solution	✓	✓	✓	✓
Physical vapor deposition	Deposition of evaporated Ti and its subsequent oxidation	✓	✓	✓	✓

Anatase (A).
Rutile (R).
Amorphous (Amp).

The development of heterostructures is also widely documented in order to promote the performance by extending the absorption range spectra to the visible or boosting the charge carrier lifetime. For this purpose, TiO_2 based photocatalysts with small amounts of components such as cations and metal oxides can be fabricated by the same described methods. Works report doping of the TiO_2 lattice, through direct hydrolysis of inorganic/organic salts, sputtering, ion implantation, ball milling, sol-gel method, hydrothermal method, solvothermal method, and oxidation of titanium nitride.[96]

Identifying the factors that govern the kinetics of photocatalytic processes and understanding the role that they play is inherent to achieve the desired goal of developing more efficient systems. Although great strides have been made in the past 25 years, a lot still remains unknown, making TiO_2 photocatalysis an interesting challenge not only for engineers but also for scientists.

1.4.5 Chemical additives for H_2 production enhancement

The performance of TiO_2 photocatalyst can be improved with the presence of sacrificial agents which act as a hole scavenger compare to the water alone. The basic principle of photocatalytic reactions using electron donors/acceptors as the sacrificial reagents is depicted schematically in Figure 1.11.

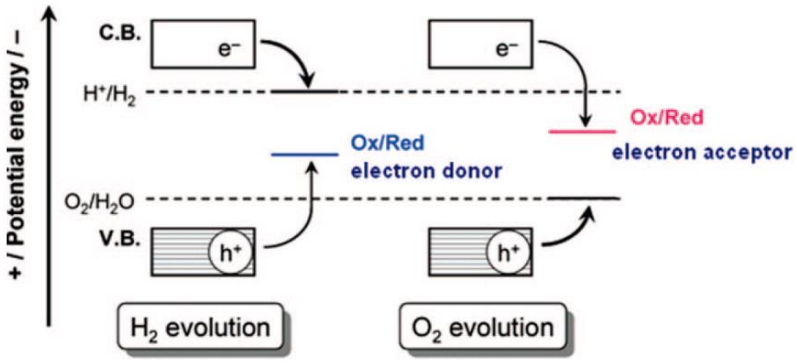

Figure 1.11 Principle of photocatalytic reactions in the presence of sacrificial reagents. Retrieved from.[120]

Organic Sacrificial Reagents. Organic compounds, such as alcohols (methanol, ethanol, isopropanol, etc.), organic acids (formic acid, acetic acid, etc.), and aldehydes (formaldehyde, acetaldehyde, etc.) can be used as electron donors. Water splitting into O_2 and H_2 (Figure 1.12a) is not an easy process because of the large up-hill reaction and rapid reverse reaction. Sacrificial H_2 production is an up-hill process but the energy change is small (Figure 1.12b). Therefore, sacrificial H_2 production proceeds smoothly compared with water splitting without sacrificial agents, thus providing a convenient method to generate H_2. Hence, most sacrificial H_2 production is performed in aqueous alcoholic solution.

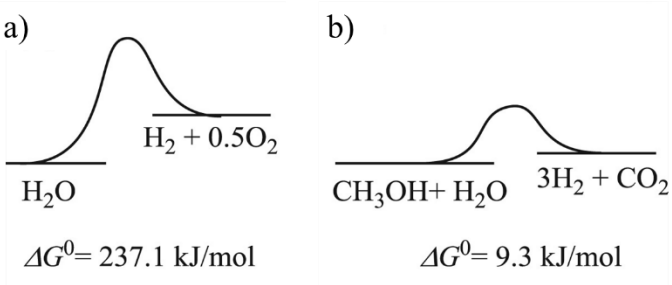

Figure 1.12 Energy diagrams for (a) water splitting (up-hill), and (b) water splitting with scavenger agent (small up-hill) processes. Retrieved from [121].

In these photocatalytic systems, organic compounds are oxidized and decomposed by the photogenerated holes. Meanwhile, the remaining photogenerated electrons reduce water to hydrogen. Methanol and ethanol are among the most used compounds, the hydrogen generation process for methanol is described as follows in Equations (1.3-1.7)[120]:

$$h^+ + H_2O \rightarrow \cdot OH + H^+ \qquad \text{Equation 1.3}$$

$$CH_3OH + \cdot OH \rightarrow \cdot CH_3OH + H_2O \qquad \text{Equation 1.4}$$

$$\cdot CH_2OH \rightarrow HCHO + H^+ + e^- \qquad \text{Equation 1.5}$$

$$2H_2O + e^- \rightarrow 2H_2 + 2OH^- \qquad \text{Equation 1.6}$$

Overall reaction:

$$CH_3OH \xrightarrow{hv\ catalyst} HCHO + H_2 \qquad \text{Equation 1.7}$$

Table 1.7 shows some typical alcoholic sacrificial agents. It has been reported that the sacrificial hole scavenger must have an α-H adjacent to the OH groups, influencing directly the H_2 production. For example, glycerol has 5 α-H atoms, hence, it can generate more H_2 than ethylene glycol, methanol and ethanol.[16] Moreover, the concentration of the scavenger agent also affects the process. A maximum concentration of methanol 5% solution was reported by Police *et al.* where the photocatalyst surface reaches saturation.[122]

Table 1.7 Chemical yield of H_2 with sacrificial agents over Pt/TiO_2 photocatalyst.[121]

Sacrificial agents	**Formula**	**Limiting mole (mol mol^{-1})**		
		H_2^{max}	**CO_2^{max}**	**CH_4^{max}**
Methanol	CH_4O	3	3	1
Ethanol	C_2H_6O	6	4	1.2
2-Propanol	C_3H_8O	18	1.3	0
1,2-Ethanediol	$C_2H_6O_2$	5	5.1	2
Glycerol	$C_3H_8O_3$	7	7.2	3.1
Formic acid	CH_2O_2	1	1	1
Ascorbic acid	$C_6H_8O_6$	10	9.8	5.9
Sorbitol	$C_6H_{14}O_6$	13	13.3	6.2

Based on this principle, organic pollutants have been used as electron donors that achieve photocatalytic production of hydrogen from polluted water and simultaneous degradation of organic pollutants; such designs received the name of bifunctional photocatalytic systems. Hashimoto *et al.*[123] achieved photocatalytic H_2 generation from aqueous solutions with fossil fuels and hydrocarbons with a Pt/TiO_2 powdered photocatalyst. Other model pollutants (azo-dyes, oxalic acid, formic acid, formaldehyde, chloroacetic acids, acetic acid, EDTA, etc.) have proved photocatalytic decomposition of organic pollutants synchronously with efficient hydrogen generation.[124]

Inorganic Sacrificial Reagents. Among inorganic agents S^{2-}/SO_3^{2-} mixture is most widely used as electron donors, since the components can be oxidized by photogenerated holes, whereas the photogenerated electrons are fully used to reduce protons for reduction of H_2. This is promising for practical applications using waste gas H_2S from chemical

industries such as natural gas utilization and desulfurization process in petrochemical plants. Also, inorganic ions have been used using the same principle by being oxidized by the photogenerated holes, some of these are Fe^{2+}, Ce^{3+}, I^- and CN^-.[120]

1.5 Current status of work and objectives

This chapter has presented the motivation for the development of solar based H_2 production systems by photocatalysis. On the first part, the status of the climate change and the current energetic demand were reviewed. Solar fuels are a promising technology to tackle the GHG emissions, with are expected to double (compared with 2009). Among these, H_2 production through photocatalytic water splitting uses solar energy which is the most abundant energy resource on the Earth.

It is followed by a description of the photocatalytic water splitting processes and a review of photocatalyst nanomaterials and their efficiency in terms of H_2 production. Among these, TiO_2 is highlighted as a benchmark photocatalyst due to its high stability, low cost, and low toxicity. A literature review was presented about TiO_2 properties with emphasis on nano- and microfabrication techniques, structural properties and band electronic structure in correlation to the photocatalytic performance. Yet, many controversies exist regarding the type of fabrication and techniques and the correct tuning of properties that lead to the water splitting reaction in order to produce H_2.

The final goal of this thesis is to study the principal structural factors and mechanisms that lead the water splitting reactions in TiO_2 thin films, and, to explore technological solutions that yield the H_2 production under UV and Visible light irradiation. TiO_2 offers a promising way for clean H_2 generation due to its low-toxicity, low-cost, and limited safety concerns. And, DC sputtering, technology available in the clean room facility at the Laboratory for Analysis and Architecture of Systems (LAAS), is a robust technique, cost-effective and industrially feasible for the fast fabrication of films with great adhesion, compact and resistant; hence sputter-deposited TiO_2 thin films were chosen as photocatalyst for this work.

The following Chapters 2 and 3, present a technological approach in which nanotechnology solutions were explored to tune and impact the H_2 production rate of thin TiO_2 films. Two approaches were considered 1) doping with Au and Pd plasmonic nanoparticles to extend the absorbance spectral range, and 2) the enlargement of the photocatalyst's specific surface. The experimental findings not only point out the complexity of the mechanisms underlying the photocatalytic activity in the heterostructures, but also raise a question about the defects present on the semiconductor surface. Hence, a specific study presented in the Chapter 4 which discusses the role of oxygen vacancies, titanium interstitials, as well as hydroxyl species, on the charge generation and transport of the polycrystalline TiO_2.

Chapter 2

Synergetic mechanisms of the photocatalytic activity in Au/TiO_2 hybrid nanostructures

The present chapter discusses the fabrication process of a heterostructure photocatalyst composed of TiO_2 thin film and Au nanoparticles. The synergy of mechanisms with origin at the semiconductor-metal junction; and the plasmonic effects of the noble metal nanoparticles, was correlated to the H_2 production rate through water splitting. In order to elucidate the specific contributions of the components on the electronic and chemical processes, the nanostructures were irradiated with ultraviolet (UV), visible (Vis) and UV+Vis light; and, by tuning the position of Au at different depths into the TiO_2 layer. Lastly, a scenario detailing the mechanisms that take place on the surface and bulk of the film, from the irradiative step until the water splitting reaction is proposed.

2.1 Introduction

As mentioned in the previous chapter a good photocatalyst should exhibit good absorption of the sunlight to achieve photogeneration and also maintain low recombination. Yet, TiO_2 photocatalyst is active only in the UV and it has a high recombination rate. As

detailed in Section 1.3, several engineering approaches based on structural and chemical modifications, have been explored to overcome these drawbacks. Among these methods, TiO_2/Au hybrid structures (mostly nanopowders) have shown great potential for solar photocatalytic conversion by photodegradation of dyes,[125] oxidation reactions of methanol or cyclohexane[126,127] and H_2 production.[23] This has been ascribed to the formation of the Schottky barrier at the interface of the metal–semiconductor, and to the local surface plasmonic resonance (LSPR) which is inherent to noble metal plasmonic nanoparticles, such as Au or Ag.

Schottky barrier

The Schottky barrier, is a potential energy barrier for electrons and is located at the junction of an n-type semiconductor —as is the case for TiO_2— and a metal. The Fermi levels in the two materials must be equal at thermal equilibrium and the vacuum level must also be continuous. For electronic transport across the interface, the Schottky barrier leads to rectifying behavior between the metal and the n-type semiconductor, meaning that the flow of electrons from the semiconductor to the metal is easier than in the opposite direction.[128] Figure 2.1 depicts the band structure of a metal and a n-type semiconductor, each one with a defined work function (Φ_M and Φ_S), respective to the vacuum level (E_0). Upon contact, the Schottky barrier (Φ_B) is formed provoking the bending of the semiconductor bands, and the equilibrium of the fermi level (E_F). Thus, photogenerated electrons at the semiconductor cannot flow to the metal unless they jump the Schottky barrier.

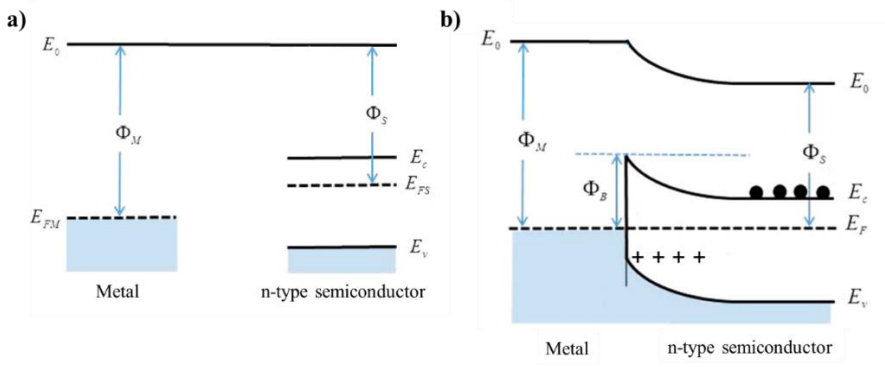

Figure 2.1 Schottky barrier (Φ_B) formed by a metal and n-type semiconductor (a) before contact and (b) after contact.

This band bending causes a depletion of electrons at the interface; hence, an accumulation of negative electrons from the metal at the interface, and a formation of the positive space charge layer *i.e.*, formation of the positive space charge layer of the semiconductor, to maintain electrical neutrality at the interface. Based on this stability, the Schottky barrier can serve as an effective electron trap where the electron is unable to flow back to the semiconductor. This enables the metal act as an electron sink for

electrons, preventing the recombination of electron–holes and extending the lifespan of the electron to conduct the reduction reaction.[24] This mechanism has been reported by Gomes et *al.*[23] among other works,[129] where Au NPs on particulate Titania exhibited a dual role as light harvesters injecting electrons into the semiconductor conduction band and as catalytic sites for gas generation. Veziroglu et *al.*[130] reported TiO_2 thin films deposited by PVD with Au agglomerates deposited on top. The role of an electron reservoir was ascribed to Au NPs, thus facilitating charge separation.

Moreover, plasmon excited electrons were also responsible for the enhanced photocatalytic activity, which was determined by tuning the irradiation ratio of vis to UV of 0.24:1 for photodegradation of methylene blue. Yet, by increasing the ratio, plasmon excited electrons seemed to promote electron-hole recombination in TiO_2. Plasmon excited electrons are one of the effects of LSPR, this mechanism is explained next.

Surface Plasmonic Resonance (SPR)

Surface plasmon resonance, also known as localized surface plasmonic resonance (LSPR) is phenomenon of charge density oscillations confined to metallic nanoparticles (sometimes referred to as metal clusters) and metallic nanostructures. Excitation by an electric field (light) at an incident wavelength where resonance occurs, results in strong light scattering, in the appearance intense surface plasmon absorption bands, and an enhancement of the local electromagnetic fields.[20] According to Warren *et al.*,[22] the electron density is decreased on one side of the conductor and increased on the other side, hence the redistribution of the charge creates an electric field inside and outside the conductor. Figure 2.2a-b depicts the asymmetric distribution of the electric field around the particle. The doping of semiconductors with plasmonic metals like Au, Ag and Cu g has been widely studied as the surface plasmons can resonate within UV-visible light.[24] The frequency and intensity of the surface plasmon absorption bands are characterized by the type of material and are highly sensitive to the size, size distribution and shape of the nanostructures, as well as to the environment which surround them.

There are three primary mechanisms of LSPR that have been identified for semiconductor/plasmonic metals structures,[24] these are:

(1) Scattering of resonant photons by the metal, when light is illuminated onto the plasmonic metal, the metal is able to spread out incident resonant photons, causing the photons to have longer optical path lengths to travel around the semiconductor.

2) Intense oscillating electric field around the metal (Figure 2.2a), the electric field must be able to transfer sufficient energy to overcome the band gap into the semiconductor, thus this energy will promote the formation of electrons and holes.

3) Hot electron generation. This is one of the primary mechanisms of LSP, some metals are able to supply the electron under visible light. These hot electrons may be injected into the semiconductor or couple to phonons and thermalize. Figure 2.2c depicts the injection of the hot electrons towards the semiconductor.

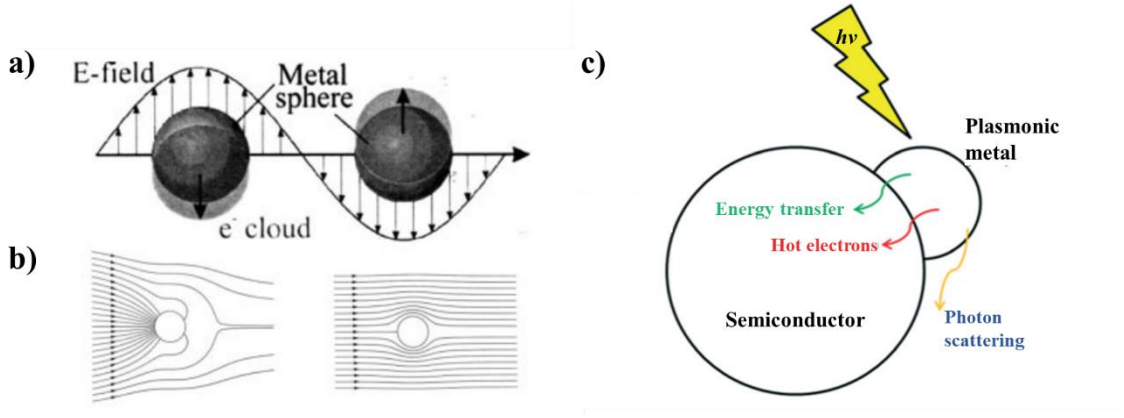

Figure 2.2 (a) Schematics for plasmon oscillation of a metal sphere, showing the displacement of the conduction electron charge cloud and (b) field lines showing resonance on the left side of sphere. (c) LSPR mechanisms in semiconductor/metal heterostructures.

However, there is still great debate between the Schottky barrier and hot electron generation function, whether the electron is flowing from the semiconductor to the metal due to the Schottky barrier or from the metal to the semiconductor due to the SPR effect. Some works reported a negative contribution of plasmonic effects: Yann *et al.*[131] reported that plasmon excited electrons under visible light would be transferred from Au NPs to TiO_2 thus increasing electron-hole recombination leading to a decrease in the photocatalytic performance.

Focusing on direct photocatalytic water splitting application using Au/TiO_2 hybrid catalyst, no quantitative information can be found on the respective role of plasmonic and non-plasmonic effects. Whether, the metal NPs can provide electron charges generated due to plasmonic excitation, and contribute to the photo-generated charges by the semiconductor. Thus, the contribution of plasmon excited electrons under visible light on the water splitting reaction chemistry or the impact on the overall charge transport still remains elusive. Another question to answer for the optimal design of these heterostructures, is whether or not the water splitting reaction can take place on the metal NPs too as is suggested in literature.[132,133]

This study focuses on the plasmonic and non-plasmonic contributions that lead the water splitting reactions, by evaluating the respective response under UV and visible light. For that purpose, various TiO_2/Au structures were prepared either by decorating a sputtered TiO_2 thin film surface with Au NPs and by embedding them into the film at different depths. A full structural, chemical and optical characterization of each structure

was conducted. The photocatalytic activity was determined by measuring the calculating the H_2 production rate under UV (353 –403 nm), visible (vis) (400 – 1100 nm) and UV+Vis (300 – 1100 nm) light. Furthermore, these findings were correlated to DDA simulations by modeling the intensity and distribution of plasmonic electric near-fields originated at the interface TiO_2/Au NPs. Finally, photoelectrochemical measurements were carried to evaluate the photocurrent response, and to determine the separation rate of the photogenerated charges by the flat-band potential. The results of this study were published in 2020 in the Journal of Physical Chemistry C.[134]

2.2 Materials

2.2.1 TiO_2 films fabrication

Physical vapor deposition (PVD) of TiO_2 was conducted by direct current magnetron sputtering of a Titanium target (20.3 × 7.6 cm size, 0.63 cm thick, 99.999% purity) on a TFE Model 644 equipment. The pressure of the chamber was 8×10^{-8} Pa. A gas mixture of 40% Oxygen and 60% Argon (99.9999% purity each) was set with a pressure of 1.07 Pa. The DC (Direct Current) power of reactive plasma was 1200 W. 4-inch and 500 µm thick Borosilicate B33 glass wafers were used as substrates. Depositions of 3 loops composed of 180 passes each, with a cooling pause of 1500 s and a cool over etch time of 1500 s, were performed to deposit a 270 nm thick layer (Figure 2.3). Substrates were cleaned with O_2 plasma (800 W, 5 min) prior to use. Finally, wafers were diced to obtain samples with an area 1 × 1 cm.

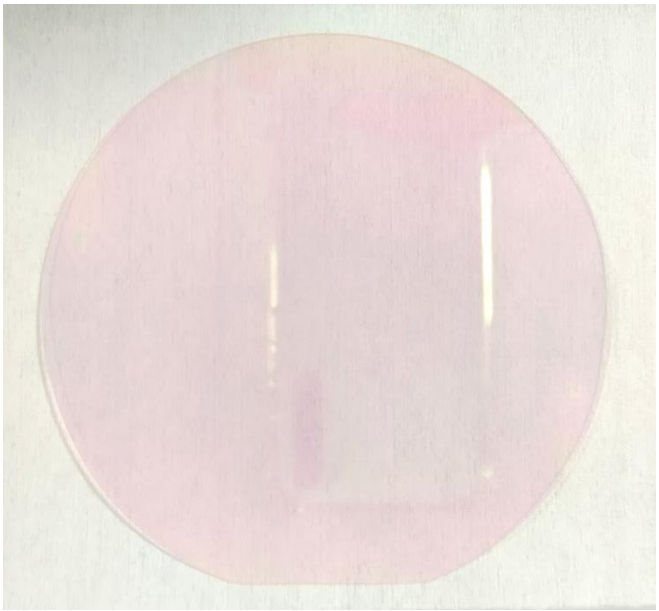

Figure 2.3 Quartz 4 inches wafer coated with TiO_2 270 nm film deposited by magnetron sputtering.

2.2.2 Au nanoparticles

Nanoparticles were synthesized directly onto the samples surface by a photo-deposition process. Substrates were deposited on a baker, subsequently filled with the reagents. Using a gold chloride trihydrate (III) acid ($HAuCl_4 \cdot 3H_2O \geq 99.9\%$, Sigma–Aldrich) aqueous solution (5 mL, 2.5×10^{-4} mol l^{-1}), a stabilizing agent of trisodium citrate dihydrate ($Na_3C_6H_5O_7 \cdot 2H_2O$ 99.0%, Alfa Aesar) solution (5 mL, 0.05 mol l^{-1}), and ethanol (99.9%, Technic) as a sacrificial agent (5 mL). Next, the baker was irradiated with a UV lamp (365 nm, 100 W) during 30 min.

An annealing step under air at 200 ˚C for 10 min was conducted to remove the organic ligands that surround the NPs and thus obtain chemical bonding to the TiO_2 surface. The stabilizing agent residuals were removed by rinsing with deionized water. Next, by direct magnetron sputtering as previously described, a second TiO_2 layer (15 and 270 nm thickness) was deposited on specific samples which will be described in the next section.

2.2.3 Heterostructures fabrication

Hierarchical TiO_2/Au NPs structures were constituted by depositing alternatively films of TiO_2 and Au NPs, detail of the samples is given in Table 2.1 and the schematics of each sample is depicted in Figure 2.4. A 270 nm thick TiO_2 layer was chosen as the basis for the heterostructures as it showed optimum performance in preliminary studies made in the research group.[25] Au NPs were deposited by chemical photo-deposition directly on top of the TiO_2 film.

Table 2.1 Description of heterostructures composed of TiO_2 thin films with Au NPs.

Sample name	Composition
TiO_2	TiO_2 (270 nm)
Au-on-TiO_2	TiO_2 (270 nm) / Au NPs
Au-in-TiO_2-15	TiO_2 (270 nm) / Au NPs / TiO_2 (15 nm)
Au-in-TiO_2-270	TiO_2 (270 nm) / Au NPs / TiO_2 (270 nm)

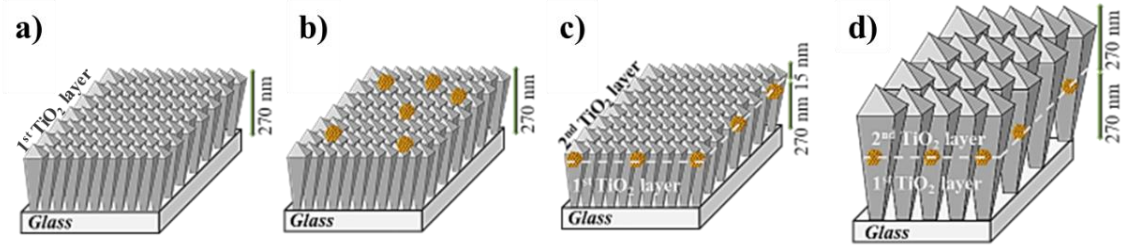

Figure 2.4 Schematic illustrations of TiO_2/Au NPs heterostructures (a) TiO_2, (b), Au-on-TiO_2, (c) Au-in-TiO_2-15 and (d) Au-in-TiO_2-270. Gray crystals: TiO_2 and yellow dots: Au NPs.

2.3 Characterization

Different characterization techniques were used to study the TiO_2/Au NPs photocatalyst morphology, structure, optical properties, and photocatalytic activity. In addition, Electric Field Simulation was used to model the intensity and distribution of plasmonic near-fields present in the heterostructure.

2.3.1 Structural and chemical characterization

2.3.1.1 Scanning electronic microscopy (SEM)

Provides a highly magnified image of the surface of a material giving topographical information, and also, information concerning the composition near surface regions of the material is provided as well. It works based on a source of electrons focused (in vacuum) into a fine probe that is sweeping over the surface of the specimen. As the electrons penetrate the surface, a number of interactions occur that can result in the emission of electrons or photons from (or through) the surface. A reasonable fraction of these electrons can be collected by appropriate detectors and the output can be used to modulate the brightness of a cathode ray tube (CRT), where the image is produced. Every point that the beam strikes on the sample is mapped directly onto a corresponding point on the screen. The principal images produced are of three types: secondary electron images, backscattered electron images, and elemental X-ray maps.

Analytical information. Experiments were carried in a SEM FEI Helios 600i (Nanolab) in the immersion mode at 20 kV and with a working distance of 4.2 mm.

2.3.1.2 High-Angle Annular Dark-Field Scanning Transmission Electronic Microscopy (HAADF-STEM)

STEM works in high vacuum is needed to prevent collisions between the high-energy electrons and air molecules. Ultrathin samples of 200 nm or less can be analyzed, so that the accelerated beam of electrons passes through the sample. The electron beam is focused into a very small spot, and then scanned over the sample. The electron beam interacts with the sample and the transmitted beam is collected by a detector. This can either be a CCD chip (when operating in TEM mode) or a High Angle Annular Dark Field (HAADF) detector. This detector receives inelastically scattered electrons or thermal diffuse scattering (TDS) at high angles using an annular dark-field (ADF) detector. HAADF image intensity is reported to be proportional to 1.4 square to a square of the atomic number (Z-contrast), heavy atoms are observed brighter, but light atoms are difficult to be observed. A high-performance STEM instrument provides a resolution better than 0.05 nm.

Analytical information. Cross-section of the samples was prepared by Focused-Ion Beam (FIB) in a FEI Helios (Nanolab). The surface of the samples was covered with

a layer of sputtered carbon before the preparation of lamellas. HAADF-STEM was performed on a JEM-ARM200F cold FEG at 200 kV with a probe CS corrector reaching a spatial correction of 0.078 nm.

2.3.1.3 Energy Dispersive X-Ray Spectrometry (EDS)

STEM imaging can be combined with several material analysis techniques such as Electron Energy Loss Spectroscopy (EELS), Energy Filtered TEM (EFTEM) and Energy Dispersive X-ray Spectrometry (EDS or EDX). EDS obtains an element analysis with a series of three major parts: an emitter, a collector, and an analyzer. High energy electromagnetic radiation (X-rays) are emitted, which allow to eject 'core' electrons (electrons that are not in the outermost shell) from an atom. Removing these electrons from the system will leave behind a hole that a higher energy electron can fill in, and it will release energy as it relaxes. The energy released during this relaxation process is unique to each element on the periodic table. This principle is known as Moseley's Law, which determines a direct correlation between the frequency of light released and the atomic number of the atom. The analyzer will determine how many X-rays are released, as well as what their energy is (in comparison to the energy of the initial X-rays that were emitted).

Although EDS is a useful technique, is not particularly sensitive when the concentration of an element in the sample is too low. Neither for elements with a low atomic number, such as Boron or lower atomic number elements.

Analytical information. STEM-EDS elemental mapping spectra were obtained from the cross-section of the samples (thin sputtered carbon layer on top) using a JEOL CENTURIO Silicon Drift Detector (SDD) detector.

2.3.1.4 Electron Energy Loss Spectroscopy (EELS) in STEM mode

EELS also provides elemental information on a nanometer scale when coupled with TEM. Compared to EDS, EELS improves the signal to noise ratio, and offers a spatial resolution (down to 1 nm), energy resolution (<1 eV for EELS) and sensitivity to the lower atomic number elements. To do this, high energy electrons (60 – 300 kV typically) pass through the sample, and these can interact either elastically (no energy exchange) or inelastically with the sample. The results will provide energy loss spectral information from the sample (spectroscopy) or images that have contrast created by the energy loss properties of the distribution of material in the sample.

Analytical information. EELS data was acquired using a GATAN GIF QUANTUM ER with a dispersion of 0.025 eV/channel (energy resolution of 0.3 eV), a collection semi-angle of 19.4 mrad and a convergence semi-angle of 15 mrad.

2.3.1.5 Atomic Force Microscopy (AFM)

AFM is a form of scanning probe microscopy (SPM) where a small probe is scanned in a raster pattern across the surface to form a map of the measured property relative to the X-

Y position. The information gathered from the probe's interaction with the surface can be as simple as physical topography or measurements of the material's physical, magnetic, or chemical properties.

The probe is placed on the end of a cantilever. The amount of force between the probe and sample is dependent on the spring constant (stiffness) of the cantilever and the distance between the probe and the sample surface. This force can be described using Hooke's Law. The movement of the cantilever is thus measured by the reflected movement of a laser on the photodiode which is converted to an electrical signal. The dominant interactions at short probe-sample distances in the AFM are Van der Waals interactions. During contact with the sample, the probe predominately experiences repulsive Van der Waals forces (contact mode). As the tip moves further away from the surface attractive Van der Waals forces are dominant (non-contact mode). Different cantilever lengths, materials, and shapes allow for varied spring constants and resonant frequencies.

Analytical information. AFM imaging of the surface morphology was carried using a Veeco AFM equipment (Dimension 3100) in tapping mode.

2.3.1.6 Grazing Incidence X-Ray Diffraction (GI-XRD)

XRD (GIXRD) is a modification of the X-ray diffraction (XRD) analytical method to measure the crystal structure of thin films. When conventional XRD analysis is performed on thin films (1-1000 nm thick) a weak signal is obtained from the surface layer and an intense signal from the lower layer of the sample. To avoid the incident angle of the X-ray beam hitting the sample is adjusted relative to the critical angle of the reflected X-rays. The incident angle is usually chosen to be slightly above the critical angle of the material in order to obtain a total reflection of the whole surface layer. Still, the penetration of the X-ray beam into the bulk material is prevented and limited only to the surface layer; making. Because the overlapping peaks in the diffractogram coming from different depths of the sample are avoided with GIXRD, it makes the diffraction phenomenon surface sensitive.

Analytical information. Crystalline phases were detected using GI-XRD, Bruker D8 Discover system with a Cu k-alpha radiation as the source. The grazing angle was set to 1.2° and two-theta collection angle is ranged from 20° to 80° with a step of 0.05° and a dwell time of 0.1 s per point.

2.3.1.7 X-Ray Photoelectron Spectroscopy (XPS)

XPS also called electron spectroscopy for chemical analysis (ESCA), is used to determine the elemental composition of a material's surface (between depths of 1 and 10 nm). It can be further applied to determine the chemical or electronic state of these elements.

Incident X-rays coming from a monochromatic X-ray source, cause the ejection of core-level electrons from sample atoms. The energy of a photoemitted core electron is

a function of its binding energy and is characteristic of the element from which it was emitted. When the core electron is ejected by the incident X-ray, an outer electron fills the core hole. The energy of this transition is balanced by the emission of an Auger electron or a characteristic X-ray. By counting the number of photoelectrons and Auger electrons as a function of their energy, a spectrum representing the surface composition is obtained. The area under a peak in the spectrum is a measure of the relative amount of the element represented by that peak. The peak shape and precise position indicate the chemical state for the element.

Analytical information. ESCALAB 250 X-Ray photoelectron spectrometer with a monochromatized Al-Kα radiation, a concentric hemispherical electron energy analyzer under vacuum (10-9 mbar) and a pass energy of 23.5 eV was used to characterize the chemical species at the interfaces of the materials.

2.3.2 Optical characterization

2.3.2.1 UV−Vis spectroscopy

Is an analytical technique that measures the number of discrete wavelengths of UV or visible light that are absorbed by or transmitted through a sample in comparison to a reference or blank sample. In some molecules and atoms, incident photons have enough energy to cause transitions between the different electronic energy levels. The wavelength of light absorbed has the energy required to move an electron from a lower energy level to a higher energy level. These transitions result in very narrow absorbance bands at wavelengths highly characteristic of the difference in energy levels of the absorbing species. However, for molecules, vibrational and rotational energy levels are superimposed on the electronic energy levels. Because many transitions with different energies can occur, the bands are broadened. The instrument then measures the light absorbed, transmitted, or reflected by the sample at each wavelength. For most applications, absorbance values are used since the relationship between absorbance and both concentration and path length is normally linear (following Beer Lambert's law).

Analytical information. Samples deposited on glass substrate were used. The absorbance spectra were recorded in the transmission mode using a Perkin-Elmer Lambda 950 UV-vis spectrometer equipped with an integration sphere (specular mode).

2.3.3 Photocatalytic activity measurement

2.3.3.1 Gas chromatography (GC)

Chromatography is a group of separation methods which rely on differences in partitioning behavior between a flowing mobile phase and a stationary phase to separate the components in a mixture. The sample is carried through the column and compounds with different retention times in the column are physically separated. As the components elute from the column they can be quantified by a detector and/or collected for further analysis. The choice of detector used in GC depends very much on the gases being

analyzed. The detectors used in the GC instrument was the Katharometer, also called the Thermal Conductivity Detector (TDC).

The Katharometer consists of two matched electronically heated filaments situated in the sample and reference streams and connected into a bridge circuit so that their resistances may be compared. When the temperatures of the filaments are not equal, their resistances also differ and the unbalanced bridge gives a signal proportional to the temperature difference. The temperature of each filament depends on the operating conditions. Thus, the bridge output is proportional to the difference in the thermal conductivity of the sample and reference streams.

Analytical information. The gas chromatography experimental is shown in Figure 2.5, where the H_2 measurements are carried by the gas chromatographer (GC) apparatus Clarus 580 (PerkinElmer) equipped a TCD detector and commercial columns PlotQ column (30 m length, 0.53 m inner diameter) and PE-molesieve column (30 m length, 0.53 m inner diameter) (PerkinElmer); and uses Argon as carrier gas. Samples with an area of 1 cm^2 were placed into a quartz reactor (60 mL) connected to the GC apparatus (Figure 2.5b). The reactor was filled with an aqueous solution (10 mL) composed by deionized water (v/v 65%) and ethanol (v/v 35%). Next, the reactor was purged previous to the test during 1 h with Ar (99.98 ± 0.1% purity) pressure of 1.2 bar (1.2×10^6 Pa); the pressure was set at 1 bar (1×10^6 Pa) was for the test. The produced H_2 was measured every 6 h over a time period of 24 h.

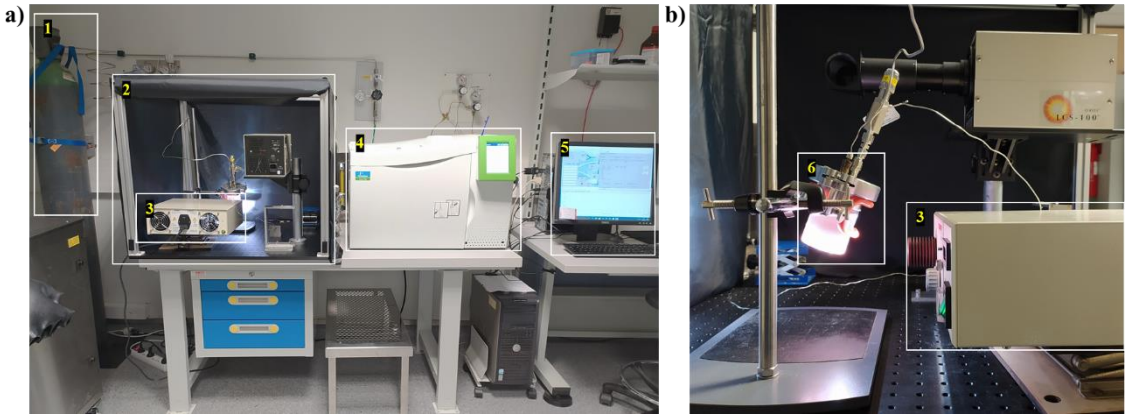

Figure 2.5 Experimental bench for H_2 production measurements. (a) Overview of the complete setup. (b) Side view of the reactor during irradiation. Setup: 1) Argon gas bottle (carrier gas), 2) protective box with blackout tissue, 3) Xenon lamp, 4) gas chromatographer (GC) apparatus, 5) PC controller, 6) quartz reactor

The irradiation was carried by a Xenon light lamp (Cermax elliptical PE300B-10F) equipped with optical filters to delimit the spectral region. The relative spectral distribution of the lamp is given in Figure 2.6, the wavelengths range from 300 nm to 1100 nm. Test under UV light were performed using a single-band bandpass filter 378/52

nm Brightline (Semrock) in from of the Xe lamp, spectral transmittance from 350 to 400 nm. Visible light irradiation was delimited with a RapidEdge long-pass filter (Laser Components), spectral transmittance ≥ 400 nm ± 2 nm.

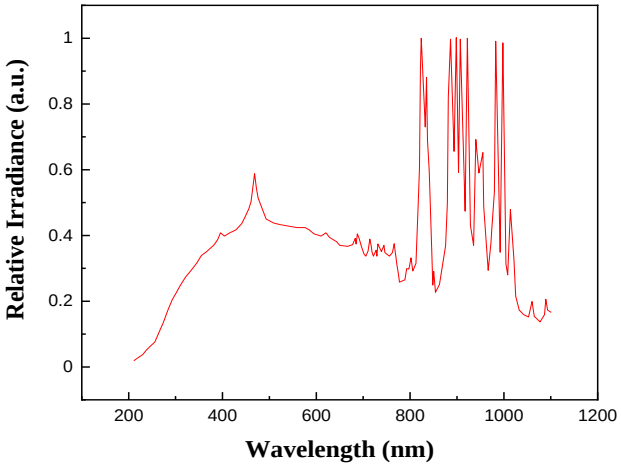

Figure 2.6 Relative spectral distribution of the Xenon lamp used for gas chromatography tests.

2.3.4 Electrochemical characterization

2.3.4.1 Photocurrent response

Measured through chronoamperometry, photocurrent generation is determined by the speed of photoexcited electrons transporting from semiconductor to the conductive substrate, and by the recombination at the electrolyte and semiconductor material interface. Herein, photocurrent response evaluates the sensitivity of a photoanode to light irradiation.

Analytical information. Measurements were carried out using a VMP-3 and a VSP Biologic potentiostat with a three-electrode setup. The working electrodes were prepared by depositing the samples onto a glass coated with Ti/Au (100 and 300 nm). The counter electrode was a platinum net and a silver chloride electrode (Ag/AgCl) was used as reference. An aqueous solution of anhydrous sodium sulfate (0.5 M, Na_2O_4S, >99%, Fluka, CAS: 7757-82-6) was used as an electrolyte. For the respective measurements, the working electrode was irradiated with an optical fiber wire (Eurosep Instruments) connected to a xenon lamp.

Chronoamperometry I-t test were run under visible light using a band pass filter described previously. The transient photocurrent curves were measured at 0 V vs. Ag/AgCl. The irradiation was turned ON and OFF periodically with 20 s interval of time.

2.3.4.2 Flat band potential by Linear Swept Voltammetry (LSV)

LSV is a powerful and popular electrochemical technique commonly employed to investigate the reduction and oxidation processes of molecular species. Experiments employ a ‘‘three-electrode’’ cell containing a working electrode, counter electrode and reference electrode (analyte). Next, a potential is applied, while the response is the resulting current passed. The method is similar to cyclic voltammetry (CV), but rather than linearly cycling over the potential range in both directions, linear sweep voltammetry involves only a single linear sweep from the lower potential limit to the upper potential limit.

The method is based on the Nernst equation to relate the potential of an electrochemical cell to the standard potential of certain species, and the relative activities of the oxidized and reduced analyte in the system. Thus, the concentration of the species in solution near the electrode changes as the potential is scanned in accordance with the Nernst equation. For example, when a system is scanned to negative potentials, the analyte will be reduced locally at the electrode, resulting in the measurement of a current and depletion of the ions at the electrode’s surface.

The Flat band potential is a key parameter affected by the recombination probability. Hence, it is used in the evaluation of photoelectrode performance. Its determination can also help to estimate the positions of band edges in new materials. At the interface between an n-type semiconductor photoanode and the electrolyte, band bending occurs and the Fermi level E_F in a semiconductor and electrochemical level (E_{redox}) in the electrolyte are equal at the equilibrium state (Figure 2.7a). This has the effect of charging the semiconductor positively, and since semiconductor carrier densities are much lower than those in solution, the diffuse charge in the semiconductor (space charge region) is counterbalanced essentially by a sheet of charge in the electrolyte. Changing the voltage of the semiconductor artificially through the use of a potentiostat causes the semiconductor and redox couple Fermi levels to separate, and hence the level of band bending owing to electron depletion in the semiconductor will change depending on the applied voltage. When the applied voltage is such that there is no band bending, or charge depletion (Figure 2.7b), then the semiconductor is at its flat-band potential, V_{fb}.[135]

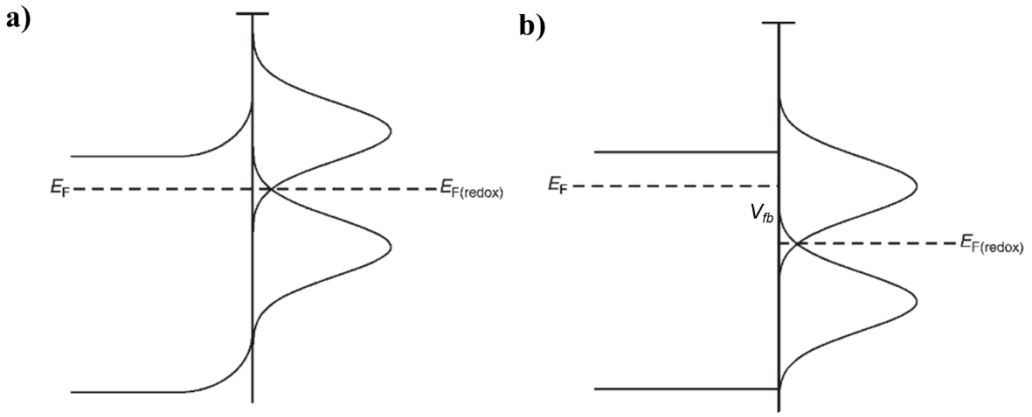

Figure 2.7 Scheme of an n-type semiconductor showing the fermi level (E_F) and the redox states of the electrolyte with its corresponding fermi level ($E_{F(redox)}$) (a) at the electronic equilibrium and (b) situation when the semiconductor is at its flat-band potential V_{fb}.

Analytical information. Previous electrochemistry setup was used for LSV. Currents were recorded in the dark and under white light illumination. The electrode potential was swept from -0.6 V to +0.50 V vs. Ag/AgCl at a scan rates of 5 mV s^{-1}. The net photocurrents were calculated according to the Equation 2.1.[136]

$$J_{Photocurrent} = J_{Light} - J_{Dark} \qquad \text{Equation 2.1}$$

2.4 Results

In this section the description of the fabricated TiO_2/Au NPs heterostructures is given, followed by the study of their structural, chemical, optical, and electrical properties. Finally, these results will be correlated to the H_2 production.

2.4.1 Structural and chemical properties

Topography of TiO_2 sample was first analyzed by SEM, image shown in Figure 2.8a-b. The film exhibited the characteristic columnar morphology with well-defined and faceted crystallites of TiO_2 films deposited by PVD. The size of the crystallites ranged from ~20 to 50 nm in diameter, accompanied by the presence of porosities between the columns with a size from ~1 to 10 nm. The surface roughness was calculated with AFM was 5.9 ± 0.1 nm (Figure 2.8b).

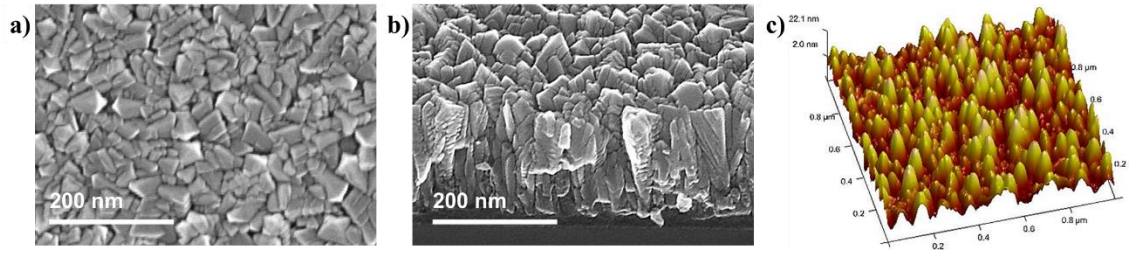

Figure 2.8 (a, b) SEM images of TiO_2 sample. (b) AFM mapping of the TiO_2 sample.

HAADF-STEM observations show the cross-sectional images of the four heterostructures (Figure 2.9 top images). The measured thickness for TiO_2 sample was 276.1 ± 5 nm. The photo-deposited Au NPs were rather spherical with a size range of 30 to 70 nm (size distribution inset in Annex Figure 2.18). The calculated areal density was 60 ± 1 NPs μm^{-2}. Small Au NPs (~7 nm in size) were found into the film porosities for all the Au containing samples, this probably results from the synthesis process where the gold precursors reach the small porosities after decomposing, its size is then constrained during the growth step by the space availability imposed from the columnar crystallites. This is corroborated by the Au NPs size distribution which increases as the Au NPs are located at lower depths into the film, see HAADF-STEM cross section images in Figure 2.9 bottom. TiO_2 covers completely the Au NPs in samples Au-in-TiO_2-15 and -270, as the film is thinner for Au-in-TiO_2-15, the contrast of the NPs is darkened on the SEM image compared to Au-on-TiO_2.

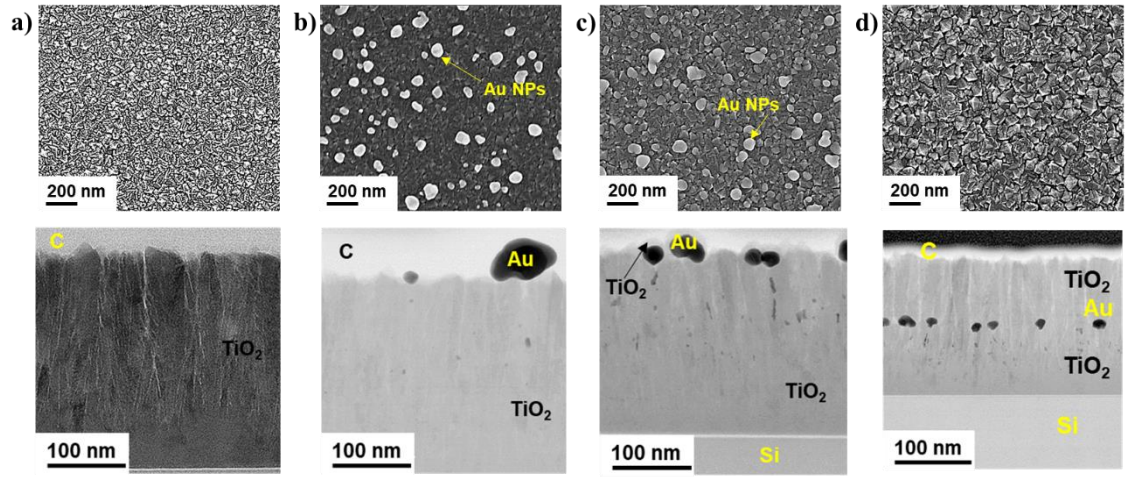

Figure 2.9 SEM (top) and HAADF-STEM (bottom) cross-sectional images of samples (a) TiO_2, (b) Au-on-TiO_2, (c) Au-in-TiO_2-15 and (d) Au-in-TiO_2-270. Letter C corresponds to the top layer of protective sputtered carbon.

The columnar morphology of TiO_2 seemed also affected upon doubling the film thickness in Au-on-TiO_2-270, grains size increased from 20 - 50 nm to 35 - 80 nm (HAADF-STEM top image in Figure 2.9d). This is related to the regrowth process of the second layer on top of the crystallites, hence the columns widen from the TiO_2/TiO_2 interface as observed in the STEM cross-section (Figure 2.9d bottom). Presence of Au was further corroborated by STEM-EDS spectroscopy. Figure 2.10 shows the elemental mapping, Au (in yellow) was observed in the three respective samples at the position of the NPs. Note that the first column of images on the left show the position of the NPs in white (due to atomic contrast), in coherence with the elemental mapping. Titanium (in blue) was observed along the depth of the compact film.

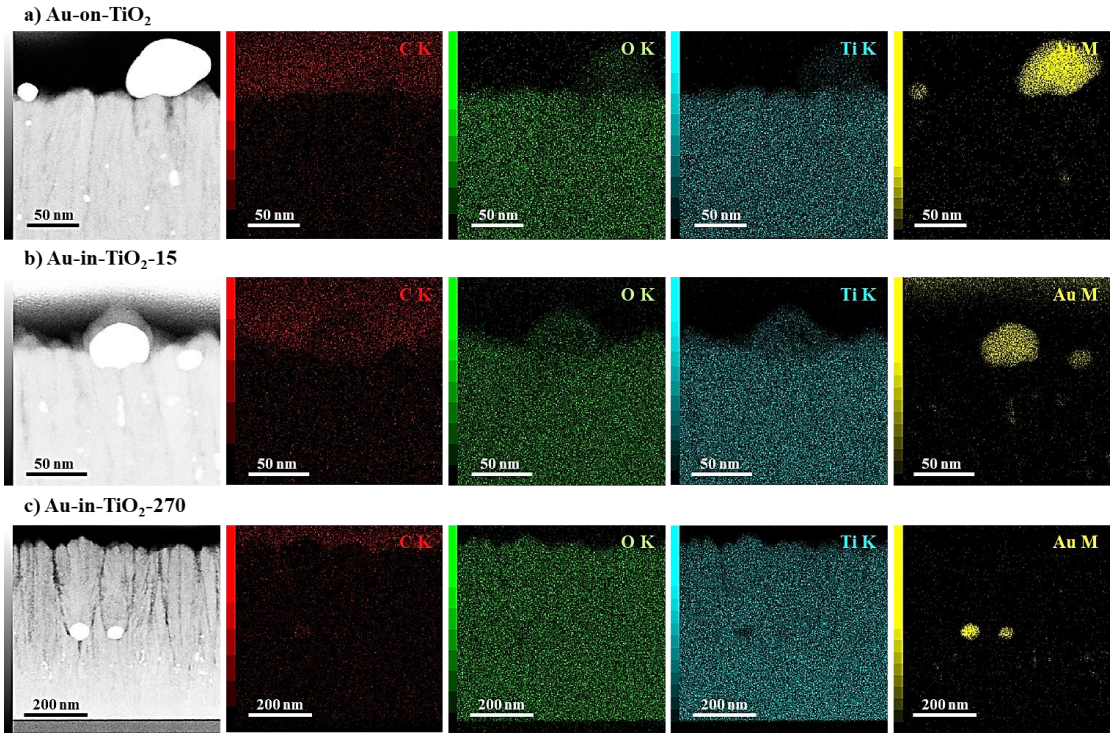

Figure 2.10 STEM-EDS mapping of cross-section of (a) Au-on-TiO_2, (b) Au-in-TiO_2-15 and (c) Au-in-TiO_2-270. Sputtered carbon layer on top. Elements depicted: C (red), O (green), Ti (cyan) and Au (yellow).

The structure composition analyzed by GI-XRD, patterns showed in Figure 2.11a. The anatase and rutile planes were identified for all the samples (labelled in Figure 2.11a), based on the intensity of the characteristic peaks of anatase at $2\theta = 25.24°$ for the (101) plane and that of rutile at $2\theta = 27.39°$ for the (110) plane, the structure composition was determined to be 84 ± 1% and 16 ± 1% for anatase and rutile, respectively. The Au peak located at $2\theta = 38°$ decreases in intensity progressively for Au-in-TiO_2-15 and Au-in-TiO_2-270, compared to Au-on-TiO_2, evidencing the thickness of the TiO_2 second layer.

In addition, the anatase/rutile peak's ratio was not affected by the short annealing step that follows the NPs photo-deposition.

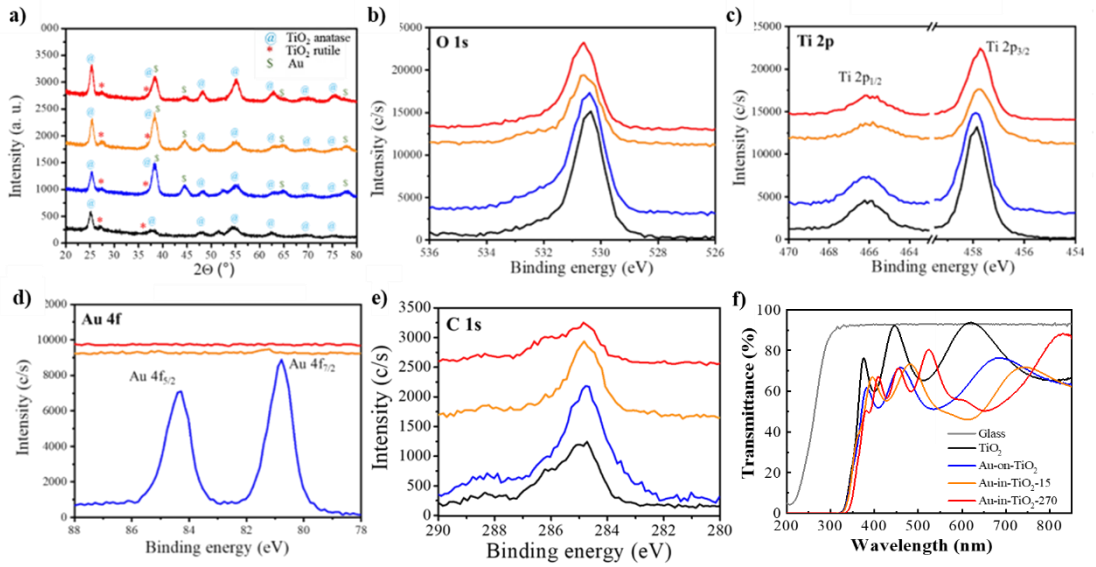

Figure 2.11 (a) GI-XRD patterns (anatase and rutile planes labelled); and XPS spectra (b) O 1s, (c) Ti 2p, (d) Au 4f and (e) C 1s. TiO_2 (black curve), Au-on-TiO_2 (blue), Au-in-TiO_2-15 (orange), and Au-on-TiO_2-270 (red). (f) UV-vis transmittance spectra (data from absorption spectra).

XPS results were consistent with XRD and SEM observations, spectra are shown in Figure 2.11b-e. The TiO_2 signature was clearly identified from O 1s and Ti 2p energy levels. Au 4f peaks were clearly observed for the Au-on-TiO_2 sample. The Au signature completely disappeared when Au NPs are embedded into the TiO_2. A slight Ti 2p peak shift (-0.2 eV) was observed for Au-in-TiO_2-15 and Au-in-TiO_2-270. This is explained by the interactions between the Au and TiO_2 that affect the Ti-O bonds by lowering Ti 2p binding energy.[137]

2.4.2 Optical properties

The transmittance of the three structures was evaluated by UV-vis spectroscopy (Figure 2.11f). As expected, the transmittance is zero from 350 to 200 nm because of the absorption iv the UV of TiO_2 (black curve). The ripples in the 400-850 nm range corresponded to the constructive and destructive interferences related to the film thickness and the difference of the refractive index between the glass substrate and TiO_2 film.[138] Because of these ripples, the analysis of the absorption properties of the materials is quite difficult. However, the TiO_2 film alone did not show a significant absorption in the range of 450-700 nm.

The TiO_2/Au heterostructures showed an enhancement of its absorption in the visible light range (450-800 nm region) (blue, orange and red curves), this phenomenon is clearly coming from the NPs. In samples Au-in-TiO_2-15 and Au-in-TiO_2-270, there is a red-shifting of the absorption compared to Au-on-TiO_2 (450-700 nm region). The addition of a 15 nm-thick TiO_2 layer (Au-in-TiO_2-15) induced a red-shift of the absorption (around ~600 nm) whereas the major ripples were only slightly red-shifted (orange curve). With a thicker film covering the Au NPs (Au-in-TiO_2-270) the red-shift was even more important, *i.e.*, localized around 650 nm (red curve). This can be ascribed to the semiconductor coupling and the localized surface plasmon resonance (LSPR) between the two components.[139] To summarize, all Au containing structures exhibited absorption in the visible light as expected. While it is hard to make a hierarchy of absorption levels between the different systems, the absorption band of the plasmonic peak seemed to shift to higher wavelengths when the Au is embedded in the semiconductor.

2.4.3 H_2 production rate

In order to elucidate the different contributions of the heterogenous structures on the photocatalytic activity, the H_2 production was measured by gas chromatography under UV+Vis (300-1100 nm), UV (353-403 nm) and visible (400-1100 nm) light. The H_2 production rate shown in Figure 2.12 was calculated after 24 h of irradiation and normalized with respect to the incident light flux on the sample. See the H_2 evolution plots on the Annex Figure 2.19, note that the H_2 release rate remains constant in time.

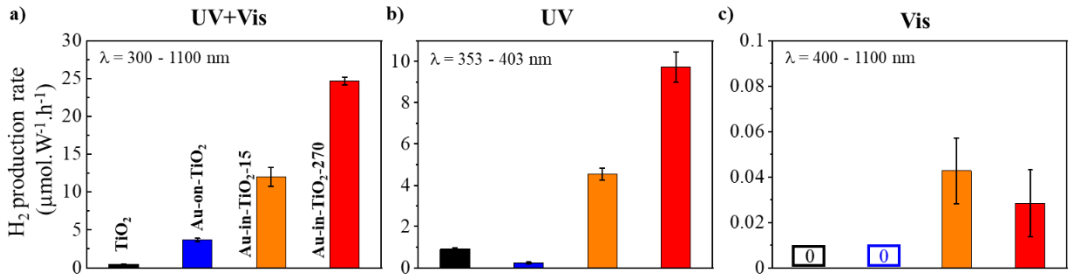

Figure 2.12 Normalized H_2 production rates per light flux and surface areas. She samples were irradiated under (a) UV + Vis (300–1100 nm, left), (b)UV (353–403 nm, middle), and (c) vis light (400–1100 nm).

Table 2.2 presents the H_2 production rates, among the samples Au-in-TiO_2-270 reached the maximum rate under UV irradiation with a value of 24.67 µmol W^{-1} h^{-1}. Under Vis and a poor rate of 0.04 and 0.03 µmol W^{-1} h^{-1} was obtained for Au-in-TiO_2-15 and Au-in-TiO_2-270, respectively. Yet, Au-onTiO_2 showed negligible production under Vis. According to this, a first observation is that, under UV light, the systems exhibit a higher H_2 production rate than under Vis light. Also, under UV, the systems with Au NPs show a clear enhancement compared to the TiO_2 reference. A second observation is that

the H_2 production rate increases drastically for TiO_2/Au structures when they are exposed to the UV+Vis compared to reference TiO_2. The measured H_2 rates reached 3.68, 12.02 and 24.67 μmol W^{-1} h^{-1}, for Au-on-TiO_2, Au-in-TiO_2-15 and Au-in-TiO_2-270, respectively, whereas the rate for plain TiO_2 was 0.47 μmol W^{-1} h^{-1}. This corresponds to an enhancement factor of 7, 23 and 48 for Au-on-TiO_2, Au-in-TiO_2-15 and Au-in-TiO_2-270, respectively, with respect to TiO_2.

Table 2.2 H_2 production rate of TiO_2 thin films with Au NPs heterostructures.

Sample name	UV+Vis	UV	Vis
TiO_2	0.47 ± 0.03	0.91 ± 0.07	0.00
Au-on-TiO_2	3.68 ± 0.23	0.24 ± 0.04	0.00
Au-in-TiO_2-15	12.02 ± 1.22	4.54 ± 0.30	0.04 ± 0.04
Au-in-TiO_2-270	24.67 ± 0.51	9.72 ± 0.74	0.03 ± 0.03
a-Au-in-TiO_2-15	24.67 ± 1.22	-	-

H_2 production rate units in μmol W^{-1} h^{-1}.

Primarily, these results evidence that the direct contact between water and Au nanoparticles is not critical to catalyze the photo-reduction of water, which suggests that the water splitting reaction takes place mostly onto the semiconductor surface. Next, a crucial understanding between the respective role of UV versus Vis light in the HER in the three TiO_2/Au systems must be addressed. As mentioned in the introduction, it is known that the band bending resulting from the Schottky barrier between the metal and the semiconductor can enhance the photocatalytic activity compared to the bare semiconductor. Hence, upon UV irradiation of TiO_2, e^-–h^+ pairs are generated; next, due to band bending associated to the Schottky barrier presence, holes located in the VB of the TiO_2 are attracted towards the metal NPs where they are annihilated by electrons from the NPs. This recombination prolongs the lifespan of the electron in the conduction band of TiO_2. This is consistent with the H_2 production rate data were the best photocatalytic activity was obtained for the heterostructures where the metal-semiconductor junction is present, such as Au-on-TiO_2 and Au-in-TiO_2. On the other hand, the plasmonic resonance effects of Au nanoparticles that take place under visible light also play an important role in the charge transport mechanisms. As SPR creates a collective oscillation of conduction electrons at the interface between the Au and the TiO_2, the energy transfer in the vicinity of the NPs and production of hot electrons are possible.

2.4.4 Study of SPR Electrical Field by Au NPs

To shed light on the SPR originated by the plasmonic NPs in the heterostructures, DDA simulations were performed to model the intensity and distribution of the plasmonic near-fields. Simulations were carried out using the discrete dipole approximation-based (DDA) open-source DDSCAT software package. Three heterogeneous TiO_2/Au model-structures were built, with NPs having 10 nm diameter. The model-systems considered

are depicted in Figure 2.13: a) *Au-surface*, NP on top of TiO_2 surface, b) *Au-subsurface*, 5 nm thick TiO_2 layer covering a NP; and, c) *Au-embedded*, NP fully embedded into TiO_2 matrix. The three model-systems were irradiated normally to the TiO_2 surface, at 550 nm corresponding to the maximum plasmonic resonance wavelength of the bare gold nanoparticle. All structures were bathed in a water medium (1.33 refractive index). The optical properties (*i.e.*, complex electric permittivity) of TiO_2 and Au were derived from Palik's handbook and Johnson *et al.* databases.[140,141]

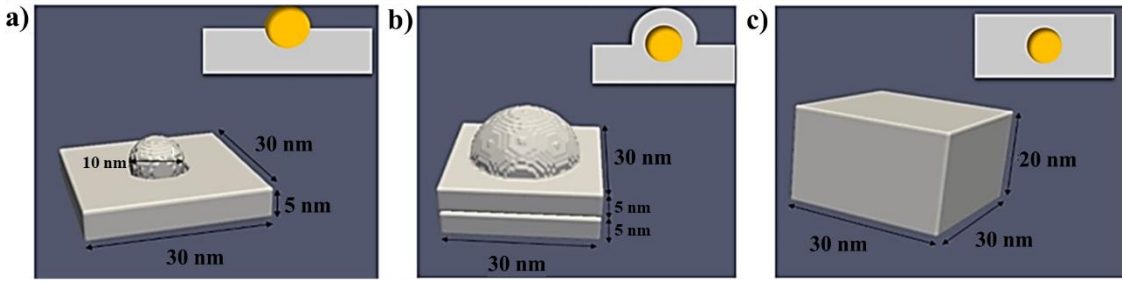

Figure 2.13 Schematics views of the three hybrid TiO_2/Au model-structures built for DDSCAT simulations. (a) Au-surface (Au 10 nm, TiO_2 is 30×30×5 nm), (b) Au-subsurface (Au 10 nm, TiO_2 is 30×30×10 nm) and (c) Au-embedded (Au 10 nm, TiO_2 is 30 × 30 × 20 nm). Inset: cross-sectional view.

In Figure 2.14, it can be observed that the structures with embedded Au NPs exhibited a more intense electric field in the vicinity of the TiO_2 surrounding the Au NP. Notably in the normal axis to the incident light, an axisymmetric electric near-field enhancement due to SPR effect exhibited four times more intensity for Au-subsurface and Au-embedded systems (55 and 53 intensity enhancement respectively), than that of Au-surface giving an intensity enhancement of 13.

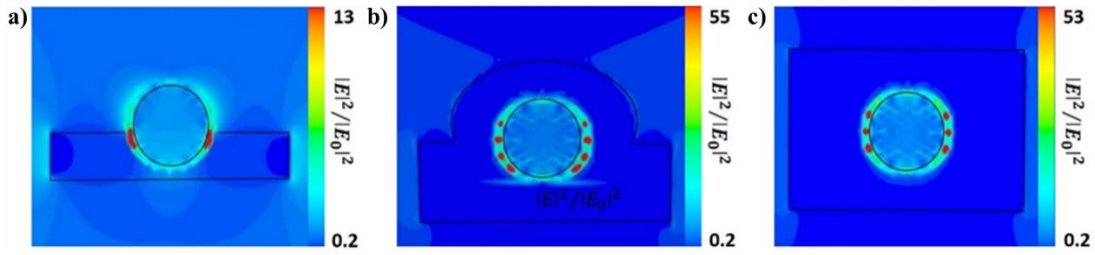

Figure 2.14 Electric near-field intensity enhancement on the cross-section of simulated TiO_2/Au model-structures (a) Au-surface corresponding to Au-on-TiO_2, (b) subsurface Au corresponding to Au-in-TiO_2-15, (c) embedded Au corresponding to Au-in-TiO_2-270. $|E|^2/|E_0|^2$, E accounts for the calculated electric near field while E_0 is the incident electric field). Solid black lines underline the Au and TiO_2 regions contours.

Now, comparing embedded-Au and subsurface-Au structures, not only the intensity, but also the spreading of the maximum intensity regions was wider than that of the Au-on-TiO_2 model system, pleading for a variation of the plasmonic intensity with increasing Au depth. Note that these results are in accordance with simulations on Janus-type nanoparticular systems.[139] The results match with the H_2 production rates under Vis, where Au-in-TiO_2-15 exhibits a slightly higher rate than Au-in-TiO_2-270, 0.04 against 0.03 µmol W^{-1} h^{-1}. However, the size limitation in simulations does not allow to address quantitatively the depth variation to address the experimental findings under UV, *i.e.*, Au-in-TiO_2-15 is lower than Au-in-TiO_2-270: 4.74 against 9.72 µmol W^{-1} h^{-1}.

In order to analyze if this is originated from the TiO_2 structure, the chemical composition of film in the vicinity of the Au NPs was analyzed for Au-in-TiO_2-15 by EELS, which is particularly appropriate to monitor the evolution of the oxidation state of oxides. Scans are provided in Figure 2.15. The spectra of Ti L_3 and L_2 edges at ~455 eV and ~465 eV was acquired near a Au NP and along the TiO_2 interface, *i.e.,* from the first 270 nm TiO_2 layer to the top TiO_2 layer (line scan of ~20 nm). The spectrum taken inside the first TiO_2 layer (Figure 2.13a, bottom layer) clearly shows the two dominant split peaks (Ti $L_{2,3}$-edges@455-465 eV and O *K*-edges@530 eV) corresponding to the TiO_2-anatase (Ti^{4+}).[142] The spectrum taken from the top layer of Au-in-TiO_2-15 is quite distinct (Figure 2.15a, top layer): two peaks can be distinguished in the L_3-edge with a higher energy peak being somewhat asymmetric and no split. The titanium oxide corresponds to a Ti_2O_3 with a low valence state (Ti^{3+}). The presence of such oxygen vacancies revealed a defective layer that could explain why the H_2 production rate decreased for this sample, either by inhibiting the surface chemical process of the photo-reduction of water, or by enhancing undesirable charge recombination on these defects. The study of oxygen vacancies is presented in Chapter 4.

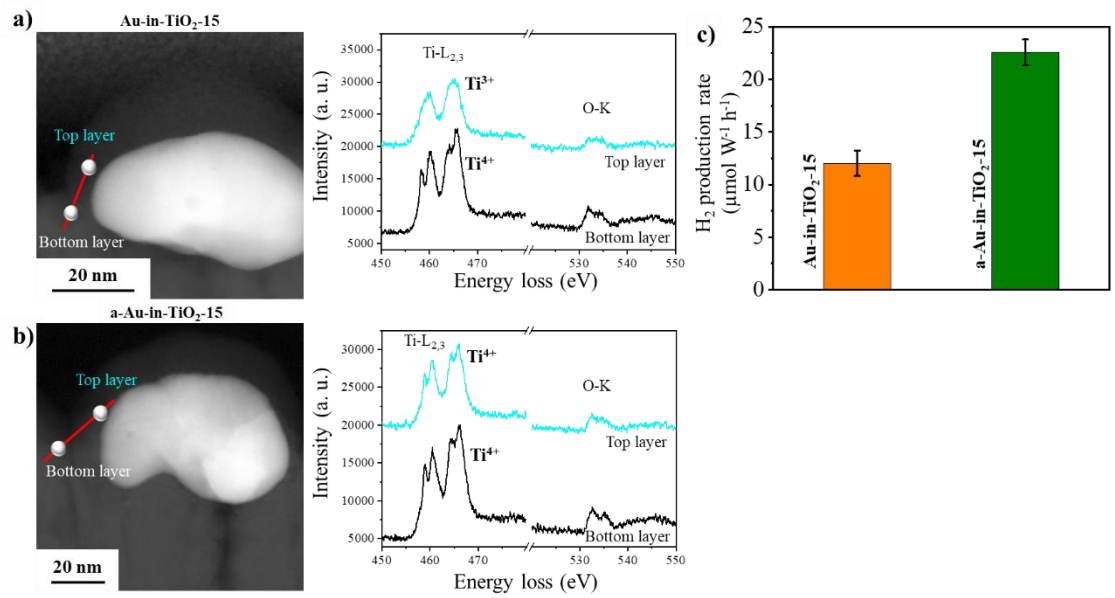

Figure 2.15 The EELS analysis is performed along the red line depicted in the STEM images for: (a) Au-in-TiO_2-15 and (b) annealed a-Au-in-TiO_2-15. EELS core loss edges are background subtracted using a power law fit before being plotted. (c) Normalized H_2 production rate under UV+Vis for: Au-in-TiO_2-15 (orange bar) and annealed a-Au-in-TiO_2-15 (green bar).

Next, continuing the analysis of the oxidation state, sample Au-in-TiO_2-15 was annealed to increase the coordination state of the surface/subsurface layers, to avoid any chemical modification of the 270 nm TiO_2 underneath layer, the sample Au-in-TiO_2-15 was annealed at 200 °C under air during 10 min and characterized again using EELS. Figure 2.13b shows the spectra of the top and bottom later for the sample, noted as a-Au-in-TiO_2-15. In this case, the top layer spectrum, showed the signature of anatase very close to that of the 270 nm TiO_2 layer, corresponding to the Ti^{4+} valence state. In addition, the chemical composition of the bottom layer was not modified upon annealing (Figure 2.15b). The annealing lowers the oxygen vacancy concentration by local recrystallization of the oxide.[143] The photocatalytic performance of a-Au-in-TiO_2-15, was measured under UV+Vis light (H_2 evolution in Figure 2.18e). The H_2 production rate shown in Figure 2.15c, increased compared to Au-in-TiO_2-15, by 22.58 against 12.02 μmol W^{-1} h^{-1}, and it is almost equivalent to Au-in-TiO_2-270 sample. Two important conclusions can be derived from these results. The TiO_2 stoichiometry and the defective nature and quality of the interface close to the Au NPs influence greatly the rate of recombination of the photo-induced charges. In addition, Ti^{3+} surface sites show a penalizing effect on the photo-reduction of water. This will be addressed more in detail in Chapter 4.

2.4.5 Study of the Transport Mechanisms of the Photogenerated Charges

All the TiO_2/Au structures exhibit a UV+Vis synergetic effect, *i.e.*, when the full spectrum is used, the H_2 production rate roughly doubles compared to UV exposure while, under

visible light H_2 production is negligible. A similar trend was observed in the study by Yan *et al.*[131] where Au NPs of various sizes (~3 to 10 nm range) were deposited on top of a TiO_2 anatase substrate. This raises questions on the exact role and impact of plasmon-induced charge generation by the Au NPs. Hence, to evaluate the response of the Au NPs in the different structures, photocurrent response by photoelectrochemical measurements under Vis light were carried. The chronoamperometric I-t curves obtained under a pulsed irradiation at 0 V (vs. Ag/AgCl) are shown in Figure 2.16a. Contrary to the H_2 production results under Vis light that showed no H_2 production, all Au-containing samples exhibited a notable photocurrent, and in addition the response with the on-off cycles was highly reproducible. Note that the hierarchy in the photocurrent intensity agrees well, qualitatively, with H_2 production, and also with the simulated intensity of the plasmonic near field. Au-in-TiO_2-270 sample showed the highest photocurrent followed by Au-in-TiO_2-15 and Au-on-TiO_2 with a photocurrent of ~4.3, 2.1, 1.2 μA cm^{-2}, respectively. Note that, even if electrons are being generated under Vis light as demonstrated by photocurrent measurements, their contribution to the H_2 reduction is not observed as seen in the H_2 production tests (Figure 2.19).

Next, as it was observed that UV+Vis contribution has a higher impact on the H_2 production, the flat band potential was determined in order to corroborate if this is due to a lower rate of recombination. Linear sweep voltammetry tests were carried under dark and UV+Vis light following the methodology to determine the flat band potential (see Figure 2.21 for the I-V dark and light curves). Figure 2.16b shows the photocurrent-potential curves for the samples with least and highest H_2 production rates, *i.e.*, TiO_2 and Au-in-TiO_2-270 (Figure 2.22 shows the photocurrent-potential curves for the rest of the samples). For semiconductor materials, negative flat band potentials are obtained when the separation of the photogenerated hole-electron becomes more easier, favoring the transfer of electrons to reduce H^+ to H_2.[144] As expected, the potential for Au-in-TiO_2-270 was more negative with a value of -0.58 V (vs. Ag/AgCl), than that of TiO_2 that was -0.18 V (vs. Ag/AgCl).

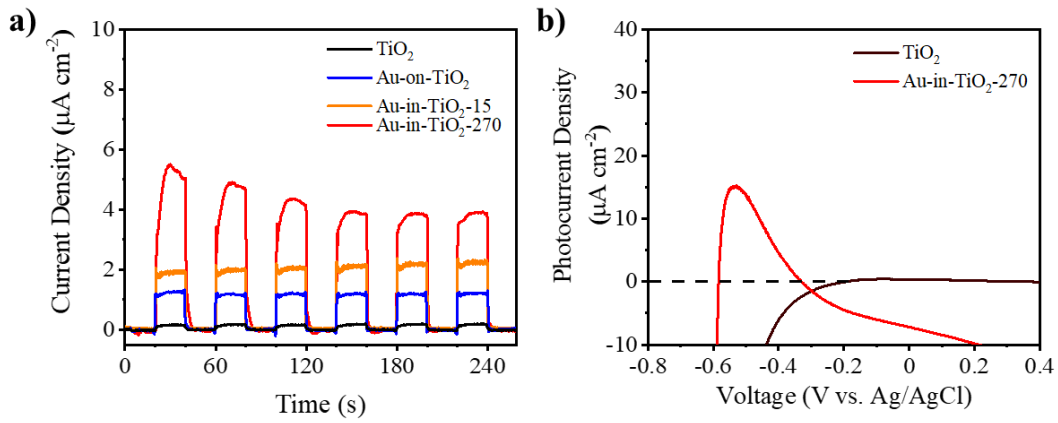

Figure 2.16 (a) On/off photocurrent measurements on TiO_2 and Au/TiO_2 hybrid structures. The samples were irradiated under visible light (400-1100 nm): TiO_2 (black curve), Au-on-TiO_2 (blue curve), Au-in-TiO_2-15 (orange curve) and Au-in-TiO_2-270 (red curve). Off corresponds to the dark current. (b) Photocurrent-potential curves in 0.05 M Na_2SO_4 solution for TiO_2 (black curve) and Au-in-TiO_2 (red curve) obtained under dark and UV+Vis light (353-1100 nm).

2.5 Discussion

At this point we can differentiate the mechanisms that contribute to the HER under UV+Vis light. Two main mechanisms of surface plasmon resonance can participate when only Vis light irradiates on a hybrid metal/semiconductor system:

(i) since under Vis light a readily photocurrent is measured, it can be inferred that, electrons are excited into the TiO_2 to populate the defect states into the gap, at the level of the transferred energy.

(ii) a localized intense oscillating electric field at the Au NPs/semiconductor interface generates hot electrons that are injected into the TiO_2.

In both mechanisms, electrons are thermalized and fast recombination processes take place preventing the electrons migration to the TiO_2 surface to catalyze the photo-reduction of water. Furthermore, hot electrons generated by the Au NPs do not participate in the reduction reaction, this is in accordance with the results showing negligible H_2 production under Vis light when the NPs where on top. Upon UV irradiation, thermalized and hot photo-excited electrons are being generated, but these are rapidly recombined before reaching the surface to catalyze the chemical reaction. This explains the lower H_2 produced under UV compared to UV+Vis. Hence, the energy transfer to the excited electrons in TiO_2 due to SPR could explain the observed synergy under UV+Vis light. Additionally, to the injection of hot electrons from Au to the CB of TiO_2, there is the contribution of the intense oscillating electric field at the Au NPs/semiconductor interface

and the existing UV excited electrons in the semiconductor located in the conduction band. These energetic electrons can migrate effectively to the TiO_2 surface and catalyze the chemical reaction. It is important to note that this synergy driven by the plasmonic near field (which increases significantly the number of hot electrons) and the Schottky barrier at the TiO_2/Au interface (extending the lifespan of the electron), is in accordance with the negative flat band potential observed in the Au-in-TiO_2 nanostructures.

To sum up, the following main steps driving the water splitting process under UV+Vis light are proposed and depicted in Figure 2.17: 1) photo excited electron-hole carriers are generated in TiO_2 (UV light contribution). The Schottky barrier allows charge separation, as photo-excited holes are being attracted by metal NPs where they can be annihilated through recombination. This process is enhanced by the semiconductor crystallinity extending the depletion layer from the metal/semiconductor Schottky contact; 2) surface plasmon resonance create an intense near field in Au nanoparticles (Vis light contribution) that transfers energy to the existing (UV originated) electrons in TiO_2, 3) electrons migrate to the semiconductor surface to perform the water splitting reaction.

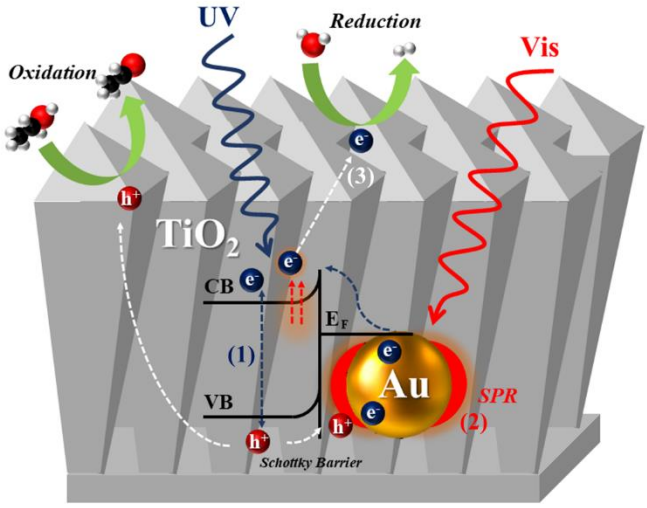

Figure 2.17 Proposed mechanisms under UV+Vis irradiation for Au-in-TiO_2-270 sample: (1) photogenerated charges with extended lifetime due to Schottky barrier, (2) energy transfer to photogenerated charges due to SPR and (3) migration of charges to TiO_2 surface to conduct redox reactions.

2.6 Conclusions

This chapter has analyzed the mechanisms of plasmon-enhanced photocatalytic water splitting and the effect of a metal/semiconductor interface, by characterizing different TiO_2/Au structures under Vis, UV and UV+Vis light. Both experimental data and numerical simulations coherently demonstrate that an important enhancement in the H_2

production rate is achieved when Au NPs are inside of a TiO_2 film and when Vis light is coupled with UV. Moreover, the depth of the Au NPs does not influence significantly the photocatalytic process and H_2 production rate efficiency if the crystallinity of the semiconductor is high.

Results indicate that the essential synergetic role of UV and Vis light consists in increasing the carrier lifetime and on the enhancement of the hot carrier generation in TiO_2, resulting from the energy transfer from the plasmonic field to the photo-excited carriers in TiO_2. Note that, as Au NPs are embedded, the plasmonic near field is more intense and spread over a larger area compared with Au positioned on the top surface. The results also reveal that the water-splitting reaction that leads to H_2 production does not occur on Au NPs, but on the semiconductor surface, contrary to what was suggested in literature. Therefore, the TiO_2 crystallinity and its surface stoichiometry are highlighted as they directly impact the charges transport and liquid-solid chemical reactions.

2.7 Annex

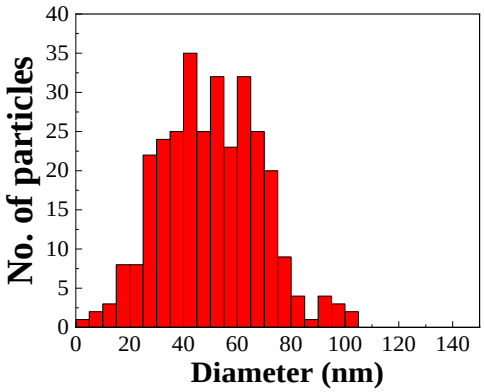

Figure 2.18 Au nanoparticules size distribution. Data extracted from SEM images.

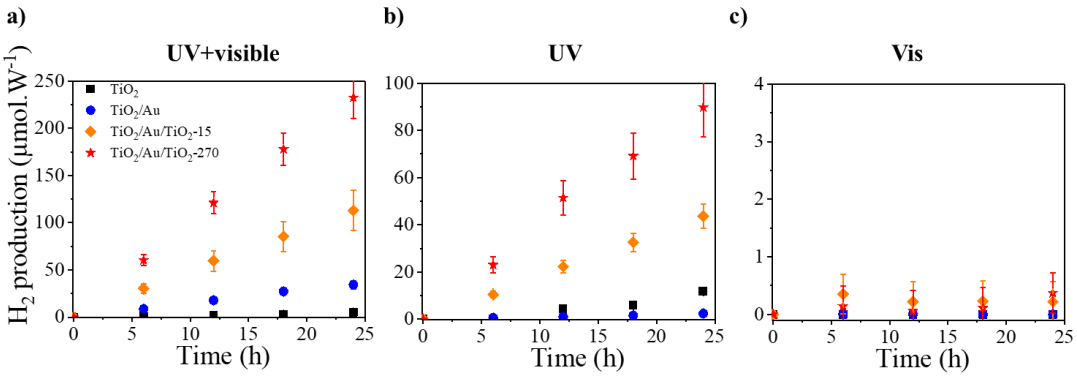

Figure 2.19 H_2 production (µmol W^{-1}) measured under: UV and visible (left), UV (middle) and visible (right) illuminations for TiO_2 (black square), Au-on-TiO_2 (blue circle), Au-in-TiO_2-15 (orange diamond) and Au-in-TiO_2-270 (red star). Values normalized by the UV and visible light flux at λ = 365 nm and λ = 405 nm, respectively and by the surface area (cm^{-2}).

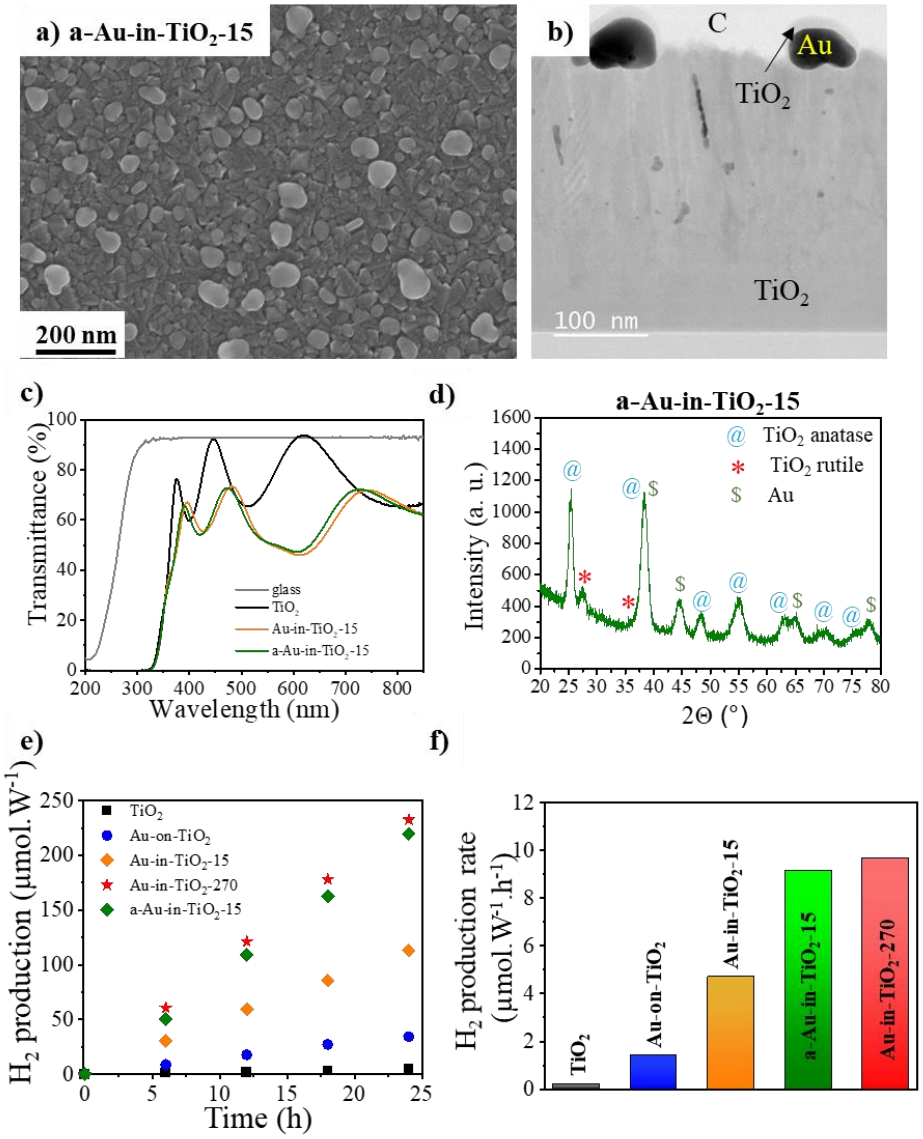

*Figure 2.20 (a) Top view SEM image, (b) HAADF-STEM cross-section image, (c) UV-visible spectra (in transmission) in the 200-850 nm region, (d) GI-XRD patterns (peaks are labelled by anatase TiO_2 (blue @), rutile TiO_2 (red *) and Au (green $)), (e) H_2 production (µmol W^{-1}) normalized by the light flux and the surface area (cm^2) and (f) normalized H_2 production rate per light flux for the annealed a-Au-in-TiO_2-15 material. For comparison, borosilicate B33 glass (grey curve), TiO_2 (black square and curve), Au-on-TiO_2 (blue circle and curve), Au-in-TiO_2-15 (orange diamond and curve), a-Au-in-TiO_2-15 (green diamond and curve) and Au-in-TiO_2-270 (red star and curve) are depicted. Note that the photocatalytic tests are performed as follows: the substrates (~1 cm^2) are immersed into a 65:35 deionized water:ethanol solution at room temperature and pressurized under argon at 2.0 bar.*

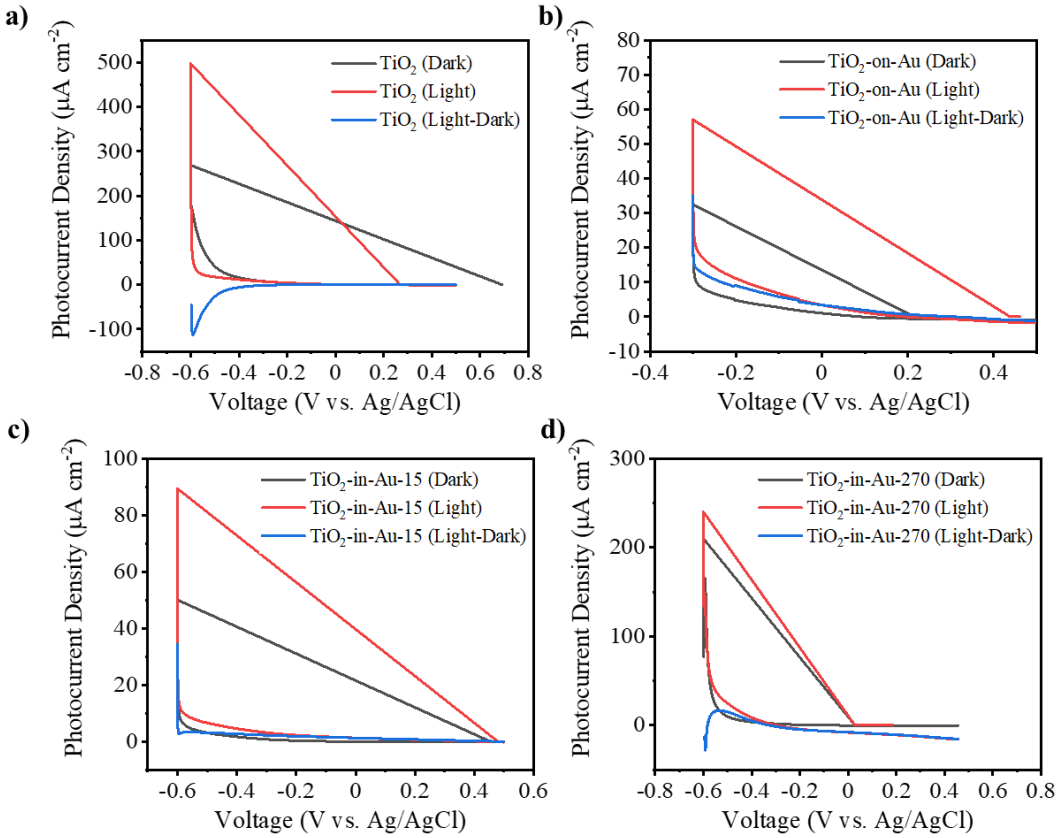

Figure 2.21 I-V dark and light, and photocurrent curves in 0.05 M Na_2SO_4 solution used to determine flat band potential.

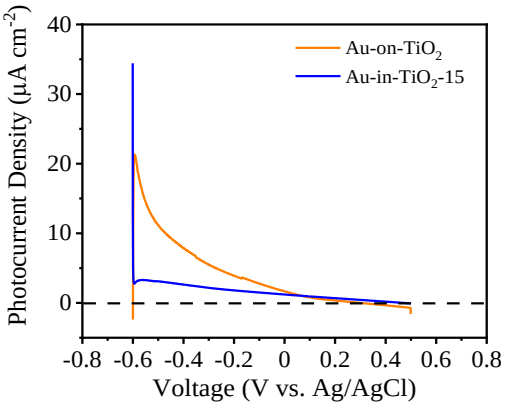

Figure 2.22 Photocurrent-potential curves in 0.05 M Na_2SO_4 solution for Au-on-TiO_2 (orange curve) and Au-in-TiO_2-15 (blue curve) obtained under dark and UV+Vis light (353-1100 nm). Flat band pointed with arrows.

Table 2.3 Flat band potential determined from photocurrent plots in 0.05 M Na_2SO_4 solution.

Sample name	**Flat band potential (V vs. Ag/AgCl)**
TiO_2	-0.180
Au-on-TiO_2	-0.602
Au-in-TiO_2-15	+0.470
Au-in-TiO_2-270	-0.583

Chapter 3

Tuning of H_2 production by surface enlargement of TiO_2 photocatalyst through silicon micromachining

This chapter presents a technological solution to tune the H_2 production of TiO_2 photocatalysts with enlarged surface, based on a silicon micromachining process prior to the TiO_2 deposition. To quantify the effect of the surface enlargement on the photocatalytic activity, different microstructured photocatalysts were fabricated. The study starts with the theoretical design and analysis of different proposed models by considering the technological restrictions. Next, the micromachining process based on deep-reactive ion etching (DRIE) is optimized to obtain robust and repeatable micromachined templates. The influence of the area enlargement factor (AEF) on the morphology, quality, and catalytic performance of the enlarged surface photocatalyst was thoroughly investigated and correlated to the H_2 production under UV/Visible irradiation. Lastly, Au and Pd plasmonic nanoparticles are deposited on the 3D photocatalysts, where the impact of their morphology and optical properties on the photocatalytic activity is discussed.

3.1 Introduction

In Chapter 1 Section 1.3, a brief introduction about the different types of nanomaterials was given, among these, the fabrication of high surface microstructures by augmenting the surface-to-volume ratio has proven to provide multifunctional properties. Many of these reported techniques for enlarged TiO_2 nanomaterials are made for powder form products, which represent two major disadvantages: 1) agglomeration upon contact with solution, which results in an adverse effect on catalyst performance, and, 2) the separation and recovery from wastewater is difficult, which limits their industrial applications.[145] Moreover, these methods are not useful since they are not compatible with the approach of this work, as it is important to maintain the large surface structure after PVD deposition of TiO_2 by sputtering.

However, these fabrication techniques allow the fabrication of random and very disperse morphologies that serve as substrates for further deposition of the photocatalyst and other sensitizing elements.

In the microtechnology field, considerable effort has been devoted to develop robust structures offering high active surface area, creating high-surface templates for the further deposition of the active material. These materials exhibiting porous, branched[146–148], or with defined high aspect-ratio patterns can indeed be separated and removed from water while at the same time support the deposition of photocatalysts materials deposited in vacuum. Such high-aspect ratio approach was conducted by Eustache *et al.*[149] for a lithium-ion microbattery based on a scaffold of silicon microtubes with a further TiO_2 thin film deposited by ALD. The use of deep reactive-ion etching processes allowed the fabrication of high-depth microtubes, which represented an enlargement in the surface of 67 times. The surface capacity was clearly impacted with the 3D topology leading to an increase in the charge/discharge rate of the 3D micro storage device.

With the goal to develop hierarchical three-dimensional (3D) high surface area photocatalysts, silicon-based substrates were fabricated by deep-reactive ion etching (DRIE) which were covered with a compact TiO_2 layer by sputter deposition. The effect of the surface augmentation was correlated to the H_2 production, evidencing the fabrication process as an accurate way to increase the aspect ratio of the photocatalyst and to create robust photocatalysts.

The present chapter is constituted hence in three parts, the first one is devoted to the fabrication of the silicon 3D substrates, starting from the theorical pattern design, the fabrication of substrates exhibiting a defined series of aspect ratios carried by photolithography, deep-reactive ion etching (DRIE) of silicon, and the sputter deposition of TiO_2; and finalized by the morphological characterization of each substrate. The second part is focused on the 3D photocatalyst, films of different thickness are deposited on the substrates, the morphology of the films is characterized and their H_2 production is

measured. Moreover, the AEF is estimated experimentally, and is further correlated with the film thickness and the photocatalytic performance. In the third part, with the aim to extend the absorbance spectra of the device, Au and Pd nanoparticles are grown separately by chemical photodeposition and by ALD, respectively. The morphological characterization and H_2 production are further correlated as well with the AEF. The results of this study were published in 2022 in the indexed journal Applied Surface Science.[150]

3.2 Characterization

3.2.1 Structural and chemical characterization

3.2.1.1 Scanning electronic microscopy (SEM)

The topology of the etched silicon substrates and the morphology of the 3D photocatalyst containing TiO_2 thin films and TiO_2/Au NPs, -/Pd NPs was determined by SEM whose mechanism was mentioned in Chapter 2 Section 2.3.

Analytical information. Experiments were carried in a SEM S-4800 Hitachi with secondary electrons (SE) signal at 5 kV and with a working distance of 7.2 mm.

3.2.1.2 Grazing Incidence X-Ray Diffraction (GI-XRD)

The diffraction pattern for the TiO_2 films was obtained for the films deposited in flat silicon by GI-XRD; whose mechanism and analytical information of the instrument were mentioned in Chapter 2 Section 2.3.

TiO_2 films with Pd NPs were characterized in a SEIFERT XRD 3000 TT XRD conducted in CIRIMAT. Cu-Ka radiation (λ = 1.54059 Å) was fitted with a diffracted-beam graphite monochromator. The diffraction angle (2θ) was scanned from 10 to 100°.

3.2.1.3 X-Ray Photoelectron Spectroscopy (XPS)

Deconvolution of the high resolution XPS O 1s and Ti 2p spectra obtained for the TiO_2 film denoted as reference (A1-T2), obtained as detailed in Chapter 2 Section 2.3, was carried using the software Avantage.

3.2.2 Optical characterization

3.2.2.1 UV−Vis spectroscopy

The absorbance spectrum was obtained for the TiO_2 film denoted as reference (A1-T2) deposited on quartz, whose mechanism was mentioned in Chapter 2 Section 2.3.

Analytical information. Experiments were carried in a PerkinElmer Lambda 650 UV−Vis spectrometer, from 200 to 800 nm in the absorbance mode.

3.2.3 Electrochemical characterization

3.2.3.1 Electrochemical Active Surface Area (EASA)

The EASA of the 3D photocatalyst was obtained by electrochemical measurements carried out in a three-electrode configuration with the instrument and setup described in Chapter 2 Section 2.3.4. Cyclic voltammetry tests were carried with a scan rate of 30 mV s^{-1} from -0.5 to 1.5 (V vs. Ag/AgCl) for 25 cycles. Area of the electrodes was carefully measured.

For the preparation of the working electrode the Si/TiO_2 photocatalysts were covered with a film of Ti/Au (50 nm and 700 nm) by sputtering. The EASA is the measured capacitance of the deposited gold which was calculated by integration of the reduction of gold oxide in cyclic voltammetry experiments: a value of 390 µC cm^{-2} in 0.5 M H_2SO_4.[151,152] The experimental area enlargement factor AEF_{EAS} was calculated with Equation 3.1. Where the 2D electrode consisted a of silicon substrate, 1 µm thick TiO_2 film covered with Ti/Au (50 nm and 700 nm).

$$AEF_{EAS} = \frac{EASA_{3D}}{EASA_{2D}} \qquad \text{Equation 3.1}$$

3.2.4 Photocatalytic activity measurement

The photocatalytic activity was measured by gas chromatography, the H_2 evolution was measured over 24 h as detailed in Chapter 2 Section 2.3. Furthermore, for cycling experiments the test was extended to 45 h, with measurements every 1 h. Xenon lamp was used directly for irradiation (no filters used to delimit the wavelength range).

3.3 Silicon 3D scaffold

3.3.1 Design: theorical considerations

The theoretical design of the pattern was determined after evaluation of the AEF of different geometries. It is important that the aspect ratio can be tuned precisely in order to allow the quantification of the H_2 production rate as a function of the total surface area. The 3D photocatalyst was designed with a planar area of 1 cm^2.

The patterns presented in Figure 3.1 were compared: square microcavities (hereafter denoted as *microcavities*), walls, pillars, rods and hollow-rods. Each pattern was characterized by a dimensionless geometric factor *g* described by Equations 3.2 to 3.6, which depends on the width of the features *a* and *w*. Where *a is the* width of walls for *microcavities*, *walls* and for *hollow-rods* pattern, and width of the columns for *pillars* and *rods* patterns. For *hollow-rods*, other two parameters were defined, column external diameter a_e and column internal diameter a_i. Parameter *w* is the separation between the features, being these, walls for *microcavities* and *walls* patterns, and columns for *pillars*,

rods and *hollow-rods* patterns. Furthermore, in *pillars* pattern *w* equals to *a*, and for *hollow-rods*, *w* equals a_i.

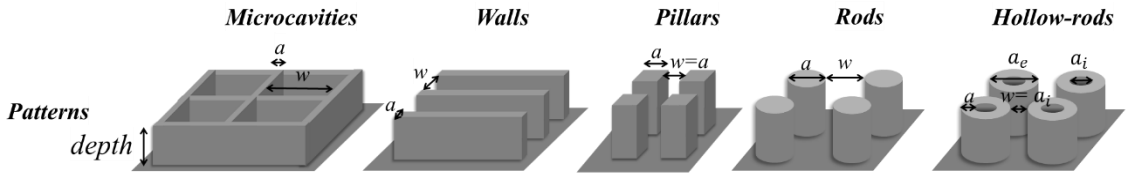

Figure 3.1 3D models of the proposed patterns: microcavities, walls, square pillars, rods and hollow-rods.

$$g = \left(\frac{2.w}{w+a}\right)^2 \qquad \text{Equation 3.2}$$

$$g = \frac{2}{w+a} \qquad \text{Equation 3.3}$$

$$g = \frac{4.a.w}{(w+a)^2} \qquad \text{Equation 3.4}$$

$$g = \frac{\pi.a.w}{(w+a)^2} \qquad \text{Equation 3.5}$$

$$g = \frac{(\pi.a_e + \pi.a_i).w}{(w+a_e)^2} \qquad \text{Equation 3.6}$$

Subsequently, the aspect ratio A_R is defined in Equation 3.7 by *depth* which is the height of the patterns and *w*. Hence, the AEF can be calculated using Equation 3.8.

$$A_R = \frac{depth}{w} \qquad \text{Equation 3.7}$$

$$AEF = 1 + gA_R \qquad \text{Equation 3.8}$$

Several technological restrictions must be considered to limit the variation of the geometrical parameters. The minor limitations are the photolithography resolution (10 µm), the critical aspect ratio of the DRIE process to ensure that the etching does not destroy the pattern, and the *depth* of etching which is limited by the wafer thickness (500 µm). The major restriction comes from the magnetron sputtering technique that is used to deposit the TiO_2 layer. To ensure a continuous sputter deposition of the TiO_2 semiconductor film on the 3D micropatterned silicon substrate, an A_R close to 2 is imposed. Next, is important to consider that *depth* can be tuned later by the etching time of DRIE, while *w* and *a* parameters would be fixed by the mask pattern. First, *w* is defined as *a* can be variated by setting a restriction to the A_R, *w* is directly correlated to A_R and *depth*. Figure 3.2 shows the variation of *w* by varying A_R, note that when *depth* is lower (50 um), *w* decreased. However, since *depth* is proportional to the AEF —as will be discussed next— is important to consider the highest *depth* value possible; hence,

considering an A_R of 1.5, 2.0 and 2.5, for a *depth* of 150 μm, *a* value would be 60, 75 and 100 μm, respectively.

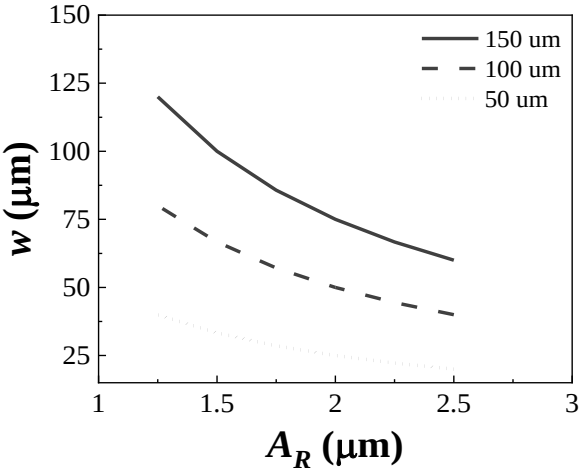

Figure 3.2 Impact of the aspect ratio A_R on the parameter w calculated using Equation 3.7 for 50, 100 and 150 μm depth. The values apply to the proposed patterns in Figure 3.3.

Based on the previous values for *w* and A_R, different scenarios can be considered by varying *a*, Figure 3.3 shows the variation of *a* when the A_R is 1.5 (a, d), 2.0 (b, e) and 2.5 (c, f); note the A_R value is kept constant for all the patterns except for *pillars* since *w* is equal to *a*. Hence, in *pillars* the A_R also defines the highest value for *a*, which is 100, 75 and 65 μm for each A_R (in Figure 3.3 a-c *pillars* plots start at this *a* value); subsequently, as *a* increases the A_R decreases. Additionally, the *depth* is set at different values, 50 (dotted lines) only for *microcavities* and *walls*, 100 (dashed lines) and 150 μm (solid lines).

When the A_R is at a maximum of 1.5 (Figure 3.3a, d), for a *depth* of 100 μm, *rods* does not change greatly by varying *a* from 10 to 60 μm, the AEF changes from 1.3 to 1.8; and by increasing the *depth* to 150 μm, the AEF goes to 1.4 to 2.1. For *hollow-rods*, when *a* goes from 10 to 60 μm, the AEF decreases, for a depth of 100 μm, the AEF changes from 2.4 to 2.0; and with a *depth* of 150 μm, the AEF goes to 3.6. to 2.5; note that for this pattern the diameter at the center of the rings a_i was also submitted to same A_R restriction. For *pillars*, when *a* is 100 μm (minimum allowed value) for a *depth* of 100 μm, the AEF is 2.0, and it increase slightly to 2.5 when *depth* is 150 μm. For *walls* the AEF for is not greatly impacted neither, when *a* goes from 10 to 60 μm, for a *depth* of 50, 100 and 150 μm, the AEF decreases from 1.9 to 1.6, 2.8 to 2.3, and 3.7 to 2.9, respectively. For *microcavities*, also by increasing *a* from 10 to 60 μm, the AEF decreases, for a *depth* of 50, 100 and 150 μm, the AEF decreases from 2.7 to 1.8, 4.3 to 2.6, and 6.0 to 3.3. Moreover, considering the A_R at a maximum of 2.5 and *depth* of 150 μm (Figure 3.3c, d) the change in the AEF is neither significant for *rods* and *pillars* the AEF is 3.0, and 3.5,

when *a* has an optimum value of 70 and 60 µm, respectively. For *hollow-rods*, the AEF reaches 4.4, when a is 10 µm. And for *walls* and *microcavities* the AEF changes to 5.3 and 8.4 when *a* is 10 µm for both.

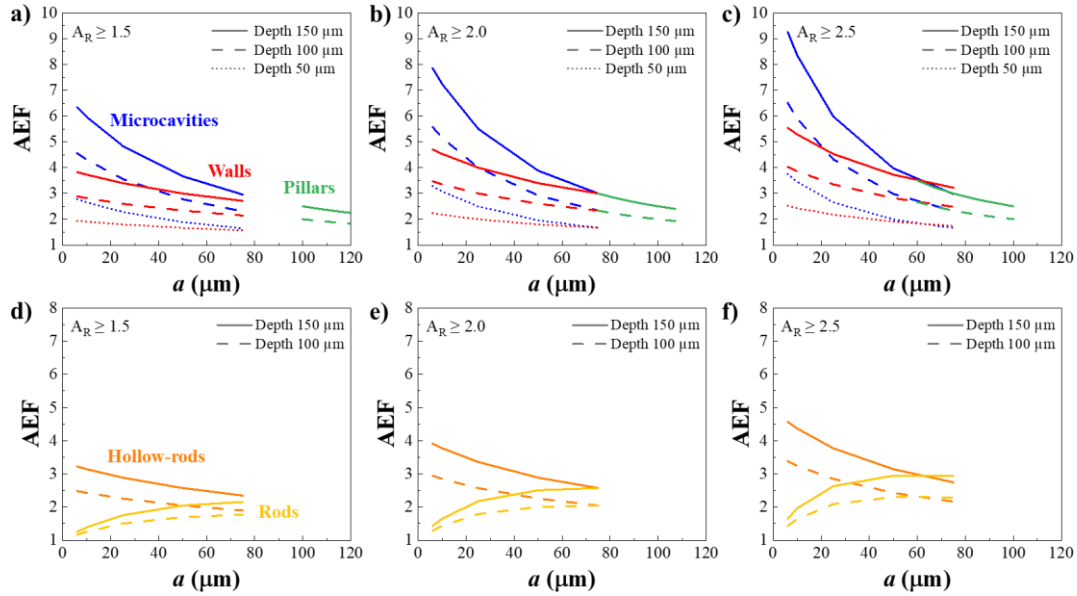

Figure 3.3 Impact of the parameter a on the area enlargement factor (AEF) calculated using Equation 3.8 for microcavities (blue), walls (red) and square pillars (green) (a-c), and hollow-rods (orange), and rods (yellow) (d-f). Aspect ratio A_R set below 1.5 (a, d), 2.0 (b, c), and 2.5 (c, f); which defines parameter w to 100, 75 and 60 µm for each A_R, except for pillars, since w equals to a. Depth set at 150 (solid line), 100 (dashed line), and 50 µm (dotted line).

Overall, *rods* and *pillars* cover a small window of AEF, even by varying significantly *a* for an A_R of 2.5, the AEF is limited to 3.5. Comparing *walls* and *hollow-rods*, a broader range of AEF can be achieved by varying *a*, and most importantly the jump in the AEF is about +1, by augmenting the *depth* +50 µm; however *hollow-rods* represents a more challenging symmetry when it comes to DRIE, as the exposition of the surfaces to the reactants is different considering the cylindrical surfaces vs. the inner cavities. Additionally, *walls* pattern is not an efficient design neither since the AEF is limited to 5.3 when A_R is 2.5; whereas *microcavities* reaches the highest surface enhancement with an AEF of 8.4 when *depth* is 150 µm. Moreover, *microcavities* pattern covers a broader range of AEF by changing *depth*, where the AEF increases +2.0 and +2.5 by augmenting the *depth* +50 µm for A_R of 2.0 and 2.5, respectively, this represents the most significant impact on the AEF among the proposed patterns.

Considering the sputtering deposition restriction, the *microcavities* pattern was chosen for the fabrication of the photolithography mask described in Section 3.2. The A_R of 2.0 was fixed with and the dimensional parameters of 10 and 75 µm for *a* and *w*. Figure 3.4 shows the variation of the AEF with *depth.* According to this, the AEF is predicted to

change from 3 to 7 when the microstructure *depth* goes from 50 µm to 150 µm, and the change on the A_R goes from 0.7 to 2.0 (inset in Figure 3.4) which ensures the deposition of a compact layer.

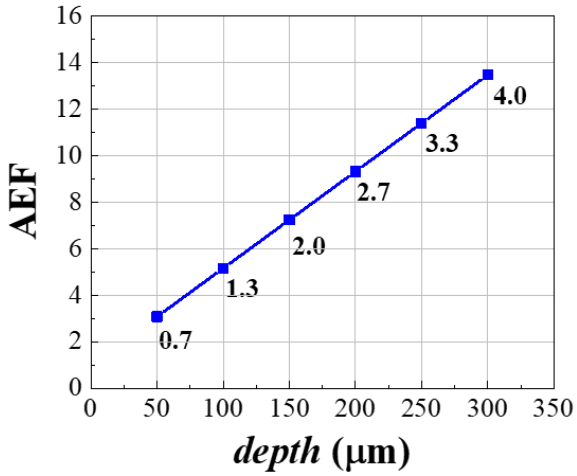

Figure 3.4 Impact of depth on the AEF for the square microcavity pattern where w and a are 75 and 10 µm. The aspect ratio is given for a specific height of the pattern (depth).

Next section will be focus on the development of the DRIE process of the silicon substrates with the chosen microcavities pattern; as sputtering is a fast rate deposition technique, the control over the profile of the 3D substrates is highly important, hence DRIE process parameters were carefully studied. Subsequently, the deposition of TiO_2 films on the silicon substrates will be carried and characterized.

3.3.2 3D scaffold fabrication

A 500 µm thickness silicon p-type 4-inch wafer single side polished was is chosen as substrate to fabricate the 3D photocatalyst. In the photolithography process a predetermined pattern printed on a glass mask is transferred to the substrate. The design of the pattern will be discussed with detail in Section 3.4 of the current chapter. Hence, just the technical aspects of the mask are given here. The pattern was designed on the software CleWin 5.2 Layout Editor (Version 5.2.3) for a 4-inch diameter substrate. The patterned was printed on a 5-inch glass mask by copper metallization. Figure 3.5 shows the scheme of the pattern with the detailed dimensions and a photograph of the glass mask.

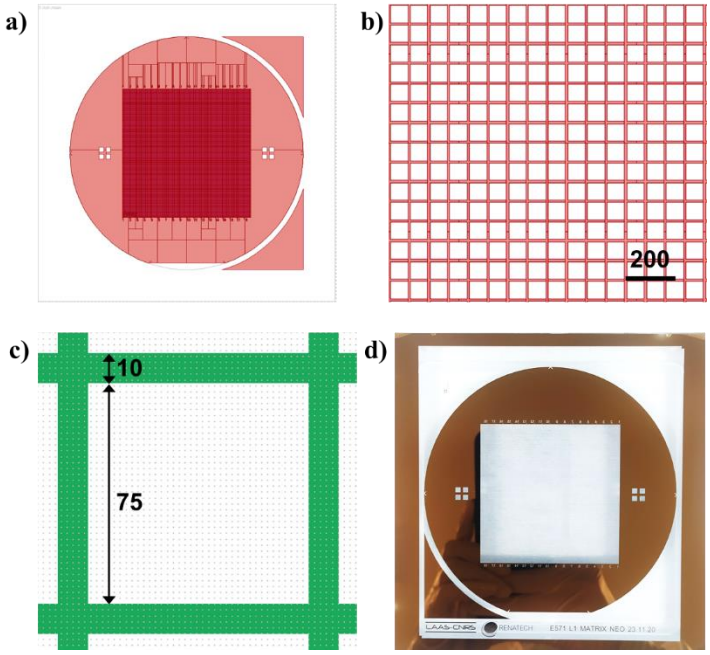

Figure 3.5 Design of mask for with pattern. (a) 5-inch view scheme, (b-c) detail of pattern with units in µm, and (d) photograph of 5-inch glass/Cu mask with printed pattern.

Figure 3.6 depicts the overall micromachining process: 1) transfer of the pattern on the mask to the substrate silicon by photolithography, 2) DRIE of silicon, 3) postprocessing by thermal oxidation of silicon followed by the removal of the oxide layer; and 4) TiO_2 layer sputter deposition followed by (optional) chemical synthesis of Au nanoparticles (NPs). Each of these steps will be detailed next.

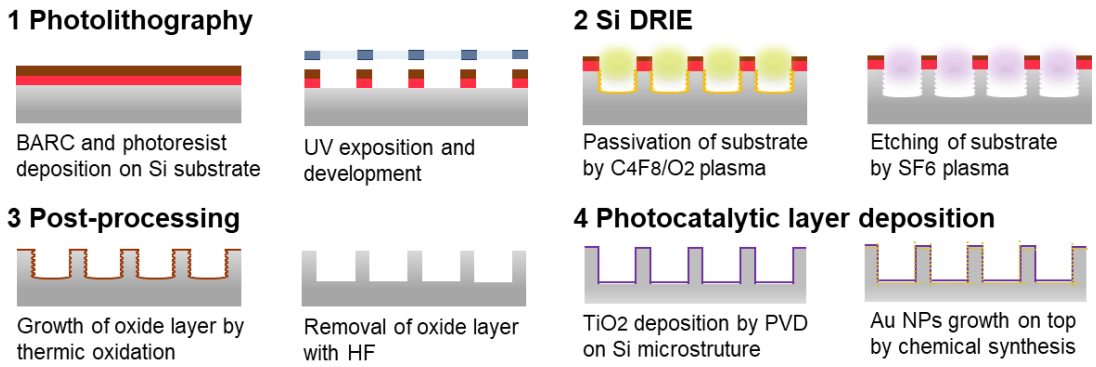

Figure 3.6 Main process steps underlining the cross-section of the 3D photocatalyst.

Prior to procedure, to ensure the removal or organic residues, the substrates were cleaned with a piranha solution. The piranha solution is a mixture of sulfuric acid (H_2SO_4 > 96%, Sigma-Aldrich, CAS: 7664-93-9) and hydrogen peroxide (H_2O_2) (1:1). The

substrate was immersed in the piranha bath for 2 min. Note: chose a beaker large enough to have space for bubbling or splashing. Since the mixture is a strong oxidizer, it removes most of the organic matter by creating a thin oxide layer, and it also hydroxylates the surface (OH^- groups) rendering it hydrophilic. After piranha solution, the wafers were rinsed with deionized (DI) water and dried in the spinner tool. Next, the removal of the oxide layer was done with buffered HF reagent (40% ammonium fluoride, NH_4; 49% hydrofluoric acid, HF). The substrate was immersed approximately 30 sec and rinsed with DI water and dried. In order to activate the surface, O_2 plasma was conducted (TEPLA, 300 semi-auto), during 5 min with 800 W power.

3.6.3.1 Photolithography

The photolithography process starts by depositing a bottom anti-reflective coating layer of 200 nm (BARC, Barki II 200, MicroChemicals) by spin-coating (rotating speed 3000 rpm, acceleration 4000 rpm/s and 30 sec time); and baked on a hot plate at 200 °C for 1 min. Next, the positive photoresist (PR) is deposited with an Automated Resist Processing System (EVG 120) with a thickness of 20 µm. The positive PR (AZ-40XT, MicroChemicals) is spin-coated onto the silicon wafer (rotating speed 5000 rpm, acceleration 500 rpm/s and 30 sec time). The PR layer is "soft baked" ramping from 65 to 126 °C, then kept at 126 °C during 2.5 min and cooled down to room temperature. The PR layer is then patterned with a manual mask aligner (Suss Microtec, MA6 Gen4), a 5-inch glass mask with predefined pattern is fix on the equipment and UV light exposure is irradiated (40 mW cm^{-2} at 405 nm) during 10 sec in vacuum contact mode.

After irradiation, the "hard bake" and developing is carried on the automated system previously used (EVG 120). The PR "hard baked" is done ramping from 65 to 105 °C, then kept at 105 °C during 80 sec and cooled down to room temperature. The pattern transfer is completed by developing the exposed PR using a developer reagent (MF-CD-26, Microposit) during 140 s, followed by rinsing with DI and dried by spinning rotation. Observations with the optical microscope after developing were done in order to ensure the correct transfer of the pattern. Likewise, the PR thickness was controlled by profilometry. Accepted PR thickness on the center and edges of the wafer were 20 ± 1.5 µm.

3.6.3.2 Deep Reactive Etching (DRIE) optimization

The etching of the substrates was performed using an AMS420 reactor (Alcatel-Adixen). In order to ensure the thermalization of the substrate by the reactor, is necessary to remove the BARC and photoresist excess from the edges of the wafer. Prior to introduction of the substrate on the chamber, the edge of the wafer was fully cleaned using a tissue with acetone. The temperature of the chamber during the etching was 10 °C. Etching and passivation cycles with SF_6 and C_4F_8/O_2 gases were set to a constant flow rate, details depicted in Table 3.1. The exposure time for each gas is critical for the profile control and

presence of defects, hence this section is focused on the optimization of such of the exposure time of each gas.

Table 3.1 Detail of DRIE main process parameters.

Gases	Flow (L min^{-1})	Power (W)	Pressure (mbar)
SF_6	0.25	2500	0.05
C_4F_8/O_2	0.25/0.035	2500/70	0.05

Table 3.2 details the DRIE parameters and the corresponding profile characteristics of the patterns observed by SEM. Figure 3.7 shows the SEM cross-sections of the etched microcavities for different SF_6:C_4F_8/O_2 exposure time ratios. The profile angle θ (Table 3.2) describes the slope of the cavity wall edge, it was calculated from the bottom and top widths of the wall and the cavity depth as described in Annex Section 3.7. When $\theta < 90°$, the profile is labeled negative (closing cavity), and when $\theta > 90°$, the profile is labeled positive (opening cavity). At a SF_6:C_4F_8/O_2 exposure time ratio of 1.67, the etch rate was 4.35 μm min^{-1}, but dropped to 1.75 μm min^{-1} when the SF_6:C_4F_8/O_2 exposure time ratio was 0.40. This difference in etch rates is due to the concentration of free fluorine radicals (F*) in the etching step in comparison to the concentration of free oxygen radicals (O*) that passivate the surface. Consequently, when the SF_6:C_4F_8/O_2 exposure time ratio is 0.40, the etching process is overcome by the passivation step, and the quantity of SiF_4 formed in each iteration is reduced, meaning that fewer silicon atoms are removed from the substrate.

Table 3.2 Etch rate, profile angle θ and defects for different SF_6 and C_4F_8/O_2 exposure times in the DRIE process of silicon.

SF_6:C_4F_8/ O_2 Ratio	Exposure time (s)		Etch rate (μm min^{-1})	Profile		Grass defects
	SF_6	C_4F_8/O_2		Angle θ (°)	Description	
1.67	2.5	1.5	4.35	89.19	Negative	No
1.10	2.2	2.0	4.17	89.63	Negative	No
0.85	1.7	2.0	2.65	89.79	Negative	No
0.75	1.5	2.0	3.00	90.28	Positive	No
0.57	2.0	3.5	2.69	90.97	Positive	Low density
0.40	2.0	5.0	1.75	91.79	Positive	High density

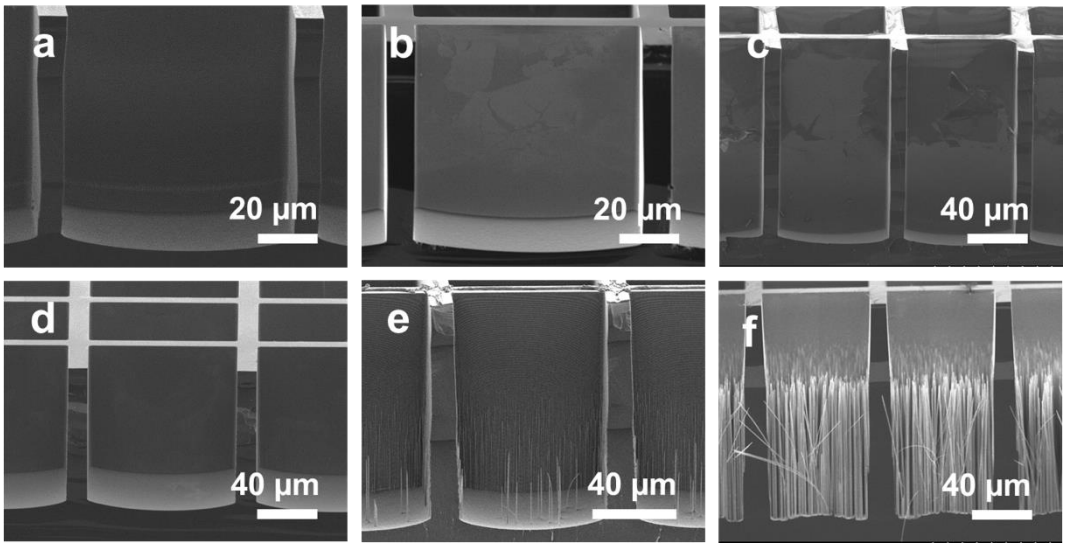

Figure 3.7 SEM cross-section images of silicon microstructures obtained by DRIE with SF_6:C_4F_8/O_2 exposure time ratios of 1.67 (a), 1.10 (b), 0.85 (c), 0.75 (d), 0.57 (e) and 0.40 (f). The depths are 74 µm (a), 75 µm (b), 127 µm (c), 75 µm (d), 109 µm (e) and 140 µm (f).

Along with the etch rate, the profile is also highly influenced by the SF_6:C_4F_8/O_2 exposure time ratio. Beyond 0.85, negative profiles are obtained, as observed in Figure 3.7 SEM cross-section images of silicon microstructures obtained by DRIE with SF_6:C_4F_8/O_2 exposure time ratios of 1.67 (a), 1.10 (b), 0.85 (c), 0.75 (d), 0.57 (e) and 0.40 (f). The depths are 74 µm (a), 75 µm (b), 127 µm (c), 75 µm (d), 109 µm (e) and 140 µm (f).Figure 3.7a-c. After decreasing to 0.75, the sidewalls become positive with a near vertical profile angle of 90.28° (Figure 3.7d). Below 0.57, positive profiles are obtained as well (Figure 3.7e-f). To understand the impact of the SF_6:C_4F_8/O_2 exposure time ratio on the profile, it is important to explain the etching and passivation mechanisms that are inherent to the Bosch DRIE process used in this study. The mechanisms are depicted in Figure 3.8, starting with the passivation of the cavities by the layer deposition by C_4F_8/O_2 (1); followed by the etching step (2), where isotropic accelerated ions remove the fluorocarbon layer that is located only at the bottom of the cavities; next, anisotropic etching takes place (3), and removes the exposed silicon in all directions also in the same bottom cavity.

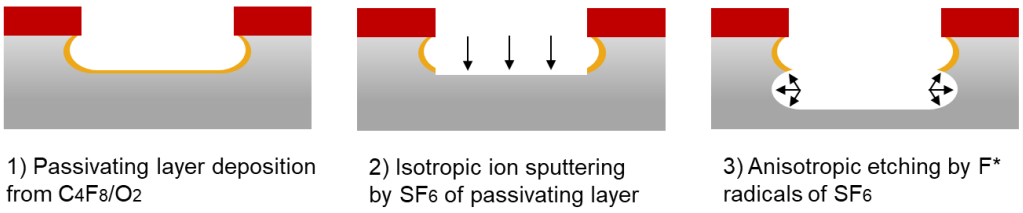

Figure 3.8 Schematic of the repetitive steps of etching and passivation until reaching high aspect ratio profiles, as developed in a Bosch DRIE process.

Hence, for SF_6:C_4F_8/O_2 exposure time ratios above 0.85, there is a higher concentration of F* radicals, therefore, anisotropic etching is favored since the passivation layer is scavenged quickly and the F* ions bounce repeatedly in the already etched trenches, removing the passivating layer and etching slightly more in each iteration, thus increasing the bottom diameter and forming a negative profile.

On the other hand, for SF_6:C_4F_8/O_2 exposure time ratios below 0.57, the profile becomes positive as expected, since the concentration of F* radicals is limited. However, another important defect appears, a high density of peaks inside the cavities also known as *grass.* For an SF_6:C_4F_8/O_2 exposure time ratio of 0.57 (Figure 3.7e) after an etch time of 26 min, the number of peaks is ~13 per cavity, whose height and width at the half-height are 22.4 µm and 0.44 µm on average, respectively. Below an SF_6:C_4F_8/O_2 exposure time ratio of 0.40, after an etch time of 80 min, the density of peaks increases drastically, as the *grass* covers the entire bottom surface of the cavities (Figure 3.7f): this results in what it is known as *black silicon*. Here, the silicon grass features an average height and width of 87.6 and 0.93 µm, respectively. Upon increasing the SF_6:C_4F_8/O_2 exposure time ratio above 0.75, no *grass* was formed (Figure 3.7a-d). Grass formation originates from the localized high concentration of oxide reaction products that are not removed from the surface before each new etch/passivation cycle.[153] This contamination acts as a *micromask* that creates a peak that is passivated and, due to isotropic etching, becomes higher with each iteration.

Another defect that is produced due to the isotropic and anisotropic etchings of the SF_6 cycle, is *scalloping.* Figure 3.9 shows SEM images of the microcavities walls, note that over the surface there are trenches that extend horizontally, creating a completely corrugated surface.

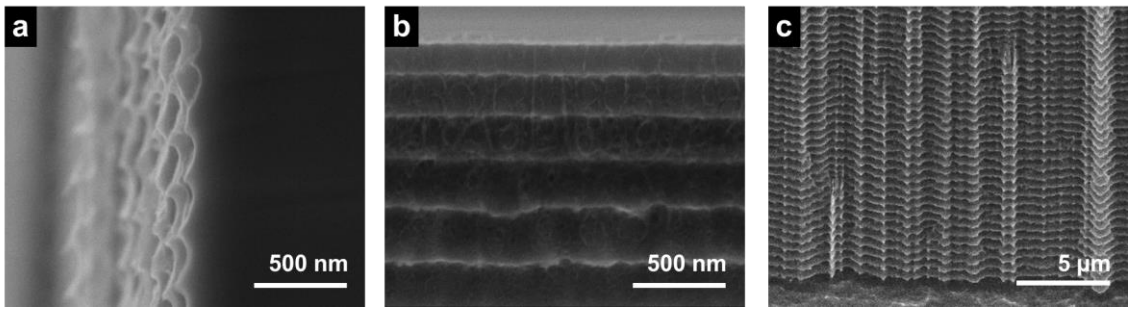

Figure 3.9 Cross-section SEM images of the microcavities showing the scalloping defect on (a) edge of walls, front of the walls at the (b) top and (c) bottom. DRIE process SF_6 and C_4F_8/O_2 exposure times of 2.0 and 2.5 s, respectively. Depth = 70 µm.

Table 3.3 shows the dimensions of the trenches that characterize the scalloping defects for the different SF_6:C_4F_8/O_2 exposure time ratios: the trench dimensions vary from 35 to 66 and 47 to 118 nm for horizontal and vertical ratios, respectively, with SF_6:C_4F_8/O_2 exposure time ratios ranging from 0.40 to 1.67. This represents a reduction of 2.5 and 2.0 times in height and width of the trenches, this is also correlated to the

SF_6:C_4F_8/O_2 exposure time ratios discussed previously, hence for a higher concentration of F* radicals, the trenches diameter increases.

Table 3.3 Radio of trenches of silicon microstructures associated to scalloping for different SF_6 and C_4F_8/O_2 exposure times used in the DRIE process (exposure times shown in Table 3.4).

SF_6 : C_4F_8 /O_2 Ratio	**Trenches radio (nm)**	
	Horizontal	**Vertical**
1.67:1.0	66.00	117.86
1.10:1.0	57.50	119.60
0.85:1.0	93.80	81.64
0.75:1.0	50.50	95.50
0.57:1.0	53.60	118.25
0.40:1.0	34.60	46.88

As a concluding remark for the DRIE process, SF_6:C_4F_8/O_2 exposure time ratio of 0.75 was chosen to fabricate the 3D photocatalysts, as it permits to obtained vertical walls with no grass defects, thus ensuring good coverage and quality of the sputter deposited TiO_2 onto the microcavities. However, the *scalloping* defect remains on the walls producing a corrugated surface, this defect is discussed next.

3.6.3.3 Post-processing of 3D scaffold

The presence of *scalloping* on the photocatalyst design imposes two questions, as is on located surface of the substrate, 1) it could generate a noncompact conformal TiO_2 layer, as the sputtering technique is highly dependent on the morphology and roughness of the substrate; and, 2) as the defect increases the specific surface of the substrate, it could boost the H_2 production, as the grooved surfaces can function as actives sites.

In order to evaluate these two aspects, it was necessary to compare both photocatalyst with *scalloping* and no *scalloping* defect. To remove it, thermal oxidation was used as it consist on growing a silicon oxide layer over the substrate, which is further removed with hydrofluoric acid (HF); and along with the oxide layer, the *scalloping* defects, rugosity and other small features on the scaffold are removed. The effectivity of the process to obtain flat and smooth surfaces depends on the oxide layer thickness, *i.e.*, the oxide layer must be thick enough to cover all the unwanted features. The optimization of this step is detailed in the Annex Section 3.7.2.1, where a 1 µm thick SiO_2 was chosen to be optimal configuration to remove effectively the *scalloping.* The process is described next:

Instrumental procedure. Thermal oxidation process was carried in a Centronic E1550HT (Centrotherm) in the following steps: 1) peroxidation: 30 min at 1070 °C under O_2 (10 L min^{-1}); 2) wet oxidation: 145 min under a mixture of O_2/H_2 (6/10 L min^{-1}); 3) dry-oxidation: 60 min under O_2 (10 L min^{-1}); and 4) oxidation: annealing for 15 min in a neutral N_2 atmosphere (10 L min^{-1}). The cooling down step is done with a ramp of -4 °C

min^{-1} down to 700 °C under N_2. The removal of the SiO_2 layer is done with HF solution, by immersing the substrates in the bath and then rinsed with DI water.

Figure 3.10 shows a silicon etched substrate after the scalloping removal, note that the microcavities exhibit smooth edges and surfaces, with barely visible trenches on the walls, which left small traces on the wall edge (Figure 3.10a) but not remarked groove, with not defined diameter (see more details and SEM images in the Annex Section 3.7.2.1), note that the post-treatment also removes the roughness from the bottom cavity.

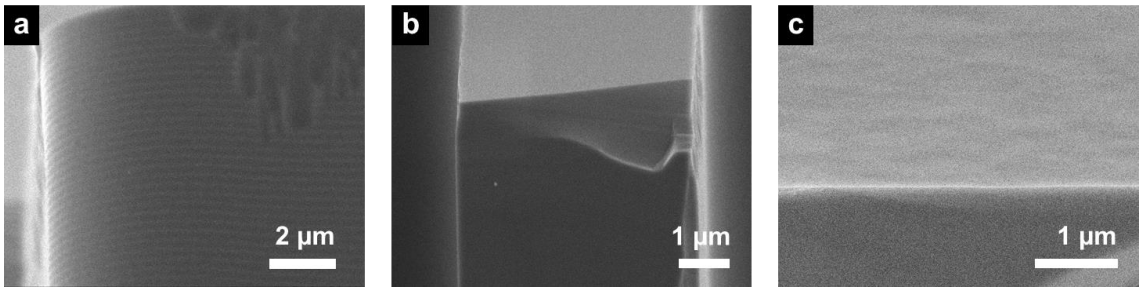

Figure 3.10 SEM cross-section images of silicon microstructure after postprocessing: (a) detail of the wall, (b) wall's edge, and (c) bottom of cavity. Depth = 97 µm, w = 75 µm and a = 10.4 µm.

3.3.3 Tuning AEF of silicon 3D scaffold by DRIE

To study the impact of the enlarged surfaces of TiO_2 on the H_2 production rate, silicon microstructures were fabricated following the previous optimized process by DRIE and the post-treatment process while maintaining high-depth microstructures with a vertical profile. The array of microcavities was fabricated into a 550 µm thick silicon p-type substrate using DRIE process, detailed before in Section 3.6.3.2. Figure 3.11a shows a photograph of the whole silicon wafer with the pattern at the center. Figure 3.11b shows the cross-section detail of the walls and bottom of the microcavities on one silicon etched substrate. It should be noted that the same profile geometry was observed over the entire substrate, demonstrating the uniform consistency of the micromachining process to create robust and repeatable patterns.

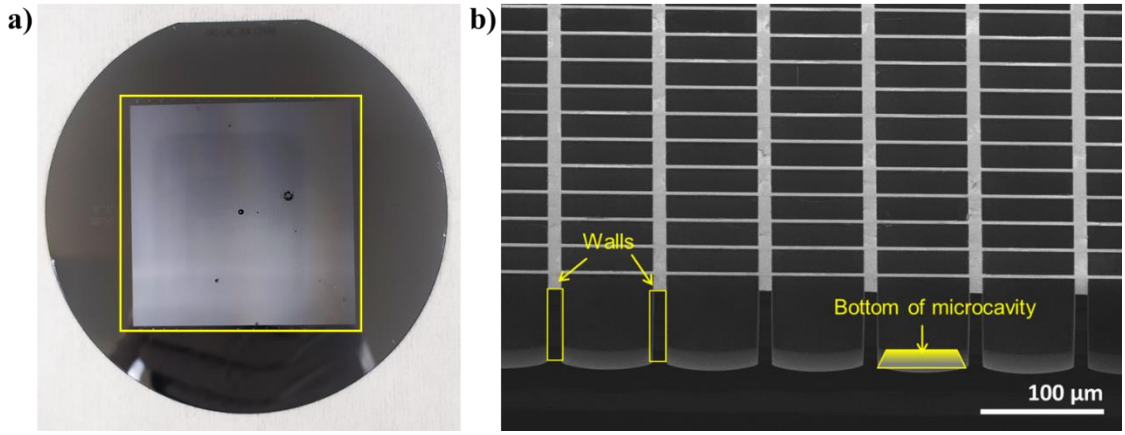

Figure 3.11(a) Silicon 4 inches wafer after DRIE and post-processing process. Micropattern highlighted with yellow frame located at the center of the wafer (approximated area of 5.4 × 5.4 cm). (b) SEM cross-section images of silicon microstructure located at the center of the wafer showing the repeatable pattern. Walls and bottom of the microcavities noted. DRIE process SF_6 and C_4F_8/O_2 exposure times of 2.0 and 2.5 s, respectively. Depth = 70 µm.

To study the enlargement impact on the photocatalyst, the silicon 3D scaffolds were fabricated with defined AEFs of 3, 5 and 7, which correspond to microcavity depths of 50, 100 and 150 µm. Hereafter the AEF will be denoted in the name of the samples as A1, A3, A5 and A7. Note that A1 indicates a flat substrate. Figure 3.12 shows the SEM images of the cross-section of the microcavities, note the change on the *Depth*; the figure also shows the photographs of the cut 3D scaffolds, with an average size of 1.5 by 1.5 cm which were used for the further 3D photocatalyst fabrication.

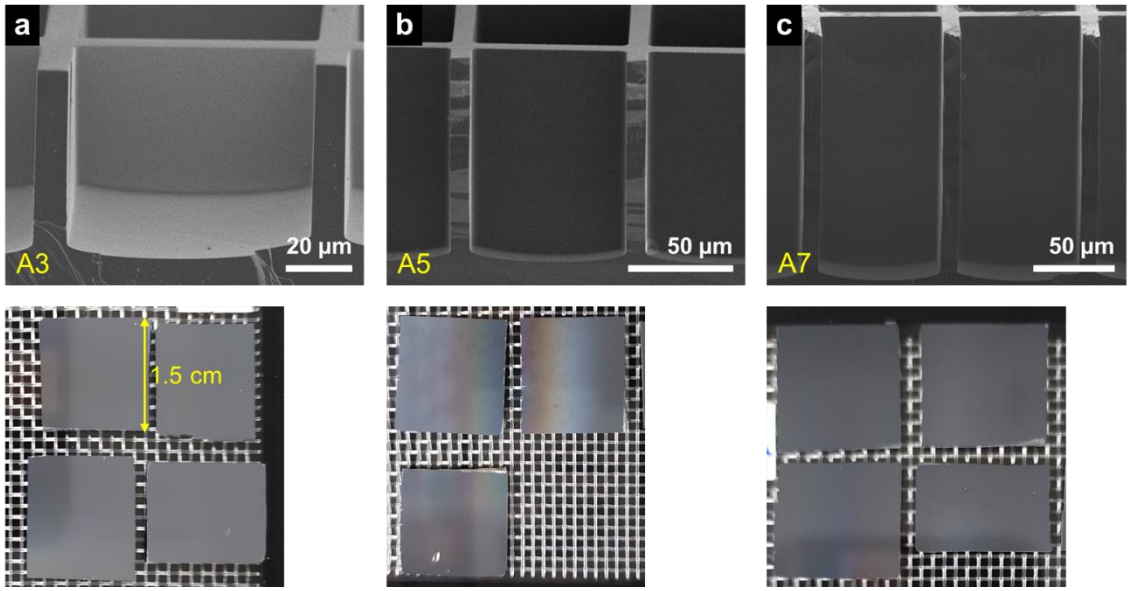

Figure 3.12 Silicon 3D scaffolds featuring different (a) AEF 3, (b) 5, and (c) 7, with a Depth of 50, 100 and 150 µm, respectively. Top: SEM cross-sectional images of the microcavities, bottom: photographs of the cut scaffolds.

Table 3.4 details the measured geometrical parameters for each of the silicon microstructures used in this section. For each AEF, the depth, *w* and *a* parameters are repeatable. Regarding the DRIE process, the etch rate diminishes from 3.0 to 2.74 µm min^{-1} when working with an aspect ratio of 2.14, *i.e.*, up to a depth of 150 µm, which still represents a reliable fast etch rate.

Table 3.4 Measured geometrical parameters and AEF of the 3D microstructures prepared by DRIE prior the TiO_2 deposition. The AEF is specified in the notation of the samples as A1, A3, A5 and A7.

Sample	**AEF**	**Silicon microstructure dimensions (µm)**		
		Depth	***w*** **[1]**	**a [2]**
A1	1.00	-	-	-
A3-1	3.08	49.50	75.31	9.530
A3-2	3.08	49.93	75.31	9.530
A3-3	3.08	49.93	74.10	NA
A5-1	5.15	94.00	76.90	9.000
A5-2	5.15	94.40	76.89	9.460
A5-3	5.15	94.40	76.20	9.800
A7-1	7.23	156.00	76.50	9.230
A7-2	7.23	147.90	76.60	9.000
A7-3	7.23	147.90	75.31	9.530

[1] Cavity's width (w).
[2] Wall's width (a).

In this section the design and fabrication of the silicon scaffold with a pattern that allows to obtain a wide window of AEF was completed. The next section will address the fabrication of the 3D photocatalyst (TiO_2 film deposited directly on the silicon scaffold) and the study of the area enlargement on the H_2 production.

3.4 3D photocatalyst fabrication and characterization

3.4.1 Physical vapor deposition of TiO_2

TiO_2 was sputter-deposited by direct current magnetron sputtering with the Ti target (PVD process described on Chapter 2 Section 2.3.1.) on the fabricated 3D scaffolds, flat silicon and quartz substrates (for the optical characterization). Depositions of the films were performed with 1, 3, 7 and 11 loops of 180 passes, corresponding to deposition thicknesses of 100, 270, 650 and 1000 nm (measured on flat surface).

3.4.2 Structural and chemical characterization of flat TiO_2 film

Characterization of the crystalline structure, optical absorbance and chemical composition were carried out only for the reference sample, as all the photocatalysts have the same TiO_2 film. The GI-XRD pattern of deposited TiO_2 (Figure 3.13a) shows the characteristic peaks of anatase at 2θ = 25.24° for the (101) plane and of rutile at 2θ = 27.39° for the (110) plane, with the composition of each phase being 77.15% and 22.85%,

respectively. Additionally, the GI-XRD pattern for the other deposited films on flat surfaces (AEF 1), was obtained for the thickness of 100 (A1-T1) and 650 nm (A1-T3), shown Figure 3.37 in the Annex Section 3.7.3. Sample A1-T1 exhibits an amorphous structure with no peaks, whereas A1-T2 exhibits the peak at 2θ = 25.24° with high intensity of the anatase (101) plane, the rutile peak at 2θ = 27.39° for the (110) plane does not appear, but the peaks at 2θ = 54.4 and 68.9° of the rutile planes (211) and (301) are present.

Next, the absorption spectra of the TiO_2 film deposited on quartz (Figure 3.13b) confirmed the strong absorption of TiO_2 in the UV range from 200 to 349 nm. XPS results (Figure 3.13c-d) are consistent with XRD and UV/Vis observations. The signals in the Ti 2p and O 1s spectra have a stochiometric signature which corresponds to TiO_2. The O 1s peak is deconvoluted into two peaks, where the main component at 530.3 eV is the typical signal of the oxygen lattice of the O^{2-} bound to Ti^{+4} in TiO_2, and the other component at 531.02 eV can be assigned to weakly adsorbed oxygen species, subsurface low-coordinated oxygen ions, surface hydroxyl groups and/or carbonate species. The Ti 2p spectrum exhibits the characteristic spin-orbit splitting with the Ti $2p_{2/3}$ and $2p_{1/2}$ peaks. The contribution of the Ti^{4+} and Ti^{3+} components in the Ti $2p_{2/3}$ peak, are located at 457.3 and 456.5 eV; and in the $2p_{1/2}$ peak, the components are located at 466.05 and 464.8 eV, respectively.[108,154]

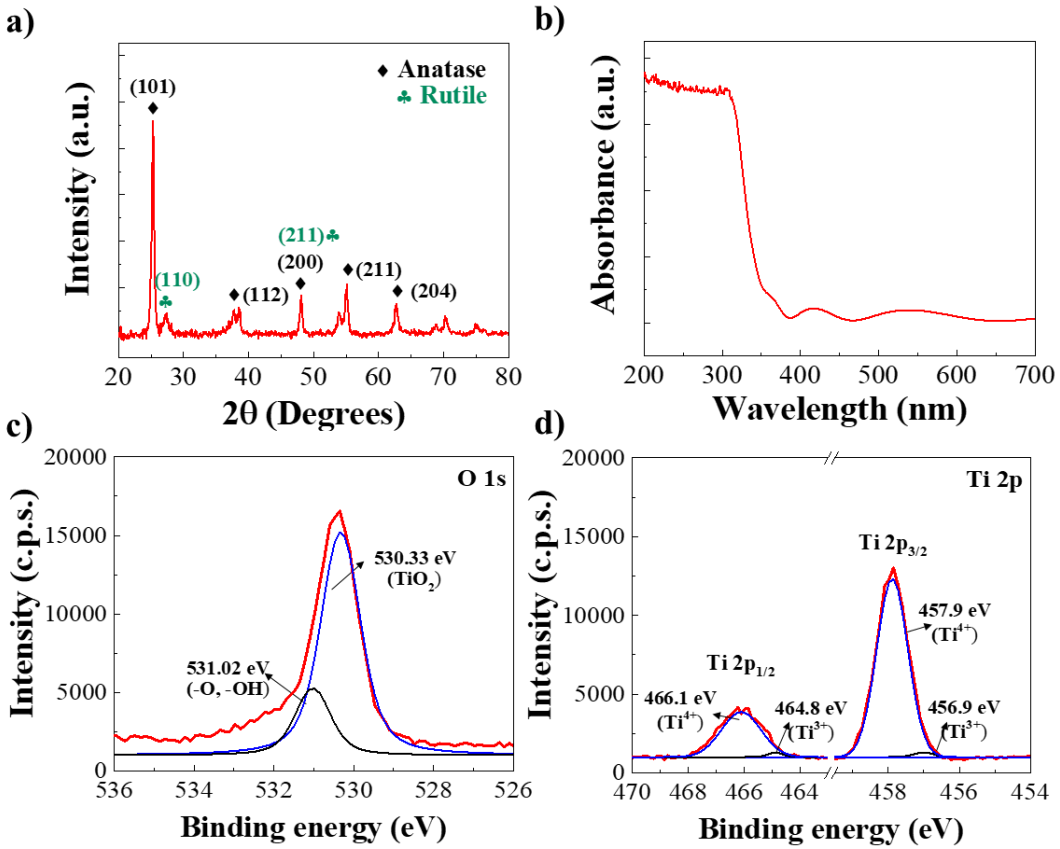

Figure 3.13 Characterization of a 270 nm sputter-deposited TiO_2 film on a flat silicon substrate (sample A1-T2): (a) GI-XRD pattern, (b) UV–Vis absorption spectra (film deposited on quartz), XPS spectra, (c) O 1 s, and (d) Ti $2p_{1/2,3/2}$ regions.

3.4.3 SEM characterization of TiO_2 3D photocatalyst

As mentioned before, TiO_2 films were deposited on the fabricated 3D scaffolds detailed in Table 3.4; the semiconductor thickness of 270, 650 and 1000 nm, is hereafter noted as T1, T2 and T3 for the scaffold A3, A5 and A7. To compare the area enlargement, 2D photocatalyst with AEF 1 were also tested, and in order to homologate the real thickness variation on the 3D scaffolds —which will be discussed next— the notation for the TiO_2 film thickness deposited on flat silicon (A1) of 100, 270 and 650 is denoted as T1, T2 and T3; samples are summarized in Table 3.5. Figure 3.14 shows the photographs of the 2D and 3D photocatalyst, an approximated of 1.5 by 1.5 cm was determined for the photocatalytic activity tests. Note that the color of the photocatalyst variates despite having the same sputtering process, for example for A1-T2, A3-T1, A5-T1 and A7-T1.

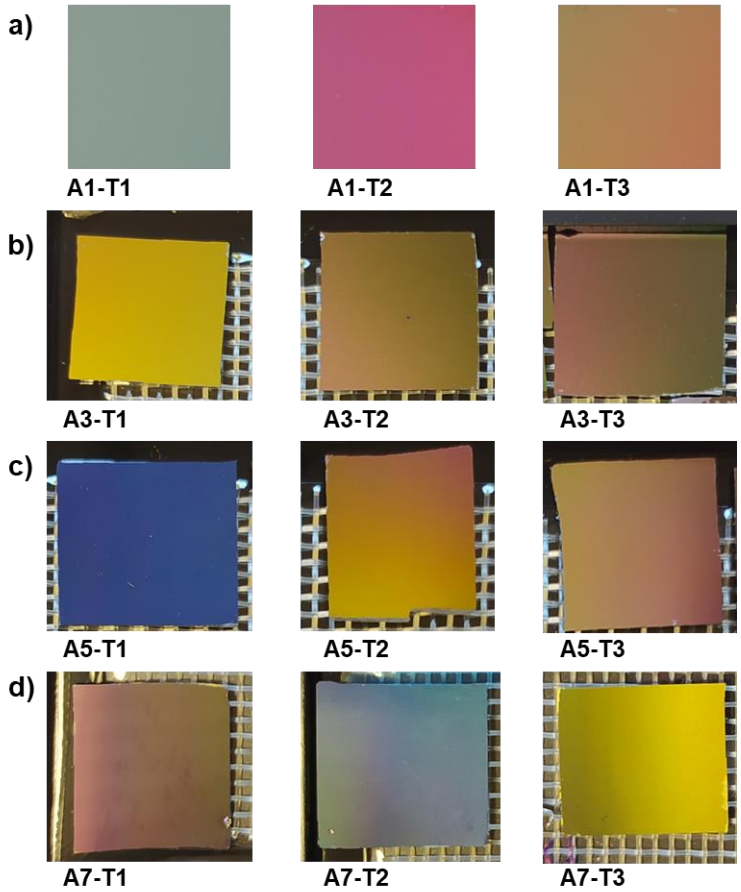

Figure 3.14 Photographs of 3D photocatalysts featuring a variable AEF and different TiO_2 thickness.

Table 3.5 summarizes the set of samples having been classified by increasing AEF and presents the TiO_2 film thickness, which will be discussed next. Sample A1-T2 with a thickness of 270 nm will be denoted as the reference sample due to its optimum photocatalytic performance, as was previously discussed in Chapter 1 for a single layer.

Table 3.5 Details of TiO_2 thickness for the 2D and 3D photocatalysts featuring a variable AEF.

Sample	**AEF**	**Depth**	**TiO_2 film thickness (nm)**			
			Top	**Bottom**	**Wall** [1]	t_{TiO2}^{av} [2]
A1-T1	1.00	0	-	100.00	-	-
A1-T2	1.00	0	-	270.00	-	-
A1-T3	1.00	0	-	650.00	-	-
A3-T1	3.08	50	283.11	129.73	80.08	108.02
A3-T2	3.08	50	573.32	224.68	203.83	237.22
A3-T3	3.08	50	1174.75	453.83	361.95	446.99
A5-T1	5.15	94	306.79	103.24	70.28	86.02
A5-T2	5.15	94	644.76	135.80	175.96	191.26
A5-T3	5.15	94	1105.00	246.50	278.65	311.44
A7-T1	7.23	156	285.77	33.87	60.75	65.17

A7-T2	7.23	148	697.13	69.66	137.43	143.33
A7-T3	7.23	148	1171.88	103.47	209.99	229.79

[1] Average calculated from the top, medium and bottom heights of the wall thickness.
[2] Average thickness calculated.

SEM observations of the 3D photocatalysts (Figure 3.15-Figure 3.17) show a continuous and compact layer for all covering the entire microcavities, *i.e.*, microstructures with aspect ratios of 0.7:1, 1.3:1 and 2:1, corresponding to AEFs of 3, 5 and 7, respectively. However notorious changes in the grain growth direction, grain diameter and thickness thought out the cavities are evident.

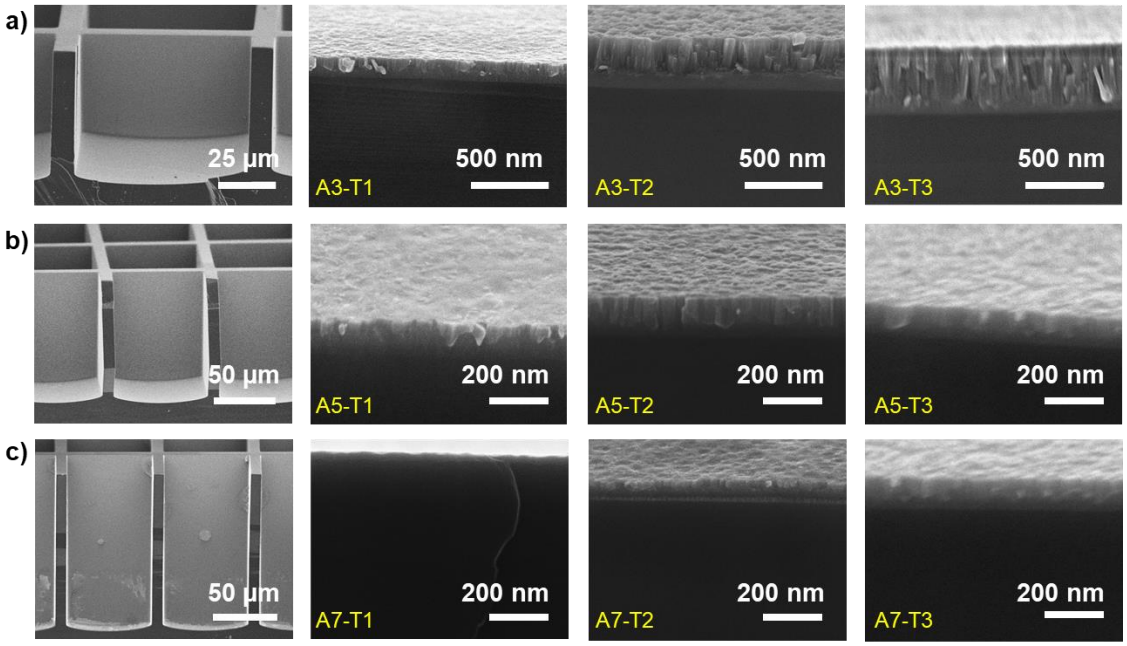

Figure 3.15 SEM cross-sectional images of the 3D photocatalysts composed of TiO_2 film thickness T1, T2 and T3, featuring AEF (a) 3, (b) 5 and (c) 7. First column: microcavities profile on the first column. Right images: bottom of microcavities.

First, the grain growth direction seemed to be merely influenced by the substrate surface position with respect to the PVD Ti target, the cross-sectional images show the characteristic columnar growth of polycrystalline TiO_2. Yet, the horizontal surfaces of the microcavities, *i.e.*, the bottoms of the cavities, and at the top surfaces of the walls exhibit the characteristic vertical growth (Figure 3.15-Figure 3.16). And, on the other side, the crystallite growth on the vertical walls follows a diagonal direction, Figure 3.17 shows the detail of the wall edge at medium height for all the samples, the columnar growth describes a diagonal direction coming from the top middle of the microcavity to the wall.

Secondly, the grain size also changes according to the thickness and AEF of the microstructure. By measuring the cross-sections at the top surface of the microcavities walls, the average grain's upper diameter is 50.8, 95.0 and 153.8 nm for thicknesses T1, T2 and T3, this value is very approximate for all the three different AEF (Figure 3.16).

Next, in order to illustrate the grain size in respect to AEF, we can take T3 as is the biggest thickness deposited. For these structures the size of the grains decreases from 153.8 nm at the top, to 74.15, 64.2 and 52.8 nm for A3-T3, A5-T3 and A7-T3 at the bottom of the cavity (Figure 3.15). Likewise, the size of the grains located at the half-height of the wall is 61.5, 33.4 and 28.11 nm, for A3-T3, A5-T3 and A7-T3 (Figure 3.17). This indicates that the grain size decreases as the local surface is located deep into the cavities.

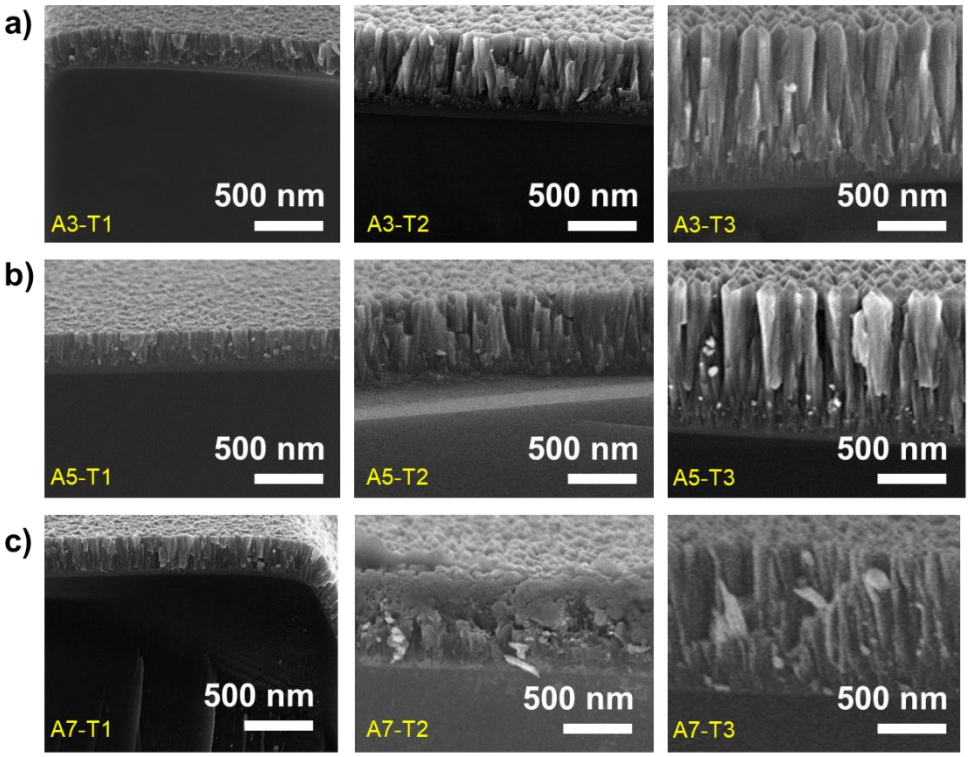

Figure 3.16 SEM cross-sectional images of the top surface of the microcavities of 3D photocatalysts composed of TiO_2 film thickness T1, T2 and T3, featuring AEF (a) 3, (b) 5 and (c) 7.

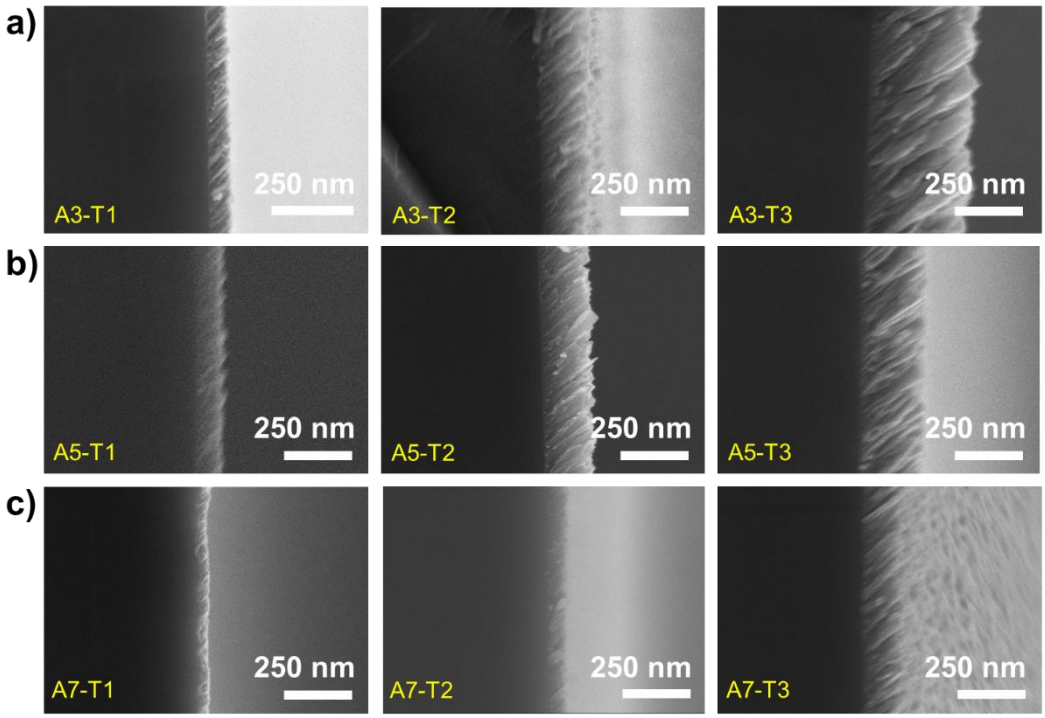

Figure 3.17 SEM cross-sectional images of the half-height of the walls of the microcavities of 3D photocatalysts composed of TiO_2 film thickness T1, T2 and T3, featuring AEF (a)3, (b) 5 and (c) 7.

Third, it is evident that the TiO_2 thickness deposited on the microstructures is not uniform with respect to the depth of the microcavities. Measurements of the thickness were taken from the SEM images for the surfaces top and bottom surfaces; and for the walls, three different positions were defined according to the height: upper, medium and lower heights. The average of the measurements is presented in Table 3.6. The thickness on the horizontal surfaces decreases from the top to bottom of the microcavities by a factor of 2.4, 4.0 and 9.9 for AEF values of 3, 5 and 7, (*i.e.*, *depths* of 50 µm, 100 µm and 150 µm) respectively. On the vertical surfaces, the thickness decreases from top to bottom of the walls by a factor of 1.9, 3.4 and 6 for AEF values of 3, 5 and 7, respectively. Nevertheless, the film remains compact and dense throughout the surface. This variation in thickness is in accordance with the grain's size measurements, and is ascribed to the sputtering deposition process, where the substrate moves in front of the target in a parallel manner, and the atoms reach the sidewalls and corners more frequently due to the periodic high oblique angles of the incident flux.

Hence, to quantify the influence of the AEF on the photocatalytic activity, it is crucial to define an average thickness ($\boldsymbol{t_{TiO2}^{av}}$) of TiO_2 to distinguish each sample. In this regard, we use Equation 3.9, which accounts for the thicknesses measured at the top and bottom surfaces, and the average thickness deduced along the wall height; these values are then multiplied by a surface factor (Annex Section 3.8 Table 3.10) that represents the percentage of the total microstructure surface.

$$\boldsymbol{t_{TiO2}^{av}} = t_1 \cdot F1_{AEF} + t_2 \cdot F2_{AEF} + t_3 \cdot F3_{AEF} \qquad \text{Equation 3.9}$$

Where:

- t_1, t_2 *and* t_3 are the averages of the TiO_2 thickness measured on the top, bottom surfaces and along the wall height, respectively.
- $F1$ is a factor defined by the AEF that represents the percentage of the total surface that is located at the horizontal top of the microstructure.
- $F2$ is a factor defined by the AEF that represents the percentage of the total surface that is located at the horizontal bottom of the microstructure.
- $F3$ is a factor defined by the AEF that represents the percentage of the total surface that is located on the walls of the microstructure.

Thus, the calculated average TiO_2 thickness for the 3D photocatalysts is reported in Table 3.5. Primarily, $\boldsymbol{t_{TiO2}^{av}}$ is thicker in the 3D photocatalyst with an AEF of 3, which is attributed to the low aspect ratio of 0.7:1 of the microstructure. We also observe that the $\boldsymbol{t_{TiO2}^{av}}$ has a similar value with regard to the wall thickness in all the samples, which is attributed to the utilization of *F3* in Equation 3.9, which represents the percentage of the total surface that is located on the walls of the microstructure, and this value is 0.67, 0.84 and 0.86 for AEF values of 3, 5 and 7, respectively. This suggests that the film quality of the overall 3D photocatalysts is determined principally by the layer thickness on the walls. Another important observation is that for AEFs 3 and 5, the bottom of the microcavities has a higher thickness than the walls, which is contrary to AEF 7, and can be attributed to the limitation of the sputter deposition technique in reaching the bottom of the microcavities.

As the thickness variation was determined for each structure, it is necessary to correlate it with the specific area of the 3D photocatalyst. Hence, in the next section, the H_2 production will be measured, as well as the experimental AEF.

3.4.4 Influence of area enlargement on the H2 production

3.2.4.1 H_2 production rate

The photocatalytic H_2 production of the 3D photocatalysts was evaluated over 24 h under UV-vis irradiation. Figure 3.18 shows the H_2 evolution over 24 h for each photocatalyst. Note that for the reference sample (A1-T2, flat photocatalyst), the quantity of H_2 evolution is linear over 24 h, whereas for sample A1-T3 and the 3D photocatalysts, the H_2 production remains constant only after 6 h of irradiation.

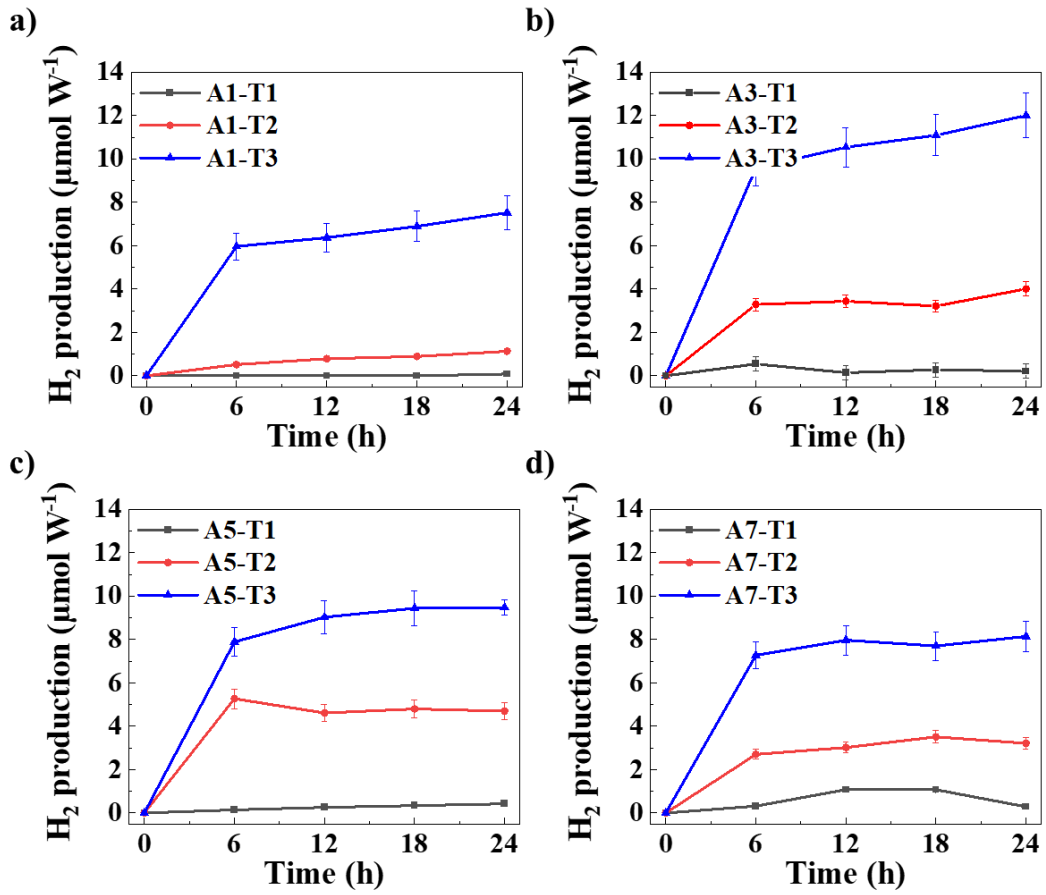

Figure 3.18 H_2 evolution over 24 h for photocatalyst composed of different TiO_2 film thickness deposited by sputter-deposition featuring an (a) AEF 1, (b) AEF 3, (c) AEF 5 and (d) AEF 7. Xenon lamp used for irradiation.

Furthermore, the H_2 production rate over 24 h was calculated and compared to the reference sample by calculating the Enhancement Factor, results are shown in Table 3.6. Among the different AEFs from 3 to 7, the photocatalysts with T3 thickness have a remarkedly higher H_2 production rate than the microstructures with the same AEF but with thickness T1 (*i.e.*, increased by a factor of 36, 31 and 11 for AEFs 3, 5 and 7, respectively). This shows that the surface area enlargement not only impacts the H_2 production rate but also prominently impacts the TiO_2 layer, which, as discussed in the previous section, has a fluctuating thickness. Therefore, it is important to consider this characteristic for the interpretation of results. When considering the photocatalysts with thickness T1 that have a t_{TiO2}^{av} = 65.17 to 108.02 nm, the highest H_2 production rate was observed for sample A3-T1 with 1.92 10^{-2} µmol W^{-1} h^{-1}. This represents a 14-factor increase compared to A1-T1 (100 nm thickness), followed closely by A3-T1 rate of 1.89 10^{-2} µmol W^{-1} h^{-1}. Next, considering photocatalysts with thickness T2, with a t_{TiO2}^{av} = 143.33 to 237.22 nm, sample A5-T2 has the highest H_2 production rate with 0.22 µmol W^{-1} h^{-1}, which represents a 6-factor increase compared to the reference sample (A1-T2 of similar thickness 270 nm), followed by A3-T2 with a rate of 0.23 µmol W^{-1} h^{-1}. Among

the photocatalysts with T3 thickness, the flat A1-T3 (650 nm thickness) shows a higher rate of 0.43 µmol W^{-1} h^{-1}; nevertheless, for the purpose of comparison within the 3D photocatalysts that have a t_{TiO2}^{av} = 229.79 to 446.99 nm, it is necessary to use a reference sample with a similar thickness, such as sample A1-T2; in this regard, samples A3-T3 and A5-T3 exhibit a remarkable 14-factor and 11-factor of enhancement with H_2 production rates of 0.70 and 0.58 µmol W^{-1} h^{-1}, respectively; moreover, their H_2 evolution exhibits the fastest rate over the 24 h test.

Table 3.6 H_2 evolution rate of 2D and 3D TiO_2 photocatalysts featuring a variable AEF.

Sample name	t_{TiO2}^{av} [1] (nm)	H_2 production rate (µmol W^{-1} h^{-1})	H_2 production rate enhancement Factor [2]
A1-T1	100.00	0.14 10^{-2} ± 0.01 10^{-2}	0.03 ± 0.82 10^{-3}
A1-T2	270.00	5.20 10^{-2} ± 0.28 10^{-2}	1.00 ± 0.05
A1-T3	650.00	43.28 10^{-2} ± 2.22 10^{-2}	8.33 ± 0.43
A3-T1	108.02	1.92 10^{-2} ± 0.08 10^{-2}	0.37 ± 0.02
A3-T2	237.22	22.57 10^{-2} ± 0.97 10^{-2}	4.34 ± 0.19
A3-T3	446.99	69.94 10^{-2} ± 3.00 10^{-2}	13.46 ± 0.58
A5-T1	86.02	1.89 10^{-2} ± 0.08 10^{-2}	0.36 ± 0.02
A5-T2	191.26	31.36 10^{-2} ± 1.36 10^{-2}	6.03 ± 0.26
A5-T3	311.44	57.99 10^{-2} ± 2.46 10^{-2}	11.16 ± 0.48
A7-T1	65.17	4.47 10^{-2} ± 0.23 10^{-2}	0.86 ± 0.04
A7-T2	143.33	20.14 10^{-2} ± 0.84 10^{-2}	3.88 ± 0.16
A7-T3	229.79	50.30 10^{-2} ± 2.16 10^{-2}	9.68 ± 0.05

[1] Thickness of photocatalyst with AEF1 is the measured value (not average).
[2] Obtained by comparison to reference sample (A1-T2).

In addition, the quantum efficiency (QE) of the optimal 3D TiO_2 photocatalysts (thickness T3) was calculated considering the spectral output of the Xenon lamp. Details are given in the Annex, Section 3.7.53.7.5. The QE for samples A3-T3, A5-T3 and A7-T is 8.74, 7.24 and 6.29%, respectively. Due to a low power irradiation of the lamp, comparison with literature is relatively difficult. Yet, we can deduce that the enhanced photon-to-H_2 production is caused by the area enlargement of the 3D photocatalysts under the same irradiation and with the same planar area.

Figure 3.19a plots the percentage of the H_2 production rate enhancement compared to planar topology as a function of t_{TiO2}^{av} (*x*-axis) and the AEF (different colored lines). The surface area enlargement clearly boosts the photocatalytic activity, which leads to a remarkable enhancement of the H_2 production rate by 1321% compared to the planar topology. A higher enhancement would be expected for the 3D photocatalysts with an AEF of 5 and 7, since the availability of the sites that conduct the water-splitting reaction is higher. However, the photocatalyst with an AEF 3 is the one that exhibits a higher photocatalytic performance; this behavior can be ascribed to the semiconductor layer uniformity. For samples A5-T3 and A7-T3, the thickness layer variation along the microcavities is high (246-1105 nm and 107-1171 nm) and the enhancement is 1136 and

968%, respectively. However, in sample A3-T3 the thickness variation is lower, from 454 to 1174 nm, and the enhancement is notably higher (1321%). This remarkable performance of a 3D photocatalyst with respect to a planar topology surpassed the expected results, where the enhancement was expected to be directly proportional to the surface area. This establishes that higher efficiencies can be achieved by increasing the AEF when a nearly conformal TiO_2 layer with a minimum thickness of 200 to 300 nm is deposited. Based on the behavior of the AEF on the H_2 production rate, Figure 3.19b shows the predicted H_2 production rate for a conformal TiO_2 layer with a thickness of 230 nm for 3D photocatalysts when varying the AEF: the H_2 production is enhanced by factors of 6, 10 and 13 for AEF values of 3, 5 and 7, respectively, when compared to a photocatalyst with an AEF of 1. This indicates that when microstructures with a higher aspect ratio ≥ 1.4 and a conformal TiO_2 layer are deposited, H_2 production linearly follows surface augmentation.

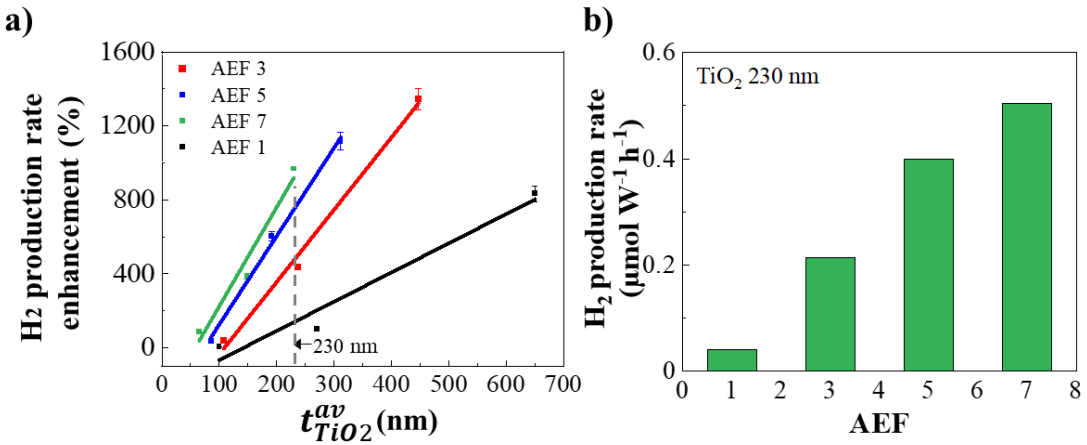

Figure 3.19 (a) H_2 production rate enhancement as a function of the TiO_2 average thickness (t^{av}_{TiO2}) for flat and 3D photocatalysts with AEFs of 3, 5 and 7. Values are compared to the H_2 production rate of the reference sample A1-T2. Solid lines are obtained by linear regression. (b) Determined impact of AEF on the H_2 production rate for a 3D photocatalyst with a t^{av}_{TiO2} of 230 nm (rate normalized per light flux and surface area).

3.2.4.2 Experimental AEF measurement by cyclic voltammetry

To estimate the experimental AEF value, cyclic voltammetry experiments were carried out on the 3D photocatalysts which were previously sputtered with Au to create the working electrode (see experimental data in Section 3.2.3). As the Au covers completely the 3D photocatalysts, hence, the electrochemically-active surface area is composed by the enlarged silicon microstructures and the inherent surface roughness originated by the TiO_2 thickness. Cyclic voltammograms are shown in Figure 3.20. The electrochemically active surface area (AEF_{EAS}) was obtained from the integration of the reduction peak of Au located at 0.85 V vs. Ag/AgCl.

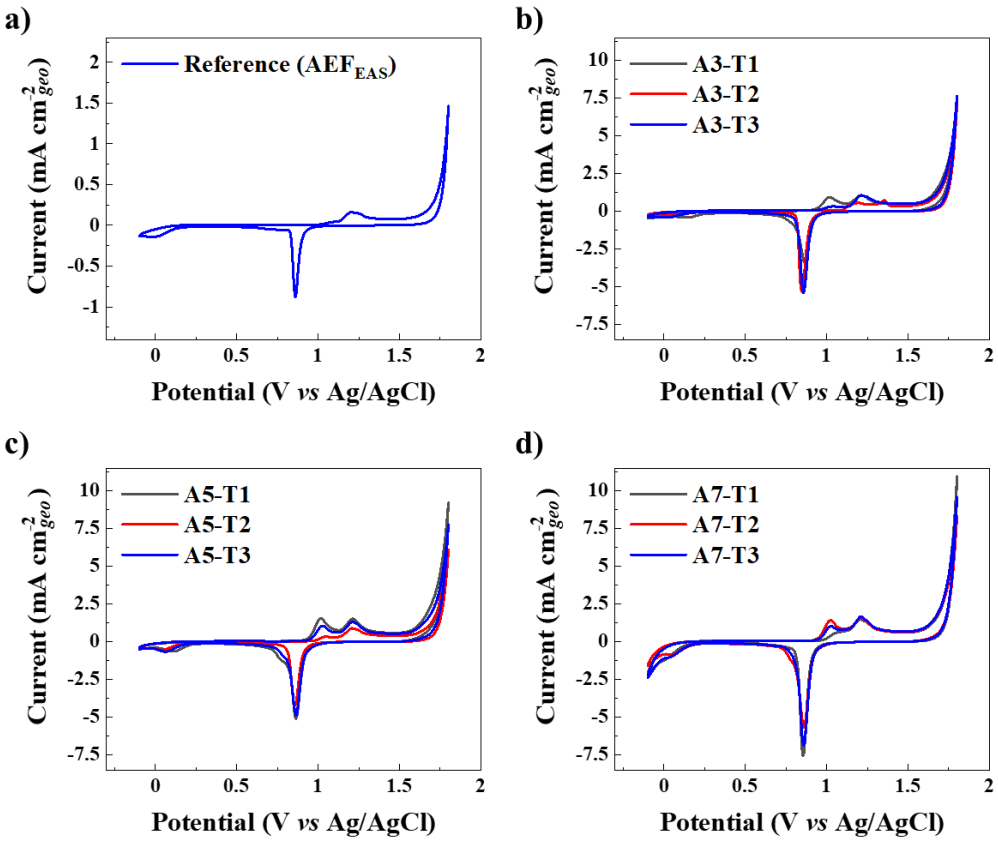

Figure 3.20 Cyclic voltammograms performed at 30 mV s^{-1} in 0.5 M H_2SO_4 of different Si/TiO_2 microstructures covered with Au (a) reference sample for AEF_{EAS} calculations and 3D photocatalyst featuring an (b) AEF 3, (c) AEF 5 and (c) AEF 7. Current normalized by the geometrical area.

The AEF_{EAS} values for the 3D photocatalyst are shown in Table 3.7, the values are higher than those of the theorical AEF of the bare silicon scaffolds, yet, they follow the same growing trend according the aspect ratio. For the structures with lower aspect ratio, *i.e.*, AEF 3 the AEF_{EAS} ranges from 5.8 to 6.5; whereas for the structures with higher aspect ratio, *i.e.* AEF 7, the AEF_{EAS} ranges from 8.6 to 9.6. Since a flat photocatalyst with a TiO_2 thickness of 1 µm was used as the reference sample for the AEF_{EAS} calculation, these results not only corroborate that the augmentation of the surface is related to the change in depth of the microcavities but also take into account the roughness and fluctuations associated with the deposited 3D structure of the TiO_2, which creates more sites where the monolayer of Au^+ is formed and reduced. Moreover, the Au sputtered layer of the electrode has a roughness that contributes also to the real surface area augmentation. Therefore, the experimental AEF_{EAS} values are higher than the calculated AEF values from Equation 3.8 but reflect a good correlation with the theoretical values.

Table 3.7 Electrochemically active surface area of 3D photocatalyst.

Sample name	AEF_{EAS}
A3-T1	5.78 ± 0.06
A3-T2	5.54 ± 0.16
A3-T3	6.53 ± 0.06
A5-T1	8.40 ± 0.05
A5-T2	5.26 ± 0.30
A5-T3	7.57 ± 0.04
A7-T1	8.59 ± 0.18
A7-T2	9.25 ± 0.03
A7-T3	9.59 ± 0.03

Figure 3.21 shows the plot of AEF_{EAS} vs. H_2 production rate enhancement where the AEF_{EAS} ranges from 5.5 to 9.6, evidencing that the thickness variation of TiO_2 allows the further enlargement of the surface. Yet, as the t_{TiO2}^{av} variates, it is difficult to resolve an overall trend, except for those values that exhibit a similar t_{TiO2}^{av}, such as 191, 237 and 229 nm. Here a proportional positive trend of the H_2 production is seen by increasing the AEF, which corroborates the estimation for the plot in Figure 3.19b. Hence, the thickness demonstrates to be a limiting factor for the H_2 production, as seen with the samples of higher thickness, *i.e.*, t_{TiO2}^{av} 311 and 447 nm (AEF_{EAS} 7.6 and 6.5, respectively), which exhibit the higher H_2 production enhancement of 1116 and 1346%.

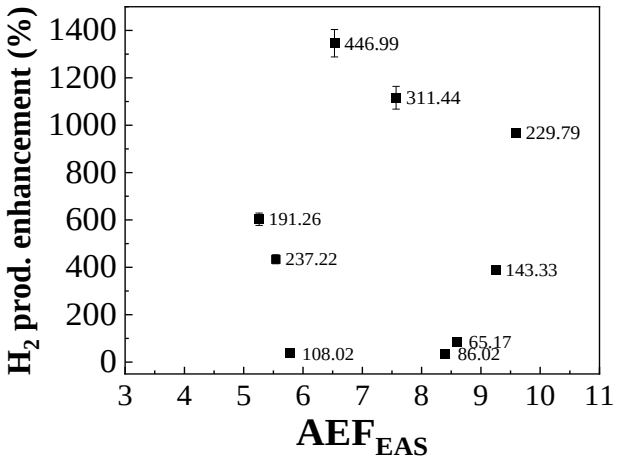

Figure 3.21 Plot of experimental AEF (AEF_{EAS}) vs H_2 production enhancements. Inset of average TiO_2 film thickness (t_{TiO2}^{av}) in nm.

It is thus evident that the conformal deposition of the semiconductor must be improved, one technological solution is the deposition of TiO_2 by atomic layer deposition (ALD). Yet, is necessary to ensure that performance of the films can reach the H_2 production rate of the TiO_2 sputtered-deposited films. In this regard, some steps were

carried in collaboration with the Eng. Cassandre Lamboux from the European Membrane Institute (Institut Européen des Membranes, IEM) at Montpellier. Who deposited TiO_2 thin films using $TiCl_4$ precursor. The structural characterization and photocatalytic activity tests were conducted at LAAS. Two preliminary studies were followed, first, as the as-deposited film (thickness of 80 nm) exhibited an amorphous structure, post-annealing treatments were carried at different temperatures; at 400 °C the film structure was entirely composed of anatase, yet the H_2 production rate reached at value of 1.06 10^{-2} µmol W^{-1} h^{-1} which corresponds to a 0.20 fraction of the TiO_2 flat film deposited by PVD. In the second study, the films were deposited varying the ALD reactor temperature, ranging from 100 to 350 °C. This parameter impacted notably the structure and photocatalytic activity, where a temperature of 200 °C was responsible for an H_2 production rate of 8.81 10^{-2} µmol W^{-1} h^{-1}, which represents a 0.64 fraction of that one of the PVD TiO_2. Thus, these preliminary results (not included in this work) establish a basis for the fabrication of enlarged 3D structures where the TiO_2 thickness does not represents a limitation.

3.4.5 TiO_2 3D photocatalyst stability

The stability of the photocatalyst is also an important issue in device applications. Therefore, a cyclic H_2 evolution test was carried out for 45 h under light irradiation and under the same conditions as the H_2 production rate tests. The optimal A3-T3 sample was tested for 5 consecutive cycles of 9 h each. The H_2 evolution, shown in Figure 3.22, remained stable, with an average H_2 evolution of 89.18 µmol W^{-1} by the end of each cycle. Additionally, a small increase was observed after the first cycle, indicating the robustness of the 3D photocatalyst.

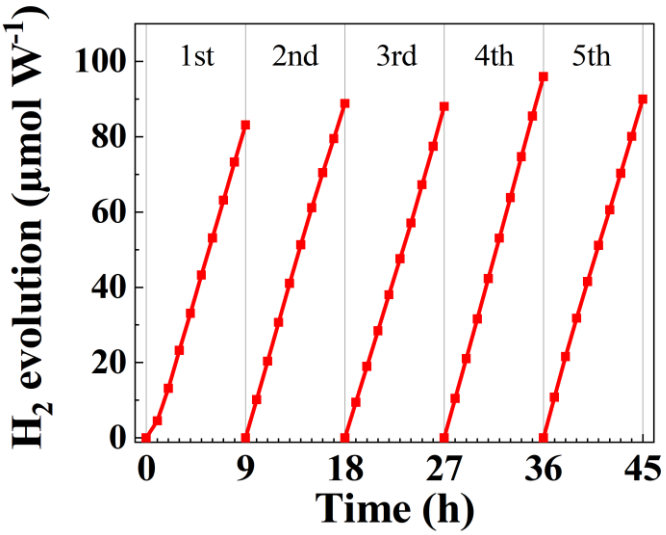

Figure 3.22 Cycling H_2 evolution of 3D photocatalyst A3-T3 composed TiO_2 film thickness referred as T3 deposited by sputter-deposition featuring an AEF of 3. Xenon lamp used for irradiation.

Thus far, the 3D photocatalysts proved to convey the water-splitting reaction showing an enhancement of the H_2 production rate with a great stability over 45 h. As on Chapter 2, the deposition of Au showed an improvement of the photocatalytic activity by extending the absorption spectra of the overall film. In the next section a final development of the microstructures is carried by loading the photocatalysts with plasmonic NPs. Moreover, a different metal and deposition technique are explored, as palladium (Pd) NPs are deposited by atomic layer deposition (ALD). Hence, in the next section, the structural and optical characterization of the 3D hetero-photocatalysts is discussed in terms of their impact on the H_2 production.

3.5 Addition of plasmonic NPs to 3D photocatalysts

The impact on the H_2 production by the addition of plasmonic NPs on top of the 3D photocatalyst (silicon scaffold and TiO_2 layer) is analyzed is this section. The structural characterization was carried by SEM and XRD and the absorbance spectra obtained by UV/Vis spectroscopy. Lastly, a discussion comparing the H_2 production rate between the Au and Pd NPs is given.

3.5.1 Au NPs by chemical photo deposition

As seen in Chapter 2, the synthesis of Au NPs on top of the TiO_2 film allows the absorption in the visible range (455-475 nm), having a positive impact on the water-splitting reaction. Thus, Au NPs were deposited on the 3D photocatalysts that exhibited best photocatalytic activity, *i.e.*, A3-T3, A5-T3 and A7-T3. The photo-deposition process was done directly on top of the semiconductor layer with the procedure used in Chapter 2, (experimental details Section 2.3.2).

Figure 3.23 shows the images of the microstructures at the top edge of the walls, half-height of the walls and the lower corners of the bottom of the microcavity. The average size of the nanoparticles was 30.3 with a standard deviation (SD) of 13.60 nm, the histogram is shown in Figure 3.23d. The average areal density decreased from 46 to 10 NPs/μm^2 from the top to the bottom of the wall. Furthermore, the NPs located at the half-height, at low height of the walls have an average size of 17 nm, which accounts for a small fraction (< 4%) of the size distribution of the NPs. This can be attributed to the diagonal crystallite growth of the walls, where small particles are retained easily during the chemical synthesis, compared to the horizontal surfaces where any NP size can be easily trapped between the crystallites.

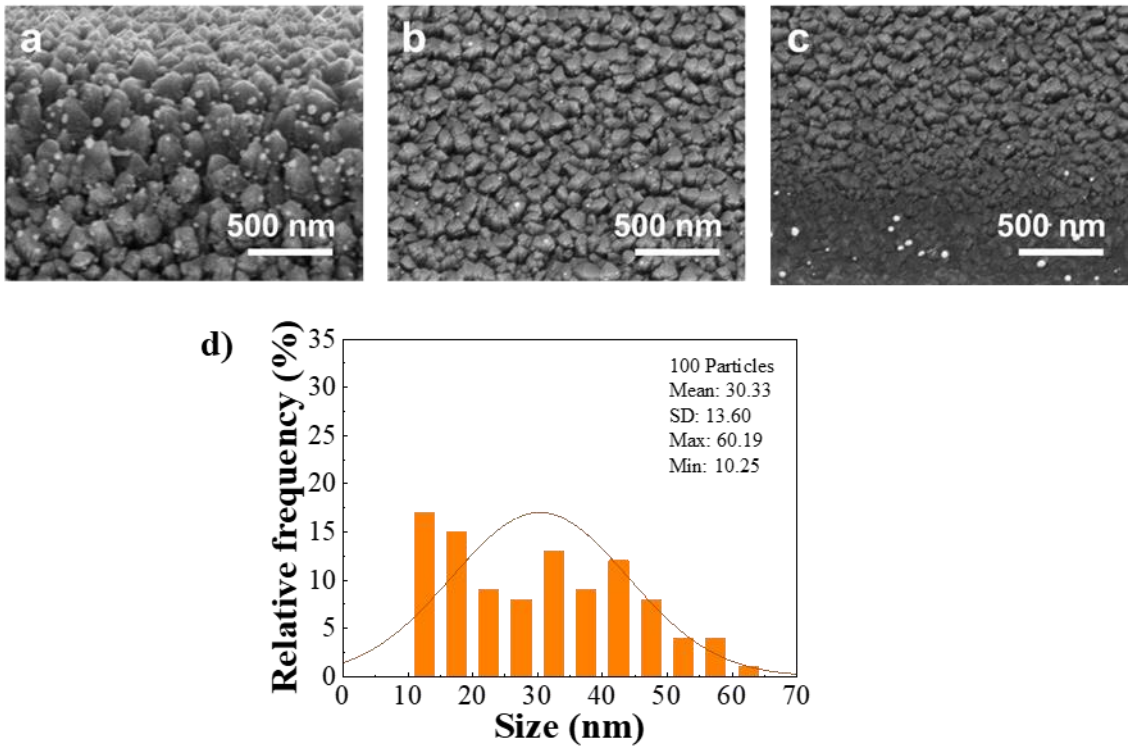

Figure 3.23 (a) H_2 evolution over 24 h for 3D photocatalyst composed TiO_2 and Au NPs featuring an AEF of 3,5 and AEF 7. SEM images of the top wall (b), wall at the half-height (c), and bottom wall (d) of the 3D photocatalyst TiO_2/Au NPs labeled A3-T3. (d) Histogram of Au NPs size dispersion (extracted from SEM measurements).

Figure 3.24 shows SEM images of the horizontal surfaces of the microcavity, it can be observed that the NPs are mainly located on the top surface and on the near vertices with an average areal density of 98 NPs/µm^2, and at the bottom of the microcavities with an average areal density of 31 NPs/µm^2, but not on the walls image [3] in Figure 3.24. This demonstrates that the NPs areal density is higher at the top horizontal surface compare to the bottom of the microcavities.

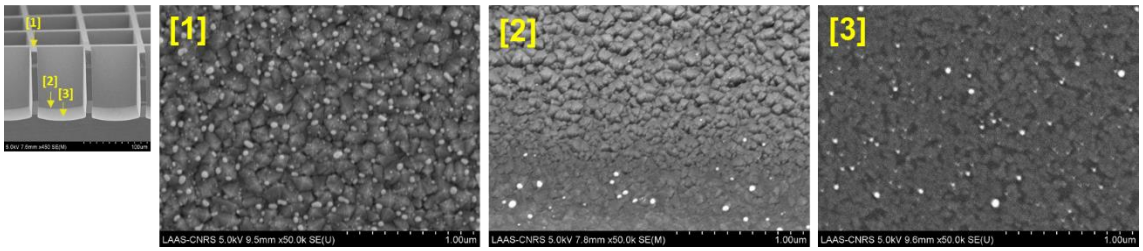

Figure 3.24 SEM images of horizontal surfaces of 3D photocatalysts composed of TiO_2/Au NPs featuring an AEF of 3 (sample A3-T3). Insets indicate the positions of the microcavity.

The photocatalytic activity was measured as in the previous sections over a duration of 24 h. The H_2 evolution in Figure 3.25 and the production rates in Table 3.8.

As expected, the H_2 production increased significantly in the all the structures compared to those without the Au NPs reaching a maximum enhancement factor of 49 for the A3-T3. However, a similar improvement was obtained for all three different microstructures, this can be explained by the morphology observations by SEM, that showed that the NPs are only located at the horizontal surfaces of the 3D microstructures, hence as the percentage of these surfaces is the same does not variate despite the AEF, therefore a similar concentration of Au NPs is present in each microstructure.

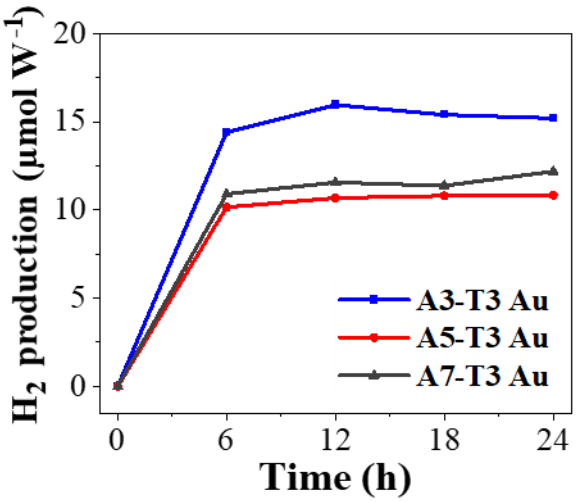

Figure 3.25 H_2 evolution over 24 h for 3D photocatalyst featuring different AEF with TiO_2 film thickness T3 with Au NPs photo-deposited.

Table 3.8 H_2 production rate of optimum 3D TiO_2 photocatalysts with Au NPs.

Sample name	H_2 production rate ($\mu mol\ W^{-1}\ h^{-1}$)	H_2 production rate enhancement Factor [1]
A3-T3 Au	2.54 ± 0.11	48.86
A5-T3 Au	1.77 ± 0.08	34.05
A7-T3 Au	1.92 ± 0.09	36.89

[1] Obtained by comparison to reference sample (A1-T2).

These results shed light on the importance of the combination of metal and semiconductor materials to enhance the performance of the photocatalyst, however, the limitations of the chemical photo-deposition technique to cover microstructures are evident. Next section evaluates the deposition of Pd NPs by atomic layer deposition.

3.5.2 Pd NPs by atomic layer deposition

Palladium (Pd) NPs were deposited by ALD at the Laboratory IEM on top of the 3D photocatalyst (silicon scaffold with TiO_2 film), see the experimental details of the ALD process in the Annex Section 3.5.1. Two defined ALD process where set, where the

number of cycles were 100 and 300 in order to obtain Pd NPs of two different sizes, which are denoted hereafter as Pd-A and Pd-B NPs, respectively. As in the Au NPs section, for this study the 3D photocatalysts featuring thickness T3 were used. Moreover, as ALD is a technique known for its high conformality, a new 3D photocatalyst with a higher aspect ratio of 2.54 is introduced in this section, with a theorical AEF of 8.89, thus the photocatalyst is denoted with the notation A9 as the AEF is close to 9. The silicon scaffold of A9-T3 was fabricated following the optimized DRIE process described previously in Section 3.3 and exhibits a *depth* of 190 μm (SEM images of the 3D photocatalyst showing the cross-section with a compact TiO_2 film are shown in the Annex Figure 3.38).

As the seen in the previous section, the deposition of NPs can variate along the depth cavity, hence SEM images of the 3D photocatalysts were taken at the top and bottom of the microcavities walls for both types of Pd NPs, shown in Figure 3.26. The presence of both types of NPs along all the structure was corroborated, yet a remarked difference between both types of NPs is evident, whereas for Pd A (Figure 3.26a) the size is smaller and with spherical shape, type Pd B (Figure 3.26b) are bigger and exhibit variated shapes where some faceted like edges. The bigger size of particles B are ascribed to the 300 number of cycles in the ALD process of B (100 cycles for A) as in ALD, the grains grow as a consequence of the repeating pulse and exposure time, next, before forming a continuous film, the grains begin to coalesce, thus explaining the bigger size of B than that of Pd A. Furthermore, the faceted shape can be explained by the crystalline structure of the nanoparticles that coalesce to form bigger crystals that grow in a preferential plane direction. On the other hand, it has also been reported that the oxide substrates where metal NPs are deposited by ALD, can influence the shape by participating in the reaction directly through the interface, introducing charge transfer from/to the nanoparticles.[155] Thus, columnar morphology of TiO_2 might have an impact on explaining the morphology of the NPs, however more studies are required to clarify this point.

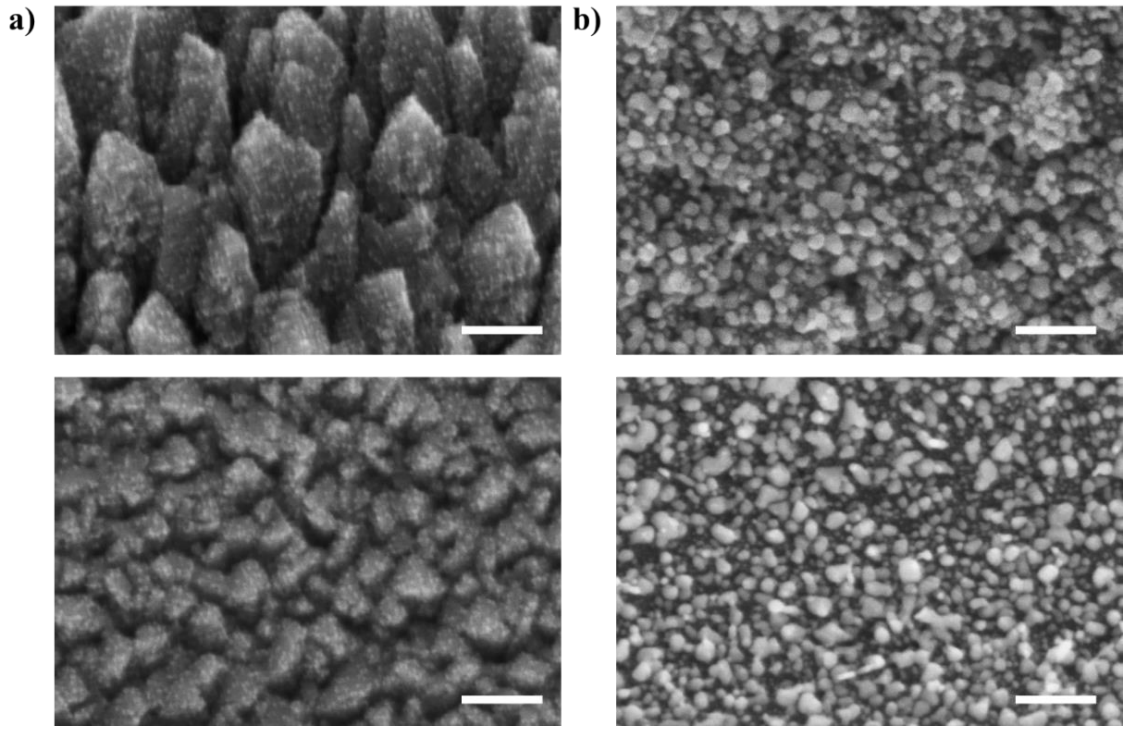

Figure 3.26 SEM cross-sectional images of A3-T3 at the upper (top images) and lower (bottom images) position of the wall's microcavity with Pd NPs deposited on top (a) A (100 ALD cycles) and (b) B (300 ALD cycles). Scale bar 200 nm.

SEM images of Pd NPs A at different heights of the wall's microcavity were also obtained for the sample A9-T3 Pd A (Figure 3.27), as seen the shape and size at three positions are similar, and the NPs are well distributed despite the high aspect ratio of the microstructure (2.5). This indicates that the ALD process allows the deposition of the NPs along all the depth of the microcavity, contrary to the chemical photo-deposition process for Au NPs.

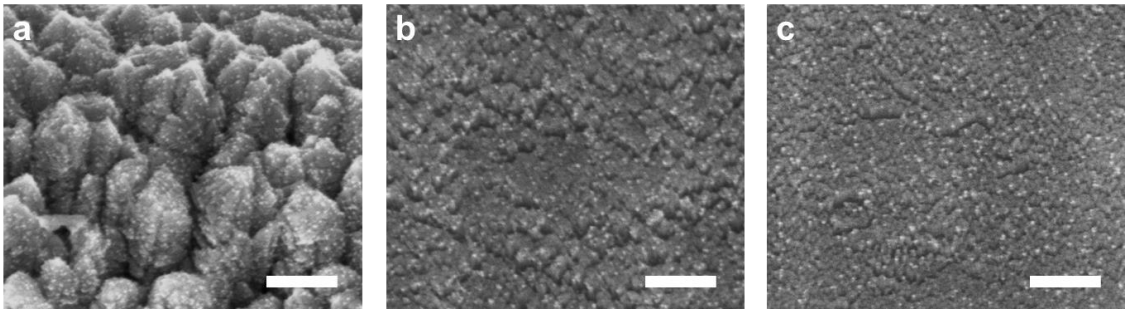

Figure 3.27 SEM cross-sectional images of A9-T3 Pd A photocatalyst at the upper (a), medium (b) and lower position of the wall's microcavity. Pd A NPs average size 8 nm. Scale bar 200 nm.

The size distribution was obtained for both NPs located at the top positions of the microcavities, histograms are shown in Figure 3.28 along with the statistical analysis determining the mean values for the diameters and the standard deviation (SD). Note that the SEM analysis shown in Figure 3.28 is unable to account for nanoparticles with diameters smaller than 5 nm. Pd A NPs have a narrow size distribution with an average size of 8.05 with a SD of 1.32 nm, whereas Pd B NPs have broad distribution with an average size of 31.04 and also with a wider SD of 10.11 nm, where some particles reach a big size of 62.5 nm. Hence, as mentioned, the size is ascribed to the difference in the number of cycles in the ALD process, which is 300 for Pd B, whereas 100 for Pd A. However, the difference in size is not proportional to the number of cycles, as B NPs size is 3.9 times bigger than A NPs, meaning that the particles grow more significantly after 100 cycles. Long nucleation in ALD can explain this non-linear growth, it has been reported for certain processes that the initiation speed of film growth can be slowed down for deposition of metals on oxides, resulting in long nucleation phases. Thus, after a determined number of cycles, linear growth begins, a few examples are 125 cycles for Al_2O_3, 160 SiO_2 and 400 for Si.[156]

Regarding the broad distribution of Pd B, it has been reported for Pd NPs a mechanism named "nucleation and growth model" where deposited single Pd atoms migrate across the surface and merge into existing nuclei. Hence, some atoms remain at their original position, those who will follow the expected growth, while others merge and will result in bigger particles. This displacement of the Pd atoms is due to the Pd precursor, $Pd(hfac)_2$ that dissociates into (hfac)* residual species. Next, the residual ligands remain on the surface as they are incompletely removed by the subsequent formalin cycles. Thus, as this species are weakly bounded, they are able to move on the surface.[157]

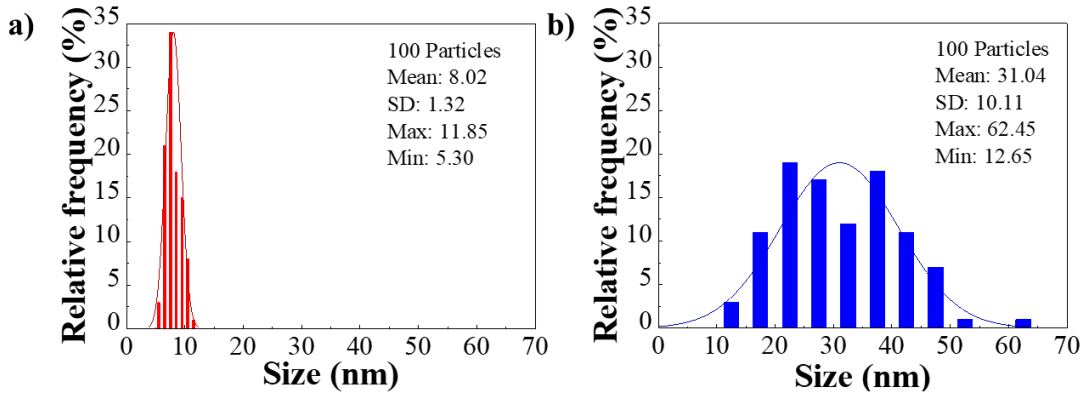

Figure 3.28 Histograms of Pd nanoparticles for (a) "A" and (b) "B" located at the top of the microcavities. Extracted from SEM images.

The NPs areal density was calculated at the top and bottom positions of the microcavity's wall for some samples in an area of 250 by 250 µm. For NPs A, the areal density calculated for sample A9-T3 Pd A, was 1120 and 592 NPs μm^{-2} at the top and bottom positions (190 µm). This difference could be ascribed to the TiO_2 film morphology that variates along the cavity, as at the top of the microstructure (Figure 3.38a top), the film's crystallites conserve their individual granular shape due to the higher thickness (~ 1 µm) which exposes a high surface of the grain where the NPs can grow. And, at the bottom of the cavity (Figure 3.38a bottom), the TiO_2 film exhibits is more compact as the thickness is low (>100 nm), thus the columnar grains do not expose their areal surface as those at the top, and there are less sites for the NPs to be deposited.

Regarding Pd B, the areal density was obtained for A3-T3 Pd B sample, and it was estimated to 560 and 976 NPs μm^{-2} also at the top and bottom positions of the wall (50 µm). These values present the contrary behavior than Pd A NPs, hence further measurements of NPs size distribution were carried out, the size distribution box plot is shown in the Annex Section Figure 3.39. The results show an average of 36.52 ± 7.67 and 28.11 ± 7.46 nm for the top and bottom positions. Hence as the NPs exhibit a smaller size at the bottom, in can be inferred that there is more coalescence of the NPs at the top, which results in bigger NPs. This is congruent with the faceted and irregular shape that Pd B NPs exhibit, and furthermore it could explain why the area density is half at the top than that at the bottom of the microcavity, as the NPs at the bottom are not merged yet.

GI-XRD patterns were obtained for the reference photocatalyst composed of flat silicon substrates with TiO_2 (denoted as A1-T2) where the Pd NPs were deposited on top. The patterns are shown in Figure 3.29a with the indexed planes. The prominent peaks at $2\theta = 33.4$, 65.31 and 70.32° correspond to Si planes (101), (103) and (040);[158,159] and at $2\theta = 63.1°$ to SiO_2 (752),[160] come from the silicon substrate. The anatase and rutile peaks present in the TiO_2 film are also present in both TiO_2 – Pd A and - Pd B patterns (detail of indexed planes discussed in Section 3.4.2). No peaks related to Pd or PdO were found.

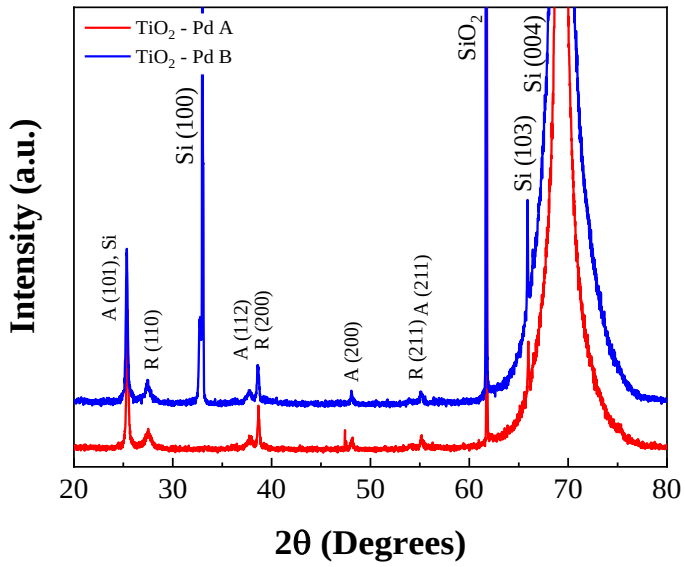

Figure 3.29 GI-XRD pattern of TiO_2 films deposited on silicon and with Pd NPs grown by ALD on top. TiO_2 reference thickness (denoted in previous sections as A1-T2).

The transmittance spectra shown in Figure 3.30a was obtained also for the reference photocatalyst deposited on quartz, with the Pd NPs on top. The main absorption of the overall film comes from the TiO_2 in the UV region as it was discussed in Chapter 2. The ripples in the 360 to 800 nm range correspond to the constructive and destructive interferences related to the film thickness and difference in the refractive index between the quartz substrate and the photocatalysts.

Next, an evident decrease of the transmittance is seen upon adding the NPs, at 367 nm the spectra diminish from 65.8 (TiO_2) to 12.97 % for –Pd B, whereas for –Pd A the transmittance is 43.8%. For TiO_2 – Pd A, an evident shoulder is also seen around 367.8 nm (highlighted in Figure 3.30a) extending the UV absorption of the TiO_2 from 358 to 386.6 nm, this defined absorption can be ascribed to the narrow and small size distribution of the "A" NPs (8 nm). Also, similar to the transmittance spectra of Au NPs (Chapter 2), for –Pd A there is a region in the visible that becomes prominent, centered at 550 nm, in the range from 475 to 670 nm. On the other side, for –Pd B, there is no defined absorption shoulder on the UV, this can be ascribed to the big size of 31 nm and their broad distribution; and a similar absorption curve in the visible is seen as in –Pd A, centered at ~560 nm but with a broader range from 488 to 712 nm. A similar absorption trend was reported for Pd nanocubes and particles fabricated by chemical synthesis, Pd particles of ~6 nm showed an absorption in the UV region, whereas larger particles and clusters absorbed in the visible region.[161,162]

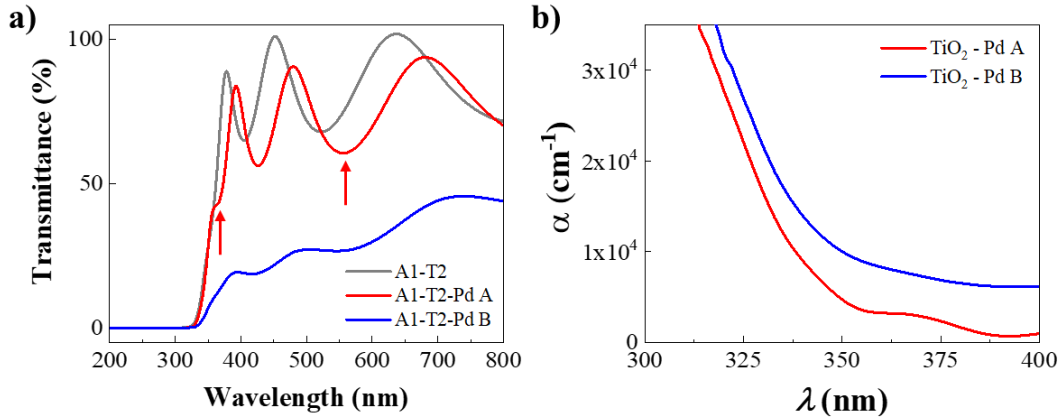

Figure 3.30 (a) Transmittance spectra, absorption shoulder highlighted for – Pd A; and (b) absorption coefficient spectra of TiO_2 films deposited on quartz. TiO_2 reference thickness (denoted in previous sections as A1-T2) with Pd NPs grown by ALD on top.

The absorption edge was determined from the absorption coefficient α spectra shown in Figure 3.30b,[163] resulting in 359. 95 nm for – Pd A sample, which indicates a slight redshift of +2.5 nm from the TiO_2 absorption edge. On the other side, the absorption edge of the - Pd B NPs increases remarkedly to 393.03 nm. Furthermore, from the α it can also be seen the light goes deeper in the TiO_2-Pd B photocatalysts, with a value of 2.16 10^4 cm^{-1} for B NPs at 330 nm, and 1.65 10^4 cm^{-1} for -Pb A.

The H_2 production was measured over 24 h, Figure 3.31 plots the H_2 production by different AEF (evolution plots in the Annex Section Figure 3.40). 3D photocatalysts with Pd A NPs exhibited a remarkedly higher photocatalytic activity, where the 3D microstructures (AEF 3 to 9) exceeded the flat photocatalyst (A1-Pd A) up to 3.9 times for A3–Pd A with an H_2 production rate of 36.40 µmol W^{-1} h^{-1}. For – Pd B samples, the performance was low for the majority of the samples, except for A5 –Pd B which exhibited the highest H_2 production rate of 7.96 µmol W^{-1} h^{-1}, followed by A1–Pd B with 1.71µmol W^{-1} h^{-1}, as for samples – Pd B

By considering the 3D microstructures an overall trend cannot be defined in terms of the H_2 production vs the AEF; although, from AEF 3 to 7-Pd A the results show a decreasing effect with the augmentation of the AEF, *i.e.*, as the aspect ratio of the microstructure decreases, however the trend is not proportional. This is surprising as the SEM characterization proved that the particles are being deposited all over the surface of interest of the microstructures, which is the walls, and that account for 67 up to 87% (Table 3.10) of the total surface. Hence, more detailed observations would be required to verify the specific changes in the areal density and size of the particles as they can variate along the microstructure due to the aspect ratio, and also due to the variant TiO_2 surface morphology.

However, the remarked performance of the – Pd A NPs can be ascribed to their optical properties, that due to their uniform size, allows the localized absorption wavelengths with an energy of 3.37 eV and on the visible. Other important aspect to consider is the synergy between TiO_2 and Pd, as in Chapter 2, where different charge generation and transport mechanisms were determined for TiO_2 and Au photocatalysts. It has been reported for ZnO/Pd that the due to differences in their work functions, a Schottky barrier is expected, inducing electron flow from the CB of ZnO to Pd.[164] As the band gap of ZnO (3.4 eV) is close to that of TiO_2, such synergy could take place. Other works, have also presented this scenario for TiO_2/Pd NPs, summed to the charge excitation by the localized plasmon resonance of the NPs and the injection of hot electrons to the semiconductor.[165,166]

Furthermore, regarding the lower performance Pd B NPs, by observing the surface morphology of the 3D microstructures with Pd B NPs, the TiO_2 seems to be completely covered by the NPs, this could represent a problem. First, as the light does not reach the TiO_2 surface due to the big and high density of NPs on the surface, thus, the photogeneration of charges by the semiconductor is limited, which is threatening for the NPs-semiconductor synergy. And, secondly, as the water splitting reaction was proved to take place on the semiconductor, not on the metallic particles (Chapter 2), the H_2 evolution cannot take place. It has been reported as well that the increase of Pd thickness might promote light scattering, thus no excitation light being absorbed.[167]

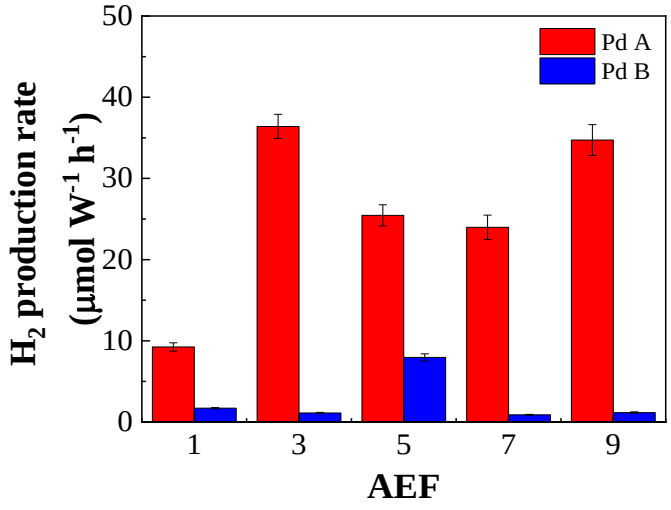

Figure 3.31 H_2 production rate for 3D photocatalyst featuring different AEF with TiO_2 film thickness T3 and Pd NPs deposited by ALD.

The H_2 production rates were compared to the reference photocatalyst to calculate the enhancement factor, the results are shown in Table 3.9. The addition of the Pd NPs allow to increase the performance of TiO_2 up to a factor of 46.7 when the NPs have a size

of 31.1 nm for an AEF 5; and an outstanding factor of 213.6 when the NPs have a size of 8 nm for an AEF 3.

Table 3.9 H_2 production rate of optimum 3D TiO_2 photocatalysts with Pd NPs.

Sample name	H_2 production rate ($\mu mol\ W^{-1}\ h^{-1}$)	H_2 production rate enhancement Factor [1]
A1 – T2 Pd A	9.24 ± 0.52	54.26 ± 3.57
A3 – T3 Pd A	36.40 ± 1.49	213.65 ± 11.48
A5 – T3 Pd A	25.45 ± 1.30	149.37 ± 9.22
A7 – T3 Pd A	23.99 ± 1.49	140.78 ± 10.01
A9 – T3 Pd A	34.73 ±1.89	203.84 ± 13.17
A1 – T2 Pd B	1.71 ± 0.08	10.01 ± 0.58
A3 – T3 Pd B	1.11 ± 0.08	6.54 ± 0.52
A5 – T3 Pd B	7.96 ± 0.45	46.72 ± 3.08
A7 – T3 Pd B	0.88 ± 0.06	5.19 ± 0.38
A9 – T3 Pd B	1.16 ± 0.10	6.81 ± 0.64

[1] Obtained by comparison to reference sample (A1-T2).

In summary, in this section a short study on the influence of Pd NPs on 3D photocatalysts was presented, where it was proved that ALD is a reliable technique to deposit particles conformably despite an aspect ratio of 2.5 in the pattern substrate. Despite the non-proportional H_2 production according to the AEF, a remarkable enhancement in the H_2 production with a factor of 214, compared to a bare TiO_2 flat photocatalyst, was observed with the addition of ~8 nm particles to 3D TiO_2 photocatalysts exhibiting an AEF of 3. It is hence suggested to deepen the study of the Pd particles to understand the behavior with respect to the AEF, considering that is difficult to establish a statistically significant measurements of the size of the nanoparticles with SEM analysis, more detail microstructural characterization is recommended, *i.e.*, TEM, providing detail about the particle minimum size, and crystalline structure. Also, importantly photocurrent measurements, flat band calculation, or time of flight analytical techniques are recommended to determine the mechanisms of the Schottky barrier and SPR mechanisms that influence the charge interactions. Moreover, the tuning of ALD parameters such as the number of cycles, precursor and reactant gases exposure and pulse times, etc., can also be modified to determine the influence of the particle size, morphology and/or the areal density. Also, the control of the growth of particles at the early stage, whether is influenced by the interfacial energy between the substrate and the Pd atoms, or the residual precursor species on the substrate; this could provide interesting results by the incorporation of small NPs with narrow distribution.

In the next section a comparison between of the incorporation Au and Pd particles to the photocatalyst with variant AEF is given. Also, recommendations for further experiments on TiO_2/Pd photocatalysts in order to understanding their interaction.

3.5.3 Discussion of role of NPs on 3D microstructures

The photocatalytic performance of the 3D photocatalyst exhibiting a variant AEF with bare TiO_2 and TiO_2 with Au NPs deposited by chemical photo-deposition and Pd NPs deposited by ALD are compared in Figure 3.32 in terms of the H_2 production enhancement factor. As seen in the previous section the addition of 8 nm Pd particles allows to improve remarkedly the H2 production, this is followed by the -Au photocatalysts when the AEF is 3 and 7, and by -Pd 31 nm particles when the AEF is 1 and 5.

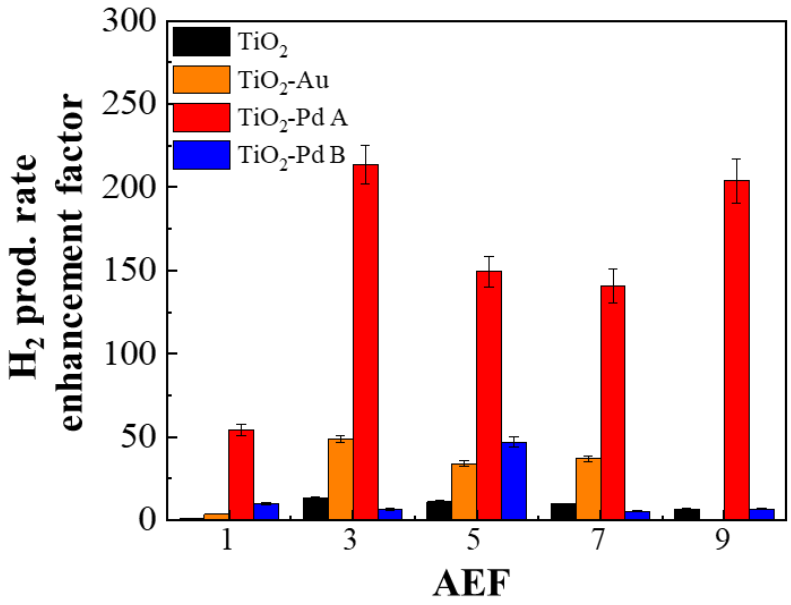

Figure 3.32 H_2 production rate enhancement compare to reference sample (A1-T2) for 3D photocatalyst featuring different AEF with TiO_2 film thickness T3. Bars in black: TiO_2, orange: TiO_2 and 30 nm Au NPs by photo-deposition, red: TiO_2 and 8 nm Pd NPs "A", and blue: TiO_2 and 31 nm Pd NPs "B" by ALD.

The morphology observations obtained by SEM, it was evident that the response of Au NPS is dictated by their areal density, as it the photodeposition method does not allow to deposit Au NPs all over the microcavities except for the parallel surfaces to the substrate which accounts for 14 to 33% of the total surface. Next, the areal density of the Pd NPs was proved to be higher than that of Au, with a maximum value of 1120 NPs μm^{-2} for Pd, and 98 for Au NPs μm^{-2}. This can explain the higher performance of Pd, yet the size of the particles is also a dominant factor, as it is known to determine the absorbance range. As Au particles presented a big size of 31 nm and broad distribution with an SD of 13.6 nm, the Pd particles that reported also low H_2 rates, also have exhibited 30 nm size with a broad distribution (SD ~13.6 nm). Whereas the best 3D photocatalysts where those with the Pd particles of the 8 nm and narrowest size distribution (SD ~1.3 nm). Regarding the Pd 31 nm particles, further experiments could shed light about the impact

of the broad size distribution, as the cause could be a simpler explanation in terms of light scattering (1), as the particles cover greatly the TiO_2 surface avoiding the light absorption; the fact that the water splitting reaction does not take place on the Pd NPs (2), or the non-activation of SPR and Schottky barrier mechanisms due to the broad range of optical absorption.

The absorbance of the photocatalysts is also a determinant factor as it delimits the light excitation absorption and thus the SPR and hot electron mechanisms in the metal. Au particles only presented a prominent wide absorption in the 450 to 700 nm range centered at 540 nm, with a transmittance of 50%. Whereas Pd particles shifted the main absorption edge of the TiO_2 located on the UV, to ~360 nm and to ~390 nm for 8 nm and 31 nm particles. Moreover, the -Pd photocatalysts also presented an absorption on the visible range centered at ~550 nm, and in the case of -Pd 8 nm. The absorption edge was extended also to the visible range from 358 to 386.6 nm, thus complementing the UV absorption of the TiO_2. This points out a sum of mechanisms between the Pd particles and the TiO_2, that boost the charge generation and transport to the surface.

3.6 Conclusions

The photocatalytic performance for the H_2 production of 3D photocatalysts composed of TiO_2 and TiO_2/Au and /Pd NPS was reported as a function of semiconductor layer thickness and the aspect ratio relative to specific AEF values. It was demonstrated that by augmenting the surface area by a factor of 3, the H_2 production is enhanced by a factor of 13, due to the increase in active surface area for the water-splitting reaction.

Moreover, a supplementary 4 and 16-factor H_2 production rate enhancement is achieved by chemical deposition of Au and Pd NPs due to the extension of the absorption spectra of the photocatalyst. Furthermore, the results indicate that further developments, such as atomic layer deposition techniques and controlled *in situ* synthesis of metal nanoparticles, can result in major enhancements for higher aspect ratio 3D photocatalysts. Lastly, this study proposes a fabrication process that can be easily implemented in the fabrication of silicon-based microdevices which is of fundamental and technological interest for electronics, sensing elements to 3D photonics and metamaterials for light-driven H_2 production.

3.7 Annex

3.7.1 Profile angle θ calculation

A scheme of the cross-section of the wall of the microcavities is detailed Figure 3.33. θ is defined as the angle formed between the microcavity bottom and the wall. From measurements on SEM images, the half of the widths of the bottom (*a*) and top (c*)* of the walls are taken, as well as the depth of the microcavity (d). Since the profile geometry of the microstructures is symmetric, it is inferred that trapezoid scheme is isosceles, meaning that angles δ and α are 90°. All together, these parameters are used to solve the equations 3.10 - 3.13 in order to determine θ.

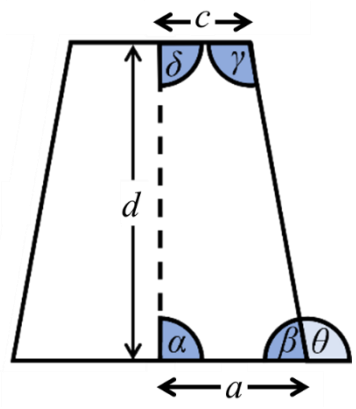

Figure 3.33 Description of the parameters for angle θ calculation of the trapezoid cross-sectional shape of the walls in the microstructures. The top and bottom width of the wall are b and a.

$$e^2 = c^2 + d^2 - 2cd \cdot \cos\delta \qquad \text{Equation 3.10}$$

$$e^2 = a^2 + b^2 - 2ac \cdot \cos\beta \qquad \text{Equation 3.11}$$

$$cos\,\alpha = \frac{d^2+(a-c)^2-b^2}{2d\cdot(a-c)} \qquad \text{Equation 3.12}$$

$$\theta = 180 - \beta \qquad \text{Equation 3.13}$$

3.7.2 Scalloping defect

3.7.2.1 Variation of oxide layer thickness in thermic oxidation process

Due to the consecutively isotropic etching in the DRIE process, tranches are engraved along the etched cavities of the substrate. To remove these scalloping trenches from the cavity walls and obtain a smooth silicon surface, the silicon microstructures undergo a thermic oxidation process that consists of growing a SiO_2 layer that uniformly covers all the substrate; and its subsequently removed with HF.

To optimize this process, oxide layer was grown with two different thickness: 700 and 1000 nm on the silicon substrates featuring an AEF 5. Figure 3.34 shows the cross-sectional SEM images of the microcavities before and after the process for both oxide layer thicknesses, where 700 and 1000 nm are noted as A5–ox–700 and –ox–1000.

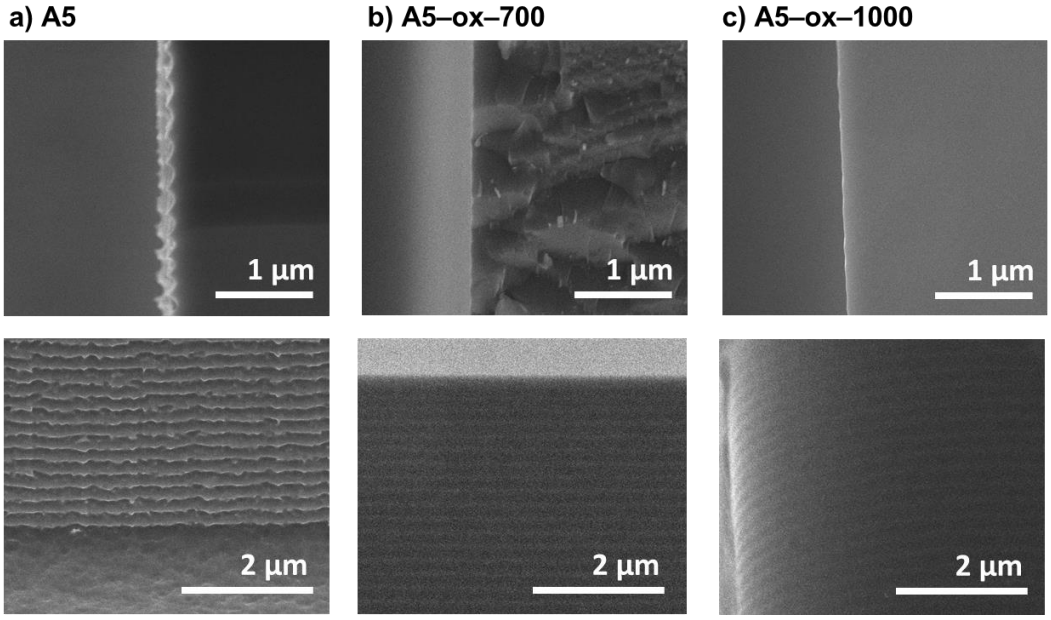

Figure 3.34 SEM cross-section images of etched silicon microstructures with AEF 5 a) before thermal oxidation treatment, after thermal oxidation treatment and removal of oxide layer for b) 700 nm oxide layer (A5–ox–700) and c) 1000 nm oxide layer (A5–ox–1000). Top: detail of wall edge of microcavities. Bottom: wall of microcavities. DRIE exposure time ratio is SF_6:C_4F_8/O_2 of 0.75. Microstructure's depth 100 µm.

The scalloping was clearly reduced, yet in sample A5–ox–700 the trenches are still visible, the scalloping horizontal radio was diminished from 96 to 20 nm. On the other hand, AEF 5–1000 ox shows more smooth edges and surfaces, with barely visible trenches on the walls, which left small traces on the wall edge (Figure 3.34c) but not remarked groove.

3.7.2.2 Impact of scalloping defect on H2 production

To elucidate the effect of the trenches as a possible enhancement of by increment of active sites, a TiO_2 film were deposited by sputtering on the silicon substrates with the scalloping defect and without it, named A5 and A5-ox-1000 before. Two TiO_2 thickness 270 and 650 nm (thickness measured on flat surface) noted as A and B were deposited. Figure 3.35 shows the detail of the wall edge of the cavities where the TiO_2 layer is clearly seen on the silicon substrate, moreover the TiO_2 layer was deposited all over the microcavities pattern. However, the difference between A and B film thickness was notorious, as it variates from the expected thickness 270 and 650 nm, respectively. For A5-TiO_2 A-scall. and A5-TiO_2 A. the measured thickness at the wall medium height (~75 µm *depth*) was 110 and 50nm; and for A5-TiO_2 B-scall. and A5-TiO_2 B, was 220 and 126.4 nm. Yet, on those samples with trenches is not possible to distinguish between the silicon and TiO_2, as the substrate roughness induce and tubular like morphology of the TiO_2, hence the measured thickness includes the scalloping defect of the substrate. On the other hand, the films deposited on the non-defective substrates exhibit the characteristic columnar growth of TiO_2, discussed in Chapter 2.

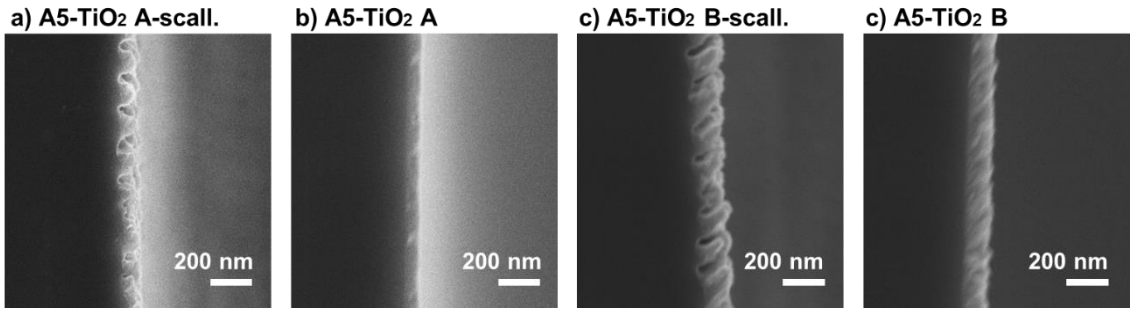

Figure 3.35 SEM cross-section images of the microcavities wall edge at medium height of 3D photocatalyst with AEF 5 and TiO_2 films with thickness 270 ("A") and 650 nm ("B"), silicon substrates "scall." present the scalloping defect. Microstructure's depth 100 µm.

The H_2 production of the 3D photocatalyst was measured by gas chromatography, the plots are shown in Figure 3.36. Samples with thickness A show almost negligible H_2 production, whereas thickness B exhibited evolution of H2 over the 24 h tests. The H_2 production rate of A5-TiO_2 B-scall. was 0.05 µmol W^{-1} h^{-1}; whereas that of A5-TiO_2 B was 0.33 µmol W^{-1} h^{-1}, this represents a difference of 5.8 times. Hence, this difference can be ascribed to the substrate surface, which by being smooth allows the formation of a more compact layer of TiO_2 which is necessary to create active sites for the water splitting reaction.

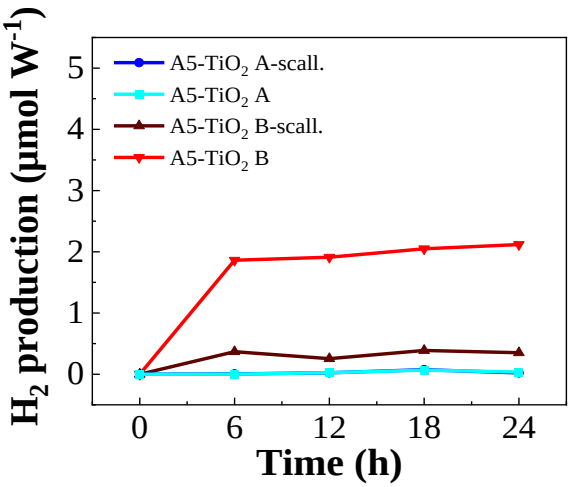

Figure 3.36 H_2 production of 3D photocatalyst exhibiting an AEF 5 with TiO_2 film before thermal oxidation treatment (A5-TiO_2) and after thermal oxidation treatment and removal of 1000 nm oxide layer (A5-TiO_2-ox). Irradiation with Xenon lamp, values normalized by the UV and visible light flux at λ = 365 nm and λ = 405 nm, respectively and by the surface area (cm^{-2}).

3.7.3 TiO_2 structure by XRD

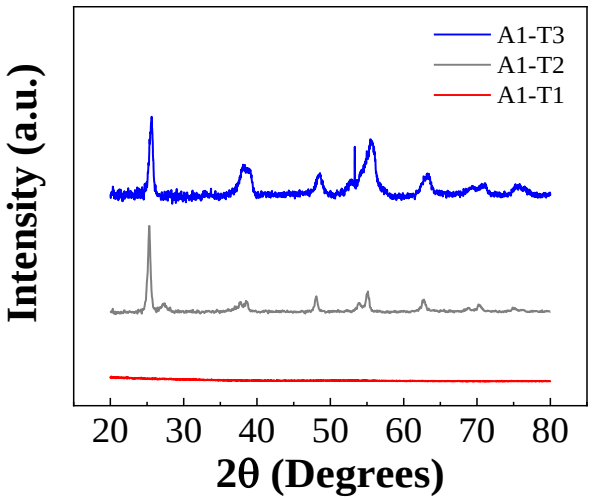

Figure 3.37 GI-XRD pattern of sputter-deposited TiO_2 films on flat silicon substrate with thickness 100 (A1-T1), 270 (A1-T2) and 650 nm (A1-T3).

3.7.4 Calculation of TiO_2 average thickness

Table 3.10 Calculated factors for specific surface percentage of the total surface of the silicon microstructure featuring a variable AEF associated to a specific depth, where w = 75 µm and a = 10.4 µm

AEF	*Depth* (µm)	Fraction of total surface		
		Top surface "F1"	Bottom surface "F2"	Walls "F3"
3	50	0.076	0.252	0.672
5	100	0.046	0.151	0.804
7	150	0.032	0.108	0.860
9	190	0.026	0.087	0.886

3.7.5 Quantum Efficiency calculation

Quantum Efficiency (QE) of the optimal 3D TiO_2 photocatalysts was calculated considering the spectral output of the used Xe lamp for irradiation. Equations 3.14-3.16 were used for the calculations. In agreement with the TiO_2 film deposited by PVD absorption spectrum, which corresponds to the UV range, $\sum_{UV} n_i$ was delimited too.

$$n = \frac{I\,\lambda}{hc} \qquad \text{Equation 3.14}$$

$$N = \frac{W\,\sum_{UV} n}{\sum I} \qquad \text{Equation 3.15}$$

$$QE = \frac{2\,N_A[H_2]}{N\,t} \qquad \text{Equation 3.16}$$

Where:

I = Lamp relative irradiance

λ = Wavelength

h = Planck's constant

c = Speed of light

W = Lamp intensity on 3D photocatalyst

N_A = Avogadro's number

$[H_2]$ = H_2 production upon irradiation over a delimited time

t = Irradiation time

3.7.6 Pd nanoparticles

Experimental details of ALD deposition process

The depositions were carried directly on the 3D photocatalyst composed of the silicon scaffold and TiO_2 film, using a home-built ALD reactor at the European Membrane Institute (Institut Européen des Membranes, IEM) at Montpellier by the Eng. Cassandre Lamboux.

The chamber temperature was 200 °C and the pressure 2 Pa. The precursors used were Palladium (II) hexafluoroacetylacetonate "$Pd(hfac)_2$" ($Pd(C_5HF_6O_2)_2$ 95%, Strem Chemical) and formaldehyde (CH_2O, Sigma Aldrich). The flow of $Pd(hfac)_2$ and formaldehyde were 0.02 and 0.04 L min^{-1}, respectively. Ar gas was used as carrier gas during formaldehyde pulse, with a flow of 0.03 L min^{-1}, no carrier gas was used for $Pd(hfac)_2$ pulse. The ALD cycle consisted of 5 s pulse, 15 s exposure and 10 s purge for $Pd(hfac)_2$; and, 1 s pulse, 15 s exposure and 60 s purge for formaldehyde. The cycle was repeated 100 times adfor the noted "- Pd A" nanoparticles, and 300 times for the "- Pd B" nanoparticles.

SEM images of 3D photocatalyst with AEF 9

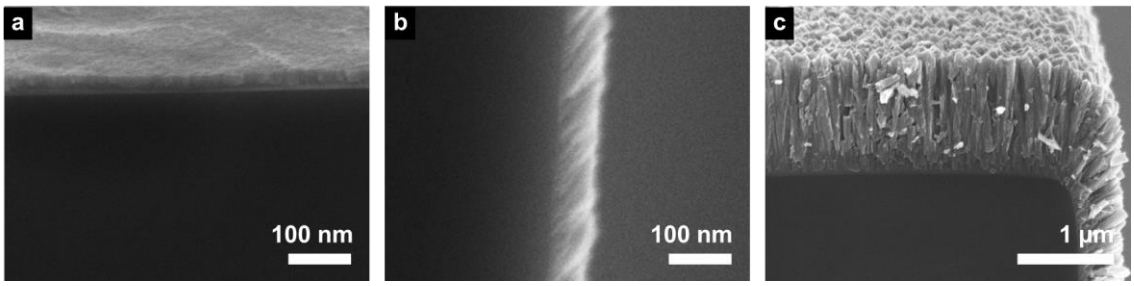

Figure 3.38 SEM cross-sectional images of 3D photocatalyst with AEF 9 and TiO_2 film thickness T3, denoted as AEF9-T3. (a) bottom surface, (b) half-height of the walls, and (c) top surface of the microcavity.

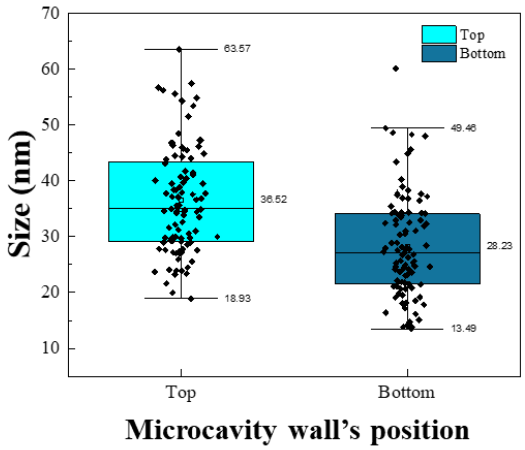

Figure 3.39 Box plot of distribution with data interval for A3–T3 Pd B at different wall's positions.

H_2 evolution plots

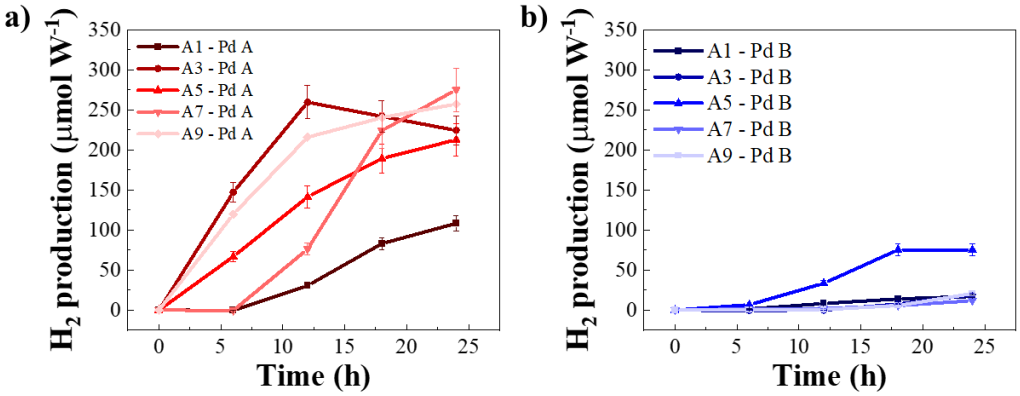

Figure 3.40 H_2 evolution over 24 h for 3D photocatalyst featuring different AEF with TiO_2 film thickness T3 with Pd NPs deposited by ALD with size of (a) 4 and (b) 8 nm.

Chapter 4

Impact of surface defects and electronic intermediate states on the water-splitting processes

As seen in Chapter 2, a thermal-annealing step can modify the crystalline structure (anatase/rutile ratio) of the sputter-deposited TiO_2 film, yet the post-process can also modify the electronic properties by the creation of localized defects. Such defects, where the most common are oxygen vacancies (Vo) and Ti interstitials (Ti(i)), are known to induce intrinsic intermediate gap states which can play a decisive role in the charge carrier kinetics.[111] *In this chapter, the type and nature of defects present on annealed TiO_2 thin films are determined and correlated to their role on the H_2 production rate from the viewpoint of the electronic structure. Structural and morphological studies, chemical and optical-electronic spectroscopy. Studies supported by photoluminescence measurements and DFT calculations were also implemented for the determination of the band structure and its correlation to the photocatalytic activity of TiO_2 films prepared by sputtering and annealed at different temperatures from 200 °C to 700 °C in inert atmosphere.*

4.1 Introduction

Photoluminescence (PL) spectroscopy is proven to be a powerful technique for studying the radiative recombination between photogenerated charge carriers, occurring in a few tenths to hundreds of nanometers below the semiconductor surface.[168] Several works have reported PL emissions correlated to intermediate states and to the over-all energetic distribution on nanocrystalline TiO_2 materials.[169–176] Knorr *et al.*[177] reported PL bands for films prepared with commercial anatase and rutile particles, being at ~650 nm and on the near IR, respectively. And for mixed film composed of anatase and rutile, a broad PL band on the red was localized at ~650 nm, which was assigned to transitions of electron traps with VB holes, revealing a carrier interphasial electron transport for a mixed anatase/rutile heterostructure. Later the same group reported a red PL response on anatase films, which was ascribed to Ti^{3+} point defects, that resulted from the reorganization energy for recombination of trapped electrons (associated to Ti^{3+}) with VB holes.[178]

More recently, Mascaretti *et al.*[176] worked on reduced anatase films prepared by pulse laser deposition (PLD). The PL measurements were conducted with UV and visible light excitation of different wavelengths on air and vacuum, a broad PL signal centered around 619 to 689 nm was found under UV, and at 689 nm under visible; suggesting the presence of Ti^{3+} ions as electron traps. Moreover, by annealing the anatase films in reducing and oxidizing atmospheres, a different degree of surface hole traps were introduced (*i.e.*, oxygen-based radicals) which were ascribed to hole traps.

Other works have classified the intermediate states as shallow or deep traps, Pallotti *et al.*,[172] conducted PL measurements with a sub-band gap excitation (2.8 eV), and ascribed a red PL band (652 nm) to radiative recombination between free holes and electrons that relax from CB and shallow subgap states to deep defect states for commercial anatase powder.

Clearly, a consensus on a framework to describe the PL processes involved in the radiative transitions and about the nature identification of the intermediate states TiO_2 thin films is still lacking. In addition, PL studies have not yet addressed the role of the energetic trap states located in the band gap in relation to the water splitting reaction at the TiO_2 surface/aqueous solution interface. One first limitation comes from the fact that PL properties vary highly with the material elaboration technique. Second, PL characterization permits to gain insights on the radiative recombination that takes place on the TiO_2 surface, but not an in-depth analysis of type and concentration of chemical defects, such as the Vo or Ti^{3+}. Third, the specific description of defects in terms of their detailed chemical nature and concentration of oxygen vacancies, Ti interstitials, Ti^{3+} sites, and hydroxyl radicals (OH^-), on the water splitting. This represents a crucial step for the design of photocatalytic systems which has never been reported.

Therefore, in this chapter, TiO_2 films deposited on silicon substrates and annealed at 200, 550 and 700 °C were studied. The effect of the annealing temperature was determined thought a complete morphological and structural characterization, and their impact on the photocatalytic water splitting was measured by the H_2 production. Chemical characterization served to identify the stoichiometry of the film on the bulk and on the surface, where the identification and quantification of OH^- and Ti^{3+} species was determined. Optical characterization served to calculate the band gap and to estimate the disorder in the electronic structure of the semiconductor. Next, an in-depth analysis of the disordered electronic structure was carried through steady-state photoluminescence, which served to identify the presence of intermediate states, revealing the dominant role of the mid-gap states on the H_2 production, rather than the hetero-crystalline nature and mesoscale structure. Finally, the correlation between the chemical species formed during the annealing step and the electronic disorder was performed through DFT calculations. The Density of States (DOS) was obtained for defective TiO_2 anatase slabs with localized Vo, Ti^{3+} and absorbed OH^- species, which revealed the presence shallow and deep intermediate states that interact selectively with the holes and electron charges, serving as an intermediate step in the oxidation and reduction reactions of the water splitting process. The results of this study were published in 2022 in the Journal Dalton Transactions.[179]

4.2 Materials and characterization

4.2.1 Samples preparation

Before deposition, O_2 plasma was carried on the silicon p-type and quartz 4 inches wafers. TiO_2 was sputter-deposited by direct current magnetron sputtering with the Ti target as described on Chapter 2 Section 2.3.1. The deposition of the film was performed with 3 loops of 180 passes, corresponding to deposition thicknesses of 270 nm.

Annealing treatments were conducted in a AET furnace with a nitrogen inert atmosphere (N_2 99.9999% purity). The annealing was conducted at 200, 550 and 700 °C for samples T-200, T-500 and T-700, respectively. Heating ramp was 5 °C min^{-1} and annealing time 1 h, the full details of the annealing recipes for each sample are shown in Table 4.1 to Table 4.3.

Table 4.1 Furnace annealing recipe for sample T-200.

Segment	Temperature (°C)	Duration (min)	Heating rate (°C min^{-1})	Flow (L min^{-1})
1	30	2	5	5
2	200	34	5	2
3	200	60	0	2

4	30	60	-2.8	2

Table 4.2 Furnace annealing recipe for sample T-550.

Segment	Temperature (°C)	Duration (min)	Heating rate (°C min^{-1})	Flow (L min^{-1})
1	30	2	5	5
2	550	104	5	2
3	550	60	0	2
4	30	120	-4.3	2

Table 4.3 Furnace annealing recipe for sample T-700.

Segment	Temperature (°C)	Duration (min)	Heating rate (°C min^{-1})	Flow (L min^{-1})
1	30	2	5	5
2	700	134	5	2
3	700	60	0	2
4	30	223	-3.0	2

4.2.2 Structural characterization

4.3.2.1 Grazing Incidence X-Ray Diffraction (GI-XRD)

The diffraction pattern was obtained for the films deposited on silicon was determined by GI-XRD; whose mechanism and analytical information of the instrument were mentioned in Chapter 2 Section 2.3.

4.3.2.2 Scanning electronic microscopy (SEM)

The morphology of the TiO_2 thin films deposited on silicon was determined by SEM whose mechanism and analytical information was mentioned in Chapter 3 Section 3.3.

4.3.2.3 Transmission electronic microscopy (TEM)

In order to analyze by TEM (principle described in Chapter 2 Section 2.3), a lamella was fabricated from the cross section of the TiO_2 film deposited on silicon using a Focused Ion Beam Helios 600i (FEI), and covered with a platinum film on top.

Analytical information. Crystallographic morphology and lattice structures were collected on a TEM JEOL 2100F equipped with a Schottky emitter gun used at 200kV with a point-to-point resolution of 0.23 nm. Images were obtained in STEM HAADF mode with a STEM recorder (JEOL), camera CMOS RIO 16IS 4k*4k (Gatan/Ametek). The tests were performed at the Castaing Center ((UAR3623 - Toulouse).

4.3.2.4 Atomic Force Microscopy (AFM)

The topology of the films deposited on silicon was observed by AFM; whose mechanism was mentioned in Chapter 2 Section 2.3.

Analytical information. AFM imaging of the surface morphology was carried using a Dimension ICON AFM equipment (Bruker) in the tapping mode with a scan size of 1 μm and a scan rate of 0.499 Hz. Roughness was also obtained by AFM using the software NanoScope Analysis 1.8.

4.3.2.5 Residual stress profilometry

The residual stress can be estimated by measuring the radii of curvature of bare silicon substrates and the substrates with the as-deposited and annealed films. After measuring the radii of curvature R due to bending, the residual stress (σ) is calculated by using Stoney's equation 4.1,[180] where E_s, υ_s, t_s and t_c are the Young's modulus, Poisson ratio and thickness of the substrate (500 um) and film (0.27 um). R_0 and R are radii of curvature of the bare substrate and sample film-substrate, respectively.

$$\sigma = \frac{E_S}{6(1-\upsilon_S)} \frac{t_S^2}{t_c} \left(\frac{1}{R} - \frac{1}{R_0}\right) \qquad \text{Equation 4.1}$$

Analytical information. The residual stress was measured with the mechanical profilometer KLA Tencor P17. In order to obtain the residual stress of the TiO_2 films, the complete 4 inches silicon wafers were measured before and after deposition and annealing step.

4.2.3 Photocatalytic activity measurement

The photocatalytic activity was measured by gas chromatography, the H_2 evolution was measured over 24 h as detailed in Chapter 2 Section 2.3. Xenon lamp was used directly for irradiation.

4.2.4 Chemical characterization

4.3.4.1 X-Ray Photoelectron Spectroscopy (XPS)

XPS spectra, whose mechanism and analytical information was mentioned in Chapter 2 Section 2.3, was recorded for the films deposited on quartz.

Analytical information. The O 1s and Ti 2p high resolution spectra were obtained in a PerkinElmer PHI System X-Ray photoelectron spectrometer at room temperature with an Al Kα (1486.6 eV) radiation. X-Ray source at a residual gas pressure < 3.99 10^{-7} Pa chamber pressure, and using a 16-channel detector with a hemispherical analyzer. Further deconvolution of the spectra was carried using the software CASA and Avantage. XPS spectrum was also recorded in the low energy range to obtain the VB spectra.

Measurements were performed by Dr. Kui Tan at the Natural Science and Engineering Research Laboratory (NSERL) at the University of Texas at Dallas (UTD).

4.3.4.2 Electron Microprobe X-Ray analysis (EPMA)

Also known as wavelength-dispersive electron microprobe analysis, is a spatially resolved, quantitative elemental analysis technique based on the generation of characteristic X-Rays by a focused beam of energetic electrons. It is useful for studying small changes in composition within the body of an artifact as the penetration depth is up to 5 μm.

Inner shell ionization is provoked when the beam electron ejects a bound atomic electron by transferring sufficient energy to the atom to exceed the critical excitation (or binding) energy of an atomic electron. The resulting atomic vacancy is filled by a transition involving one or more outer shell electrons. The energy difference between shell levels can be manifested as an emitted X-ray photon, or the energy can be transferred to another outer shell electron, which is ejected as an Auger electron. The energy distribution of the X-Rays emitted are measured with an energy-dispersive or wavelength dispersive spectrometer (both formed part of the EPMA). Interpretation of the emitted X-Ray or Auger electron is assessed due to the characteristic energy of the atom species originally ionized by the electron beam.

Analytical information. EMP analysis was carried on the samples deposited on silicon with a Cameca SXFive FE microprobe at low voltage (7 kV) for a sub-μm X-ray generation volume. The measurements were obtained by setting the probe depth in a range of 228.1 to 256 nm from the surface to the bulk of the film.

Next, the atomic composition of the films was obtained using a quantitative analysis by comparing the intensities of the characteristic X-rays for elemental O and Ti with the respective intensities of standard natural minerals.

4.2.5 Optical characterization

4.3.5.1 UV−Vis spectroscopy

UV-Vis absorbance, whose mechanism and analytical information was mentioned in Chapter 2 Section 2.3, was obtained for the films deposited on quartz wafers.

Analytical information. Experiments were carried in a PerkinElmer Lambda 650 UV−Vis spectrometer, from 200 to 800 nm with 1 nm step, in the transmittance mode.

4.3.5.2 Photoluminescence spectroscopy (PL)

PL is a powerful technique for investigating the electronic structure, both intrinsic and extrinsic, of semiconducting and semi-insulating materials. The detection and analysis of this emission is widely used as an analytical tool as due to its sensitivity, simplicity, and low cost. Sensitivity is one of the strengths of the PL technique, allowing very small quantities (nanograms) or low concentrations (parts-per-trillion) of material to be

analyzed. Precise quantitative concentration determinations are difficult unless conditions can be carefully controlled, and many applications of PL are primarily qualitative.

In PL, a material gains energy by absorbing light at some wavelength by promoting an electron from a low to a higher energy level. This may be described as making a transition from the ground state to an excited state of an atom or molecule, or from the VB to the CB of a semiconductor crystal (electron-hole pair creation). The system then undergoes a nonradiative internal relaxation involving interaction with crystalline or molecular vibrational and rotational modes, and the excited electron moves to a more stable excited level, such as the bottom of the conduction band or the lowest vibrational molecular state.

After the lifetime in the excited state, which may last from picoseconds to many seconds, the electronic system will return to the ground state. In luminescent materials some or all of the energy released during this final transition is in the form of light, in which case the relaxation is said to be radiative. The wavelength of this emission is longer than that of the incident light. This emitted light is detected as photoluminescence, and the spectral dependence of its intensity is analyzed to provide information about the properties of the material.

A difficulty with extracting accurate composition information from room temperature PL spectra is that the peak position depends on the excitation wavelength and intensity. The spectrum shifts to lower energy as the intensity is raised, and the peak position is at lower energy for the shorter-wavelength light. The explanation for this effect probably lies in local heating of the sample by the rather high intensities used. The heating is greater for higher energy (blue) photons because a greater fraction of each photon's energy is converted to phonons.

Analytical information. The PL spectra of samples deposited on silicon were recorded at room temperature on a custom-made set-up. The excitation was provided by a frequency-doubled picosecond Titanium:Saphire laser (Spectra Physics, Tsunami) at $\lambda = 355$ nm (1 mW average power, 1 ps pulse duration and 80 MHz repetition frequency). The luminescence spectrum was dispersed by a 500 mm focal length imaging spectrometer (Princeton Instrument, Acton 2500i) and its intensity recorded with a silicon UV-enhanced, liquid-nitrogen-cooled charge-coupled device detector (CCD Princeton Instrument, Pylon Excelon 400). Figure 4.1 shows the diagram and photographs of the setup.

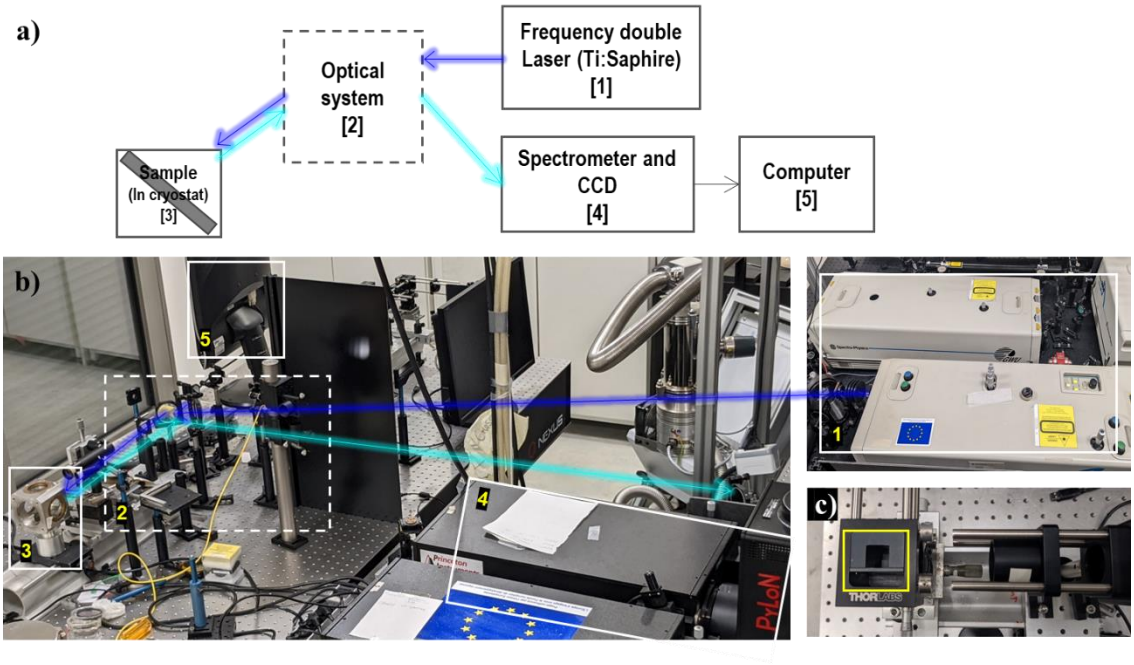

Figure 4.1 Setup of photoluminescence bench at LPCNO, (a) diagram and (b) photographs of the setup depicting the main components. (c) Holder for quartz cuvette used for tests with ethanol.

Steady-state PL measurements in ethanol were performed by locating the sample in a quartz cuvette with ethanol (99.9%, Technic), (see Figure 4.1c). For measurements in vacuum, samples were located onto a Cu holder located inside a cryostat connected to a diaphragm pump, shown as number [3] in Figure 4.1b.

The measurements were carried at the Laboratory of Physics and Chemistry of Nano-objects (LPCNO) with the help of Dr. Andrea Balocchi.

4.2.6 Density Functional Theory (DFT) details

Spin-polarized DFT calculations were performed using the generalized gradient approximation (GGA) with the Perdew-Burke-Ernzehof (PBE)[181] exchange-correlation functional as implemented in the Vienna ab-initio Simulation Package (VASP).[182,182–184] Projector augmented waves (PAW) pseudopotentials were employed to describe ion-electron interactions,[185,186] and the electron wave functions were expanded in terms of plane wave basis sets, with a kinetic energy cutoff of 400 eV. Wavefunctions were optimized until the change in total energy was less than 10^{-6} eV.

Grimme's DFT-D3 method was employed to include dispersion contributions to the energy values.[187] The anatase (101) supercell, with lattice parameters a = b = 3.8073 Å and c = 9.7318 Å[188,189] was built using a vacuum of 10 Å between anatase slabs along the direction normal to the surface. The 1 × 3 supercell surface contains a total of 108 atoms, and the bottom layer of TiO_2 was held fixed while all other atoms were allowed to relax in all directions during minimization of the total energy. The models used were

based on this slab including a series of defects and adsorbed species. The Brillouin zone was sampled at the gamma point. The density of states calculations was performed using the DFT+U method. The calculations were planned in collaboration and directed by Dr. Kolade Oyekan from UTD.

4.3 Annealing impact on TiO_2 film properties and H_2 production

4.3.1 Structural characterization

Figure 4.2 displays the XRD patterns of the films. T-AD sample shows the characteristic peaks of PVD polycrystalline TiO_2 at $2\theta = 25.37$, 37.89, 38.72, 48.22, 53.88, 53.30, 62.77 and 70.42° corresponding to the anatase planes (101), (004), (112), (200), (105), (211), (204) and (215); [25,134] and at $2\theta = 27.42$, 54.37 and 68.93°, corresponding to the rutile planes (110), (211) and (301),[103,190] respectively. Both structures were confirmed with COD database, patterns number 1010942 and 9009083, for anatase and rutile, respectively. No peaks related to impurities are observed.

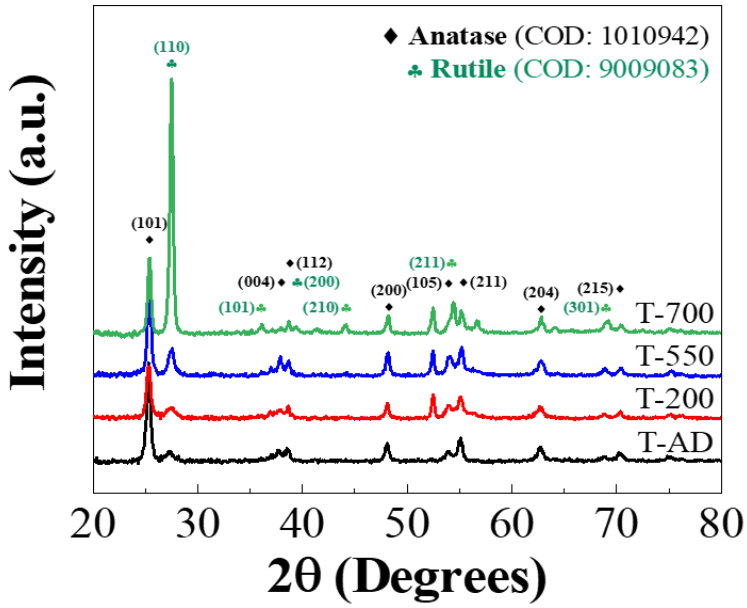

Figure 4.2 GI-XRD patterns of TiO_2 thin films deposited on silicon and annealed at different temperatures. Anatase and rutile crystalline planes identified.

Upon annealing at 200 °C (T-200), the intensities of the peaks corresponding to the anatase planes (101), (004), (112), (105) and (211), increase with respect to the as-deposited film (T-AD); and a further increase is observed by annealing at 550 °C (T-550). However, by annealing at 700 °C (T-700), the intensities of the anatase peaks become weaker, while the peaks associated to rutile planes (110), (211) and (301), increase

notably. Subsequently, new rutile peaks also appeared at 2θ = 36.10 and 44.17°, associated to (101) and (210) planes, respectively. The major change is observed in the intense narrow peaks located at 2θ = 25.37 and 27.42° that correspond to tetragonal anatase plane (101) and rutile plane (110). For T-AD, the ratio of the intensity anatase (101) peak with respect to rutile (110) is 3.5; and it increases up to 3.7 and 4.2 by annealing at 200 (T-200) and 550 °C (T-550), respectively. Upon annealing at 700 °C (T-700), this ratio decreases drastically to 0.3.

In order to quantify the composition of each crystalline phase, the percentage composition of rutile was estimated using Equation 4.2:

$$[R]\ \% = \frac{1}{1+0.884\frac{I_A}{I_R}} \times 100 \qquad \text{Equation 4.2}$$

Where I_A and I_R correspond to the area of the anatase (101) and rutile (110) peaks, respectively. The number 0.884 is a scattering coefficient. Therefore, the anatase composition is equal to [A] = 100 – [R].[191] Results reported in Table 4.4 as Crystalline structure in percentage, note that anatase phase dominates the film structure for the T-AD with 60.58% and, it increases almost linearly by annealing at 200 °C and furthermore to 71.36% at 550 °C. Inversely, by increasing the thermal treatment up to 700 °C, the anatase phase transforms greatly into rutile: 71.36% of rutile.

Table 4.4 Crystalline structure and dimensions of crystallite, grain and pores of TiO_2 thin films deposited on silicon.

Sample	Crystalline structure		Crystallite diameter [1] (nm)	AGS [2] (nm)	APS [3] (nm)	Average Stress [4]	
	(wt%)	Err.				(MPa)	Std. Dev.
T-AD	60.58 (A), 39.42 (R)	$5.12\ 10^{-5}$	21.00 ± 0.14 (A), 6.95 ± 0.05 (R)	32.0 ± 0.9	8.8 ± 0.5	191.0	$7.46\ 10^{-8}$
T-200	66.36 (A), 33.64 (R)	$5.12\ 10^{-5}$	17.11 ± 0.11 (A), 5.53 ± 0.04 (R)	30.4 ± 0.8	6.3 ± 0.3	315.5	$7.78\ 10^{-8}$
T-550	71.36 (A), 28.64 (R)	$5.12\ 10^{-5}$	25.52 ± 0.17 (A), 13.55 ± 0.09 (R)	29.2 ± 0.7	6.6 ± 0.4	605.5	$8.24\ 10^{-8}$
T-700	21.63 (A), 78.37 (R)	$5.02\ 10^{-5}$	21.96 ± 0.15 (A), 24.66 ± 0.16 (R)	59.1 ± 2.0	15.6 ± 0.7	638.3	$7.76\ 10^{-8}$

A and R denote anatase and rutile, respectively.
[1] Calculated with Scherrer formula from XRD patterns.
[2] Average grain size measured by SEM.
[3] Average pore size measured by SEM.
[4] Average stress measured by profilometry.

The crystallite diameter of anatase and rutile was also estimated by using the Scherrer's formula (see details in Annex Section 4.6.1),[192] the size for each structure is reported in Table 4.4**.** The crystallite diameter of anatase does not change notably upon annealing, with 21.00, 17.11, 25.52 and 21.96 nm for T-AD, T-200, T-550 and T-700, respectively. In contrast, rutile crystallite exhibits minor changes by annealing at 200 °C, with relatively small crystallite diameters (6.95 and 5.53 nm, for T-AD and T-200). Moreover, a noticeable increase is observed at higher temperatures (13.55 and 24.66 nm,

for T-550 and T-700). These results demonstrate that both crystalline structures are present in the polycrystalline films where anatase is the predominant phase even when films are annealed to 200 and 550 °C.

In order to corroborate the presence of both structures in the films, the morphology was further analyzed by TEM for the as-deposited sample (T-AD). Figure 4.3a-b show a TEM images of the cross-section, the measured thickness of the film was 283.6 nm which is approximate to the specified value in the sputtering process (270 nm); it can be also be identified a first amorphous layer right on top of the silicon substrate with a thickness of 33.6 ± 3.3 nm, followed by an entirely crystallized region with a thickness of 253 ± 3.7 nm, composed of crystallites growing vertically.

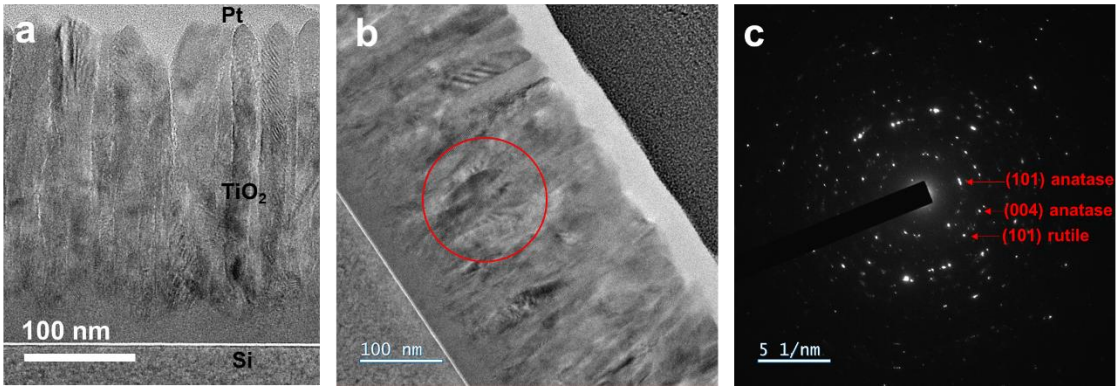

Figure 4.3 (a-b) TEM images of cross-section of TiO_2 film as-deposited (T-AD) and (b) SAED pattern taken from the selected area in (b). Planes indexed by radius of the rings.

Next the crystallography was analyzed, Figure 4.3c shows the selected area electron diffraction (SAED) of the circular area with a diameter of 100 nm (area delimited by the instrument) in the TEM image (Figure 4.3b). The pattern exhibits defined rings, indicating the polycrystalline structure of the bulk of the film. Additionally, the distance between the planes, known as d-spacing, was calculated from the inverse of the radius of the rings, giving a value of 3.57, 2.37 and 2.45 Å which are ascribed to the anatase planes (101) and (004), rutile (101) (noted in the SAED pattern), respectively.[193,194] Fast Fourier Transform patterns were also recorded from selected areas of 10 nm size, which corroborated the polycrystalline film structure, however is was not possible to identify the individual structural patterns (see Figure 4.22 in Annex Section 4.6.1).

Enlarged high-resolution TEM (HR-TEM) images of the crystallites are given in Figure 4.4, the polycrystalline growth can also be identified from the random orientation of several lattice planes. The d-spacing was also measured on HRTEM images, Figure 4.4a gives the planes indexed for anatase planes (004) and (101), with a d-spacing of 0.35 and 0.23 nm, and for rutile plane (101) a d-spacing of 0.24 nm, which agree with the measurements from the SAED pattern.

The boundaries between anatase and rutile were not observed, as no isolated regions of the structures were identified, this in accordance with the FFT patterns; and it can be ascribed also to the small crystallite size obtained from GI-XRD, of 20 and 7 nm for anatase and rutile (Table 4.4), and also to the high percent percentage of both structures (61 and 39%, for anatase and rutile). Moreover, the combination of both structures was confirmed by the presence of repeated wrinkles that were in several regions (in Figure 4.4a highlighted with arrows), these regular stripes are called Moiré fringes and are generated by the combination of lattice fringes from different planes with a degree of rotation, as shown in the inset, these curved fringes have been reported for anatase (101) and rutile (110) by Lee *et al.*[195]

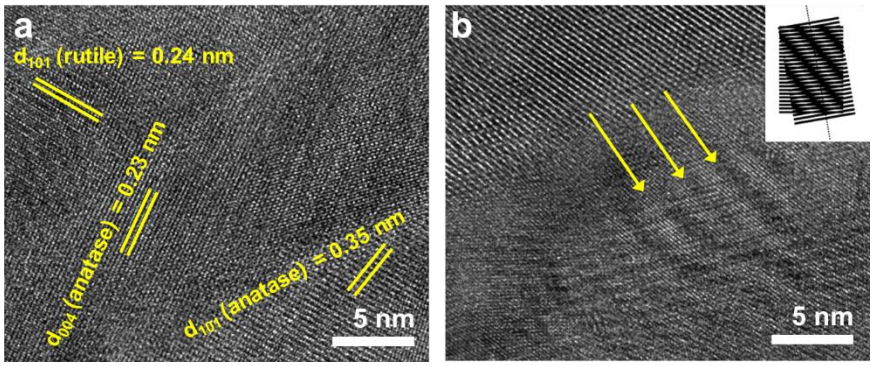

Figure 4.4 Cross-sectional HRTEM lattice images of TiO_2 film as-deposited (T-AD) (a) d-spacing planes indexed, and (b) Moiré fringes highlighted, inset: origin of repeated fringes.

The surface morphology was observed by SEM, Figure 4.5 shows the images of the images collected the four samples. In agreement with XRD and TEM results, the polycrystalline surface is composed of faceted grains with well-defined boundaries characteristic of the columnar morphology of TiO_2 deposited by PVD.[134] The average grain and pore size were measured, the values are plotted in Figure 4.5e-f (see the individual size distribution in the Annex Section 4.6.1). The average values are reported in Table 4.4 and Figure 4.5 as AGS and APS. Upon annealing at 550 °C the morphology remains almost unchanged, indicating a negligible effect of the temperature on the film morphology; yet, the grains and pores size decreases slightly, from ~32 to 29 nm and ~8 to 6 nm, for AGS and APS, respectively; leading to a more compact structure. However, by annealing at 700 °C, AGS increases notably to 59 nm. Likewise, APS doubles. Note that some big grains in T-700 show the remaining embossed grain boundaries of the individual merged grains.

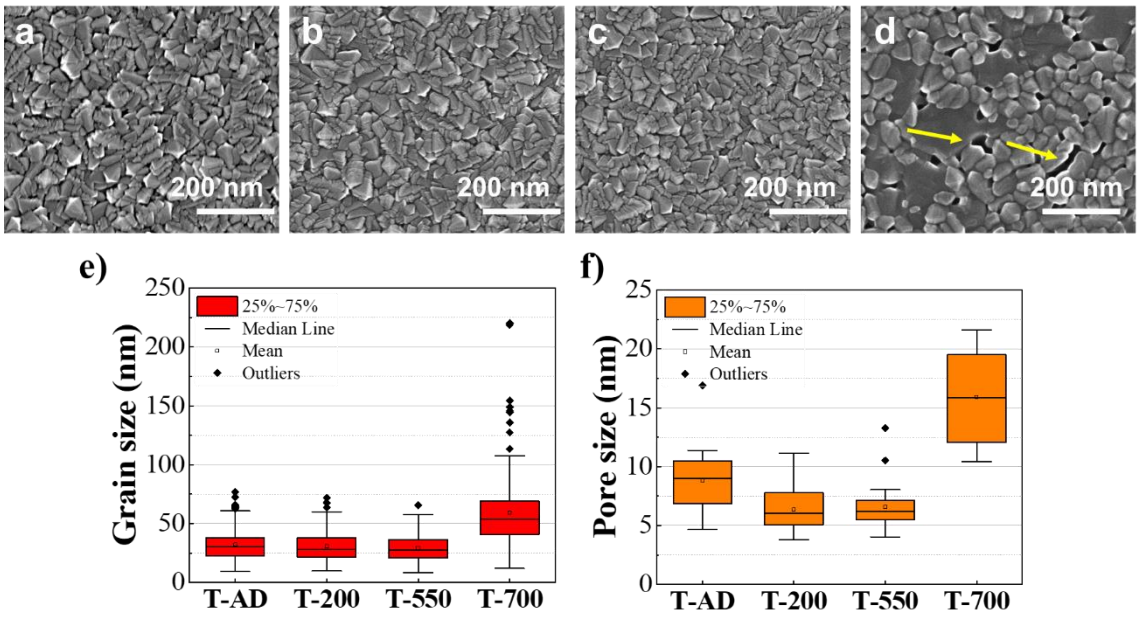

Figure 4.5 SEM images of TiO_2 thin films deposited by PVD on silicon (a) T-AD, (b) T-200, (c) T- 550 and (d) T-700 (the arrows indicate pores in the film). Comparative of size distribution for (e) grains and (f) pores obtained from SEM measurements.

The four samples were also analyzed by AFM, Figure 4.6 shows the mapping of the surface, note that samples T-550 and T-700 exhibit an increase in the grain's size, which is more notable for T-700 as in SEM. The surface roughness was also determined from AFM, from the mapped area of 1 μm^2, the values were 4.21, 4.21, 4.29 and 5.44 nm for T-AD, T-200, T-550 and T-700 samples, respectively. 2D and 3D images are shown in the Annex Section Figure 4.25.

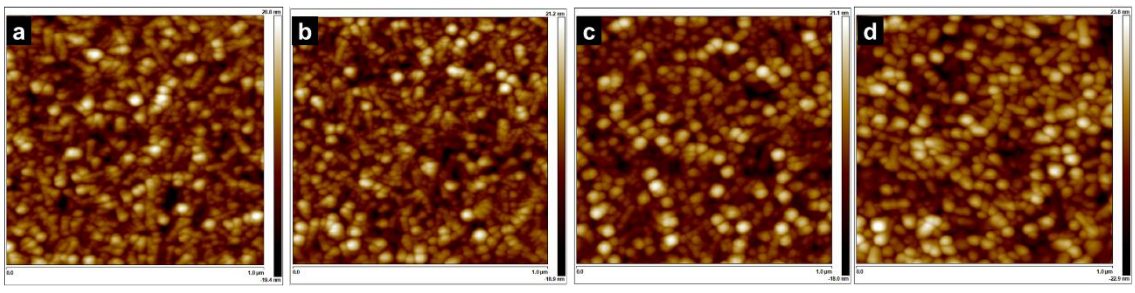

Figure 4.6 2D AFM images of TiO_2 films deposited on silicon (a) T-AD, (b) T-200, (c) T-550 and (d) T-700. Scan area 1 μm^2.

As the changes in the morphology affect the homogeneity of the film, the measurement of the induced stress can give more information about the annealing effect as the intrinsic stress generated has been proved to be correlated to several factors such

as pre-coalescence of grains, boundary formation, grain growth, thermal stress, or inherent to the energetic sputtering process. Hence the stress was measured by the wafer curvature method by profilometry, as it measures the bending that a stress film induces in an elastic surface, here being a whole silicon wafer. The average tensile stress values are reported in Table 4.4 (see more details of the results in Annex Section Table 4.7).

The reference sample T-AD exhibits a tensile stress of 191 MPa, which is ascribed to their compact film with defined grains. Next, for T-200 the tensile stress increases +124.5 MPa compared to T-AD. It has been reported that an increment in the tensile stress is observed for grain growth, as observed for T-500 and T-700, which will be discussed next. Yet T-200 exhibits a reduced grain and crystallites size of anatase and rutile compared to T-AD, and this could be related to the grain boundary formation, which increases as the grains are smaller. Hoffman *et al.*[196] proposed that formation of grain boundaries between neighboring islands could reduce their interfacial energy between them to reduce the number of broken bonds on the free surface of the isolated islands. Moreover, the XRD pattern of T-200 showed an increase intensity of the anatase (101) planes compare to that of T-AD, these planes have been reported to be thermodynamically stable due to a low surface energy.[175,197,198] Hence the Hoffman's mechanism can explain the reduction in the grain size for T-200, in which the boundaries increase in order to the reduce the interfacial energy among the grains, hence leading to the decrease of the grain's size.

Next, for the higher temperatures where the grains start to coalesce, the tensile stress continues to increase. This can be observed for sample T-550 where the tensile stress triples compared to T-AD and a notorious change in the crystallite size of both anatase and rutile is observed (+1.2 and +2.0 times, respectively). And also, for T-700 with a higher tensile stress value (+414.5 MPa times compared to T-AD), and the crystallite size of rutile increases as well (+3.6 times compared to that of T-AD). Moreover, according to Hoffman, the change of the grain's size in the bulk of the film leads to shrinking of the film's dimensions while it is constrained by the substrate leading to tensile stress. Hence, since the change in the tensile stress between T-550 and T-700 is rather small (+32.8 MPa), we could assume that the grain size of the bulk starts increasing from 550 °C, hence inducing a big change compared to the T-AD, and later at 700 °C, the grain growth also is produced on the surface leading to the incremental stress.

In summary, the morphological crystallographic analysis, indicate that up to 550 °C, anatase structure dominates the films, yet its crystallite diameter does not change significantly; whereas at 700 °C, a rich rutile phase is obtained, and the crystallite size also increased significantly. Moreover, these changes in morphology were confirmed to have an impact on the residual stress of the films, where in overall the grain size has a tensile contribution.

In the next subsections the photocatalytic activity determined by the H_2 production, chemical and optical characterization are presented and analyzed.

4.3.2 H_2 production

The evolution plots and normalized H_2 production rates are presented in Figure 4.7 and Table 4.5. Except for the sample annealed at 200 °C, with 2.0 µmol W^{-1} h^{-1}, all other films production rate is below 0.4 µmol W^{-1} h^{-1}. T-200 exhibits a 4.6 enhancement factor compared to the reference sample T-AD. This suggests a very narrow annealing pathway in order to optimize the TiO_2 water splitting performance. Note that at this stage, the linear increase of anatase structure with the temperature up to 550 °C does not coincide with the H_2 production enhancement.

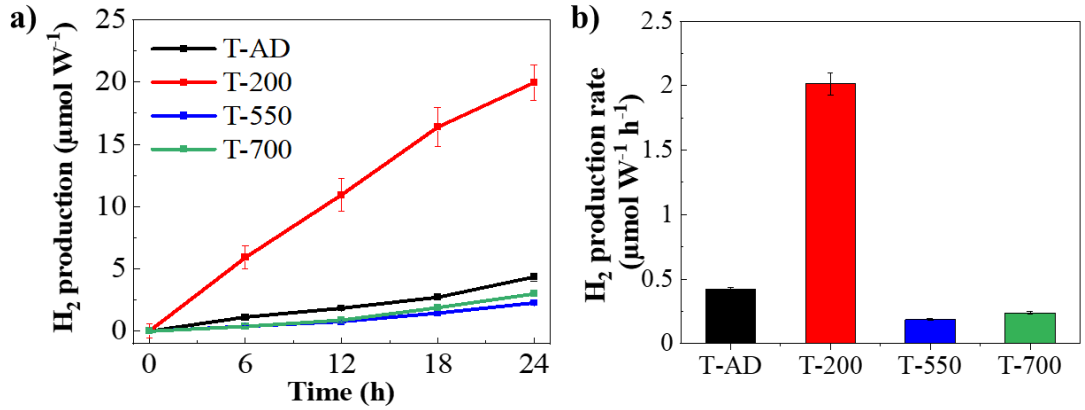

Figure 4.7 (a) H_2 production over 24 h and (b) normalized H_2 production rate of TiO_2 films deposited on silicon: as-deposited (T-AD) and annealed at 200 (T-200), 550 (T-550) and 700°C (T-700). Xenon lamp used for irradiation.

Table 4.5 H_2 production rate of TiO_2 annealed films.

Sample name	H_2 production rate (µmol W^{-1} h^{-1})	H_2 production rate enhancement Factor [1]
T-AD	0.42 ± 1.72 10^{-2}	1.00 ± 0.06
T-200	2.01 ± 8.45 10^{-2}	4.81 ± 0.28
T-550	0.19 ± 0.83 10^{-2}	0.44 ± 0.03
T-700	0.24 ± 1.10 10^{-2}	0.57 ± 0.03

[1] Obtained by comparison to reference sample (T-AD).

Importantly, this indicates that the nanoscale surface morphology and structural composition are not the determinant factors in maximizing the TiO_2 water splitting process, pointing to the potential role of the TiO_2 surface/subsurface chemical states. In the next sections, an in-depth study of the effect of the thermal annealing on the TiO_2

films will be conducted by chemical, optical and theoretical studies to shed light on its relationship with the photocatalytic activity results. In order to establish a hierarchy of the potential contributions, the TiO_2 stoichiometry (surface and bulk), defect presence, their electronic structure and chemical nature identification is analyzed next.

4.3.3 Chemical characterization

The chemical composition of the bulk film was determined by Electron Probe Microscopy (EMP) analysis, where the probe depth was set in a range of 228.1 to 256 nm from the surface to the bulk of the film. Results are in Annex Section 0 in Table 4.8. Hence, the O/Ti bulk atomic ratios were calculated (Table 4.6), as expected, the stoichiometry of the bulk is close to 2.0 following the TiO_2 chemical formula. Yet, upon annealing a film slightly richer in O is observed for T-200; while, O/Ti atomic ratio decreases in T-550 and T-700.

Table 4.6 Details of EMP measurements and XPS Ti 2p and O 1s spectra of TiO_2 thin films.

Samples	O / Ti bulk atomic ratio [1]	Ti^{3+} / Ti^{4+} ratio	O1s HE / LE [2] ratio	O / Ti surface atomic ratio [3]	VBE (eV) [4]
T-AD	$2.07 \pm 4.8\ 10^{-3}$	$3.04\ 10^{-2} \pm 2.1\ 10^{-6}$	$0.96 \pm 1.1\ 10^{-4}$	$1.92 \pm 2.0\ 10^{-3}$	$2.85 \pm 5.0\ 10^{-3}$
T-200	$2.08 \pm 3.5\ 10^{-3}$	$4.64\ 10^{-2} \pm 4.0\ 10^{-4}$	$1.14 \pm 1.1\ 10^{-4}$	$1.91 \pm 2.6\ 10^{-3}$	$2.69 \pm 5.0\ 10^{-3}$
T-550	$2.02 \pm 3.4\ 10^{-3}$	$2.77\ 10^{-2} \pm 2.5\ 10^{-4}$	$0.59 \pm 2.9\ 10^{-5}$	$1.80 \pm 2.2\ 10^{-3}$	$2.89 \pm 5.0\ 10^{-3}$
T-700	$2.02 \pm 3.2\ 10^{-3}$	$4.16\ 10^{-2} \pm 3.9\ 10^{-4}$	$0.62 \pm 3.0\ 10^{-5}$	$1.77 \pm 2.3\ 10^{-3}$	$2.58 \pm 5.0\ 10^{-3}$

[1] Calculated with electron microprobe analysis (EMP).

[2] High energy (HE) and low energy components (LE) of O 1s XPS spectra.

[3] Calculated with XPS spectroscopy.

[4] Relative to Fermi level.

XPS is a powerful method to study the surface chemical composition and the oxidation states of TiO_2, moreover is possible to estimate the VB position. Figure 4.8 shows the deconvoluted Ti 2p core-level XPS spectra. The two distinct peaks corresponding to Ti $2p_{3/2}$ and $2p_{1/2}$ are present in all the samples (see binding energies in Annex Section 0 Table 4.9). Both peaks are dominated by the Ti^{4+} oxidation state component, located at 459.16 and 464.90 eV in T-AD; with a minor presence of the reduced Ti^{3+} species component, located at 457.72 and 463.32 eV in T-AD. Upon annealing, a slight shift to lower energies of both Ti $2p_{2/3}$ and $2p_{1/2}$ peaks is observed. This has been associated to the presence of Vo defects.[137] To analyze the Ti^{4+} and Ti^{3+} components, gaussian deconvolution was carried out, Table 4.6 shows the Ti^{3+}/Ti^{4+} ratios for the samples where T-200 has the maximum number of Ti^{3+} species ($4.6\ 10^{-2}$ ratio), followed by T-700 ($4.2\ 10^{-2}$ ratio).

The presence of Ti^{3+} sites is commonly associated with the formation of Vo,[199,200] resulting in surface excess charge in the form of localized Ti^{3+} sites with an unpaired electron.[201] Jin *et al.*[202] showed that annealing in inert atmospheres can induce the removal of oxygen atoms creating a lone pair of electrons neighboring two Ti^{4+} sites, which are then oxidized to Ti^{3+}. This was also documented by Sajines *et al.*[203] who stated that by

removing an oxygen atom, two adjacent titanium atoms become fivefold coordinated. Therefore, the Vo is negatively charged in order to maintain the local charge neutrality. This charge is shared by the two adjacent titanium atoms changing its oxidation state from Ti^{4+} to Ti^{3+}. Note that Ti^{3+} species can also be attributed to Ti(i), as Finazzi *et. al.*[204] demonstrated when a Ti(i) is located in a host crystal, it spontaneously transforms into a Ti^{3+} ion with a single electron localized, surrounded by a polaronic distortion which favors its localization; whereas the remaining electrons of Ti^{3+} are distributed on the titanium ions of the lattice with a small exchange interaction. However, XPS characterization does not allow to clearly differentiate the origin of Ti^{3+} species (*i.e.*, due to Vo or Ti(i) formation). Yet, the increased intensity of Ti^{3+} species in T-200 and T-700 samples, denotes a higher density of defects which contrast with the structural characterization and photocatalytic activity, where both samples show remarkedly dissimilar characteristics.

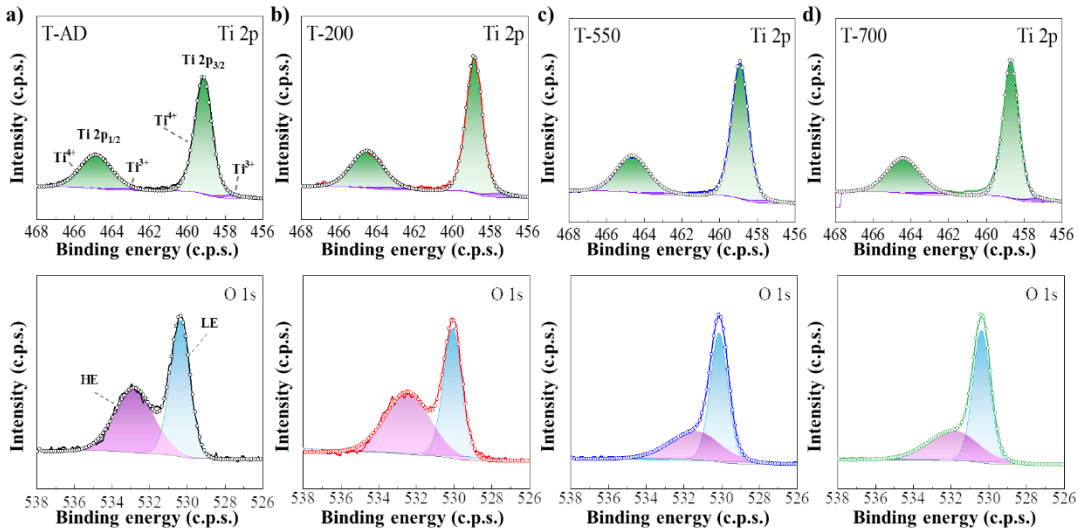

Figure 4.8 XPS core level spectra for Ti 2p (top) O 1s (bottom) of TiO_2 films (a) as-deposited (T-AD) and annealed at (b) 200 (T-200), (c) 550 (T-500) and (d) 700 °C (T-700).

The O 1s core-level XPS shown in Figure 4.8, was also deconvoluted; the asymmetrical spectra exhibited two defined components in all samples, the first at high energy (noted HE), commonly assigned to weakly adsorbed oxygen species in the form of hydroxyl groups (−OH) or bounded to carbon (−C) (as contaminants) and/or lattice oxygen atoms bounded to undercoordinated titanium atoms, making it an indirect signature of Vo.[137] And, the second component at lower energy (noted LE) is ascribed to the metal oxide bond, in this case the O^{-2} bound to Ti^{+4}. In T-AD these components are located at 532.8 and 530.3 eV, respectively.

A shift of the HE component (OH^-, O−C) to lower binding energies is seen for T-550 and T-700, decreasing from ~532.6 to ~531.6 eV; whereas the LE component (O−Ti)

remains at ~530 eV for all the samples. Components associated with −OH groups may also be influenced by defects created by thermal treatment.[203] Within the HE component, the OH^- species position has been located at 532.2 eV.[108,154] Note that surface bound OH^- radicals have been found to generate hole traps,[200] which will be discussed later in the paper. The HE/LE ratio (Table 4.6 and Table 4.9) points out a higher content of OH^- radicals for low temperatures samples, notably T-200, followed by T-AD, which decreases upon annealing above 550 °C. This suggests that the presence of such species in T-200 is related to intermediate states within the band gap possibly improving the charge transfer.

The surface stoichiometry was calculated from the XPS O1s and Ti2p core level spectra, from the O/Ti atomic ratio, in terms of the O^{2-}/Ti^{4+} atomic ratio using Equation 4.3. Where O^{2-} is the mathematical area of the O 1s LE component (I_O), and Ti^{4+} is the mathematical area of Ti $2p_{1/2}$ ($I_{Ti\ 2p_{\frac{1}{2}}}$) and Ti $2p_{2/3}$ ($I_{Ti\ 2p_{\frac{3}{2}}}$) peaks, as follows:

$$\frac{O}{Ti} = \frac{I_O}{I_{Ti\ 2p_{\frac{1}{2}}} + I_{Ti\ 2p_{\frac{3}{2}}}} \qquad \text{Equation 4.3}$$

The atomic ratios are reported in Table 4.6; however, contrary to the atomic ratio of the bulk obtained by EMP, all the samples exhibit a lower oxygen content on the surface, even below the expected $TiO_{2.0}$ stoichiometry. Interestingly, T-AD presents the most stoichiometric surface with $TiO_{1.92}$, which decreases consistently upon increasing the annealing temperature until $TiO_{1.77}$ for T-700.

In summary, thermal annealing above 550 °C affects notably the surface stoichiometry, exhibiting a highly reduced surface, whereas the bulk stoichiometry remains closest to $TiO_{2.0}$. This can be related to H_2 production results, where samples T-200 and T-AD exhibit the best performances. T-AD and T-200 samples present a similar stoichiometry: the surface composition is the closest to $TiO_{2.0}$, whereas the bulk presents a richer oxygen content, (higher atomic content compared to T-550 and T-700). Yet, T-200 sample which exhibits the best H_2 production yield, possesses a higher density of defects associated to Ti^{3+} and OH^- species, both pointing to the dominant role of surface defects. In order to investigate further on these defects in relation to the photocatalytic activity, optical characterization (UV-Vis and PL) and first principles calculations are discussed in the next sections.

4.3.4 Optical properties and electronic structure

UV-vis spectroscopy is a convenient method for analyzing the optical performance of thin semiconductor films and also offers a good estimation of the optical band gap, since it probes electronic transitions between the VB and the conduction band. The transmittance spectra reported in Figure 4.9a, was obtained for the TiO_2 films deposited on quartz substrates. The films exhibit the characteristic absorption of TiO_2 in the UV

region from 200 to ~350 nm. The fringes observed on the visible result from multiple interference of the light reflected from the optical interface air-thin film and thin-film-substrate.

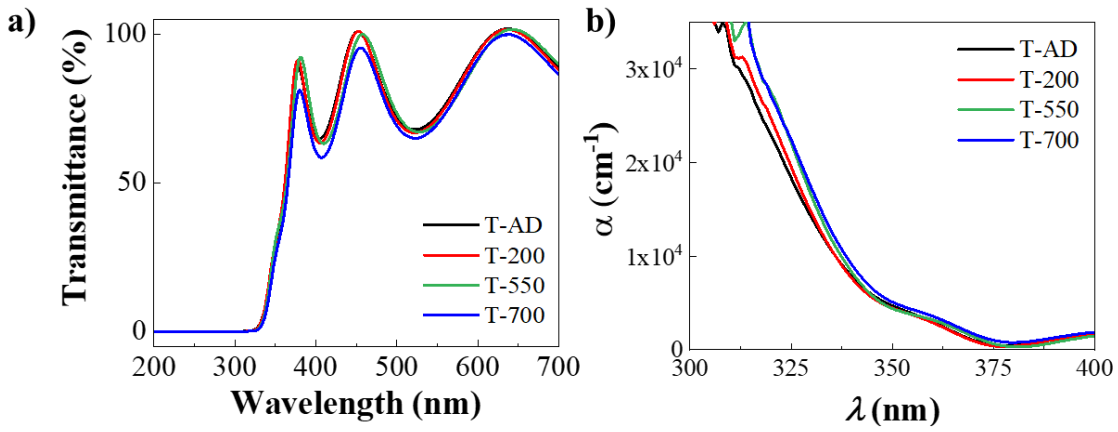

Figure 4.9 (a) UV-Vis transmittance spectra and (b) absorption coefficient spectra of TiO_2 films deposited on quartz (determined from transmittance spectra).

The absorption coefficient α, which determines how far light of a specific wavelength can penetrate in a material, was calculated from the transmittance spectra (see details in Annex Section 4.6.3). The absorption coefficient plot is shown in Figure 4.9b. The change of α on the range of 300 to 330 nm presents an increase of 1.07 times for T-200, and it reaches a highest value for T-550 and T-700 almost overlapping by 1.2 times. This means that light penetration increases with the annealing temperature. Furthermore, the absorption edge was estimated from the absorption coefficient plot (see calculation details and table of results in Annex Section 4.6.3). The absorption edge for T-AD film is 356.13 nm and upon annealing decreases to 354.02 and 354.07 nm for T-200 and T-550, respectively. At 700 °C, the absorption edge shifts back to higher wavelengths to 357.29 nm.

The study of the electronic properties can help to correlate the chemical species with defects on the band structure, hence the determination of the band gap, disorder, and VB and CB position, are discussed here. In order to have an approximation of the band gap, Tauc's plots were obtained from the transmittance spectrum to determine the optical band gap (E_{op}) the plots are given in Figure 4.10a. The E_{op} energies were obtained as detailed in the Annex Section 4.6.3, and the values range from 3.28 to 3.38 eV and are plotted in Figure 4.11**.** The indirect band gap values for TiO_2 reported in literature for anatase and rutile are 3.2 and 3.0 eV.[205] This could explain the higher E_{op} calculated for T-200 and T-550, since they have a higher content of anatase; consequently, T-700 has a lower E_{op} since the dominant phase is rutile.

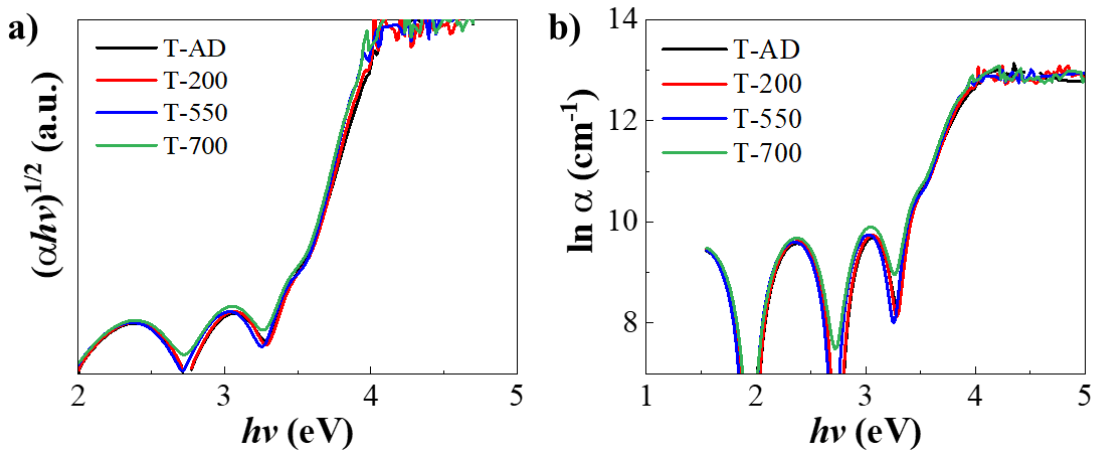

Figure 4.10 (a) Tauc's plots and (b) plot of ln α versus hv for the Urbach energy determination of TiO_2 films deposited by PVD on quartz. Determined from transmittance spectra.

Next, from the α, the Urbach energy (E_u) was determined, as is closely related to the structural disorder in the band gap since it is defined by the width of the band gap tails, which are formed due to the presence of defect states in the band gap.[206] The Eu was determined from the plot of *ln α* versus *hv* given in Figure 4.10b (see details in Annex 4.6.3), and the values which range from 165.07 to 205.80 meV are plotted in Figure 4.11.

By analyzing the band gap and the structural disorder, *i.e.*, E_{og} and E_u (Figure 4.11), a first change is seen for T-200 as the E_{og} is wider than that of T-AD by +0.03 eV. Also, the structure disorder is relatively high in T-200 (E_u = 189.24 meV), which suggests the presence of intermediate states in the band gap. Upon annealing at 550 °C the E_u is the lowest, but the E_{og} is the widest. These results contribute to elucidate the difference between these two samples, since both samples have a similar structure in terms of anatase to rutile ratio, and a similar morphology; yet the photocatalytic activity drops dramatically for T-550. This is also in coherence with XPS analysis, indicating that upon annealing at 200 °C, more defective sites are induced, that contribute somehow to the water splitting reaction.

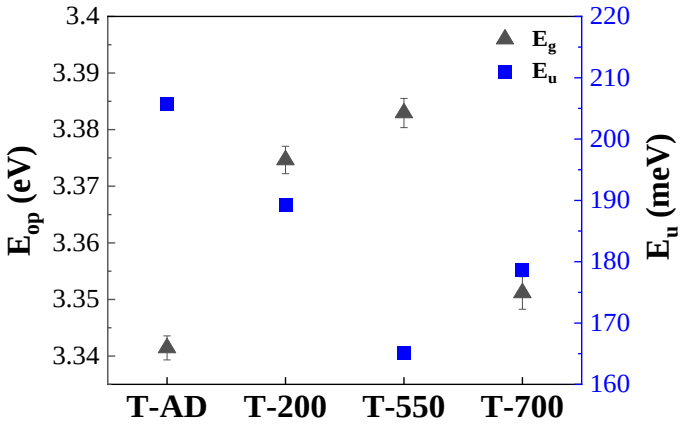

Figure 4.11 Variation of the optical band gap (E_{op}) and Urbach energy (E_u) of TiO_2 films deposited on quartz. Data obtained from transmittance spectra. E_u error bars range from 0.04 to 0.06 meV.

As mentioned in the previous section, the valence band edge (VBE) can be obtained with XPS from the low energy range of the spectrum. The VB spectra, shown in Figure 4.12, is located between 3 and 9 eV. The deconvolution shows two peaks, which correspond mainly to π (nonbonding) and σ (bonding) O 2p orbitals, located at higher and lower energies, respectively.[137] The VBE energy was obtained from the intersection of the leading edge to the base line of the spectrum,[207] the lines are drawn in the plots. The VBE values for T-AD, T-200, T-550 and T-700 were 2.85, 2.69, 2.89 and 2.58 eV; indicating the Fermi level (E_F) is closer to the conduction band. It has been reported that upon annealing the VB tends to shift towards lower energies,[176] nevertheless the VB increases for T-550. According to the E_{og} obtained by UV-Vis spectroscopy, the position of the edge of the conduction band (CBE) can be estimated by establishing the fermi level at zero ($E_F = 0$). Hence, the CBE was estimated at 0.49, 0.68, 0.49 and 0.77 eV above the E_F for T-AD, T-200, T-550 and T-700, respectively. These values are in coherence with the reported n-type nature of TiO_2.[176]

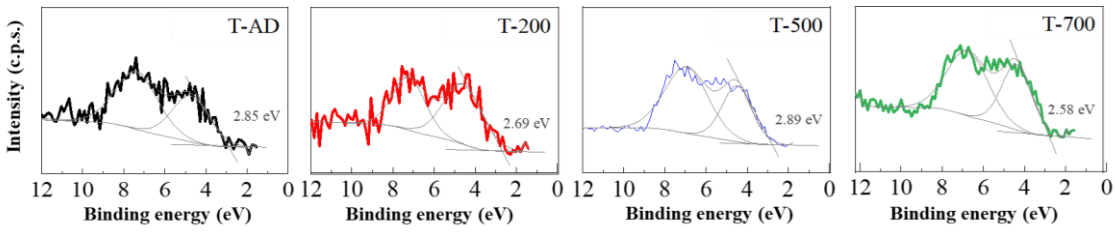

Figure 4.12 Calculated valence band edge of TiO_2 films as-deposited (T-AD) and annealed at 200 (T-200), 550 (T-500) and 700 °C (T-700). Lines indicate the intersection of the TiO_2 O2p orbital with the baseline. Valence band edge (VBE) noted.

In order to locate the intermediate states in the band gap, PL measurements were carried out. Figure 4.13 shows the spectra recorded in vacuum. Two clear signals are present in samples T-AD, T-200 and T-550, located at ~425 and ~530 nm, which hereafter will be named blue and green PL, respectively. Upon increasing the annealing temperature above 550 °C, the intensities decrease. At 700 °C the blue and green PL signals are completely quenched, and a minor band appears at 450 nm. The quenching is ascribed to the rich rutile composition of T-700, whose characteristic PL signals are in the near-IR region.[177]

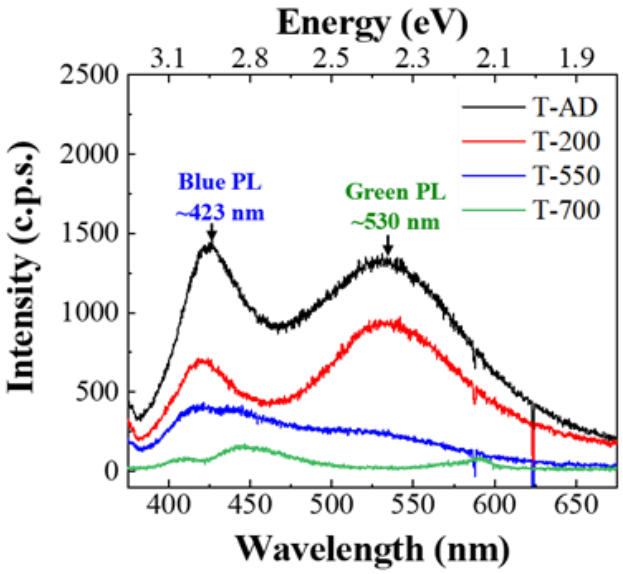

Figure 4.13 Photoluminescence spectra excited at 355 nm in vacuum of TiO_2 thin films. Blue and green PL bands signals assigned to the recombination of electrons in the CB with hole traps, and to deep trapped electrons with holes in the VB.

The blue PL is well defined in T-AD and T-200 compared to T-550 which features broader bands. Even though these samples and T-550 have a rich anatase composition, they exhibit a very different PL spectrum. Therefore, the blue and green PL signals cannot be mainly assigned to the anatase rich structure. Interestingly, the relative intensity of the blue to green PL bands is higher for T-AD and T-550, while for T-200 is the opposite. PL responses have been reported in a similar range, from 400 to 800 nm, but with one single broad component for anatase films annealed above 500 °C composed of particles[172] or deposited by pulsed laser deposition.[176] A PL feature similar to green PL centered at ~550 nm, was also obtained for sol-gel nanostructured anatase with a small portion of brookite; and it was assigned to Vo, which are ascribed to displacements of the oxygen atoms position in the bond lengths (Ti–O) creating a degree of structural disorder.[154] Furthermore, for anatase films, two defined PL bands have been reported: a green component at ~520 nm, assigned to recombination between electrons in the CB and deeply-trapped holes; and a red component at ~650 nm, assigned to the recombination

between holes in VB and deeply-trapped electrons. Yet for a mixed anatase/rutile phase, the second radiative transition was quenched.[188]

Moreover, the band to band transitions are not present in the PL spectra, since the signals are located at lower energy than the calculated E_{op} (< 3.34 eV in T-AD). Hence, the PL bands can be assigned to intermediate states located in the band gap. Based on the most recent studies,[172,176] the blue and green PL signals have been attributed to recombination with intermediate states, the schemes in Figure 4.14 illustrate the recombinations. The blue PL signal is attributed to the recombination of electrons in the CB with hole traps located in the band gap (Figure 4.14a); whereas, the green PL signal is attributed to the recombination of deep trapped electrons with holes in the VB (Figure 4.14b), this will be demonstrated next by steady-state PL measurements by exposing the samples to scavenging agents. Importantly, a direct correlation can be presumed between the enhanced photocatalytic activity, *i.e.*, the H_2 production of samples T-AD and T-200, and the presence of intermediate states associated with Ti^{3+} and OH^- species. Indeed, studies reported that the introduction of Ti^{3+} species accompanied by high Vo concentration leads to the formation of defect states with energies of 0.75 to 1.18 eV below the CB; hence, since these energies are closer to the CB, these defects states act as electron traps.[208] On the other hand, OH^- radicals are related to the presence trapped holes as mentioned previously.[200]

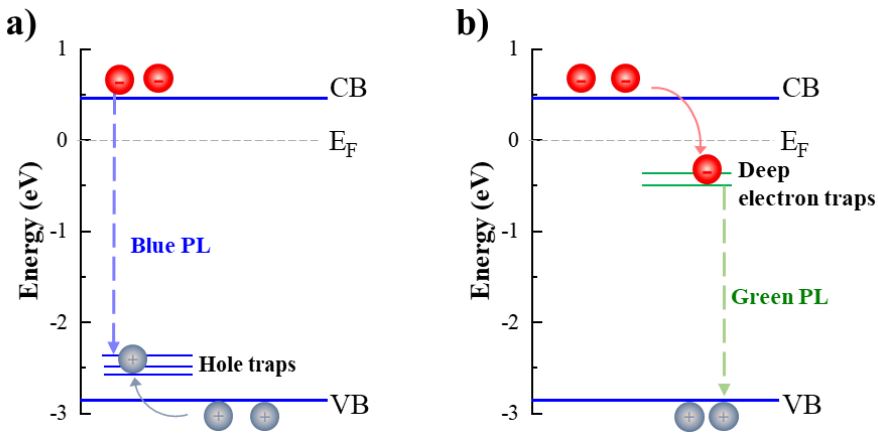

Figure 4.14 Scheme of the band gap structure of TiO2 film showing the PL radiative recombination (a) blue and (b) green. Conduction and valence band, with CBE and CVE values determined for as-deposited (T-AD) sample.

The next study will focus on T-AD and T-200 samples, which shown notable intensities of the PL bands and a high concentration of defects, notably Ti^{3+} and OH^- species. Yet, it is necessary to corroborate the assignation of the radiative recombination to specific electron or holes traps. This will be addressed in the following section by steady-state PL measurements conducted in different scavenging media (air and ethanol) in order to elucidate the quenching of specific transitions.

4.4 Correlation of band gap structure with surface defects

4.4.1 Identification of intermediate states with scavenging agents

Air and ethanol were used in steady-state PL measurements to elucidate the quenching of specific transitions. Figure 4.15 shows the interaction of the charges located either on the CB or VB, with the scavenging media. As oxygen present in air can scavenge electrons from the CB, electrons located in the CB are readily scavenged by the oxygen (Figure 4.15a), and hence they do not participate to the blue PL band. On the other hand, ethanol is known to be an efficient hole scavenger, hence the holes located on the VB do not contribute to the green PL band (Figure 4.15b). Therefore, if the intermediate states exist, depending on the scavenging media, only the photogenerated charges trapped at these localized states would contribute to the radiative recombination.

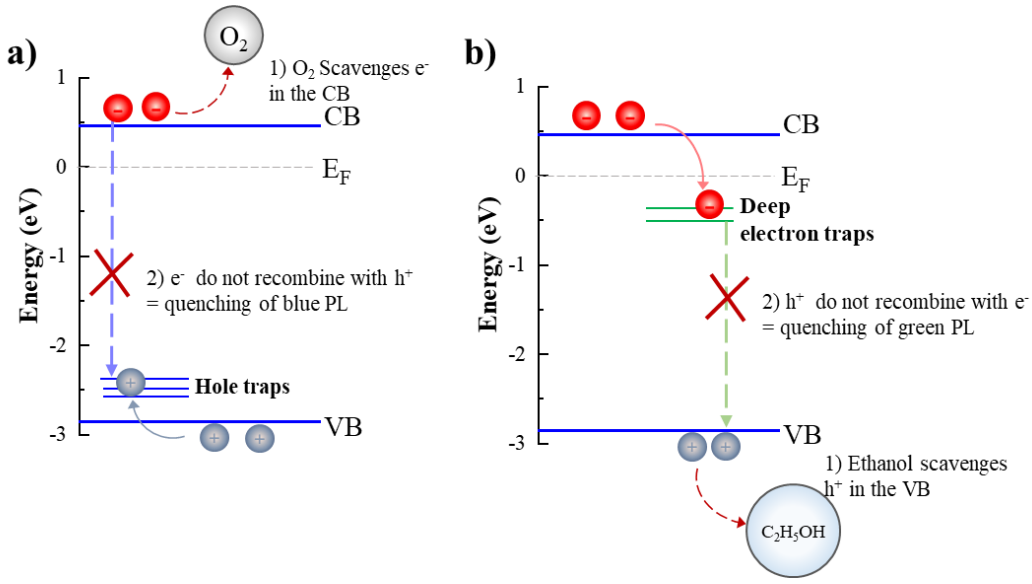

Figure 4.15 Schemes explaining the role of intermediate states in the PL radiative recombinations under (a) air and (b) ethanol.

Upon air exposure (Figure 4.16 blue plots), the blue PL intensity in T-AD sample is quenched from 1 to 0.5 a.u., meaning that oxygen scavenges the electrons on the CB, thus quenching the signal associated to recombination of CB electrons with hole traps, following the mechanism depicted in (Figure 4.15a). In contrast, the blue PL intensity of T-200 in air decreases just from 0.75 to 0.70 a.u, and it shifts to slightly higher wavelengths, meaning that a recombination within the band gap with a lower energy remains active under air. This could be attributed to the presence of shallow electron traps below the band gap where electrons are trapped after excitation before recombining with

the hole traps. Next, the green PL remains at the same wavelength upon air exposure in both samples, this is consistent with the presence of deep electron traps that prevent the electrons from being scavenged by oxygen, and subsequently undergo recombination with holes in the VB.

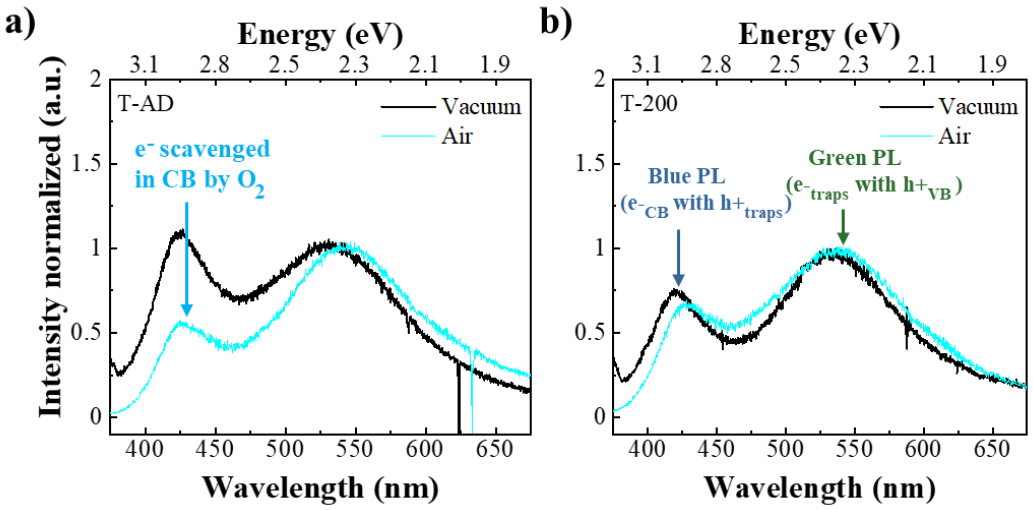

Figure 4.16 Photoluminescence spectra excited at 355 nm of TiO_2 thin films T-AD and T-200 in different media. Blue lines: air, and black: vacuum. Plots normalized to green PL band.

It is important to note that these intermediate traps can be classified as shallow or deep traps, depending on their relative position to the conduction or valence bands. Regarding electron traps, experiments have identified the presence of deep electron traps for intermediate states located around 0.75 – 1.00 eV below the CBE.[176] Therefore, for T-200, as the PL response under air indicates the presence of electron traps, by using the calculated E_{og} and the energy of the blue PL (~2.92 eV), the position of the electron traps is determined to be at -0.44 eV below the CB for T-200 (and -0.39 for T-AD), this corroborates the shallow electron traps in both samples. Such traps have been correlated to titanium ions in the lattice, which are characterized by a small interaction within the lattice, compared to Ti^{3+}; therefore do not affect greatly the total stability.[204] As explained in Chemical characterization Section, the titanium ions in the lattice are originated by the donated electrons of the reduced Ti^{3+} species induced by Ti(i). Regarding electron deep traps, these are determined as well using the energy of the green PL, which accounts for the recombination of trapped electrons with holes in the VB, being ~2.32 eV (530 nm) for both samples, hence the electron traps are calculated to be located at 1.0 eV below the CB, evidencing its role as deep electron traps.

Following with the PL steady state tests with ethanol, in order to avoid misinterpretation of the bands associated to the radiative recombination at the TiO_2/ethanol interface, PL spectra of ethanol was recorded in order to identify its

characteristic PL response (Figure 4.26**).** The spectra of the films in ethanol (Figure 4.17 green plots) are normalized with respect to the blue PL, as it is the most stable band and not affected by scavenging. As expected, the green PL of T-AD sample is quenched, since ethanol scavenges the holes in the VB, eliminating the possibility of radiative recombination with trapped electrons (mechanism explained in Figure 4.15b).

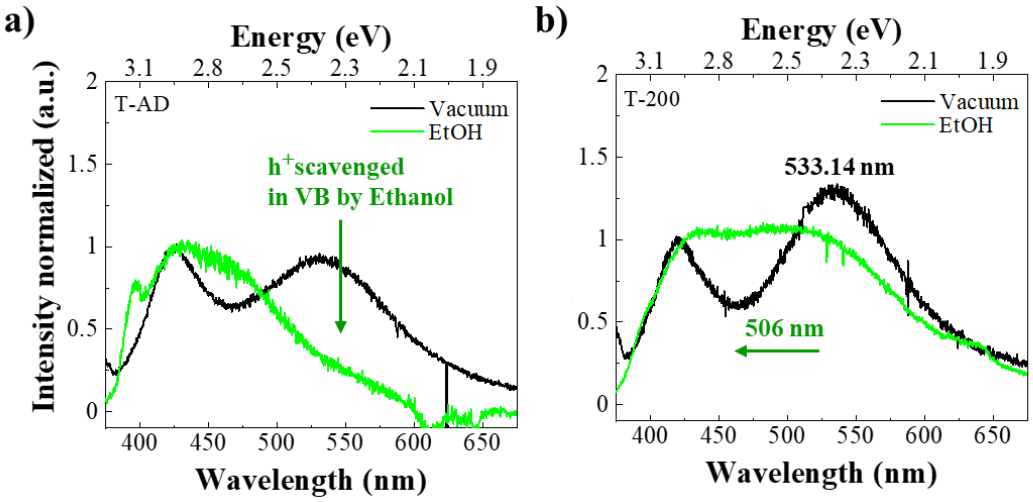

Figure 4.17 Photoluminescence spectra excited at 355 nm of TiO_2 thin films T-AD and T-200 in different media. Green lines: ethanol, and black: vacuum. Plots normalized to blue PL band.

In T-200, the green PL is mildly quenched by comparison with vacuum, this indicates that the holes in the VB are partially scavenged. This could be explained by the presence of holes in deep traps which cannot be scavenged by ethanol. The green PL signal shifts to higher energies (+0.12 eV), positioning the radiative emission at ~506 nm (hereafter named Cyan PL). After considering the recombination of holes positioned at these traps with electrons located in shallow traps below the CB, the Cyan PL is associated to deep hole traps. It has been reported that deep holes traps are chemically equivalent to surface-bound OH^- radicals which have been proposed as an important intermediate in the oxidation reaction of the water splitting process by various authors.[200] This agrees with the XPS results where the T-200 exhibits the highest HE/LE O 1s ratio, plus the position of the HE component is assigned to OH^- radicals. To shed more light in the identification of the defects that are associated with the observed radiative recombination and how these are generated, DFT calculations were performed on model surfaces screening the defects identified in the chemical characterization.

4.4.2 Density of states of defective anatase TiO_2

The Density of States (DOS) was based on a stoichiometric 1 × 3 anatase (101) slab (pristine slab) with specific defective model surfaces, as the anatase was proved to be the dominant phase in the TiO_2 thin films. The scheme and DOS of the slab anatase structure

are given in Figure 4.18. The DOS shows the CB and VB well defined on the right and left extremes, respectively, on the energy axis, where no intermediate states are observed in the band gap.

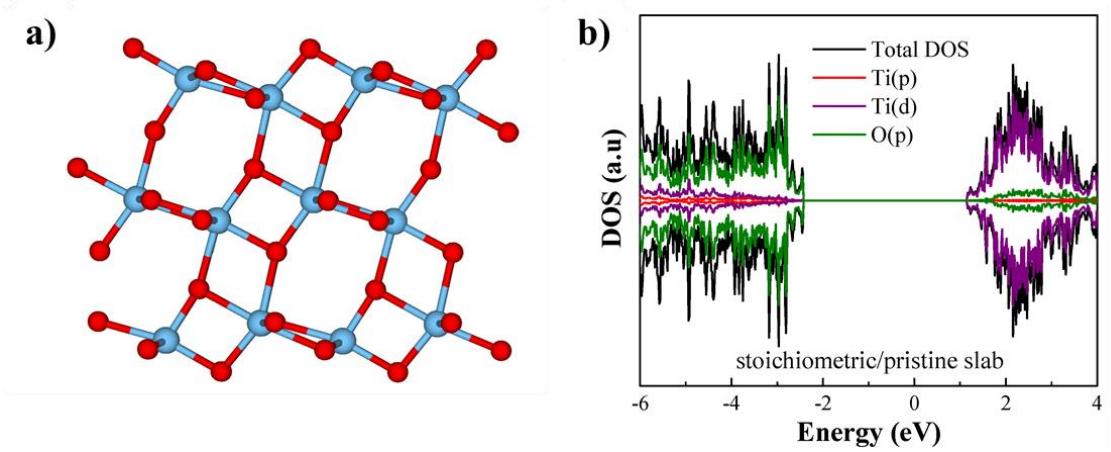

Figure 4.18 (a) Side view of stoichiometric 1 × 3 anatase (101) slab., red: titanium, cyan: oxygen atoms. (b) Density of states (DOS) plot of anatase (101) slab. Green area: valence band, purple: conduction band.

As mentioned in the previous sections, Ti^{3+} species are correlated to Ti^{3+} sites coupled to Vo (Ti^{3+}–Vo), but also to the presence of Ti(i). Figure 4.19a shows the slab and DOS of the anatase with a subsurface Ti(i), which leads to the formation of shallow states, and deep states, close to the CB, therefore deep and shallow electron traps (indicated with green arrows); this in coherence with the nature of Ti^{3+} species originated from the localization of Ti(i). In addition, the DOS of the slab with an Vo localized on Ti^{3+} atoms was also calculated (Figure 4.19b), the DOS also shows a prominent line positioned as a deep electron trap, corroborating the presence of Ti^{3+} sites neighboring Vo in addition to the creation of shallow electron states, as expected, since Ti(i) provide more electrons to the lattice than the Vo.[204]

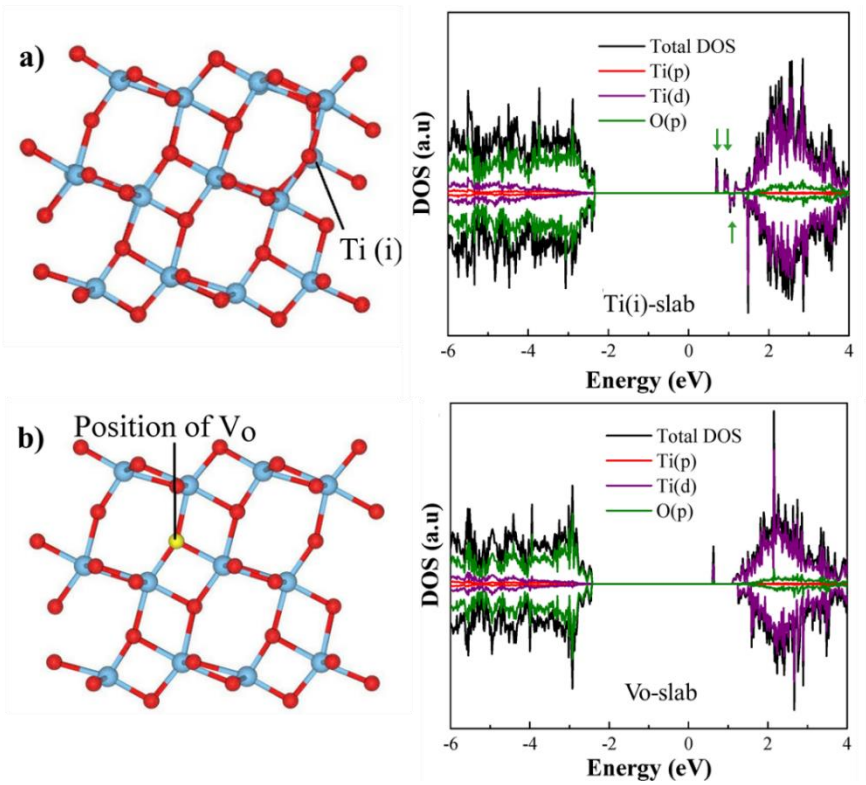

Figure 4.19 Stoichiometric 1 × 3 anatase (101) slab and DOS plots with (a) with a Ti interstitial (Ti(i)-slab) and (b) with an oxygen vacancy (Vo). Arrows indicate intermediate states.

Next, in the presence of adsorbed −OH groups on Ti^{3+} sites in Figure 4.20a, shallow hole traps are created close to the VBE, which confirms the assignment of the blue PL to shallow hole traps.[188] By combining both defects Ti(i)-slab with an adsorbed OH^- (Figure 4.20b), shallow and deep electron traps remain present (indicated with green arrows) and interestingly, the deep traps are more prominent; yet, the hole traps do not appear. In order to emulate the hole scavenging as in steady-state PL, Figure 4.20c shows the DOS with the T(i)-slab after dissociative chemisorption of ethanol onto TiO_2. Here, the appearance of hole traps is evident (blue arrows), meaning that in a defective structure with Ti(i), the traps near the VB relocate creating deep hole traps. The DOS results indicate a clear correlation between the creation of intermediate states and the presence of Ti(i), Vo localized on Ti^{3+} atoms, and OH^- adsorbates located on the surface and subsurface.

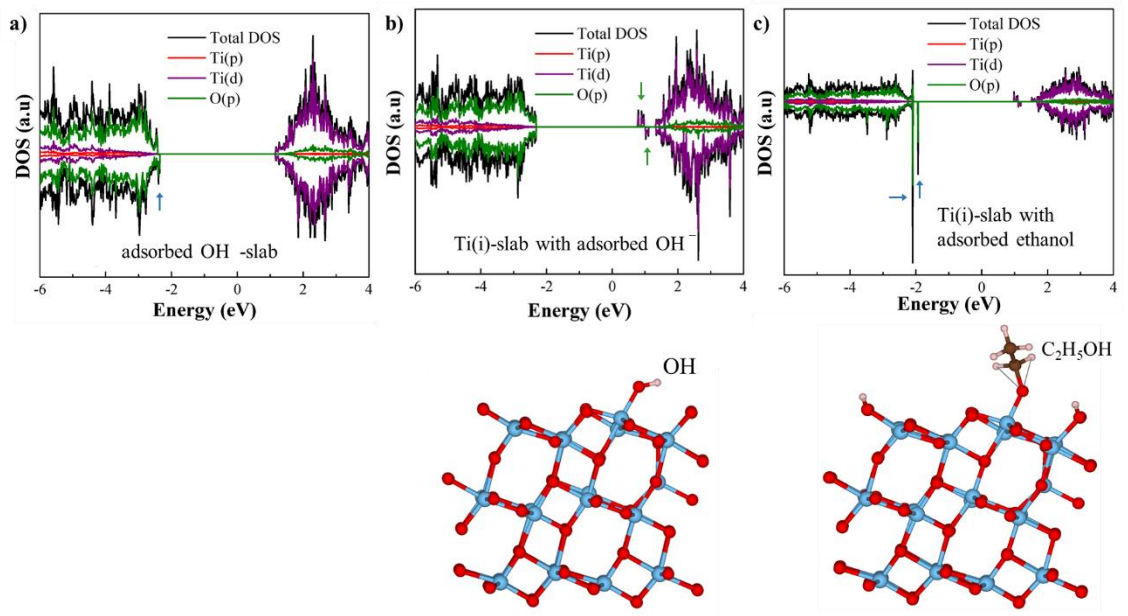

Figure 4.20 DOS plots and slabs of stoichiometric 1 × 3 anatase (101) slab with (a) an adsorbed OH^-, (b) a Ti(i)-slab with an adsorbed OH^- and (c) a Ti(i)-slab with an adsorbed ethanol molecule. Arrows indicate intermediate states, green: electron traps, blue: hole traps.

According to the XPS results, T-200 sample, followed by T-AD showed a higher concentration of such species, in the form of Ti^{3+} and OH^-, compared to the T-550 and T-700. The presence of shallow and deep electron traps is therefore associated to Ti(i) which transform to Ti^{3+} sites coupled to Vo (Ti^{3+}–Vo), both present in T-AD and T-200.

Hence, the increased Ti^{3+}/Ti^{4+} ratio for T-200 compared with T-AD, can now be attributed to a higher concentration of Ti(i). Furthermore, since the O1s HE component was already ascribed to OH^- species due to their shifted position (Section 3.3), both samples also possess a high content of adsorbed OH^-, where T-200 also exhibited an increased O1s HE/LE ratio, accounting for the presence of deep hole traps. In addition, OH^- bond species have been proposed as an important intermediate in photocatalytic oxidation processes,[200] promoting the charge transport. Both contributions (*i.e.*, Ti^{3+} and OH^-) lead to an extended region of electron deep traps in T-200. This is confirmed by the remarked quenching of the blue PL on air for T-AD (Figure 4.16), whereas in T-200, electrons are trapped in deep states avoiding scavenging by oxygen. Finally, the presence of deep hole traps is elucidated by the adsorption of ethanol on a slab with Ti(i) in the subsurface. Since T-200 possess a higher concentration of Ti(i), upon ethanol exposure, the holes located in shallow states are trapped in these deep traps and avoid scavenging by ethanol, this explains the broadening of the blue PL into the lower-wavelength (cyan PL) and the quenching of the green PL for T-AD, where such deep traps are not present. Figure 4.21 summarizes the main findings of this study just discussed, based on a mapping of states and radiative processes within the gap for T-AD and T-200.

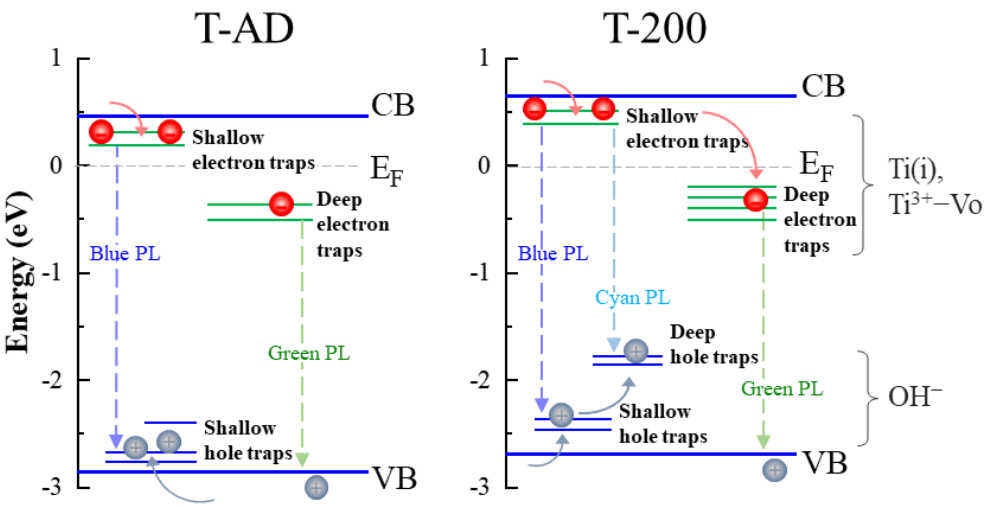

Figure 4.21 Band gap scheme with localized intermediate traps of electron and holes in TiO_2 thin films T-AD and T-200. PL radiative recombination are represented by dashed lines. Electron traps are created by the presence of Ti^{3+} species associated to Ti interstitials Ti(i) and oxygen vacancy Vo located on Ti^{3+} sites, whereas hole traps are associated to OH^- radicals adsorbed on the surface.

4.5 Conclusions

A study of local defects was conducted on planar TiO_2 films of 270 nm thickness, carried by varying the crystal structure ratio of anatase to rutile, and the presence of local defects on the surface of the photocatalysts by annealing treatments at 200, 550 and 700 °C in a N_2 atmosphere.

In the structural characterization, the crystallite size and structure composition of the polycrystalline film were determined through XRD studies. The anatase structure was dominant from the as-deposited sample and those annealed up to 550 °C, this inverted to rutile at 700 °C. TEM SAED corroborated the polycrystalline film composition, and by high-resolution imaging the interplanar atomic distance was measured where the characteristic distance for the anatase and rutile planes (101) and (101) of 0.35 and 0.24 nm, was corroborated. Further imaging also showed the superposition of anatase and rutile planes indicating the presence of Moiré fringes which originated from the combination of lattice fringes by different planes. SEM imaging showed a stable surface of the films up to 550 °C in terms of grain and pores size, where the average grain and pore size was ~30.5 and ~7.2 nm, and at 700 °C —on the rich rutile film— the grains and pores grow drastically to 59.1 and 15.6 nm. AFM tests showed minor changes in the roughness, with a value of ~4.2 nm up to 550 °C, which increased to 5.4 nm at 700 °C. Stress tests completed the structural characterization which revealed a notable

incremental tensile stress at 200 °C of 315.5 MPs, which increased and remained around ~622 MPa above 550 °C, these changes were ascribed to the grain growth with the temperature that undergo further coalescence. This leads to shrinking of the film's dimensions while it is constrained by the substrate.

Photocatalytic measurements revealed the best performance at 200 °C with and H_2 production rate of 2.0 μmol W^{-1} h^{-1} while other rates fell below 0.4 μmol W^{-1} h^{-1}, thus indicating the secondary role of the anatase mesoscale structure.

Chemical characterization determined the stoichiometry on the bulk and surface, where up to 200 °C samples presented a similar stoichiometry: the surface composition was the closest to stoichiometric $TiO_{2.0}$, whereas the bulk presents a richer oxygen content. XPS deconvolution determined shifts and higher intensities of the peaks corresponding to Ti^{3+} species, and OH^- radicals, where the former are being reported to be associated to oxygen vacancies (Vo) and Titanium interstitials (T(i)), this exposed the dominant role of surface defects on the H_2 production.

From optical characterization the electronic properties: optical band gap, Urbach energy were determined, these showed a structure disorder relatively high for the best photocatalyst (E_u = 189.24 meV), which suggests the presence of intermediate states in the band gap (E_{og} = 3.37 eV). Moreover, the positions of the CBE and VBE were estimated for the four different structures.

Next, defined PL bands were determined for the anatase rich films, where a high energy blue PL signal (423 nm) was attributed to the recombination of electrons in the CB with the hole traps located in the band gap, and lower energy (530 nm) green PL signal was attributed to the recombination of the deeply trapped electrons with holes in the VB. This was further corroborated by steady state PL measurements with scavenging agents. The rutile dominant film PL band was quenched on the measured spectral range (~350 to 700 nm), since rutile's characteristic PL signals are in the near IR region.

Ab initio calculations correlated the local defects to mid-gap traps, by obtaining the Density of States (DOS) of specific defective model surfaces: with a subsurface Ti(i) and Vo localized on Ti^{3+}. The presence of Ti^{3+} species on the surface was correlated to Ti(i) that generate shallow and deep electron traps, whereas OH^- adsorbates create deep hole traps, hence selectively enhancing the lifetime of the photogenerated charges. Also, the scavenging agent role was determined from the DOS of a defective Ti(i) slab after dissociative chemisorption of ethanol, leading to the relocation of hole traps farer from the VB, thus creating deep hole traps.

Overall, this study indicated the secondary role of the crystalline anatase structure on the H_2 production, whereas the presence of Vo and Ti(i) defects proved to impact the photocatalytic performance by creating deep intermediate gap states in the band gap that selectively extend the lifetime of the photogenerated charges.

4.6 Annex

4.6.1 Structural, morphological and mechanical properties

Crystallite diameter calculation with Scherrer's formula

The respective crystallite diameter for the anatase and rutile was estimated from the GI-XRD pattern using the Scherrer's formula (Equation 4.4), where *k* is the shape factor for Cu target (0.89), λ is the X-ray wavelength of the Cu Kα radiation (0.154 nm), θ is the Bragg's angle of anatase (101) and rutile (110) peaks, and β is the full-width half-maximum (FWHM) of the corresponding diffraction peak.[180]

$$D_{hkl} = \frac{k\,\lambda}{\beta_{hkl}\,cos\theta} \qquad \text{Equation 4.4}$$

TEM characterization

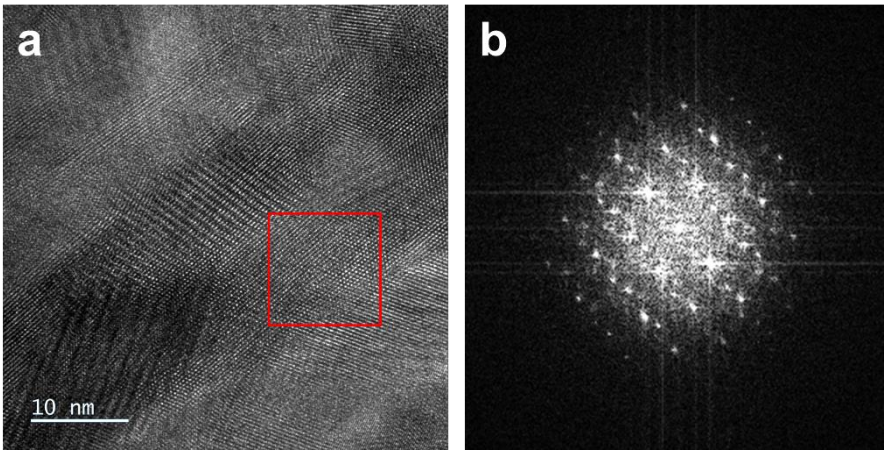

Figure 4.22 (a) TEM image of TiO_2 film as-deposited (T-AD). (b) FFT pattern recorded from the selected area in (a). The FFT pattern indicates the polycrystalline film structure; however, it not possible to obtain the specific pattern either for anatase or rutile due to the film characteristics. As the lamella is thick enough, TEM collects information from superposed both structures from the bulk film.

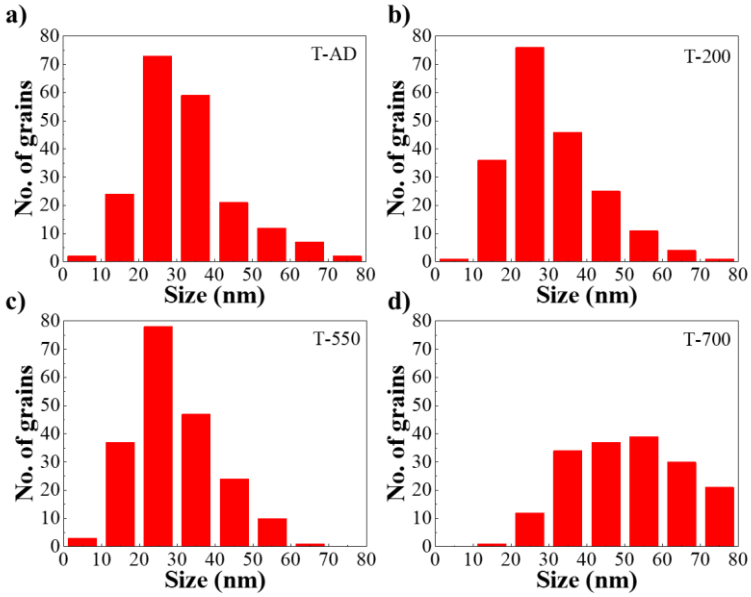

Figure 4.23 Grain size distribution obtained from SEM measurements for TiO_2 films on silicon (a) as-deposited, and annealed at (b) 200, (c) 550 and (d) 700°C.

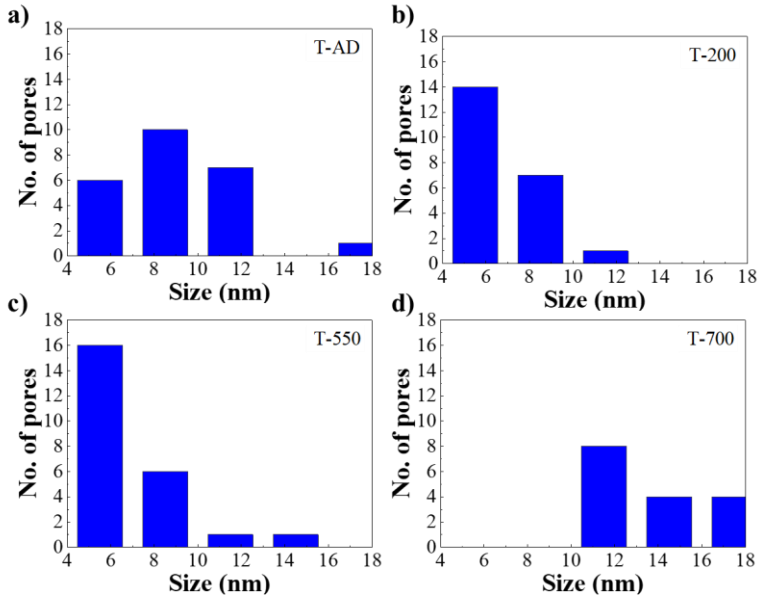

Figure 4.24 Pore size distribution obtained from SEM measurements for TiO_2 films on silicon (a) as-deposited, and annealed at (b) 200, (c) 550 and (d) 700°C.

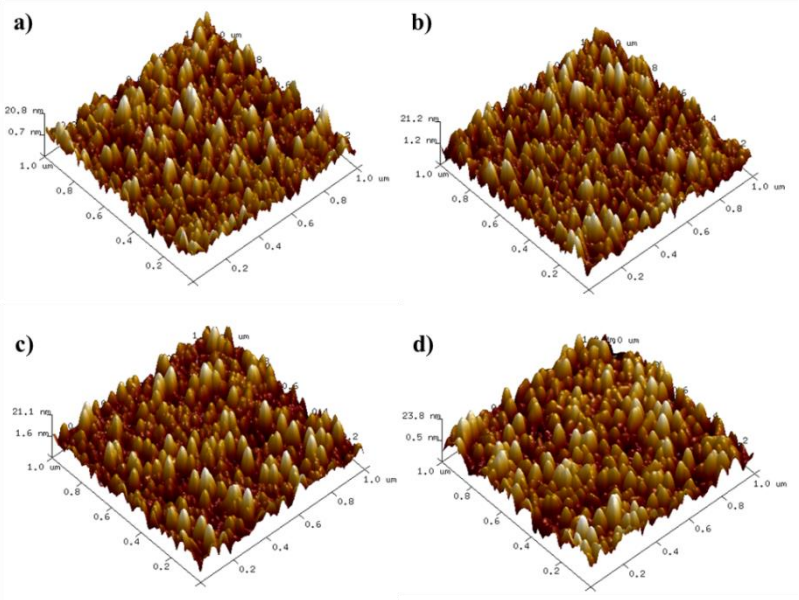

Figure 4.25 AFM 3D images of TiO_2 films deposited on silicon (a) as-deposited, and annealed at (b) 200, (c) 550 and (d) 700°C.

Table 4.7 Average residual tensile stress parameters of TiO_2 thin films.

Sample	Average Stress (MPa)	R (m)	Std. Dev. (MPa)
T-AD	191.00	160.8	$7.46\ 10^{-8}$
T-200	315.50	97.35	$7.78\ 10^{-8}$
T-550	605.50	50.72	$8.24\ 10^{-8}$
T-700	638.30	48.11	$7.76\ 10^{-8}$

4.6.2 Chemical characterization

Table 4.8 Electron Micron Probe (EMP) results of the bulk chemical composition for TiO_2 thin films on silicon.

T-AD		T-200		T-550		T-700	
O [1]	Ti [2]	O [1]	Ti [2]	O [1]	Ti [2]	O [1]	Ti [2]
66.99	32.74	67.13	32.38	66.39	32.93	66.54	32.80
67.16	32.63	67.18	32.33	66.45	32.93	66.36	32.95
67.48	32.26	67.04	32.46	66.58	32.76	66.42	32.87
67.28	32.45	66.97	32.57	66.36	32.90	66.40	32.93
67.39	32.36	67.13	32.39	66.16	33.17	66.54	32.73
67.26	32.47	67.24	32.28	66.39	32.87	66.42	32.88
67.10	32.63	67.26	32.22	66.28	33.05	66.39	32.92
67.28	32.47	67.31	32.25	66.50	32.88	66.48	32.85
67.42	32.30	67.24	32.32	66.37	32.99	66.31	32.98
67.31	32.46	67.27	32.23	66.40	32.95	66.15	33.10

[1] Oxygen atomic percentage.
[2] Titanium atomic percentage.

Table 4.9 Details of XPS spectra binding energies of TiO_2 thin films.

Samples	Ti^{4+} (2p 3/2)	Ti^{3+} (2p 3/2)	Ti^{4+} (2p 1/2)	Ti^{3+} (2p 1/2)	O1s HE	O1s LE
T-AD	459.16	457.72	464.86	463.32	532.82	530.37
T-200	458.85	457.51	464.53	463.11	532.46	530.06
T-550	458.94	457.46	464.63	463.06	531.39	530.12
T-700	458.71	457.23	464.41	462.93	531.88	530.36

Binding energy units in eV.

4.6.3 Optical properties

Calculation of absorption coefficient

The absorption coefficient α, was determined from the transmittance spectra, using the Equation 4.5, where T is the transmittance of the film at teach wavelength and d is the thickness of the film in cm.[209]

$$\alpha = \frac{\ln\left(\frac{1}{T}\right)}{d} \qquad \text{Equation 4.5}$$

Calculation of absorption edge

The absorption edge was estimated from the absorption coefficient plot (Figure 4.9b) in the exponential tail with values of $\alpha < 1\ 10^4$ cm^{-1} with a linear fitting where $R^2 = 0.99$.[163] The absorption edge values are reported in Table 4.10.

Table 4.10 Absorption edge of TiO_2 thin films determined from transmittance spectra.

Sample	Absorption edge (nm)
T-AD	356.13
T-200	354.02
T-550	354.07
T-700	357.29

Calculation of optical band gap

The optical band gap E_g was calculated from using the Equation 4.6, where hv is the photon energy (eV) and n is 2 for the indirect allowed transition in TiO_2. The Tauc's

plots were obtained by plotting $(\alpha hv)^{\frac{1}{2}}$ versus hv as shown in Figure 4.10a. The slope located at high energies was extrapolated by linear fit to the baseline ($R^2 = 0.99$).[163]

$$\alpha hv \propto \left(hv - E_g\right)^n \qquad \text{Equation 4.6}$$

Calculation of Urbach energy

The Urbach energy E_u is defined by Equation 4.7, where α is the absorption coefficient α and α_0 is a constant. [210]

$$\alpha = \alpha_0 \left(\frac{hv}{E_u}\right) \qquad \text{Equation 4.7}$$

Hence, E_u is calculated from the reciprocal of the slope in the linear portion of the plotting $\ln \alpha$ versus hv (Figure 4.10b), which in this case is located from ~3.43 to ~3.86 eV.

4.6.4 PL measurements

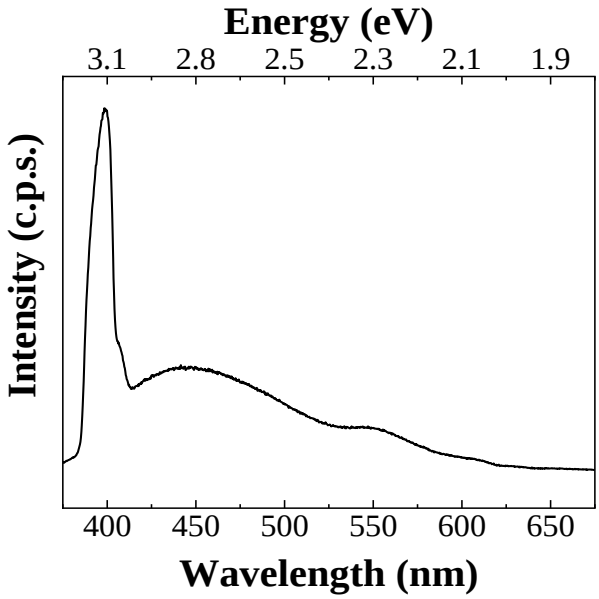

Figure 4.26 Photoluminescence spectra at room temperature of ethanol excited at 355 nm. Ethanol in quartz cell.

Conclusions

This work has been developed at the LAAS-CNRS as part of the NEO research team on the axe of nanoengineering of materials and catalysts for H_2 production.[211,212,212–243] This line investigates the fundamental mechanisms of the water splitting processes, the design of novel photocatalyst nanomaterials and their implementation in built-on devices.

Up to now, TiO_2 continues to be the most important photocatalyst due to its excellent advantages over other photocatalytic materials. Although great strides have been made over the last decades on the development of TiO_2 based nanomaterials, identify the factors that govern the kinetics of photocatalytic processes and understand the role that they play is fundamental to developed more efficient systems. Moreover, these contributions are necessary to respond the increasing global energetic demand that requires the clean, reliable, and sustainable energy sources.

Preliminary works conducted on the research group, highlighted the potential of TiO_2 based photocatalyst for H_2 production under UV and visible light irradiation. Based on the later, this work was focused on the study of the structural factors and mechanisms that lead the water splitting reactions and the exploration of technological solutions to yield the photocatalytic activity. The materials under consideration were sputter-deposited TiO_2 thin films which were further assembled in heterostructures with particles, constituting a fabrication process industrially feasible for the fast fabrication of robust photocatalysts. These photocatalysts were assembled and characterized at the laboratory, using the clean room facility for the principal fabrication, and the characterization was conducted as well at LAAS and complemented in collaboration with other institutions as the University of Texas at Dallas (UTD), the Laboratory of Physics and Chemistry of Nano-objects (LPCNO), the Castaing Center, the European Membrane Institute (IEM)

and the Microcharacterization Center Raimond Castaing. Hence these efforts constitute a contribution with fundamental and technological appealing solutions for applications in electronics, sensing elements to 3D photonics and metamaterials for light driven H_2 production.

This document has therefore addressed the integral study in four chapters as follows:

In Chapter 1 the motivations of the study were presented, followed by an introduction to the fundamentals of water splitting photocatalysts, which allowed us to outline the recent works on TiO_2-based nanostructures materials, in order to compare their photocatalytic activity and structural aspects that served to identify their limitations and advantages. Also, structural, chemical, and electronic properties of TiO_2 were introduced, as well the presence of third additives (*i.e.*, scavenger agents) that contribute to the water splitting reaction.

Chapter 2 presented a first study about the fabrication of hybrid nanostructures, where Au NPs were added by chemical photodeposition to TiO_2 films. Proving a positive impact on the photocatalyst spectral absorption to the visible, and the reduction of the charge recombination rate inherent to TiO_2. The H_2 evolution measured separately under UV, Vis and UV+Vis light, evidenced a synergy that overcomes the response of the heterostructures only under UV and Vis light, resulting in a 52-fold enhancement of the H_2 production compared to that of the bare TiO_2. Photocurrent and flat band potential tests shed light on the two main mechanisms: Schottky barrier and the plasmonic effects that improve the charge transport. Moreover, the systems where Au NPs are embedded in the films outperformed the one where NPs are positioned on the surface, which revealed that the water-splitting reaction occurs primarily on the TiO_2 surface rather than on the metal. Numeric simulations showed the formation of localized surface plasmon electric field that occurs at the metal/semiconductor. Which demonstrated the LSPR of the plasmonic NPs and highlighting the role of the crystallinity matrix in the vicinity of the particles and the surface stoichiometry.

In Chapter 3, the photocatalysts were fabricated with a 3D topology consisting of an array of microcavities. The fabrication of high-surface structures was performed by:

1) theorical design, where five patters were compared considering the aspect ratio and area enlargement factor (AEF), which was defined as the ratio between the 3D and 2D surfaces areas,
2) fabrication of robust and defect free silicon 3D scaffold with smooth surfaces, conducted by DRIE, this process was optimized for the specific pattern in order to have the control over the microstructure profile and height, which was needed to predict the AEF and crucial aspect ratio for the further deposition of the active materials;

3) deposition of compact TiO_2 active film on the 3D scaffolds; this and the previous step were greatly supported by SEM characterization as the morphology was a decisive point in the performance of the photocatalysts; and,
4) incorporation of Au and Pd NPs by chemical photodeposition and ALD, respectively, where Au and Pd exhibited a final 48- and 213-ehancement factor on the H_2 production rate.

The impact of the AEF on the H_2 production pointed out the film thickness and conformality as a limiting factor, since even the photocatalysts with an aspect ratio ≥ 0.7 showed a high thickness fluctuation. Nevertheless, the photocatalytic activity was drastically increased with a 13-enhancement factor when the surface was enlarged 3 times compared to the TiO_2 2D topology, combined with an average thickness of 447 nm. Moreover, the results established that enhancement could increase 6, 10 and 13 for AEF values of 3, 5 and 7 for a nearly conformal TiO_2 layer with a thickness of 200 to 300 nm. Electrochemical tests allowed the experimental measurement of the specific surface area (AEF_{EAS}) of the 3D photocatalysts, the AEF_{EAS} obtained was 1.5 to 2.0 times higher than the theorical value, thus proving the impact of the film microscopic morphology and the thickness fluctuation. Lastly, cycling tests showed a great stability over 45 h for the AEF 3 photocatalyst, with an average H_2 evolution of 89.18 μmol W^{-1} by the end of each 9 h cycle.

In Chapter 4, a final study of local defects was conducted on planar TiO_2 films of 270 nm thickness. The crystal structure ratio of anatase to rutile was verified, as well as the presence of local defects on the surface of the photocatalysts by annealing treatments from at 200, 550 and 700 °C in a N_2 atmosphere. Structural and morphological studies, chemical and optical-electronic spectroscopy techniques supported by photoluminescence measurements and DFT calculations were used for the determination of the band structure and its correlation to the photocatalytic activity of TiO_2 films prepared by sputtering and annealed at different temperatures from 200 °C to 700 °C in inert atmosphere. A narrow post annealed temperature window was observed at 200 °C, which enhances H_2 production (×5 compared to the as-deposited sample). The structural properties and SEM results pointed to a similar rich anatase phase for the films annealed up to 550 °C, pushing the structural aspects to a secondary role for what concerns H_2 production. Rather, we find that the higher photocatalytic TiO_2 performance correlate with the dual presence of OH^- and Ti^{3+}. While Ti^{3+} are commonly associated to oxygen vacancies in the literature, we demonstrate that Ti(i) are also a potential contributor to the Ti^{3+} PL signature. Furthermore, the chemically active role of ethanol was also highlighted, commonly used as a hole scavenger, it was demonstrated that upon adsorption and dissociation on the surface it induces deep hole traps. We believe that these results give new directions to optimize TiO_2 for achieving the water splitting mechanisms, and more generally to extend its photocatalytic activity.

5.1 Outlook and perspectives

In this thesis, significant progress has been made on the explanation of mechanisms that underly the water-splitting reaction by photocatalysis in TiO_2 films and hybrid TiO_2 -Au, and -Pd heterostructures. This work also constitutes a significant milestone on the technological development of a robust and simplified microfabrication process for large surface and compact photocatalysts. There is still, however, much important work to be done on both subjects.

Hence the points below discussed attractive directions for future research:

- Study of deposition of TiO_2 by ALD, as preliminary tests were performed on TiO_2 ALD films of 100 nm thickness, reaching an H_2 production rate close to that one of TiO_2 sputtered-deposited. Thus, deepen the study of the ALD parameters that influence the film structure, stoichiometry, and optical properties. This would represent a significant opportunity —as films are highly conformal— for the fabrication of silicon scaffolds with higher aspect ratio than those fabricated in this study (2.5 aspect ratio). The DRIE process with the microcavities pattern can be adapted to reach an AEF up to 34.
- Systematic investigation of the photo-oxidation of hole scavengers to determine their interaction with the photocatalysts surface. Study of different agents, *i.e.*, methanol, triethanolamine, ethylene glycol, etc. By varying the concentration and volume, determination of the origin of is dissociation on the surface (anatase/rutile mixed structures) and also the impact on the suppression of the recombination of charges.
- Study of the formation, relaxation, recombination, and transfer processes of photogenerated charge carriers. Time-resolved analytical tools can excite a sample by a laser pulse and measured the initial photon absorption in the time scale region from femtoseconds to microseconds. Some techniques are time resolved absorption spectroscopy (TAS), -microwave conductivity (TRMC), -optical second harmonic generation (SHG), etc.
- Prototyping of photocatalyst by the assembly of films in panels, rigorous and systematic testing will be needed to validate their stability.
- Continue the study of integration of Pd NPs (Chapter 3) by tuning of ALD parameters to variate the NPs size and areal density loading, and determine the influence on the charge generation and transport. Further assembly of film-NPs-films, or triptych heterostructures (*i.e.*, TiO_2 / Pd / Au) is suggested; as well as the exploration of other with materials such as g-C_3N_4, Pt, Ag, CdS and NiO.

References

[1] N.S. Lewis and D.G. Nocera, Proc. Natl. Acad. Sci. U.S.A. **103**, 15729 (2006).
[2] H. Tan, J. Li, M. He, J. Li, D. Zhi, F. Qin, and C. Zhang, Journal of Environmental Management **297**, 113382 (2021).
[3] N. Nakicenovic and R. Swart, *Special Report on Emissions Scenarios* ((Intergovernmental Panel on Climate Change, Washington, DC, 2000), pp. 48–55.
[4] J.C. Goldemberg, *UN World Energy Assessment Report: Energy and the Challenges of Sustainability* (United Nations, New York, 2003).
[5] H. Ritchie, M. Roser, and P. Rosado, Our World in Data (2020).
[6] L.D.D. Harvey, Climatic Change **82**, 1 (2007).
[7] Y. Tian and C.Y. Zhao, Applied Energy **104**, 538 (2013).
[8] U. Bossel, Proc. IEEE **94**, 1826 (2006).
[9] IEA, *Hydrogen* (IEA, Paris, 2021).
[10] J. Schneider, M. Matsuoka, M. Takeuchi, J. Zhang, Y. Horiuchi, M. Anpo, and D.W. Bahnemann, Chem. Rev. **114**, 9919 (2014).
[11] A. Fujishima and K. Honda, Nature **238**, 37 (1972).
[12] N. Armaroli and V. Balzani, Chem. Eur. J. **22**, 32 (2016).
[13] S. Chen, T. Takata, and K. Domen, Nat Rev Mater **2**, 17050 (2017).
[14] Q. Wang and K. Domen, Chem. Rev. **120**, 919 (2020).
[15] X. Li, Z. Wang, and L. Wang, Small Science **1**, 2000074 (2021).
[16] N. Fajrina and M. Tahir, International Journal of Hydrogen Energy **44**, 540 (2019).
[17] S.I. Kato and F. Masuo, Kogyo Kagaku Zasshi **67**, 1136 (1964).
[18] M. Ni, M.K.H. Leung, D.Y.C. Leung, and K. Sumathy, Renewable and Sustainable Energy Reviews **11**, 401 (2007).
[19] Pratibha, A. Kapoor, and J.K. Rajput, International Journal of Hydrogen Energy S0360319922013829 (2022).
[20] E. Hutter and J.H. Fendler, Adv. Mater. **16**, 1685 (2004).
[21] A. Rani, R. Reddy, U. Sharma, P. Mukherjee, P. Mishra, A. Kuila, L.C. Sim, and P. Saravanan, J Nanostruct Chem **8**, 255 (2018).
[22] S.C. Warren and E. Thimsen, Energy Environ. Sci. **5**, 5133 (2012).
[23] C. Gomes Silva, R. Juárez, T. Marino, R. Molinari, and H. García, J. Am. Chem. Soc. **133**, 595 (2011).
[24] M.R. Khan, T.W. Chuan, A. Yousuf, M.N.K. Chowdhury, and C.K. Cheng, Catal. Sci. Technol. **5**, 2522 (2015).
[25] J. Cure, K. Cocq, A. Nicollet, K. Tan, T. Hungria, S. Assie-Souleille, S. Vivies, L. Salvagnac, M. Quevedo-Lopez, V. Maraval, R. Chauvin, A. Estève, and C. Rossi, Adv. Sustainable Syst. **4**, 2000121 (2020).
[26] J. Cure, K. Cocq, A. Mlayah, T. Hungria, P. Alphonse, Y.J. Chabal, V. Maraval, R. Chauvin, A. Estève, and C. Rossi, International Journal of Hydrogen Energy **44**, 26347 (2019).
[27] J. Cure, H. Assi, K. Cocq, L. Marìn, K. Fajerwerg, P. Fau, E. Bêche, Y.J. Chabal, A. Estève, and C. Rossi, Langmuir **34**, 1932 (2018).
[28] I. Sue Wing, Resource and Energy Economics **30**, 21 (2008).
[29] Energy Information Administration, *Annual Energy Outlook* (US Dept. of Energy, Washington, DC, 2005).
[30] BP, *BP Statistical Review of World Energy 2021* (London, UK, 2021).
[31] M. Ball and M. Wietschel, International Journal of Hydrogen Energy **34**, 615 (2009).

[32] J.D. Holladay, J. Hu, D.L. King, and Y. Wang, Catalysis Today **139**, 244 (2009).
[33] J. Hansen, Scientific American **290**, 68 (2004).
[34] J.R. Petit, J. Jouzel, D. Raynaud, N.I. Barkov, J.-M. Barnola, I. Basile, M. Bender, J. Chappellaz, M. Davis, G. Delaygue, M. Delmotte, V.M. Kotlyakov, M. Legrand, V.Y. Lipenkov, C. Lorius, L. PÉpin, C. Ritz, E. Saltzman, and M. Stievenard, Nature **399**, 429 (1999).
[35] T.M.L. Wigley, R. Richels, and J.A. Edmonds, Nature **379**, 240 (1996).
[36] A.A. Lacis, G.A. Schmidt, D. Rind, and R.A. Ruedy, Science **330**, 356 (2010).
[37] U. Siegenthaler, T.F. Stocker, E. Monnin, D. Luthi, J. Schwander, B. Stauffer, and J. Jouzel, Science **310**, 1313 (2005).
[38] Intergovernmental Panel on Climate Change, *Climate Change 2001: Synthesis Report* (Intergovernmental Panel on Climate Change, Washington, DC, 2001).
[39] S. Sharma and S.K. Ghoshal, Renewable and Sustainable Energy Reviews **43**, 1151 (2015).
[40] R. Warren, W. Cramer, N. Nakicenovic, T. Wigley, and G. Yohe, Avoiding Dangerous Climate Change 93 (n.d.).
[41] J.B. Ruhl, Environmental Law **40**, 363 (2010).
[42] N.S. Lewis, G. Crabtree, A.J. Nozik, M.R. Wasielewski, P. Alivisatos, H. Kung, J. Tsao, E. Chandler, W. Walukiewicz, M. Spitler, R. Ellingson, R. Overend, J. Mazer, M. Gress, J. Horwitz, C. Ashton, B. Herndon, L. Shapard, and R.M. Nault, *Basic Research Needs for Solar Energy Utilization. Report of the Basic Energy Sciences Workshop on Solar Energy Utilization, April 18-21, 2005* (2005), p. 899136.
[43] J. Esch, Proc. IEEE **98**, 39 (2010).
[44] E. Kabir, P. Kumar, S. Kumar, A.A. Adelodun, and K.-H. Kim, Renewable and Sustainable Energy Reviews **82**, 894 (2018).
[45] A. Razmjoo, S. Mirjalili, M. Aliehyaei, P.A. Østergaard, A. Ahmadi, and M. Majidi Nezhad, Energy **248**, 123540 (2022).
[46] M. Jeong, I.W. Choi, E.M. Go, Y. Cho, M. Kim, B. Lee, S. Jeong, Y. Jo, H.W. Choi, J. Lee, J.-H. Bae, S.K. Kwak, D.S. Kim, and C. Yang, Science **369**, 1615 (2020).
[47] M. Green, E. Dunlop, J. Hohl-Ebinger, M. Yoshita, N. Kopidakis, and X. Hao, Prog Photovolt Res Appl **29**, 3 (2021).
[48] F.H. Alharbi and S. Kais, Renewable and Sustainable Energy Reviews **43**, 1073 (2015).
[49] T. Jafari, E. Moharreri, A. Amin, R. Miao, W. Song, and S. Suib, Molecules **21**, 900 (2016).
[50] M. Rakowski Dubois and D.L. Dubois, Acc. Chem. Res. **42**, 1974 (2009).
[51] J.H. Montoya, L.C. Seitz, P. Chakthranont, A. Vojvodic, T.F. Jaramillo, and J.K. Nørskov, Nature Mater **16**, 70 (2017).
[52] R.R. Ikreedeegh and M. Tahir, Journal of CO2 Utilization **43**, 101381 (2021).
[53] B.A. Rosen, A. Salehi-Khojin, M.R. Thorson, W. Zhu, D.T. Whipple, P.J.A. Kenis, and R.I. Masel, Science **334**, 643 (2011).
[54] A. Ursua, L.M. Gandia, and P. Sanchis, Proc. IEEE **100**, 410 (2012).
[55] A.M. Abdalla, S. Hossain, O.B. Nisfindy, A.T. Azad, M. Dawood, and A.K. Azad, Energy Conversion and Management **165**, 602 (2018).
[56] Y. Manoharan, S.E. Hosseini, B. Butler, H. Alzhahrani, B.T.F. Senior, T. Ashuri, and J. Krohn, Applied Sciences **9**, 2296 (2019).
[57] N.S. Bobbitt, J. Chen, and R.Q. Snurr, J. Phys. Chem. C **120**, 27328 (2016).
[58] W.C. Lattin and V.P. Utgikar, International Journal of Hydrogen Energy **32**, 3230 (2007).
[59] Gasunie Bbl. B.V., (2020).
[60] R. Farrauto, S. Hwang, L. Shore, W. Ruettinger, J. Lampert, T. Giroux, Y. Liu, and O. Ilinich, Annu. Rev. Mater. Res. **33**, 1 (2003).
[61] M. Fowles and M. Carlsson, Top Catal **64**, 856 (2021).
[62] R.R. Davda, J.W. Shabaker, G.W. Huber, R.D. Cortright, and J.A. Dumesic, Applied Catalysis B: Environmental **56**, 171 (2005).
[63] D. Levin, International Journal of Hydrogen Energy **29**, 173 (2004).
[64] S. Grigoriev, V. Porembsky, and V. Fateev, International Journal of Hydrogen Energy **31**, 171 (2006).
[65] J. Turner, G. Sverdrup, M.K. Mann, P.-C. Maness, B. Kroposki, M. Ghirardi, R.J. Evans, and D. Blake, Int. J. Energy Res. **32**, 379 (2008).
[66] National Research Council (U.S.), National Academy of Engineering, and National Academy of Sciences (U.S.), editors , *The Hydrogen Economy: Opportunities, Costs, Barriers, and R&D Needs* (National Academies Press, Washington, D.C, 2004).

[67] J.M. Norbeck and University of California, Riverside, editors , *Hydrogen Fuel for Surface Transportation* (Society of Automotive Engineers, Warrendale, Pa, 1996).
[68] C. Acar and I. Dincer, Int. J. Energy Res. **39**, 1757 (2015).
[69] H. Ahmad, S.K. Kamarudin, L.J. Minggu, and M. Kassim, Renewable and Sustainable Energy Reviews **43**, 599 (2015).
[70] V.N.H. Nguyen, R. Amal, and D. Beydoun, Chemical Engineering Science **58**, 4429 (2003).
[71] C. Mansilla, C. Bourasseau, C. Cany, B. Guinot, A. Le Duigou, and P. Lucchese, in *Hydrogen Supply Chains* (Elsevier, 2018), pp. 271–292.
[72] IEA, *Global Hydrogen Review 2021* (IEA, Paris, 2021).
[73] M.Z. Rahman, K. Davey, and C.B. Mullins, Adv. Sci. **5**, 1800820 (2018).
[74] J. Joy, J. Mathew, and S.C. George, International Journal of Hydrogen Energy **43**, 4804 (2018).
[75] P. Dias and A. Mendes, in *Encyclopedia of Sustainability Science and Technology*, edited by R.A. Meyers (Springer New York, New York, NY, 2018), pp. 1–52.
[76] P. Dias, T. Lopes, L. Andrade, and A. Mendes, Journal of Power Sources **272**, 567 (2014).
[77] P. Dias, T. Lopes, L. Meda, L. Andrade, and A. Mendes, Phys. Chem. Chem. Phys. **18**, 5232 (2016).
[78] J. Park, P.R. Deshmukh, Y. Sohn, and W.G. Shin, Journal of Alloys and Compounds **787**, 1310 (2019).
[79] W. Shi and N. Chopra, Nanomaterials and Energy **2**, 158 (2013).
[80] I.S. Cho, Z. Chen, A.J. Forman, D.R. Kim, P.M. Rao, T.F. Jaramillo, and X. Zheng, Nano Lett. **11**, 4978 (2011).
[81] S. Tabata, H. Nishida, Y. Masaki, and K. Tabata, Catal Lett **34**, 245 (1995).
[82] D. Jose, C.M. Sorensen, S.S. Rayalu, K.M. Shrestha, and K.J. Klabunde, International Journal of Photoenergy **2013**, 1 (2013).
[83] N.L. Reddy, M. Karthik, and M.V. Shankar, Adv Porous Mat **5**, 122 (2017).
[84] A.G. Dosado, W.-T. Chen, A. Chan, D. Sun-Waterhouse, and G.I.N. Waterhouse, Journal of Catalysis **330**, 238 (2015).
[85] Z.H.N.A. Azri, V. Jovic, W.T. Chen, D.S. Waterhouse, J.B. Metson, and G.I.N. Waterhouse, IJNT **11**, 695 (2014).
[86] R. Camposeco, S. Castillo, V. Rodriguez-González, M. Hinojosa-Reyes, M.I. Medina-Álvares, and I. Mejía-Centeno, Journal of Photochemistry and Photobiology A: Chemistry **353**, 114 (2018).
[87] J. Huang, G. Li, Z. Zhou, Y. Jiang, Q. Hu, C. Xue, and W. Guo, Chemical Engineering Journal **337**, 282 (2018).
[88] P.A. Mangrulkar, V. Polshettiwar, N.K. Labhsetwar, R.S. Varma, and S.S. Rayalu, Nanoscale **4**, 5202 (2012).
[89] Y. Noda, B. Lee, K. Domen, and J.N. Kondo, Chem. Mater. **20**, 5361 (2008).
[90] Y. Sakata, Y. Matsuda, T. Yanagida, K. Hirata, H. Imamura, and K. Teramura, Catal Lett **125**, 22 (2008).
[91] Y. Sakata, Y. Miyoshi, T. Maeda, K. Ishikiriyama, Y. Yamazaki, H. Imamura, Y. Ham, T. Hisatomi, J. Kubota, A. Yamakata, and K. Domen, Applied Catalysis A: General **521**, 227 (2016).
[92] J. Kim, D.W. Hwang, H.G. Kim, S.W. Bae, J.S. Lee, W. Li, and S.H. Oh, Top Catal **35**, 295 (2005).
[93] A. Kudo and H. Kato, Chemical Physics Letters **331**, 373 (2000).
[94] A. Iwase, H. Kato, and A. Kudo, ChemSusChem **2**, 873 (2009).
[95] G.N. Schrauzer and T.D. Guth, J. Am. Chem. Soc. **99**, 7189 (1977).
[96] P.S. Basavarajappa, S.B. Patil, N. Ganganagappa, K.R. Reddy, A.V. Raghu, and Ch.V. Reddy, International Journal of Hydrogen Energy **45**, 7764 (2020).
[97] D.A.H. Hanaor and C.C. Sorrell, J Mater Sci **46**, 855 (2011).
[98] M. Landmann, E. Rauls, and W.G. Schmidt, J. Phys.: Condens. Matter **24**, 195503 (2012).
[99] U. Diebold, Applied Physics A: Materials Science & Processing **76**, 681 (2003).
[100] O. Carp, Progress in Solid State Chemistry **32**, 33 (2004).
[101] F. Labat, P. Baranek, and C. Adamo, J. Chem. Theory Comput. **4**, 341 (2008).
[102] Y. Yu, *Sodium-Ion Batteries: Energy Storage Materials and Technologies*, 1st ed. (Wiley, 2022).
[103] D. Li, S. Dai, A. Goullet, M. Carette, A. Granier, and J.P. Landesman, J Mater Sci: Mater Electron **29**, 13254 (2018).
[104] D. Zhang and S. Dong, Progress in Natural Science: Materials International **29**, 277 (2019).
[105] M. Mohamad, B. Ul Haq, R. Ahmed, A. Shaari, N. Ali, and R. Hussain, Materials Science in Semiconductor Processing **31**, 405 (2015).
[106] E. Rosencher and B. Vinter, *Optoelectronics* (Cambridge University Press, Cambridge, UK; New York, NY, 2002).
[107] J. Zhang, P. Zhou, J. Liu, and J. Yu, Phys. Chem. Chem. Phys. **16**, 20382 (2014).

[108] T. Cottre, M. Fingerle, M. Kranz, T. Mayer, B. Kaiser, and W. Jaegermann, Adv. Mater. Interfaces **8**, 2002257 (2021).
[109] S. Gong and B.-G. Liu, Chinese Phys. B **21**, 057104 (2012).
[110] D. Reyes-Coronado, G. Rodríguez-Gattorno, M.E. Espinosa-Pesqueira, C. Cab, R. de Coss, and G. Oskam, Nanotechnology **19**, 145605 (2008).
[111] B. Liu, X. Zhao, J. Yu, I.P. Parkin, A. Fujishima, and K. Nakata, Journal of Photochemistry and Photobiology C: Photochemistry Reviews **39**, 1 (2019).
[112] Q. Guo, Z. Ma, C. Zhou, Z. Ren, and X. Yang, Chem. Rev. **119**, 11020 (2019).
[113] A. Smieszek, A. Seweryn, K. Marcinkowska, M. Sikora, K. Lawniczak-Jablonska, Bartlomiej.S. Witkowski, P. Kuzmiuk, M. Godlewski, and K. Marycz, Materials **13**, 4817 (2020).
[114] E.G. Villabona-Leal, A.G. Escobar-Villanueva, V.M. Ovando-Medina, E.B. Pérez-Pérez, P.E. Díaz-Flores, A. Romero-Galarza, and A. Marquez-Herrera, J Mater Sci: Mater Electron **31**, 12178 (2020).
[115] S. Kalaiarasi and M. Jose, Appl. Phys. A **124**, 589 (2018).
[116] Z. Fan, F. Meng, M. Zhang, Z. Wu, Z. Sun, and A. Li, Applied Surface Science **360**, 298 (2016).
[117] S. Tang, J. Wang, Q. Zhu, Y. Chen, and X. Li, ACS Appl. Mater. Interfaces **6**, 17157 (2014).
[118] L. Meng, H. Chen, C. Li, and M.P. dos Santos, Front. Mater. **1**, (2014).
[119] D. Fang, Z. Luo, K. Huang, and D.C. Lagoudas, Applied Surface Science **257**, 6451 (2011).
[120] X. Chen, S. Shen, L. Guo, and S.S. Mao, Chem. Rev. **110**, 6503 (2010).
[121] M. Yasuda, T. Matsumoto, and T. Yamashita, Renewable and Sustainable Energy Reviews **81**, 1627 (2018).
[122] A.K.R. Police, S. Basavaraju, D.K. Valluri, S. Muthukonda V., S. Machiraju, and J.S. Lee, Chemical Engineering Journal **247**, 152 (2014).
[123] K. Hashimoto, T. Kawai, and T. Sakata, J. Phys. Chem. **88**, 4083 (1984).
[124] X. Zhang, H. Liu, W. Li, G. Cui, H. Xu, K. Han, and Q. Long, Catal Lett **125**, 371 (2008).
[125] T. Ma, M. Akiyama, E. Abe, and I. Imai, Nano Lett. **5**, 2543 (2005).
[126] A.A. Ismail and D.W. Bahnemann, Green Chem. **13**, 428 (2011).
[127] J.T. Carneiro, C.-C. Yang, J.A. Moma, J.A. Moulijn, and G. Mul, Catal Lett **129**, 12 (2009).
[128] R.T. Tung, Applied Physics Reviews **1**, 011304 (2014).
[129] V. Kumaravel, S. Mathew, J. Bartlett, and S.C. Pillai, Applied Catalysis B: Environmental **244**, 1021 (2019).
[130] S. Veziroglu, M. Ullrich, M. Hussain, J. Drewes, J. Shondo, T. Strunskus, J. Adam, F. Faupel, and O.C. Aktas, Surface and Coatings Technology **389**, 125613 (2020).
[131] J. Yan, G. Wu, N. Guan, and L. Li, Chem. Commun. **49**, 11767 (2013).
[132] S. Wang, Y. Gao, S. Miao, T. Liu, L. Mu, R. Li, F. Fan, and C. Li, J. Am. Chem. Soc. **139**, 11771 (2017).
[133] J. Huang, W. Niu, C. Li, C. Tan, P. Yin, H. Cheng, Z. Hu, N. Yang, Q. He, G.-H. Nam, and H. Zhang, ACS Materials Lett. **2**, 409 (2020).
[134] M.-I. Mendoza-Diaz, J. Cure, M.D. Rouhani, K. Tan, S.-G. Patnaik, D. Pech, M. Quevedo-Lopez, T. Hungria, C. Rossi, and A. Estève, J. Phys. Chem. C **124**, 25421 (2020).
[135] K. Gelderman, L. Lee, and S.W. Donne, J. Chem. Educ. **84**, 685 (2007).
[136] A. Hankin, F.E. Bedoya-Lora, J.C. Alexander, A. Regoutz, and G.H. Kelsall, J. Mater. Chem. A **7**, 26162 (2019).
[137] N. Kruse and S. Chenakin, Applied Catalysis A: General **391**, 367 (2011).
[138] T.M. Wang, S.K. Zheng, W.C. Hao, and C. Wang, Surface and Coatings Technology **155**, 141 (2002).
[139] Z.W. Seh, S. Liu, M. Low, S.-Y. Zhang, Z. Liu, A. Mlayah, and M.-Y. Han, Adv. Mater. **24**, 2310 (2012).
[140] E.D. Palik, *Handbook of Optical Constants of Solids* (Academic press, Orlando San Diego New York, 1985).
[141] P.B. Johnson and R.W. Christy, Phys. Rev. B **6**, 4370 (1972).
[142] L. Lin, Y. Ma, J. Wu, F. Pang, J. Ge, S. Sui, Y. Yao, R. Qi, Y. Cheng, C. Duan, J. Chu, and R. Huang, J. Phys. Chem. C **123**, 20949 (2019).
[143] N. Dwivedi, R.J. Yeo, H.R. Tan, R. Stangl, A.G. Aberle, C.S. Bhatia, A. Danner, and B. Liao, Adv. Funct. Mater. **28**, 1707018 (2018).
[144] J. Lei, X. Li, W. Li, F. Sun, D. Lu, and J. Yi, International Journal of Hydrogen Energy **36**, 8167 (2011).
[145] X. Zhang, F. Zhang, and K.-Y. Chan, Applied Catalysis A: General **284**, 193 (2005).
[146] W. Wang, M. Tian, A. Abdulagatov, S.M. George, Y.-C. Lee, and R. Yang, Nano Lett. **12**, 655 (2012).
[147] J. Wang, H. Shao, S. Ren, A. Hu, and M. Li, Applied Surface Science **539**, 148045 (2021).

[148] P. Champigneux, C. Renault-Sentenac, D. Bourrier, C. Rossi, M.-L. Delia, and A. Bergel, Bioelectrochemistry **128**, 17 (2019).
[149] E. Eustache, P. Tilmant, L. Morgenroth, P. Roussel, G. Patriarche, D. Troadec, N. Rolland, T. Brousse, and C. Lethien, Adv. Energy Mater. **4**, 1301612 (2014).
[150] M.-I. Mendoza-Diaz, A. Lecestre, L. Salvagnac, B. Bounor, D. Pech, M. Djafari-Rouhani, A. Esteve, and C. Rossi, Applied Surface Science **588**, 152919 (2022).
[151] S. Trasatti and O.A. Petrii, Pure and Applied Chemistry **63**, 711 (1991).
[152] M. Łukaszewski, Soszko, M, and Czerwiński, A, Int. J. Electrochem. Sci. 4442 (2016).
[153] H. Jansen, M. de Boer, R. Legtenberg, and M. Elwenspoek, J. Micromech. Microeng. **5**, 115 (1995).
[154] E. Silva Junior, F.A. La Porta, M.S. Liu, J. Andrés, J.A. Varela, and E. Longo, Dalton Trans. **44**, 3159 (2015).
[155] W.L. Winterbottom, Acta Metallurgica **15**, 303 (1967).
[156] G. Pardon, H.K. Gatty, G. Stemme, W. van der Wijngaart, and N. Roxhed, Nanotechnology **24**, 015602 (2013).
[157] B.-R. Chen, C. George, Y. Lin, L. Hu, L. Crosby, X. Hu, P.C. Stair, L.D. Marks, K.R. Poeppelmeier, R.P. Van Duyne, and M.J. Bedzyk, Surface Science **648**, 291 (2016).
[158] Q. Zhao, J. Xu, X.Y. Xu, Z. Wang, and D.P. Yu, Appl. Phys. Lett. **85**, 5331 (2004).
[159] A.D. Elliot, Acta Crystallogr B Struct Sci **66**, 271 (2010).
[160] J. Kim-Zajonz, S. Werner, and H. Schulz, editors , Zeitschrift Für Kristallographie - Crystalline Materials **214**, 324 (1999).
[161] Y. Xiong, J. Chen, B. Wiley, Y. Xia, Y. Yin, and Z.-Y. Li, Nano Lett. **5**, 1237 (2005).
[162] P.-F. Ho and K.-M. Chi, Nanotechnology **15**, 1059 (2004).
[163] E.A. Davis and N.F. Mott, Philosophical Magazine **22**, 0903 (1970).
[164] J.-H. Kim, A. Mirzaei, H.W. Kim, and S.S. Kim, Sensors and Actuators B: Chemical **297**, 126693 (2019).
[165] K.H. Leong, H.Y. Chu, S. Ibrahim, and P. Saravanan, Beilstein J. Nanotechnol. **6**, 428 (2015).
[166] E. Coy, K. Siuzdak, M. Pavlenko, K. Załęski, O. Graniel, M. Ziółek, S. Balme, P. Miele, M. Weber, M. Bechelany, and I. Iatsunskyi, Chemical Engineering Journal **392**, 123702 (2020).
[167] A.A. Nada, B.O. Orimolade, H.H. El-Maghrabi, B.A. Koiki, M. Rivallin, M.F. Bekheet, R. Viter, D. Damberga, G. Lesage, I. Iatsunskyi, E. Coy, M. Cretin, O.A. Arotiba, and M. Bechelany, Applied Materials Today **24**, 101129 (2021).
[168] A. Erbe, S. Nayak, Y.-H. Chen, F. Niu, M. Pander, S. Tecklenburg, and C. Toparli, in *Encyclopedia of Interfacial Chemistry* (Elsevier, 2018), pp. 199–219.
[169] C.C. Mercado, F.J. Knorr, J.L. McHale, S.M. Usmani, A.S. Ichimura, and L.V. Saraf, J. Phys. Chem. C **116**, 10796 (2012).
[170] R.E. Rex, Y. Yang, F.J. Knorr, J.Z. Zhang, Y. Li, and J.L. McHale, J. Phys. Chem. C **120**, 3530 (2016).
[171] M.V. Dozzi, C. D'Andrea, B. Ohtani, G. Valentini, and E. Selli, J. Phys. Chem. C **117**, 25586 (2013).
[172] D.K. Pallotti, L. Passoni, P. Maddalena, F. Di Fonzo, and S. Lettieri, J. Phys. Chem. C **121**, 9011 (2017).
[173] R.E. Rex, F.J. Knorr, and J.L. McHale, J. Phys. Chem. C **118**, 16831 (2014).
[174] S. Leytner and J.T. Hupp, Chemical Physics Letters **330**, 231 (2000).
[175] W.F. Zhang, M.S. Zhang, Z. Yin, and Q. Chen, Applied Physics B: Lasers and Optics **70**, 261 (2000).
[176] L. Mascaretti, V. Russo, G. Zoppellaro, A. Lucotti, C.S. Casari, Š. Kment, A. Naldoni, and A. Li Bassi, J. Phys. Chem. C **123**, 11292 (2019).
[177] F.J. Knorr, C.C. Mercado, and J.L. McHale, J. Phys. Chem. C **112**, 12786 (2008).
[178] F.J. Knorr and J.L. McHale, J. Phys. Chem. C **117**, 13654 (2013).
[179] M.I. Mendoza Diaz, A. Balocchi, K. Oyekan, K. Tan, W.G. Vandenberghe, A. Esteve, and C. Rossi, Dalton Trans. 10.1039.D2DT01871C (2022).
[180] Z. Matěj, R. Kužel, and L. Nichtová, Metall and Mat Trans A **42**, 3323 (2011).
[181] J.P. Perdew, K. Burke, and M. Ernzerhof, Phys. Rev. Lett. **77**, 3865 (1996).
[182] G. Kresse and J. Furthmüller, Computational Materials Science **6**, 15 (1996).
[183] G. Kresse and J. Hafner, Phys. Rev. B **47**, 558 (1993).
[184] G. Kresse and J. Hafner, Phys. Rev. B **49**, 14251 (1994).
[185] G. Kresse and D. Joubert, Phys. Rev. B **59**, 1758 (1999).
[186] P.E. Blöchl, Phys. Rev. B **50**, 17953 (1994).
[187] B.J. Berne, G. Ciccotti, and D.F. Coker, in World Scientific (1998), pp. 385–404.
[188] X. Liu and J. Fu, Optik **206**, 164342 (2020).

[189] J.K. Burdett, T. Hughbanks, G.J. Miller, J.W. Richardson, and J.V. Smith, J. Am. Chem. Soc. **109**, 3639 (1987).
[190] O. Secundino-Sánchez, J. Diaz-Reyes, J.F. Sánchez-Ramírez, and A.J.L. Jiménez-Pérez, Rev. Mex. Fís. **65**, 459 (2019).
[191] X. Fu, L.A. Clark, Q. Yang, and M.A. Anderson, Environ. Sci. Technol. **30**, 647 (1996).
[192] G.H. Yue, P.X. Yan, and J. Wang, Journal of Crystal Growth **274**, 464 (2005).
[193] K. Zhang, Q. Liu, H. Wang, R. Zhang, C. Wu, and J.R. Gong, Small **9**, 2452 (2013).
[194] L. Miao, P. Jin, K. Kaneko, A. Terai, N. Nabatova-Gabain, and S. Tanemura, Applied Surface Science **212–213**, 255 (2003).
[195] G.-H. Lee and J.-M. Zuo, J Mater Sci **46**, 1780 (2011).
[196] R.W. Hoffman, Thin Solid Films **34**, 185 (1976).
[197] A.S. Barnard and L.A. Curtiss, Nano Lett. **5**, 1261 (2005).
[198] M. Lazzeri, A. Vittadini, and A. Selloni, Phys. Rev. B **63**, 155409 (2001).
[199] L. Liang, P. Ling, Y. Li, L. Li, J. Liu, Q. Luo, H. Zhang, Q. Xu, Y. Pan, J. Zhu, B. Ye, and Y. Sun, Sci. China Chem. **64**, 953 (2021).
[200] D.W. Bahnemann, M. Hilgendorff, and R. Memming, J. Phys. Chem. B **101**, 4265 (1997).
[201] V.-A. Glezakou and R. Rousseau, Nature Mater **17**, 856 (2018).
[202] C. Jin, B. Liu, Z. Lei, and J. Sun, Nanoscale Res Lett **10**, 95 (2015).
[203] R. Sanjinés, H. Tang, H. Berger, F. Gozzo, G. Margaritondo, and F. Lévy, Journal of Applied Physics **75**, 2945 (1994).
[204] E. Finazzi, C. Di Valentin, and G. Pacchioni, J. Phys. Chem. C **113**, 3382 (2009).
[205] H. Lin, L. Li, M. Zhao, X. Huang, X. Chen, G. Li, and R. Yu, J. Am. Chem. Soc. **134**, 8328 (2012).
[206] B. Choudhury, M. Dey, and A. Choudhury, Int Nano Lett **3**, 25 (2013).
[207] Y. Von Lim, T.I. Wong, and S. Wang, Thin Solid Films **518**, e107 (2010).
[208] M. Xing, J. Zhang, F. Chen, and B. Tian, Chem. Commun. **47**, 4947 (2011).
[209] A.H. Sofi, M.A. Shah, and K. Asokan, Journal of Elec Materi **47**, 1344 (2018).
[210] J.D. Dow and D. Redfield, Phys. Rev. B **5**, 594 (1972).
[211] B. Larangot, C. Rossi, T. Camps, A. Berthold, P. Pham, D. Briand, M. Puig-Vidal, P. Miribel, D. Esteve, N. De Rooij, E. Montanes, G. Macias, and J. Samitier, in *NanoTech 2002 - "At the Edge of Revolution"* (American Institute of Aeronautics and Astronautics, Houston, Texas, 2002).
[212] J.-L. Pouchairet and C. Rossi, Micromachines **12**, 118 (2021).
[213] H. Wang, B. Julien, D.J. Kline, Z. Alibay, M.C. Rehwoldt, C. Rossi, and M.R. Zachariah, J. Phys. Chem. C **124**, 13679 (2020).
[214] B. Larangot, V. Conedera, P. Dubreuil, T. Do Conto, and C. Rossi, in (Avignon, France, n.d.).
[215] S. Orieux, C. Rossi, and D. Estève, Review of Scientific Instruments **73**, 2694 (2002).
[216] C. Rossi, Prop., Explos., Pyrotech. **44**, 94 (2019).
[217] H. Pezous, C. Rossi, M. Sanchez, F. Mathieu, X. Dollat, S. Charlot, and V. Conédéra, Journal of Physics and Chemistry of Solids **71**, 75 (2010).
[218] G.A. Ardila Rodríguez, S. Suhard, C. Rossi, D. Estève, P. Fau, S. Sabo-Etienne, A.F. Mingotaud, M. Mauzac, and B. Chaudret, J. Micromech. Microeng. **19**, 015006 (2009).
[219] C. Rossi, B. Larangot, P.-Q. Pham, D. Briand, N.F. de Rooij, M. Puig-Vidal, and J. Samitier, J. Microelectromech. Syst. **15**, 1805 (2006).
[220] C. Rossi, M.D. Rouhani, and D. Estève, Sensors and Actuators A: Physical **87**, 96 (2000).
[221] L. Glavier, A. Nicollet, F. Jouot, B. Martin, J. Barberon, L. Renaud, and C. Rossi, Prop., Explos., Pyrotech. **42**, 308 (2017).
[222] S. Orieux, C. Rossi, and D. Estève, Sensors and Actuators A: Physical **101**, 383 (2002).
[223] G. Lahiner, A. Nicollet, J. Zapata, L. Marín, N. Richard, M.D. Rouhani, C. Rossi, and A. Estève, Journal of Applied Physics **122**, 155105 (2017).
[224] I. Abdallah, J. Zapata, G. Lahiner, B. Warot-Fonrose, J. Cure, Y. Chabal, A. Esteve, and C. Rossi, ACS Appl. Energy Mater. **1**, 1762 (2018).
[225] G. Lahiner, J. Zappata, J. Cure, N. Richard, M. Djafari-Rouhani, A. Estève, and C. Rossi, Combustion Theory and Modelling **23**, 700 (2019).
[226] L. Marín, Y. Gao, M. Vallet, I. Abdallah, B. Warot-Fonrose, C. Tenailleau, A.T. Lucero, J. Kim, A. Esteve, Y.J. Chabal, and C. Rossi, Langmuir **33**, 11086 (2017).
[227] G. Lahiner, A. Nicollet, J. Zapata, L. Marín, N. Richard, M.D. Rouhani, C. Rossi, and A. Estève, Journal of Applied Physics **122**, 155105 (2017).
[228] V. Baijot, D.-R. Mehdi, C. Rossi, and A. Estève, Combustion and Flame **180**, 10 (2017).

[229] L. Marín, B. Warot-Fonrose, A. Estève, Y.J. Chabal, L. Alfredo Rodriguez, and C. Rossi, ACS Appl. Mater. Interfaces **8**, 13104 (2016).
[230] S. Palussière, J. Cure, A. Nicollet, P. Fau, K. Fajerwerg, M.L. Kahn, A. Estève, and C. Rossi, Phys. Chem. Chem. Phys. **21**, 16180 (2019).
[231] T. Wu, G. Lahiner, C. Tenailleau, B. Reig, T. Hungria, A. Esteve, and C. Rossi, Chemical Engineering Journal **418**, 129432 (2021).
[232] B. Julien, J. Cure, L. Salvagnac, C. Josse, A. Esteve, and C. Rossi, ACS Appl. Nano Mater. **3**, 2562 (2020).
[233] E. Tichtchenko, A. Estève, and C. Rossi, Combustion and Flame **228**, 173 (2021).
[234] M. Mursalat, C. Huang, B. Julien, M. Schoenitz, A. Esteve, C. Rossi, and E.L. Dreizin, ACS Appl. Nano Mater. **4**, 3811 (2021).
[235] B. Julien, H. Wang, E. Tichtchenko, S. Pelloquin, A. Esteve, M.R. Zachariah, and C. Rossi, Nanotechnology **32**, 215401 (2021).
[236] T. Wu, F. Sevely, B. Julien, F. Sodre, J. Cure, C. Tenailleau, A. Esteve, and C. Rossi, Combustion and Flame **219**, 478 (2020).
[237] A. Nicollet, L. Salvagnac, V. Baijot, A. Estève, and C. Rossi, Sensors and Actuators A: Physical **273**, 249 (2018).
[238] C. Lanthony, J.M. Ducéré, M.D. Rouhani, A. Hemeryck, A. Estève, and C. Rossi, The Journal of Chemical Physics **137**, 094707 (2012).
[239] C. Lanthony, M. Guiltat, J.M. Ducéré, A. Verdier, A. Hémeryck, M. Djafari-Rouhani, C. Rossi, Y.J. Chabal, and A. Estève, ACS Appl. Mater. Interfaces **6**, 15086 (2014).
[240] T. Calais, D. Bourrier, A. Bancaud, Y. Chabal, A. Estève, and C. Rossi, Langmuir **33**, 12193 (2017).
[241] T. Wu, B. Julien, H. Wang, S. Pelloquin, A. Esteve, M.R. Zachariah, and C. Rossi, ACS Appl. Energy Mater. **5**, 3189 (2022).
[242] S. Orieux, C. Rossi, and D. Estève, Sensors and Actuators A: Physical **101**, 383 (2002).
[243] F. Sevely, T. Wu, F.S. Ferreira de Sousa, L. Seguier, V. Brossa, S. Charlot, A. Esteve, and C. Rossi, Sensors and Actuators A: Physical **346**, 113838 (2022).